SOCIETÀ NAZIONALE DI SCIENZE LETTERE E ARTI IN NAPOLI

RENDICONTO DELL'ACCADEMIA DELLE SCIENZE FISICHE E MATEMATICHE

SERIE IV - VOL. LXXXII - ANNO CLIV

(2015)

LIGUORI EDITORE

La pubblicazione è stata resa possibile dai contributi
– della Regione Campania
– della Fondazione Banco di Napoli
– del Ministero dell'Istruzione, Università e Ricerca
– del Ministero per i Beni Culturali
– dell'associazione "Amici della Società Nazionale di Scienze Lettere e Arti in Napoli"
– del Dipartimento di Matematica e Applicazioni "Renato Caccioppoli"

N. 82 - Dicembre 2015

ISSN 0370-3568

Direttore responsabile: Carlo Sbordone

Prima edizione italiana Dicembre 2015
Finito di stampare in Italia nel mese di Dicembre 2015 da Liguori Editore - Napoli

Autorizzazione del Tribunale di Napoli n. 780 del 14/08/1954

ISBN-13 **978 - 88 - 207 - 6662 - 7**

La carta utilizzata per la stampa di questo volume è inalterabile, priva di acidi, a PH neutro, conforme alle norme UNI EN ISO 9706 ∞, realizzata con materie prime fibrose vergini provenienti da piantagioni rinnovabili e prodotti ausiliari assolutamente naturali, non inquinanti e totalmente biodegradabili
(FSC, PEFC, ISO 14001, Paper Profile, EMAS).

Indice

Appendice

Rend. Acc. Sc. fis. mat. Napoli
Vol. LXXXII, (2015) pp. 1-45

Geometric Action Principles in Classical Dynamics

Nota di Giovanni Romano*, Raffaele Barretta* e Marina Diaco*

Presentata dal socio Giovanni Romano
(Adunanza del 16 gennaio, 2015)

Key words: Action principles, continuum dynamics, control manifolds, Hamilton principle, Maupertuis principle, Poincaré-Cartan principle, Hamilton-Pontryagin principle.

Abstract - General principles of classical dynamics are usually developed in the framework of phase spaces, that is tangent or cotangent bundles over the control manifold. A more effective approach is proposed here by applying POINCARÉ-CARTAN theory of differential forms directly to the control manifold, so that lifting operations are completely avoided. The basic distinction between action principles and stationarity of functionals is pointed out. The EULER-LAGRANGE-HAMILTON variational theory is formulated without end constraints on the trajectory variations. A careful treatment of natural and essential conditions for the variational problem leads to a proper formulation of MAUPERTUIS action principle and to assess its equivalence to HAMILTON principle. POINCARÉ-CARTAN and HAMILTON-PONTRYAGIN hybrid principles, involving vertical variations of vector and covector fields, are addressed with an appropriate geometric approach.

Riassunto - I principi della dinamica classica sono usualmente sviluppati nel contesto di spazi delle fasi e cioè di fibrati tangenti o cotangenti sulla varietà di controllo. Si propone qui una impostazione più efficace la quale, applicando la teoria di POINCARÉ-CARTAN delle forme differenziali direttamente alla varietà di controllo, consente di evitare il sollevamento a spazi delle fasi. Una basica distinzione tra principi d'azione e stazionarietà di funzionali è posta in luce. La teoria variazionale di EULER-LAGRANGE-HAMILTON è svilup-

*Department of Structures for Engineering and Architecture, University of Naples Federico II, via Claudio 21, 80125 - Naples, Italy. e-mail: romano@unina.it, rabarret@unina.it, diaco@unina.it.

pata senza imporre condizioni sui punti estremi della traiettoria. Una attenta trattazione delle condizioni naturali ed essenziali per il problema variazionale conduce ad una corretta formulazione del principio di azione di MAUPERTUIS e ad asserirne l'equivalenza al principio di HAMILTON. I principi ibridi di POINCARÉ-CARTAN ed HAMILTON-PONTRYAGIN, con variazioni verticali di campi vettoriali e covettoriali, sono discussi in un appropriato contesto geometrico.

1 INTRODUCTION

Classical dynamics may be conventionally considered to be born about 1687 with NEWTON's *Principia* and grew up to a well-developed theory in the fundamental works by D'ALEMBERT, EULER, LAGRANGE, POISSON, HAMILTON, JACOBI, BERTRAND, during the XVIII century and the first half of the XIX century (d'Alembert, 1743; Euler, 1744, 1761; Lagrange, 1788; Poisson, 1811; Hamilton, 1834, 1940; Jacobi, 1837a,b, 1884; Bertrand, 1852).

The differential geometric point of view, with the introduction of the notions of nonlinear configuration manifolds, convective derivatives along a motion and derivatives according to a parallel transport, is based on notions and methods mainly due to SOPHUS LIE, HENRI POINCARÉ, ÉLIE CARTAN (Lie and Engel, 1888-1890-1893; Poincaré, 1892-1893-1899; Cartan É., 1922) and accounted, for instance, in (Klein, 1962; Godbillon, 1969; Souriau, 1970; Choquet-Bruhat, 1970; Deschamps, 1970; Spivak, 1970; Choquet-DeWitt-Dillard, 1982; Romano G., 2007).

Classical analytical mechanics deals with particle dynamics or rigid body motions. Extensions to continuous systems were treated in (Arnold, 1974; Abraham and Marsden, 1988; Marsden and Hughes, 1983; Abraham et al., 2002), by considering manifolds modeled on BANACH spaces. In these treatments the formal structure of the dynamics of finite dimensional systems is however still reproduced and most results are still proposed in coordinates notation.

Our presentation makes no essential use of coordinates, with all notions and results defined and expressed in intrinsic geometrical terms. For finite dimensional control manifolds, the translation into coordinate notation is however straightforward and is explicitly reported to provide a direct comparison with existing treatments. The advantages of a geometric formulation are conceptual, since mechanical objects are properly described and retain their respective roles and rules of mutually interacting entities, and also operational, since a general formulation permits to choose the representation more suitable for the problem at hand.

We follow the common choice of taking HAMILTON principle, inspired by earlier ideas by FERMAT and HUYGENS in optics, as the basic axiom of dynamics since it has the pleasant flavour of an extremality property and, much more than this, because it leads in a natural and direct way to a general formulation of LAGRANGE dynamics.

In this respect we do not share the opinion in (Abraham and Marsden, 1988, Part II), *Analytical Dynamics*, section 3.8 *Variational Principles in Mechanics*, where variational principles are placed on the same ground of differential equations, with a preference for the latter in operative tasks. However, the leading position of action principles has been subsequently acknowledged in (Marsden, Patrick and Shkoller, 1998).

In fact, while it is certainly true that differential formulations are the ones more suitable for specific analytical tasks, on the other hand variational formulations, in the form of action principles, are more basic. The main motivation is that action principles just require the notions of LAGRANGE function, mass form and motion in the metric space-time.

According to the principle of geometric naturality, exposed in (Romano and Barretta, 2011, 2013; Romano et al., 2014a,b,c), the formulation of laws of dynamics must involve, as geometric objects, only the space metric in the event manifold and the motion along the trajectory. This requirement gives to integral variational principles of dynamics, a leading position in the theory. On the contrary operative differential formulations are based on the choice of a connection in the events manifold. Moreover, basic issues such as invariance under change of observer, are most readily and properly discussed in terms of action principles formulated with intrinsic treatments.

Last but not least, effective computational strategies make direct reference to variational formulations (Bailey, 1975; Riff and Baruch, 1984; Borri et al., 1985; Peters and Izadpanah, 1988; Borri et al., 1992; Borri and Bottasso, 1993). Computational issues will however not be explicitly dealt with in this contribution but a detailed geometric investigation is in progress.

Fine mathematical issues concerning calculus of variations, such as the ones discussed in (Ambrosio et al., 2000; Fonseca and Leoni, 2007), are outside the range of this presentation.

In section 2 we provide the abstract definition of an *action principle* as a variational condition for the integral of a differential form along a path which is dragged by virtual motions. No fixed end point conditions are imposed and the effect of dynamical forces is included in the formulation. A special attention is devoted to the required extension of the domain of definition of the governing differential form, an issue usually not considered in treatments akin to classical analytical mechanics.

Even in most appreciable formulations, such as (Cartan H., 1967), variations are intended to be evaluated on a functional, expressed as the integral of a differential form, along a class of curves. This interpretation leads to difficult and also critical statements concerning the topological properties of the functional space in which stationarity is to be imposed, especially if the fixed ends condition is retained (Oliva, 1798; Terra and Kobayashi, 2004a,b).

In continuum dynamics, the differential forms to be integrated on the trajectory depend on the velocity field and on the mass form, and these fields are defined only on the trajectory. In performing the variations, an extension by push along each virtual flow must then be assumed. Therefore, variational formulations in dynamics do not involve functionals to be evaluated on a class of curves.

A synthesis of notions, definitions and results of differential geometry, strictly needed in the paper, is provided in the appendix for reference and readers' convenience.

Sect. 3 presents a brief introduction to space-time kinematics and a summary of relevant definitions of mechanical objects. Sect. 4 and 5 are dedicated to the formal construction of the control manifold by means of a correspondence which is an injective immersion in the configuration manifold. Fields based in body placements are then translated into geometrico-dynamical objects in the control manifold.

HAMILTON principle and LAGRANGE action principle are enunciated and discussed in detail in Sects.6 and 7 and NOETHER theorem is deduced as a special case. MAUPERTUIS action principle is revisited in Sect.8 in the general form of a constrained action principle, in which the constraint of mechanical power balance is imposed on virtual velocities, and its equivalence to all other action principles is assessed. POINCARÉ-CARTAN action principle is introduced in Sect.9 and DONKIN theorem provides the relations to transform the canonical equation of dynamics in terms of the momentum field. Extensions to hybrid POINCARÉ-CARTAN and HAMILTON-PONTRYAGIN action principles, by the inclusion of vertical virtual variations of tangent and cotangent fields, are discussed in Sect.10.

Sect. 11 is dedicated to the formulation of action principles in terms of time integrals, and to amendment of non geometric treatments. Formulations in terms of a linear connection provide powerful theoretical and computational tools, when translated from the control manifold to the event manifold.

Comments and remarks are exposed in the final Sect.12, with a synoptic table collecting main issues and results.

2 ABSTRACT ACTION PRINCIPLE AND EULER CONDITIONS

A status of the system is described by a point in $\mathbf{M}$, the *state space*.

Definition 2.1 (Action integral). *The action integral associated with a path* Γ *in the state-space* $\mathbf{M}$ *is the signed-length of the* $1D$ *oriented compact submanifold* Γ, *evaluated according to the action* 1*-form* ω^1 *on* Γ*:*

$$\int_\Gamma \omega^1 . \tag{1}$$

A proper statement of the action principle requires a definition of the *virtual displacements* along which the trajectory is assumed to be varied and a definite criterion to extend the domain of definition of the action 1-form on the sheet spanned by the trajectory dragged by the virtual flow.

In formulating an action principle, virtual velocities at Γ are assumed to belong to a suitable set $\mathscr{H}_{\mathbf{M}}$ of sections of the tangent bundle $T_\Gamma\mathbf{M}$. Source terms are represented by differential forms α^1, α^2 on $T_\Gamma\mathbf{M}$.

The source 2-form α^2 is *potential* if it is defined on a neighbourhood $U(\Gamma) \subset \mathbf{M}$ of the path and is exact. This means that there exists a differential 1-form $\beta^1 : U(\Gamma) \mapsto T^*\mathbf{M}$ such that $\alpha^2 = d\beta^1$, with d exterior differentiation on $\mathbf{M}$.

Definition 2.2 (Abstract action principle). *An action principle, governed by differential 1-form ω^1 on $\mathbf{M}$, is a variational condition involving the rate of geometric variation of the integral of the action form along a path $\Gamma \subset \mathbf{M}$, due to a virtual flow, and source terms, distributed along the path (source 2-form α^2) and concentrated at singular points* SING(Γ) *(source 1-form α^1), evaluated on the virtual velocity $\delta\mathbf{v} = \partial_{\lambda=0}\mathbf{Fl}^{\mathbf{v}}_\lambda \in \mathscr{H}_{\mathbf{M}}$ of virtual flows $\mathbf{Fl}^{\mathbf{v}}_\lambda : \Gamma \mapsto \mathbf{M}$*

$$\boxed{\partial_{\lambda=0} \int_{\mathbf{Fl}^{\mathbf{v}}_\lambda(\Gamma)} \omega^1 - \oint_{\partial\Gamma} \omega^1 \cdot \delta\mathbf{v} = \int_\Gamma \alpha^2 \cdot \delta\mathbf{v} + \oint_{\Gamma_{\mathrm{SING}}} \alpha^1 \cdot \delta\mathbf{v}.} \tag{2}$$

A path Γ fulfilling the action principle is called a *trajectory* for the action form ω^1, under the effect of the sources α^1 and α^2.

Eq. (2) may be stated by saying that the rate of variation along the virtual displacement of the ω^1-integral on the oriented trajectory Γ, minus the outward boundary flux of the ω^1-virtual power (*formule de* JOSEPH BERTRAND (Cartan H., 1967, p. 132)), is equal to the virtual power performed by the source form.

Denoting by $\mathbf{x}_1$ and $\mathbf{x}_2$ the initial and final end points of Γ, it is $\partial\Gamma = \mathbf{x}_2 - \mathbf{x}_1$ (a 0-chain) and the boundary integral may be written as

$$\oint_{\partial\Gamma} \omega^1 \cdot \delta\mathbf{v} = (\omega^1 \cdot \delta\mathbf{v})(\mathbf{x}_2) - (\omega^1 \cdot \delta\mathbf{v})(\mathbf{x}_1). \tag{3}$$

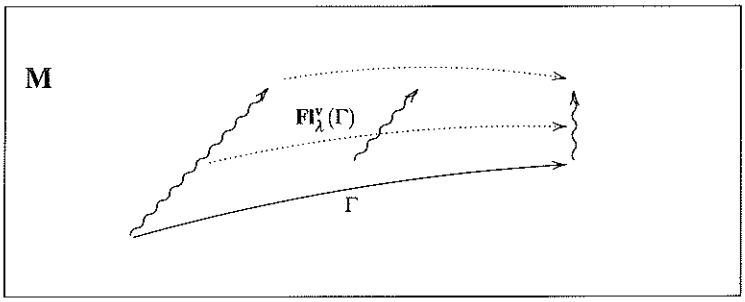

(4)

Definition 2.3 (Extremality principle). *The variational condition in the geometric action principle, in absence of source terms, takes the expression of an extremality condition*

$$\boxed{\partial_{\lambda=0} \int_{\mathbf{Fl}^{\mathbf{v}}_{\lambda}(\Gamma)} \omega^1 - \oint_{\partial\Gamma} \omega^1 \cdot \delta\mathbf{v} = 0.} \tag{5}$$

Eq. (5) *has a simple motivation when interpreting* ω^1 *as a measure of length. In changing the position of a geodesic by a virtual flow, the length tends to be invariant when boundary virtual velocity vectors fulfill the* equiprojectivity *property (vanishing of Eq.* (3)*). A familiar special instance is a straight line in* EUCLID *space.*

When the differential form to be integrated is independent of the parametrization of the integration path Γ, also the action principle, as enunciated in Eq. (2), is purely geometrical, in the sense that the variational condition results to be independent of the parametrization. This is indeed the case for FERMAT principle of least time in geometrical optics.

Time parametrization plays instead a basic role in dynamics and so the governing action principle must depend on the trajectory parametrization.

The issue is enlightened by the treatment provided in the sequel by observing explicitly that the 1-form involved in the stationarity action principle is in fact expressed by the composition of the LAGRANGE scalar-valued map with the velocity field. The governing 1-form depends then on the velocity and hence the time parametrization of the trajectory takes a central position in the theory.

The new approach to geometric dynamics reveals also that an intrinsic treatment is feasible by considering only fields in the control manifold.

Lifting to the tangent bundle can thus be bypassed, with the advantage of simplicity and reconciliation with (but also amendments to) standard treatments in coordinates. A full discussion in provided in the sequel.

The necessary and sufficient differential condition for a path to be a trajectory, a result due to Euler (1744), is provided by the next theorem.

The classical result deals with regular paths and fixed end points. The new statement considers displaceable end points and piecewise regular paths, so that extremality is expressed in terms of differential and jump conditions.

It is to be remarked that, as already evidenced in Sect. 1, the explicit appearance of the final point of the trajectory in the expression of the action principle, plays a basic role in computational implementation of dynamical problems.

Theorem 2.1 (Euler's condition). *A path $\Gamma \subset \mathbf{M}$ is a trajectory if and only if the tangent vector field $\mathbf{v}_\Gamma : \Gamma \mapsto T\Gamma$ meets, at regular points, the differential condition*

$$(d\omega^1 - \alpha^2) \cdot \delta\mathbf{v} \cdot \mathbf{v}_\Gamma = 0\,, \quad \forall\, \delta\mathbf{v} \in \mathscr{H}_\mathbf{M}\,, \tag{6}$$

and, at singularity interfaces, the jump conditions

$$[[\omega^1 \cdot \delta\mathbf{v}]] = \alpha^1\,, \quad \forall\, \delta\mathbf{v} \in \mathscr{H}_\mathbf{M}\,. \tag{7}$$

Proof. Applying the integral extrusion formula:

$$\partial_{\lambda=0} \int_{\mathbf{FI}^\mathbf{v}_\lambda(\Gamma)} \omega^1 - \oint_{\partial\Gamma} \omega^1 \cdot \delta\mathbf{v} = \int_\Gamma d\omega^1 \cdot \delta\mathbf{v}\,, \tag{8}$$

the result follows upon localization. ■

Remark 2.1 (Faithful and hybrid principles). *A special nomenclature is adopted in the present paper. Variational statements conforming to the definition in Eq.* (2) *will be labeled as (*faithful*)* action principles. *In these action principles a single action* 1*-form is involved both in the line integral and in the boundary integral. Other variational statements in which two distinct* 1*-forms appear in the line integral and in the boundary integral, will be instead labeled as* hybrid action principles. *The distinction is significant because only* faithful *action principles are associated with an* EULER *condition expressed in terms of the exterior derivative of a* 1*-form, as shown by the abstract treatment leading to Eq.* (6) *of Th. 2.1.*

Remark 2.2 (Action principles vs stationarity of functionals). *As evidenced by Def. 2.2, the variational condition enunciated in the statement of an action principle, is not the stationarity condition for a functional. The basic distinction is that in an action principle the involved* 1*-form is defined only on the* 1*D trajectory manifold and is declaratively extended along each virtual flow in a natural manner. So, there is in fact no functional to be differentiated along virtual directions. Rather, in an action principle, the extensions of the* 1*-form, to be integrated on dragged trajectories, are performed according to each dragging virtual flow. The distinction is further put into evidence by the formulation expressed by Eq.* (2)*, with the elimination of the fixed-ends condition, usually included into the statement of action principles, as depicted in frame* (4)*, and with the inclusion of the boundary integral and of the effects of distributed and singular sources.*

3 KINEMATICS IN THE EVENT MANIFOLD

In the 4D manifold of events $\mathbf{e} \in \mathscr{E}$ each observer defines a *time-projection* $t_{\mathscr{E}} : \mathscr{E} \mapsto \mathscr{Z}$, that is a surjective submersion on the real line $\mathscr{Z}$ of time instants[1] and a vector field $\mathbf{Z} : \mathscr{E} \mapsto T\mathscr{E}$ of *time-arrows* in the tangent bundle $\tau_{\mathscr{E}} : T\mathscr{E} \mapsto \mathscr{E}$, fulfilling tuning $t_{\mathscr{E}} \uparrow \mathbf{Z} := 1$, as described by the commutative diagram

$$\begin{tikzcd} \mathscr{Z} \arrow[r, "1"] & T\mathscr{Z} \\ \mathscr{E} \arrow[u, "t_{\mathscr{E}}"] \arrow[r, "\mathbf{Z}"] & T\mathscr{E} \arrow[u, "dt_{\mathscr{E}}"'] \end{tikzcd} \quad \Longleftrightarrow \quad \langle dt_{\mathscr{E}}, \mathbf{Z} \rangle = 1 \circ t_{\mathscr{E}} . \tag{9}$$

A double foliation of the 4D events manifold $\mathscr{E}$ into complementary 3D *space-slices* $\mathscr{S}$ of *isochronous* events (with a same corresponding time instant) and 1D *time-lines* of *isotopic* events (with a same corresponding space location) is thus introduced according to FROBENIUS theorem.

The projector $dt_{\mathscr{E}} \otimes \mathbf{Z} : T\mathscr{E} \mapsto T\mathscr{E}$ splits the tangent bundle into complementary time-vertical $V\mathscr{E}$ and time-horizontal $H\mathscr{E}$ sub-bundles, with time-vertical vectors in the kernel of $dt_{\mathscr{E}} : T\mathscr{E} \mapsto T\mathscr{Z}$.

These sub-bundles are respectively called *space bundle* and *time bundle*.

In the familiar EUCLID setting of classical Mechanics, the time projection is the same for all observers (universality of time).

A reference frame $\{ \mathbf{d}_i ; i = 0, 1, 2, 3 \}$ for the event manifold is *adapted* if $\mathbf{d}_0 = \mathbf{Z}$ and $\mathbf{d}_i \in V\mathscr{E}$, $i = 1, 2, 3$.

Definition 3.1 (Trajectory). *The* trajectory manifold *is the geometric object investigated in Mechanics, characterized by an embedding*[2] $\mathbf{i} : \mathscr{T} \mapsto \mathscr{E}$ *into the event manifold* $\mathscr{E}$ *such that the image* $\mathscr{T}_{\mathscr{E}} := \mathbf{i}(\mathscr{T})$ *is a submanifold.*

Definition 3.2 (Motion). *The* motion *along the trajectory*

$$\{ \varphi_\alpha^{\mathscr{T}} : \mathscr{T} \mapsto \mathscr{T} , \alpha \in \mathscr{Z} \}, \tag{10}$$

is a simultaneity preserving one-parameter family of maps fulfilling the composition rule

$$\varphi_\alpha^{\mathscr{T}} \circ \varphi_\beta^{\mathscr{T}} = \varphi_{(\alpha+\beta)}^{\mathscr{T}} , \tag{11}$$

for any pair of time-lapses $\alpha, \beta \in \mathscr{Z}$. *Each* $\varphi_\alpha^{\mathscr{T}} : \mathscr{T} \mapsto \mathscr{T}$ *is a* displacement.

---

[1] A submersion has a surjective differential at each point. *Zeit* is the German word for *Time*.

[2] An immersion has an injective differential at each point. An embedding is an injective immersion whose co-restriction is continuous with the inverse.

The trajectory will alternatively be considered as a $(1+n)$D manifold $\mathscr{T}$ by itself or as a submanifold $\mathscr{T}_{\mathscr{E}} = \mathbf{i}(\mathscr{T}) \subset \mathscr{E}$ of the event manifold.

Then, a coordinate system is adopted on $\mathscr{T}$ while an adapted 4D space-time coordinate system in $\mathscr{E}$ is adopted on $\mathscr{T}_{\mathscr{E}}$.

The trajectory inherits from the events manifold the time projection $t_{\mathscr{T}} := t_{\mathscr{E}} \circ \mathbf{i} : \mathscr{T} \mapsto \mathscr{Z}$ which defines a time-bundle denoted by $V\mathscr{T}$ and called the *material bundle*. A fiber of simultaneous events is a *body placement*, denoted by $\Omega \subset \mathscr{T}$.

The space-time displacement $\varphi_\alpha : \mathscr{T}_{\mathscr{E}} \mapsto \mathscr{T}_{\mathscr{E}}$ and the trajectory displacement $\varphi_\alpha^{\mathscr{T}} : \mathscr{T} \mapsto \mathscr{T}$ are related by the commutative diagram

$$\begin{tikzcd}
\mathscr{T}_{\mathscr{E}} \arrow[r, "\varphi_\alpha"] \arrow[d, bend right, "t_{\mathscr{E}}"'] & \mathscr{T}_{\mathscr{E}} \arrow[d, bend left, "t_{\mathscr{E}}"] \\
\mathscr{T} \arrow[u, "\mathbf{i}"] \arrow[r, "\varphi_\alpha^{\mathscr{T}}"] \arrow[d, "t_{\mathscr{T}}"'] & \mathscr{T} \arrow[u, "\mathbf{i}"'] \arrow[d, "t_{\mathscr{T}}"] \\
\mathscr{Z} \arrow[r, "t_\alpha"] & \mathscr{Z}
\end{tikzcd} \iff t_{\mathscr{E}} \circ \varphi_\alpha = t_\alpha \circ t_{\mathscr{E}}\,, \tag{12}$$

where the time translation $t_\alpha : \mathscr{Z} \mapsto \mathscr{Z}$ is defined by

$$t_\alpha(t) := t + \alpha\,, \quad t, \alpha \in \mathscr{Z}\,. \tag{13}$$

Definition 3.3 (Material particles and body manifold). *The physical notion of* material particle *corresponds in the geometric view to a time-parametrized curve of events in the trajectory, related by the motion as follows*

$$\mathbf{e}_1, \mathbf{e}_2 \in \mathscr{T} : \mathbf{e}_2 = \varphi_\alpha^{\mathscr{T}}(\mathbf{e}_1)\,. \tag{14}$$

Accordingly, we will say that a geometrical object is defined along *(not* at*) a material particle. Events belonging to a* material particle *form a class of equivalence and the quotient manifold so induced in the trajectory is the* body manifold.

The space-time *velocity* of the motion is defined by the derivative

$$\mathbf{v}_{\mathscr{E}} := \partial_{\alpha=0}\, \varphi_\alpha \in T\mathscr{T}_{\mathscr{E}}\,. \tag{15}$$

Taking the time derivative of (12) we have

$$\partial_{\alpha=0}\,(t_{\mathscr{E}} \circ \varphi_\alpha) = \langle dt_{\mathscr{E}}, \mathbf{v}_{\mathscr{E}} \rangle = (\partial_{\alpha=0} t_\alpha) \circ t_{\mathscr{E}} = 1 \circ t_{\mathscr{E}}\,, \tag{16}$$

and comparing with Eq. (9) we get the decomposition into space and time components

$$\mathbf{v}_{\mathscr{E}} = \mathbf{v}_{\mathscr{S}} + \mathbf{Z}\,, \tag{17}$$

with $\langle dt_{\mathscr{E}}, \mathbf{v}_{\mathscr{S}} \rangle = 0$. The motions of a body is characterised by the conservation property concerning the mass, represented by a volume form $\mathbf{m} : \mathscr{T} \mapsto \mathrm{VOL}(V\mathscr{T})$ on the material bundle over the trajectory.

Definition 3.4 (Mass conservation). *Mass conservation along the motion is expressed by the pull-back and* LIE*-derivative conditions*

$$\varphi_\alpha{\downarrow}\mathbf{m} = \mathbf{m} \iff \mathscr{L}_{\mathbf{v}_{\mathscr{E}}}\mathbf{m} = \mathbf{0}\,, \tag{18}$$

or by the equivalent integral condition for all placements Ω

$$\int_{\varphi_\alpha(\Omega)} \mathbf{m} = \int_\Omega \varphi_\alpha{\downarrow}\mathbf{m} = \int_\Omega \mathbf{m}\,. \tag{19}$$

Let us set forth some basic definitions where $\mathbf{g}_{\text{SPA}}$ denotes the metric tensor in the space bundle $V\mathscr{E}$.

The local LAGRANGE function per unit mass $L_{\mathscr{E}} : V\mathscr{E} \mapsto \text{FUN}(V\mathscr{E})$ is defined for any time-vertical tangent vector $\mathbf{v}_{\mathscr{S}} \in V\mathscr{E}$, by

$$L_{\mathscr{E}}(\mathbf{v}_{\mathscr{S}}) := \tfrac{1}{2}\,\mathbf{g}_{\text{SPA}}(\mathbf{v}_{\mathscr{S}}, \mathbf{v}_{\mathscr{S}}) - \Pi(\tau_{\mathscr{E}}(\mathbf{v}_{\mathscr{S}}))\,, \tag{20}$$

and is therefore the sum of two contributions:

- the local *kinetic energy* per unit mass $K_{\mathscr{E}} : V\mathscr{E} \mapsto \text{FUN}(V\mathscr{E})$, a scalar quadratic field over the space bundle, given by

$$K_{\mathscr{E}}(\mathbf{v}_{\mathscr{S}}) := \tfrac{1}{2}\,\mathbf{g}_{\text{SPA}}(\mathbf{v}_{\mathscr{S}}, \mathbf{v}_{\mathscr{S}}) \tag{21}$$

- and a convex *scalar potential* $\Pi : \mathscr{E} \mapsto \text{FUN}(V\mathscr{E})$ defined in the whole event manifold.

Definition 3.5 (Fiber derivative of Lagrange function). *The* fiber derivative *of the function* $L_{\mathscr{E}} : V\mathscr{E} \mapsto \text{FUN}(V\mathscr{E})$ *is the covariant tensor* $d_F L_{\mathscr{E}} : V\mathscr{E} \mapsto (V\mathscr{E})^*$ *pointwise defined, for any pair* $(\mathbf{v}_{\mathscr{S}}, \delta\mathbf{v}_{\mathscr{S}}) \in V\mathscr{E} \times_{\mathscr{E}} V\mathscr{E}$ *of space vectors* $\mathbf{v}_{\mathscr{S}}, \delta\mathbf{v}_{\mathscr{S}} \in V\mathscr{E}$ *having the same base point in* $\mathscr{E}$*, by*

$$\begin{aligned}\langle d_F L_{\mathscr{E}}(\mathbf{v}_{\mathscr{S}}), \delta\mathbf{v}_{\mathscr{S}}\rangle &:= \partial_{\lambda=0}\, L_{\mathscr{E}}(\mathbf{v}_{\mathscr{S}} + \lambda\,\delta\mathbf{v}_{\mathscr{S}}) \\ &= T L_{\mathscr{E}}(\mathbf{v}_{\mathscr{S}}) \cdot \text{VLIFT}(\mathbf{v}_{\mathscr{S}}, \delta\mathbf{v}_{\mathscr{S}})\,,\end{aligned} \tag{22}$$

where the vertical lifting is given by $\text{VLIFT}(\mathbf{v}_{\mathscr{S}}, \delta\mathbf{v}_{\mathscr{S}}) := \partial_{\lambda=0}(\mathbf{v}_{\mathscr{S}} + \lambda\,\delta\mathbf{v}_{\mathscr{S}})$*. In standard terms, taking the fiber derivative means that the derivative is taken while keeping fixed the base point of the argument vector.*

The fiber derivative of the LAGRANGE function is given by

$$d_F L_{\mathscr{E}} = d_F K_{\mathscr{E}} = \mathbf{g}_{\text{SPA}}\,, \tag{23}$$

and provides a linear isomorphism between the dual space bundles $V\mathscr{E}$ and $(V\mathscr{E})^*$. Thus a means, to transform back and forth in a biunivocal and fiberwise linear manner between these bundles, is available.

Definition 3.6 (Parallel derivative of Lagrange function). *The* parallel derivative *of the function* $L_{\mathscr{E}} : V\mathscr{E} \mapsto \text{FUN}(V\mathscr{E})$ *is the covariant tensor field* $\nabla L_{\mathscr{E}} : V\mathscr{E} \mapsto (V\mathscr{E})^*$ *defined by*

$$\langle \nabla L_{\mathscr{E}}(\mathbf{v}_{\mathscr{S}}), \delta\mathbf{v}_{\mathscr{S}} \rangle := \partial_{\lambda=0}\, L_{\mathscr{E}}(\delta\varphi^{\mathscr{C}}_{\lambda})\Uparrow\mathbf{v}_{\mathscr{S}}\,, \tag{24}$$

where $(\mathbf{v}_{\mathscr{S}}, \delta\mathbf{v}_{\mathscr{S}}) \in V\mathscr{E} \times_{\mathscr{E}} V\mathscr{E}$ *and* $\delta\varphi^{\mathscr{C}}_{\lambda}\Uparrow$ *is the parallel transport along the flow* $\delta\varphi^{\mathscr{C}}_{\lambda}$ *associated with the vector field* $\delta\mathbf{v}_{\mathscr{S}}$.

In standard terms, the parallel derivative is enunciated by saying that the derivative is taken while keeping the argument vector *constant*, which means *parallel transported* along the curve chosen to change its base point. The parallel derivative depends therefore on the adoption of a linear connection, see Sect. A.

Definition 3.7 (Euler-Legendre transform). *The convex local* LAGRANGE *function* $L_{\mathscr{E}} : V\mathscr{E} \mapsto \text{FUN}(V\mathscr{E})$ *and the convex conjugate local* HAMILTON *function* $H_{\mathscr{E}} : (V\mathscr{E})^* \mapsto \text{FUN}((V\mathscr{E})^*)$ *on the dual bundle are related by the transform*[3]

$$\begin{cases} \mathbf{v}^*_{\mathscr{S}} = d_F L_{\mathscr{E}}(\mathbf{v}_{\mathscr{S}})\,, \\ H_{\mathscr{E}}(\mathbf{v}^*_{\mathscr{S}}) := \langle \mathbf{v}^*_{\mathscr{S}}, \mathbf{v}_{\mathscr{S}} \rangle - L_{\mathscr{E}}(\mathbf{v}_{\mathscr{S}})\,, \\ \mathbf{v}_{\mathscr{S}} = d_F H_{\mathscr{E}}(\mathbf{v}^*_{\mathscr{S}})\,, \end{cases} \tag{25}$$

where $\mathbf{v}_{\mathscr{S}} \in V\mathscr{E}$ *and* $\mathbf{v}^*_{\mathscr{S}} \in (V\mathscr{E})^*$. *When expressed in terms of velocities, the* HAMILTON *function yields the* energy *function* $E_{\mathscr{E}} : V\mathscr{E} \mapsto \text{FUN}(V\mathscr{E})$, *defined by the composition*

$$E_{\mathscr{E}} = H_{\mathscr{E}} \circ d_F L_{\mathscr{E}}\,. \tag{26}$$

The action *function* $A_{\mathscr{E}} : V\mathscr{E} \mapsto \text{FUN}(V\mathscr{E})$ *is defined by the transform Eq.* (25) *as*

$$A_{\mathscr{E}}(\mathbf{v}_{\mathscr{S}}) := \langle d_F L_{\mathscr{E}}(\mathbf{v}_{\mathscr{S}}), \mathbf{v}_{\mathscr{S}} \rangle = L_{\mathscr{E}}(\mathbf{v}_{\mathscr{S}}) + E_{\mathscr{E}}(\mathbf{v}_{\mathscr{S}})\,. \tag{27}$$

Definition 3.8 (Time invariance). *Invariance along the motion of a material morphism* $\phi_{\mathscr{T}} : \text{TENS}(V\mathscr{T}) \mapsto \text{TENS}(V\mathscr{T})$ *and of a space morphism* $\phi_{\mathscr{E}} : \text{TENS}(V\mathscr{E}) \mapsto \text{TENS}(V\mathscr{E})$ *are respectively defined by the conditions*

$$\begin{aligned} \phi_{\mathscr{T}}(\varphi_\alpha\uparrow\mathbf{s}) = \varphi_\alpha\uparrow(\phi_{\mathscr{T}}(\mathbf{s})) &\iff (\mathscr{L}_{\mathbf{v}_{\mathscr{T}}}\phi_{\mathscr{T}})(\mathbf{s}) = \mathbf{0}\,, \\ \phi_{\mathscr{E}}(\varphi_\alpha\Uparrow\mathbf{s}_{\mathscr{E}}) = \varphi_\alpha\Uparrow(\phi_{\mathscr{E}}(\mathbf{s}_{\mathscr{E}})) &\iff (\nabla_{\mathbf{v}_{\mathscr{E}}}\phi_{\mathscr{E}})(\mathbf{s}_{\mathscr{E}}) = \mathbf{0}\,. \end{aligned} \tag{28}$$

The invariance conditions in Eq. (28) should not be confused with the condition of time independence that will be introduced in Eq. (82).

[3] The LEGENDRE transform was first introduced by EULER, see (Arnold et al., 1988, p. 23).

4 CONFIGURATION AND CONTROL MANIFOLDS

The geometric picture of continuum dynamics takes advantage from the introduction of a possibly infinite dimensional manifold of configurations, which is a natural extension of the simplest case considered in NEWTON point-particle dynamics, where the configuration manifold is just the EUCLID space time.

Mathematical aspect of the matter are treated in (Eliasson, 1967, Th. 5.2, p. 186), and (Palais, 1968, Th. 13.6 p. 51), as discussed in (Romano et al., 2009b).

Definition 4.1 (Configuration manifold). *A* placement manifold *is a submanifold of the event manifold $\mathscr{E}$, made of isochronous events, diffeomorphic to the body placements along the trajectory. The collection of all placement manifolds is the infinite dimensional* configuration manifold $\mathscr{P}(\mathscr{E})$.

Definition 4.2 (Connection in the configuration manifold). *A linear connection $\nabla^{\mathscr{E}}$, with parallel transport $\Uparrow^{\mathscr{E}}$, in the event manifold $\mathscr{E}$ induces a linear connection and a parallel transport in the configuration manifold $\mathscr{P}(\mathscr{E})$, still denoted by the same symbols. Considering a parametrized path $\mathbf{c} : \Re \mapsto \mathscr{P}(\mathscr{E})$ and the corresponding congruence of paths in $\mathscr{E}$, the parallel transport in $\mathscr{P}(\mathscr{E})$ is performed by acting with the parallel transport along each path of the corresponding congruence in $\mathscr{E}$.*

Definition 4.3 (Control manifold). *The* control manifold $\mathscr{C}$ *is the domain of a* representation map [4]

$$\xi : \mathscr{C} \mapsto \mathscr{P}(\mathscr{E}), \tag{29}$$

which is an injective immersion into the configuration manifold $\mathscr{P}(\mathscr{E})$. We will consider two kinds of controls.

1. *A* perfect control *in which the manifold $\mathscr{C}$ is infinite dimensional modeled on a suitable* BANACH *space and the* representation map *is a diffeomorphism between the control and the configuration manifolds.* [5]
2. *A* discrete control *in which the manifold $\mathscr{C}$ is finite dimensional and the* representation map *is just a (non surjective) injective immersion. Discrete controls are adopted in computational procedures. Placements in the range of the representation map are then said to be* controllable.

[4] The notion of representation map $\xi : \mathscr{C} \mapsto \mathscr{P}(\mathscr{E})$ extends to possibly infinite dimensional manifolds the map adopted for description of finite dimensional dynamical systems or for discretization of continua, in computational procedures.

[5] Perfect control of dynamical systems was investigated in (Romano et al., 2009b).

To each point $\mathbf{x} \in \mathscr{C}$ there corresponds a compact placement submanifold $\Omega = \xi(\mathbf{x}) \subset \mathscr{E}$ and hence a time instant $t_{\mathscr{E}}(\mathbf{e}) \in \mathscr{Z}$ evaluated at any $\mathbf{e} \in \Omega$. On the control manifold, a time projection $t_{\mathscr{C}} : \mathscr{C} \mapsto \mathscr{Z}$ is then defined by the composition

$$\begin{tikzcd} \mathscr{C} \arrow[rr, "\xi"] \arrow[dr, "t_{\mathscr{C}}"'] & & \mathscr{P}(\mathscr{E}) \arrow[dl, "t_{\mathscr{E}}"] \\ & \mathscr{Z} & \end{tikzcd} \quad \Longleftrightarrow \quad t_{\mathscr{C}} := t_{\mathscr{E}} \circ \xi \,. \tag{30}$$

In the manifold $\mathscr{C}$ the *control trajectory* is a 1D path $\Gamma \subset \mathscr{C}$ whose image by $\xi : \mathscr{C} \mapsto \mathscr{P}(\mathscr{E})$ is a trajectory of controllable placements.

A motion $\varphi_\alpha^{\mathscr{C}} : \Gamma \mapsto \Gamma$ along the control trajectory Γ generates a space-time motion along the corresponding a trajectory $\mathscr{T}_{\mathscr{E}} := \xi(\Gamma) \subset \mathscr{E}$ in the event manifold, as described by the commutative diagram

$$\begin{tikzcd} \Gamma \arrow[r, "\varphi_\alpha^{\mathscr{C}}"] \arrow[d, "\xi"] & \Gamma \arrow[d, "\xi"] \\ \mathscr{P}(\mathscr{T}_{\mathscr{E}}) \arrow[r, "\varphi_\alpha"] \arrow[d, "t_{\mathscr{E}}"] & \mathscr{P}(\mathscr{T}_{\mathscr{E}}) \arrow[d, "t_{\mathscr{E}}"] \\ \mathscr{Z} \arrow[r, "t_\alpha"] \arrow[uu, bend left=60, "\gamma"] & \mathscr{Z} \arrow[uu, bend right=60, "\gamma"'] \end{tikzcd} \quad \Longrightarrow \quad \begin{cases} t_{\mathscr{E}} \circ \xi \circ \gamma = \mathrm{ID}_{\mathscr{Z}} \,, \\ \varphi_\alpha \circ \xi := \xi \circ \varphi_\alpha^{\mathscr{C}} \,. \end{cases} \tag{31}$$

The injective immersion $\gamma : \mathscr{Z} \mapsto \mathscr{C}$, with $\gamma(\mathscr{Z}) = \Gamma \subset \mathscr{C}$, provides the time-parametrization of the control trajectory.

Defining the control velocity $\mathbf{V} := \partial_{\alpha=0} \varphi_\alpha^{\mathscr{C}}$, from Eqs. (30) and (31) we infer that the time-component of the space-time velocity in an adaptted frame is unitary:

$$\begin{aligned} \langle dt_{\mathscr{C}}, \mathbf{V} \rangle &= \langle \xi{\downarrow} dt_{\mathscr{E}}, \mathbf{V} \rangle = \xi{\downarrow} \langle dt_{\mathscr{E}}, \xi{\uparrow} \mathbf{V} \rangle \\ &= \langle dt_{\mathscr{E}}, \mathbf{v}_{\mathscr{E}} \rangle \circ \xi = \mathbf{1} \circ t_{\mathscr{C}} \,. \end{aligned} \tag{32}$$

Definition 4.4 (Lagrange bundle). *The* LAGRANGE *bundle is the time-vertical subbundle of the tangent bundle $V\mathscr{C} \subset T\mathscr{C}$ over the control manifold, that is the collection of time-vertical subspaces of tangent linear spaces attached at all points of the control manifold.*

Definition 4.5 (Hamilton bundle). *The* HAMILTON *bundle $(V\mathscr{C})^*$ is the dual subbundle of the* LAGRANGE *bundle, identifiable with the quotient bundle*

$$(T\mathscr{C})^* / (V\mathscr{C})^\circ \,. \tag{33}$$

of the cotangent bundle $(T\mathscr{C})^*$ over the subbundle $(V\mathscr{C})^\circ$ of covectors vanishing on the LAGRANGE *bundle.*

The projection maps $\tau_{\mathscr{C}} : T\mathscr{C} \mapsto \mathscr{C}$ and $\tau^*_{\mathscr{C}} : (T\mathscr{C})^* \mapsto \mathscr{C}$ bring the information about base points of tangent and cotangent vectors.

Definition 4.6 (Pontryagin bundle). *The* PONTRYAGIN *bundle* $V\mathscr{C} \times_{\mathscr{C}} (V\mathscr{C})^*$ *is the* WHITNEY *product of the bundles* $V\mathscr{C}$ *and* $(V\mathscr{C})^*$*, that is the collection of pairs, of time-vertical tangent subspaces and their duals, attached at the same points in the control manifold.*

The bundles $V\mathscr{C}$, $(V\mathscr{C})^*$ and $V\mathscr{C} \times_{\mathscr{C}} (V\mathscr{C})^*$ are geometric pictures of the *phase spaces* of analytical dynamics.

Definition 4.7 (Tangent mapping). *To the injective representation map* $\xi : \mathscr{C} \mapsto \mathscr{P}(\mathscr{E})$ *there corresponds a tangent map* $T\xi : T\mathscr{C} \mapsto T(\mathscr{P}(\mathscr{E}))$ *which provides an injective correspondence between vectors* $\mathbf{V} \in T\mathscr{C}$ *tangent to the control manifold, and space-time tangent vector fields* $\mathbf{v}_{\mathscr{E}} : \Omega \mapsto T\mathscr{E}$ *based at a* placement submanifold $\Omega \subset \mathscr{E}$ *and tangent to the event manifold* $\mathscr{E}$*, as expressed by*

$$\mathbf{v}_{\mathscr{E}} = \xi\uparrow\mathbf{V} \overset{\text{def}}{\Longleftrightarrow} \mathbf{v}_{\mathscr{E}} \circ \xi = T\xi \cdot \mathbf{V}. \tag{34}$$

To time-vertical control vectors $\mathbf{v} \in V\mathscr{C}$*, fulfilling condition* $\langle dt_{\mathscr{C}}, \mathbf{v} \rangle = 0$*, there correspond space vector fields* $\mathbf{v}_{\mathscr{S}} : \Omega \mapsto V\mathscr{E}$*, fulfilling condition* $\langle dt_{\mathscr{E}}, \mathbf{v}_{\mathscr{S}} \rangle = 0$*, according to the relation*

$$\boxed{\mathbf{v}_{\mathscr{S}} = \xi\uparrow\mathbf{v}.} \tag{35}$$

Definition 4.8 (Controllable fields). *Vector fields in the image of the tangent morphism* $T\xi : V\mathscr{C} \mapsto T(\mathscr{P}(\mathscr{E}))$ *are said to be* controllable.

Definition 4.9 (Adapted parallel transport). *A parallel transport* $\Uparrow^{\mathscr{S}}$ *in the space bundle* $V\mathscr{E}$*, such that the transport of a controllable field along a path of controllable placements is still a controllable field, is said to be* adapted *to the subbundle* $T\xi(V\mathscr{C})$ *and the induced parallel transport will be denoted by* $\Uparrow$.

Definition 4.10 (Connection in the control manifold). *A linear connection* $\nabla^{\mathscr{S}}$ *in the space bundle* $V\mathscr{E}$*, with adapted parallel transport* $\Uparrow^{\mathscr{S}}$*, induces a linear connection* ∇*, with parallel transport* $\Uparrow$*, in the control manifold* $\mathscr{C}$*, as described by the commutative diagram*

$$\begin{array}{ccc} V\mathscr{C} & \xrightarrow{\Uparrow} & V\mathscr{C} \\ {\scriptstyle T\xi}\downarrow & & \downarrow{\scriptstyle T\xi} \\ T\xi(V\mathscr{C}) & \xrightarrow{\Uparrow^{\mathscr{S}}} & T\xi(V\mathscr{C}) \end{array} \quad \Longleftrightarrow \quad T\xi \circ \Uparrow = \Uparrow^{\mathscr{S}} \circ T\xi. \tag{36}$$

By fiberwise injectivity of the tangent map $T\xi : V\mathscr{C} \mapsto T(\mathscr{P}(\mathscr{E}))$, *the parallel transport* $\Uparrow$ *is uniquely defined by the diagram Eq.* (36) *and the associated connection* ∇ *is well-defined by the relation*

$$\xi\uparrow(\nabla_{\delta\mathbf{v}}\mathbf{v}) = \nabla^{\mathscr{S}}_{\xi\uparrow\delta\mathbf{v}}(\xi\uparrow\mathbf{v}). \tag{37}$$

It is readily verified that symmetry of the connection $\nabla^{\mathscr{S}}$ implies symmetry of the connection ∇.

Indeed, being $\xi\uparrow[\mathbf{v},\delta\mathbf{v}] = [\xi\uparrow\mathbf{v},(\xi\uparrow\delta\mathbf{v})]$ by push naturality of LIE-brackets Eq. (**??**), the torsion forms of the two connections are related by

$$\begin{aligned}\xi\uparrow(\mathbf{T}(\mathbf{v},\delta\mathbf{v})) &= \xi\uparrow(\nabla_{\mathbf{v}}\delta\mathbf{v} - \nabla_{\delta\mathbf{v}}\mathbf{v} - [\mathbf{v},\delta\mathbf{v}])\\ &= \nabla^{\mathscr{S}}_{\xi\uparrow\mathbf{v}}(\xi\uparrow\delta\mathbf{v}) - \nabla^{\mathscr{S}}_{\xi\uparrow\delta\mathbf{v}}\xi\uparrow\mathbf{v} - [\xi\uparrow\mathbf{v},(\xi\uparrow\delta\mathbf{v})]\\ &= \mathbf{T}^{\mathscr{S}}(\mathbf{v}_{\mathscr{S}},\delta\mathbf{v}_{\mathscr{S}})).\end{aligned} \tag{38}$$

The torsion operator $\mathbf{T}(\mathbf{v})$ is defined by the identity $\mathbf{T}(\mathbf{v})\cdot\delta\mathbf{v} = \mathbf{T}(\mathbf{v},\delta\mathbf{v})$.

Remark 4.1 (A noteworthy example). *The control manifold adopted in the implementation of the* F.E.M. *(Finite Element Method) in structural analysis is naturally endowed with a connection induced by the spatial connection in the* EUCLID *space. The adapted connection is defined by performing the parallel transport of the space vectors based at the nodes of the discretizing space mesh and then interpolating by the shape functions to get the transported space vector fields.*

5 DYNAMICS IN THE CONTROL MANIFOLD

As we have seen, the trajectory manifold $\mathscr{T}_{\mathscr{E}}$ is naturally sliced into a family of non intersecting body placements, transversal to material lines. Integration of a material volume form μ, over a compact trajectory segment $\mathscr{T}_{\mathscr{E}}$ corresponding to a compact time interval I, can thus be performed by a space-time split based on FUBINI's theorem. Setting

$$\mu_I(\alpha) := \int_{\varphi_\alpha(\Omega)} \mu \in \Lambda^1(I), \qquad \mu_{\mathscr{C}} = \gamma\uparrow\mu_I \in \Lambda^1(\Omega), \tag{39}$$

with γ trajectory path defined by Eq. (31), we have that

$$\int_{\mathscr{T}_{\mathscr{E}}} dt_{\mathscr{E}} \wedge \mu = \int_I d\alpha \int_{\varphi_\alpha(\Omega)} \mu = \int_I \mu_I(\alpha)\, d\alpha = \int_\Gamma \gamma\uparrow\mu_I = \int_\Gamma \mu_{\mathscr{C}}, \tag{40}$$

where Ω is a compact placement manifold.

Definition 5.1 (Lagrange functional). *In the* LAGRANGE *bundle* $(V\mathscr{C})_\Gamma$ *restricted to the control trajectory, the convex* LAGRANGE *functional* $L : (V\mathscr{C})_\Gamma \mapsto \mathrm{FUN}((V\mathscr{C})_\Gamma)$ *is defined in terms of the convex local function* $L_{\mathscr{E}} : (V\mathscr{E})_{\mathscr{T}_{\mathscr{E}}} \mapsto \mathrm{FUN}((V\mathscr{E})_{\mathscr{T}_{\mathscr{E}}})$ *in the space bundle* $(V\mathscr{E})_{\mathscr{T}_{\mathscr{E}}}$*, by setting*

$$L(\mathbf{v}) := \int_\Omega L_{\mathscr{E}}(\xi\uparrow\mathbf{v})\,\mathbf{m}\,. \tag{41}$$

The definition is well-posed since the mass $\mathbf{m}$ is a material property of any placement in the trajectory. Variational principles require however to evaluate the LAGRANGE functional outside the trajectory, on placement submanifolds generated by virtual flows as images of trajectory placements. This evaluation is performed by natural extension of mass, by push along virtual flows, see Remark 6.2.

Definition 5.2 (Kinetic energy). *The* Kinetic energy $K : (V\mathscr{C})_\Gamma \mapsto \mathrm{FUN}((V\mathscr{C})_\Gamma)$ *is the quadratic functional defined in the* LAGRANGE *bundle* $(V\mathscr{C})_\Gamma$ *by*

$$K(\mathbf{v}) := \int_\Omega K_{\mathscr{E}}(\xi\uparrow\mathbf{v})\,\mathbf{m}\,. \tag{42}$$

Definition 5.3 (Action functional). *The* Action *functional* $A : (V\mathscr{C})_\Gamma \mapsto \mathrm{FUN}((V\mathscr{C})_\Gamma)$ *is defined by*

$$A(\mathbf{v}) := \int_\Omega A_{\mathscr{E}}(\xi\uparrow\mathbf{v})\,\mathbf{m}\,. \tag{43}$$

Definition 5.4 (Energy functional). *The* Energy *functional* $E : (V\mathscr{C})_\Gamma \mapsto \mathrm{FUN}((V\mathscr{C})_\Gamma)$ *is defined, in accord with Eq.* (27)*, by*

$$E(\mathbf{v}) := \int_\Omega E_{\mathscr{E}}(\xi\uparrow\mathbf{v})\,\mathbf{m} = A(\mathbf{v}) - L(\mathbf{v})\,. \tag{44}$$

Definition 5.5 (Duality pairing). *A duality pairing between space vector fields* $\delta\mathbf{v}_{\mathscr{S}} : \Omega \mapsto V\mathscr{E}$ *and covector fields* $\mathbf{p}_S : \Omega \mapsto (V\mathscr{E})^*$ *is given by*

$$\langle \mathbf{p}_S, \delta\mathbf{v}_{\mathscr{S}}\rangle_\Omega := \int_\Omega \langle \mathbf{p}_S, \delta\mathbf{v}_{\mathscr{S}}\rangle\,\mathbf{m}\,. \tag{45}$$

A direct evaluation shows that the fiber derivative $d_F L : (V\mathscr{C})_\Gamma \mapsto (V\mathscr{C})^*_\Gamma$ of the LAGRANGE functional $L : (V\mathscr{C})_\Gamma \mapsto \mathrm{FUN}((V\mathscr{C})_\Gamma)$, and its counterpart in the event manifold defined by Eq. (22), are related by

$$\boxed{\langle d_F L(\mathbf{v}), \delta\mathbf{v}\rangle = \int_\Omega \langle d_F L_{\mathscr{E}}(\xi\uparrow\mathbf{v}), \xi\uparrow\delta\mathbf{v}\rangle\,\mathbf{m}\,,} \tag{46}$$

which, in terms of the duality pairing Eq.(45), can be rewritten as

$$\begin{cases} \mathbf{p} = d_F L(\mathbf{v}), \\ \mathbf{v}_{\mathscr{S}} = \xi\uparrow\mathbf{v}, \\ \mathbf{p}_S = d_F L_{\mathscr{E}}(\mathbf{v}_{\mathscr{S}}) \\ \delta\mathbf{v}_{\mathscr{S}} = \xi\uparrow\delta\mathbf{v}, \end{cases} \quad \Longrightarrow \quad \langle \mathbf{p}, \delta\mathbf{v} \rangle = \langle \mathbf{p}_S, \delta\mathbf{v}_{\mathscr{S}} \rangle_\Omega . \tag{47}$$

Proposition 5.1 (Euler-Legendre isomorphism in control manifold). *The positive definiteness of the fiber derivative* $d_F L_{\mathscr{E}} = \mathbf{g}_{\mathrm{SPA}} : (V\mathscr{E})_{\mathscr{T}_{\mathscr{E}}} \mapsto (V\mathscr{E})^*$ *implies positive definiteness of the fiber derivative* $d_F L : (V\mathscr{C})_\Gamma \mapsto (V\mathscr{C})^*_\Gamma$, *that is*

$$\langle d_F L_{\mathscr{E}}(\mathbf{v}_{\mathscr{S}}), \mathbf{v}_{\mathscr{S}} \rangle > 0, \quad \forall \mathbf{v}_{\mathscr{S}} \in V\mathscr{E} - \{\mathbf{0}\}, \tag{48}$$

implies that

$$\langle d_F L(\mathbf{v}), \mathbf{v} \rangle > 0, \quad \forall \mathbf{v} \in V\mathscr{C} - \{\mathbf{0}\}. \tag{49}$$

Proof. Positivity of the mass measure and Eq. (48) imply Eq. (49). Invertibility follows from injectivity, for finite dimensional control manifolds. ■

The result in Prop. 5.1 assures that the EULER-LEGENDRE transform based on the LAGRANGE functional $L : (V\mathscr{C})_\Gamma \mapsto \mathrm{FUN}((V\mathscr{C})_\Gamma)$ results in a smooth one-to-one correspondence, between the LAGRANGE bundle $\tau_{\mathscr{C}} : (V\mathscr{C})_\Gamma \mapsto \mathscr{C}$ and the HAMILTON bundle $\tau^*_{\mathscr{C}} : (V\mathscr{C})^*_\Gamma \mapsto \mathscr{C}$.

Definition 5.6 (Hamilton functional). *The conjugate to the convex* LAGRANGE *functional* $L : (V\mathscr{C})_\Gamma \mapsto \mathrm{FUN}((V\mathscr{C})_\Gamma)$, *according to* EULER-LEGENDRE *transform, is the convex* HAMILTON *functional* $H : (V\mathscr{C})^*_\Gamma \mapsto \mathrm{FUN}((V\mathscr{C})^*_\Gamma)$ *defined by*

$$\begin{cases} \mathbf{p} = d_F L(\mathbf{v}), \\ H(\mathbf{p}) := \langle \mathbf{p}, \mathbf{v} \rangle - L(\mathbf{v}), \\ \mathbf{v} = d_F H(\mathbf{p}). \end{cases} \tag{50}$$

Let us now introduce the injective map $\mathbf{F} : (V\mathscr{C})^*_\Gamma \mapsto T^*(\mathscr{P}(\mathscr{E}))$ which, due to invertibility of the fiber derivative $d_F L : (V\mathscr{C})_\Gamma \mapsto (V\mathscr{C})^*_\Gamma$, is well-defined by the commutative diagram

$$\begin{array}{ccc} (V\mathscr{C})^*_\Gamma & \xrightarrow{\ \mathbf{F}\ } & T^*(\mathscr{P}(\mathscr{E})) \\ {\scriptstyle d_F L}\uparrow & & \uparrow{\scriptstyle d_F L_{\mathscr{E}}} \\ (V\mathscr{C})_\Gamma & \xrightarrow{\ \xi\uparrow\ } & T(\mathscr{P}(\mathscr{E})) \end{array} \quad \Longleftrightarrow \quad \mathbf{F} \circ d_F L = d_F L_{\mathscr{E}} \circ \xi\uparrow . \tag{51}$$

Proposition 5.2. *The* HAMILTON *functional* $H : (V\mathscr{C})^*_\Gamma \mapsto \mathrm{FUN}((V\mathscr{C})^*_\Gamma)$, *defined according to the* EULER-LEGENDRE *transform Eq.* (50), *is related to the local* HAMILTON *function* $H_\mathscr{E} : (V\mathscr{E})^*_{\mathscr{T}_\mathscr{E}} \mapsto \mathrm{FUN}((V\mathscr{E})^*_{\mathscr{T}_\mathscr{E}})$ *by the integral*

$$H(\mathbf{p}) = \int_\Omega H_\mathscr{E}(\mathbf{F}(\mathbf{p}))\,\mathbf{m}\,. \tag{52}$$

Proof. Setting $\mathbf{p} = d_F L(\mathbf{v})$ in Eq. (52), and $\mathbf{v}_\mathscr{S} := \xi\uparrow\mathbf{v}$, being

$$\mathbf{F}(\mathbf{p}) = d_F L_\mathscr{E}(\mathbf{v}_\mathscr{S})\,, \tag{53}$$

from Eq. (47) and Eq. (51) we infer that

$$\langle \mathbf{p}, \mathbf{v} \rangle = \langle \mathbf{F}(\mathbf{p}), \mathbf{v}_\mathscr{S} \rangle_\Omega\,. \tag{54}$$

Then the evaluation

$$\begin{aligned} H(\mathbf{p}) &= \int_\Omega H_\mathscr{E}(\mathbf{F}(\mathbf{p}))\,\mathbf{m} = \int_\Omega \Big(\langle \mathbf{F}(\mathbf{p}), \mathbf{v}_\mathscr{S} \rangle - L_\mathscr{E}(\mathbf{v}_\mathscr{S}) \Big)\,\mathbf{m} \\ &= \langle \mathbf{p}, \mathbf{v} \rangle - L(\mathbf{v})\,, \end{aligned} \tag{55}$$

yields Eq. (50). ■

Definition 5.7 (Vector and covector fields). *We will denote by* $\mathscr{H}_\mathscr{C}$ *a space of smooth time-vertical vector fields tangent to the control manifold* $\mathscr{C}$ *and by* $\mathscr{H}^*_\mathscr{C}$ *the dual space.*

The correspondence in Eq. (50) induces a diffeomorphism $\theta_L : \mathscr{H}_\mathscr{C} \mapsto \mathscr{H}^*_\mathscr{C}$ between the corresponding manifold of sections, with inverse $\theta_H : \mathscr{H}^*_\mathscr{C} \mapsto \mathscr{H}_\mathscr{C}$.

The EULER-LEGENDRE transform between the fields in $\mathscr{H}_\mathscr{C}$ and in $\mathscr{H}^*_\mathscr{C}$ is then expressed by

$$\begin{cases} \mathbf{p} = \theta_L(\mathbf{v})\,, \\ H(\mathbf{p}) + L(\mathbf{v}) = \langle \mathbf{p}, \mathbf{v} \rangle\,, \\ \mathbf{v} = \theta_H(\mathbf{p})\,. \end{cases} \tag{56}$$

The action and coaction functionals are given by

$$\begin{aligned} A(\mathbf{v}) &:= \langle \theta_L(\mathbf{v}), \mathbf{v} \rangle\,, \\ B(\mathbf{p}) &:= \langle \theta_H(\mathbf{p}), \mathbf{p} \rangle\,. \end{aligned} \tag{57}$$

To avoid overburden of notations we write $\theta_L(\mathbf{v}) = (d_F L) \circ \mathbf{v}$ also as $\theta_L \circ \mathbf{v}$, the meaning being clear from the context, and similarly for other fields.

Definition 5.8 (Kinetic momentum). *The* kinetic momentum *associated with a control velocity field* $\mathbf{v} \in \mathscr{H}_{\mathscr{C}}$ *is the* 1*-form* $\theta_L(\mathbf{v}) \in \mathscr{H}^*_{\mathscr{C}}$.

Definition 5.9 (External force). [6] *The* 1*-form* $\mathbf{f}_{\text{EXT}}(\mathbf{b},\mathbf{t}) \in \mathscr{H}^*_{\mathscr{C}}$, *describing the* external force *acting on a controllable body placement* Ω, *is the representation of the contributing surficial and volumetric space forces forms, according to the formula*

$$\langle \mathbf{f}_{\text{EXT}}(\mathbf{b},\mathbf{t}), \delta\mathbf{v} \rangle := \int_{\Omega} \langle \mathbf{b}, \xi\uparrow\delta\mathbf{v} \rangle \, \mu + \int_{\partial\Omega} \langle \mathbf{t}, \xi\uparrow\delta\mathbf{v} \rangle \, \partial\mu \,. \tag{58}$$

Definition 5.10 (Internal force). *The* 1*-form* $\mathbf{f}_{\text{INT}}(\sigma) \in \mathscr{H}^*_{\mathscr{C}}$ *is the representation of the* internal force *acting on a controllable body placement* Ω, *by the formula*

$$\langle \mathbf{f}_{\text{INT}}(\sigma), \delta\mathbf{v} \rangle := \int_{\Omega} \langle \sigma, \varepsilon(\xi\uparrow\delta\mathbf{v}) \rangle \, \mathbf{m} \,. \tag{59}$$

Clearly $\langle \mathbf{f}_{\text{INT}}(\sigma), \delta\mathbf{v} \rangle = 0$ for all $\xi\uparrow\delta\mathbf{v} \in \text{Ker}(\varepsilon)$.

Definition 5.11 (Dynamical force). *The* 1*-form* $\mathbf{f}_{\text{DYN}} \in \mathscr{H}^*_{\mathscr{C}}$, *is the representation of the* dynamical force *acting on a controllable body placement* Ω. *It is defined by the difference between external and internal forces, as expressed, at regular points, by the formula*

$$\mathbf{f}_{\text{DYN}} := \mathbf{f}_{\text{EXT}}(\mathbf{b},\mathbf{t}) - \mathbf{f}_{\text{INT}}(\sigma) \,. \tag{60}$$

Impulsive forces at singular points, collectively denoted by Γ_{SING}, *are represented by* 1*-forms* $\mathbf{f}_{\text{SING}} \in \mathscr{H}^*_{\mathscr{C}}$.

6 HAMILTON PRINCIPLE

Let us now provide a geometrical formulation of classical action principles of dynamics. In so doing, we drop the standard, but needlessly restrictive, assumption that variations of a trajectory segment must leave the end points fixed. By this more general approach jump conditions at singular interfaces are directly provided by the variational condition. Moreover, a satisfactory formulation is thus given from the epistemological viewpoint, as explicated in Remark 6.3. On the other hand, we add the explicit statement about the way extensions of the involved geometrical objects are performed along virtual flows. Usual treatments are substantially silent in this respect.

[6] Force systems are often ignored in variational treatments of dynamics and sometimes improperly defined as morphisms $\mathbf{f}_{\text{EXT}} : V\mathscr{C} \mapsto (V\mathscr{C})^*$ from the LAGRANGE to the HAMILTON bundle, see e.g. (Terra and Kobayashi, 2004a; Yoshimura and Marsden, 2006), a definition that violates GALILEI principle of relativity.

Definition 6.1 (Synchronous virtual variations). *Synchronous virtual variations are performed when the virtual flow* $\delta\varphi_\lambda^{\mathscr{C}} : \Gamma \mapsto \mathscr{C}$ *preserves the time projection* $t_{\mathscr{C}} : \mathscr{C} \mapsto \mathscr{Z}$, *that is*

$$\boxed{t_{\mathscr{C}} = \delta\varphi_\lambda^{\mathscr{C}} \downarrow t_{\mathscr{C}} = t_{\mathscr{C}} \circ \delta\varphi_\lambda^{\mathscr{C}}\,,} \tag{61}$$

as depicted in frame (70). *Virtual velocities are then time vertical, since*

$$\langle dt_{\mathscr{C}}, \delta\mathbf{v}\rangle = \langle dt_{\mathscr{C}}, \partial_{\lambda=0}\,\delta\varphi_\lambda^{\mathscr{C}}\rangle = \partial_{\lambda=0}(t_{\mathscr{C}} \circ \delta\varphi_\lambda^{\mathscr{C}}) = 0\,. \tag{62}$$

Consequently, due to commutativity, time differentials fulfil the conditions

$$dt_{\mathscr{C}} = d(\delta\varphi_\lambda^{\mathscr{C}} \downarrow t_{\mathscr{C}}) = \delta\varphi_\lambda^{\mathscr{C}} \downarrow dt_{\mathscr{C}} \iff \mathscr{L}_{\delta\mathbf{v}} dt_{\mathscr{C}} = d(\mathscr{L}_{\delta\mathbf{v}} t_{\mathscr{C}}) = \mathbf{0}\,, \tag{63}$$

so that

$$\langle dt_{\mathscr{C}}, \delta\varphi_\lambda^{\mathscr{C}} \uparrow \mathbf{V}\rangle = \langle \delta\varphi_\lambda^{\mathscr{C}} \uparrow dt_{\mathscr{C}}, \delta\varphi_\lambda^{\mathscr{C}} \uparrow \mathbf{V}\rangle = \delta\varphi_\lambda^{\mathscr{C}} \uparrow \langle dt_{\mathscr{C}}, \mathbf{V}\rangle = 1 \circ \delta\varphi_\lambda^{\mathscr{C}}\,. \tag{64}$$

Remark 6.1 (Natural extension of the velocity field). *The space-time velocity field* $\mathbf{V} : \Gamma \mapsto T\mathscr{C}$ *along the control trajectory is extended, in a natural way, along a virtual flow by considering the velocity of the pushed motion*

$$\partial_{\alpha=0}(\delta\varphi_\lambda^{\mathscr{C}} \circ \varphi_\alpha^{\mathscr{C}}) = T\delta\varphi_\lambda^{\mathscr{C}} \cdot \mathbf{V} = (\delta\varphi_\lambda^{\mathscr{C}} \uparrow \mathbf{V}) \circ \delta\varphi_\lambda^{\mathscr{C}}\,. \tag{65}$$

The extended velocity is thus pushed along the virtual flow

$$\boxed{\mathbf{V} = \delta\varphi_\lambda^{\mathscr{C}} \uparrow \mathbf{V} \overset{\text{def}}{\iff} \mathbf{V} \circ \delta\varphi_\lambda^{\mathscr{C}} = T\delta\varphi_\lambda^{\mathscr{C}} \cdot \mathbf{V}\,,} \tag{66}$$

so that $[\mathbf{V}, \delta\mathbf{v}] = \mathscr{L}_{\delta\mathbf{v}}\mathbf{V} = \mathbf{0}$.

Remark 6.2 (Natural extension by virtual mass conservation). *In evaluating the* LAGRANGE *functional by Eq.* (41) *over body a placement transformed by a virtual flow, the mass* $\mathbf{m}$, *which is defined only on the trajectory, is also assumed to be extended, in a natural way, by push along the virtual flow. This procedure has the physical interpretation of virtual mass conservation and is tacitly assumed in analytical dynamics.*

Proposition 6.1 (Hamilton action principle). *The motion along the trajectory* Γ *in the control manifold* $\mathscr{C}$*, is characterized by the variational condition*[7]

$$\boxed{\begin{aligned}\partial_{\lambda=0}\int_{\delta\varphi^{\mathscr{C}}_{\lambda}(\Gamma)} L(\mathbf{v})\,dt_{\mathscr{C}} - \oint_{\partial\Gamma}\langle\,\theta_L(\mathbf{v}),\delta\mathbf{v}\rangle \\ = \int_{\Gamma}(dt_{\mathscr{C}}\wedge\mathbf{f}_{\mathrm{DYN}})\cdot\delta\mathbf{v} - \oint_{\Gamma_{\mathrm{SING}}}\langle\mathbf{f}_{\mathrm{SING}},\delta\mathbf{v}\rangle\,,\end{aligned}} \tag{67}$$

for all synchronous virtual flows with velocity $\delta\mathbf{v}\in\mathscr{H}_{\mathscr{C}}$*. At regular points, the variational condition Eq.* (67)*, expressed in terms of a linear connection* ∇*, is equivalent to* EULER-LAGRANGE-POINCARÉ *differential equation*

$$\boxed{\langle\nabla_{\mathbf{V}}(\theta_L\circ\mathbf{v}) - \nabla L(\mathbf{v}) + \theta_L(\mathbf{v})\cdot\mathbf{T}(\mathbf{V}),\delta\mathbf{v}\rangle = \langle\mathbf{f}_{\mathrm{DYN}},\delta\mathbf{v}\rangle\,,} \tag{68}$$

which is tensorial in the synchronous virtual velocity $\delta\mathbf{v}\in\mathscr{H}_{\mathscr{C}}$*. At singular points the motion is governed by the jump conditions*

$$[[\langle\,\theta_L(\mathbf{v}),\delta\mathbf{v}\rangle]] = \langle\mathbf{f}_{\mathrm{SING}},\delta\mathbf{v}\rangle\,. \tag{69}$$

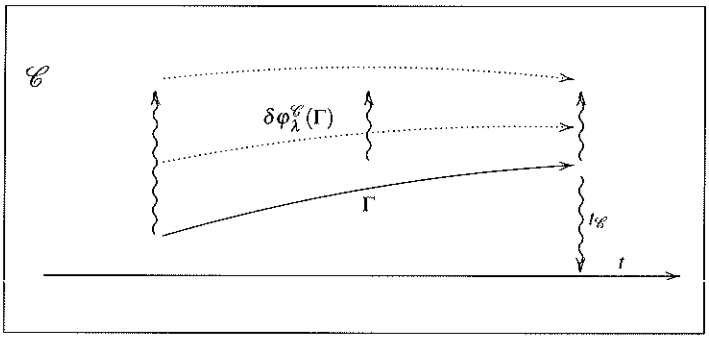

(70)

Proof. Equivalence between Eqs. (67) and (68) will be proven in Prop. 7.1. ■

[7] As reported in (Arnold et al., 1988, 2.1, p.10), FELIX KLEIN (1926) observed that: *It is astonishing that in Lagrange's work this statement may be read only between the lines. This explains the strange situation that this relation - mainly through Jacobi's influence - is generally known in Germany, and therefore also in France, as Hamilton's principle. In England no one understands this expression; there this equation is known under the correct if intuitive name of principle of stationary action.*

Remark 6.3. *The boundary integral appearing in the expression of the action principle Eq.* (67) *is usually eliminated by imposing that virtual velocities must vanish at trajectory endpoints, see e.g. (Abraham and Marsden, 1988, Sect. 3.8). This needless constraint on test fields, depicted in frame* (71)*, has however unpleasant consequences and is therefore advisable that it be eliminated. A trouble concerns the qualification of the action principle as characteristic property of the dynamical trajectory. In this respect, a natural requirement is that two subsequent trajectory segments should be chained into a resultant trajectory segment. This chain property is not fulfilled by the constrained formulation, while it is clearly met by the unconstrained formulation. Another significant advantage is that jump conditions at singular points are directly provided by the action principle. The same procedure, applied to* FERMAT *principle of least time in optics, leads the differential equation of optical geodesic and to* SNELL *interface jump conditions (Romano G., 2007).*

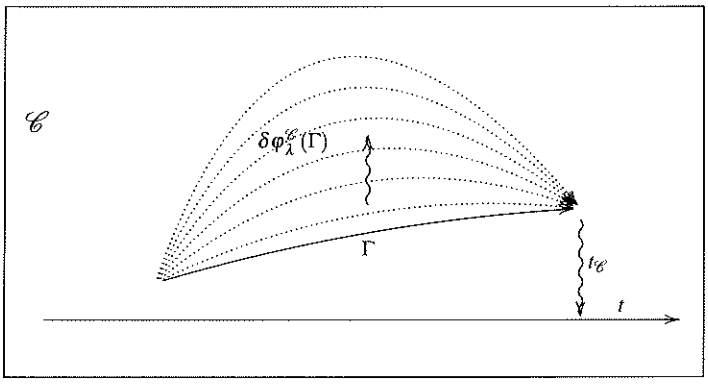

(71)

Remark 6.4 (Coordinates and natural frames). *In a finite dimensional control manifold, with* $\dim\mathscr{C} = m+1$, *let us consider a coordinate system in the slices of isochronous placements*

$$\phi = \{q_i, i = 1, \dots m\} : \Re^m \mapsto \mathscr{C}, \tag{72}$$

Denoting by $\mathbf{a}_i$ *and* $\mathbf{a}^k$, *with* $i,k = 1, \dots m$, *the usual frame and the dual coframe in* $\Re^m$, *the natural frame (*repère naturel*) and coframe associated with the coordinate system are given by*

$$\begin{cases} \partial_i := \phi\uparrow\mathbf{a}_i, \\ dq^k := \phi\uparrow\mathbf{a}^k, \\ \langle dq^k, \partial_i\rangle = \phi\uparrow\langle\mathbf{a}^k, \mathbf{a}_i\rangle = \delta^k_{\cdot i}. \end{cases} \tag{73}$$

Remark 6.5. *The differential law of motion Eq.* (68) *may be expressed in coordinates and in terms of the connection induced by the natural frame associated with the coordinate system. The relevant torsion form vanishes identically. Indeed, being* $\nabla_{\partial_i}\partial_j = \mathbf{0}$ *by assumption and* $[\partial_i, \partial_j] = \mathbf{0}$ *by commutativity of coordinate flows, we have that*

$$\mathbf{T}(\partial_i, \partial_j) = \nabla_{\partial_i}\partial_j - \nabla_{\partial_j}\partial_i - [\partial_i, \partial_j] = \mathbf{0}. \tag{74}$$

The EULER-LAGRANGE *law then writes*

$$\langle \nabla_{\mathbf{V}}(\theta_L \circ \mathbf{v}) - \nabla L(\mathbf{v}), \delta\mathbf{v} \rangle = \langle \mathbf{f}_{\mathrm{DYN}}, \delta\mathbf{v} \rangle, \tag{75}$$

which in coordinates takes the familiar expression

$$\frac{d}{dt}\left(\frac{dL}{d\dot{q}}\right) - \frac{dL}{dq} = Q, \tag{76}$$

where $\dot{q}$, $dL/d\dot{q}$, dL/dq *and* Q *are the numerical vectors of components respectively of* $\mathbf{v}$, $d_F L(\mathbf{v}) = \theta_L \circ \mathbf{v}$, $\nabla L(\mathbf{v})$ *and* $\mathbf{f}_{\mathrm{DYN}}$.

Remark 6.6. *A special case of the differential law of motion Eq.* (68) *is described in coordinates in (Arnold et al., 1988, 2.4, p. 13), reproducing the original treatment in (Poincaré, 1901). There, the term* quasi-velocities *is adopted for the components of the space velocity in a* repère mobile *(Cartan É., 1937)* $\{\mathbf{d}_1, \ldots, \mathbf{d}_m\}$, *that is a set of* m *smooth fields which form a basis at each point. If the parallel transport of a vector is defined by the property that its components in the* repère mobile *are constant, then the parallel derivatives of the basis vector fields, according to the path independent induced connection* ∇, *vanish identically. By tensoriality of the torsion form* $\mathbf{T}(\mathbf{v}, \delta\mathbf{v})$ *the arguments can be extended by parallel transport. Consequently the torsion form can be computed at each point as coincident with the negative of the* LIE-*bracket of the vector fields generated by the extension. The components* $c_{ij}^{\cdot\cdot k}$ *of the brackets of basis vectors in the* repère mobile, *are the* structure constants *defined by*

$$[\mathbf{d}_i, \mathbf{d}_j] = c_{ij}^{\cdot\cdot k}\, \mathbf{d}_k. \tag{77}$$

The POINCARÉ *law takes then the expression*

$$\langle \nabla_{\mathbf{V}}(\theta_L \circ \mathbf{v}) - \nabla L(\mathbf{v}), \delta\mathbf{v} \rangle + \theta_L(\mathbf{v}) \cdot [\mathbf{v}, \delta\mathbf{v}] = \langle \mathbf{f}_{\mathrm{DYN}}, \delta\mathbf{v} \rangle, \tag{78}$$

and in coordinates

$$\frac{d}{dt}\left(\frac{dL}{d\dot{q}}\right)_k - \left(\frac{dL}{dq}\right)_k + c_{ik}^{\cdot\cdot j}\, \dot{q}^i \left(\frac{dL}{d\dot{q}}\right)_j = Q_k. \tag{79}$$

In a repère naturel *all structure constants vanish and the law of motion in the control manifold takes the standard form in coordinates Eqs.* (75), (76), *as given in (Lagrange, 1788).*

Singular forces $\mathbf{f}_{\text{SING}}$ and jump conditions will be neglected in the sequel, to simplify the presentation. In classical mechanics a direct consequence of EULER-LAGRANGE-POINCARÉ condition, Eq. (68) in Prop. 6.1, is known as EMMY NOETHER theorem, see (Noether, 1918; Arnold, 1974, Sect. 20, p. 88).

Corollary 6.1 (E. Noether). *For synchronous virtual flows with* $\delta\mathbf{v} \in \mathscr{H}_{\mathscr{C}}$, *the following implication holds*

$$\boxed{\begin{aligned}&\nabla_{\delta\mathbf{v}} L(\mathbf{v}) = \mathbf{0} \implies \\ &\langle \nabla_{\mathbf{V}}(\theta_L \circ \mathbf{v}) - \nabla L(\mathbf{v}) + \theta_L(\mathbf{v}) \cdot \mathbf{T}(\mathbf{V}), \delta\mathbf{v} \rangle = \langle \mathbf{f}_{\text{DYN}}, \delta\mathbf{v} \rangle .\end{aligned}} \tag{80}$$

Statements in literature refer to the special case in which the connection is symmetric ($\mathbf{T} = \mathbf{0}$) *and dynamical forces vanish* ($\mathbf{f}_{\text{DYN}} = \mathbf{0}$), *so that* NOETHER *theorem writes*

$$\boxed{\nabla_{\delta\mathbf{v}} L(\mathbf{v}) = 0 \implies \langle \nabla_{\mathbf{V}}(\theta_L \circ \mathbf{v}), \delta\mathbf{v} \rangle = 0 .} \tag{81}$$

Proposition 6.2 (Balance of mechanical power). *Under the assumption that the* LAGRANGE *functional is time independent, that is*

$$\nabla_{\mathbf{Z}} L(\mathbf{v}) = 0 \iff \nabla_{\mathbf{V}} L(\mathbf{v}) = \nabla_{\mathbf{v}} L(\mathbf{v}) , \tag{82}$$

the motion fulfills the mechanical power balance

$$\boxed{\nabla_{\mathbf{V}}(E \circ \mathbf{v}) = \langle \mathbf{f}_{\text{DYN}}, \mathbf{v} \rangle ,} \tag{83}$$

stating that the time rate of the energy functional along the motion is equal to the power expended by dynamical forces.

Proof. Setting $\delta\mathbf{v} = \mathbf{v}$ in Eq. (68) and noting that $\mathbf{T}(\mathbf{V}, \mathbf{v}) = \mathbf{T}(\mathbf{v}, \mathbf{v}) = \mathbf{0}$, the proof follows by the relations

$$\begin{aligned}&\langle \nabla_{\mathbf{V}}(\theta_L \circ \mathbf{v}), \mathbf{v} \rangle - \nabla_{\mathbf{v}} L(\mathbf{v}) \\ =& \langle \nabla_{\mathbf{V}}(\theta_L \circ \mathbf{v}), \mathbf{v} \rangle - \nabla_{\mathbf{V}} L(\mathbf{v}) + \nabla_{\mathbf{Z}} L(\mathbf{v}) \\ =& \nabla_{\mathbf{V}} \langle \theta_L \circ \mathbf{v}, \mathbf{v} \rangle - \langle \theta_L \circ \mathbf{v}, \nabla_{\mathbf{V}} \mathbf{v} \rangle - \nabla_{\mathbf{V}} L(\mathbf{v}) + \nabla_{\mathbf{Z}} L(\mathbf{v}) \\ =& \nabla_{\mathbf{V}} \langle \theta_L \circ \mathbf{v}, \mathbf{v} \rangle - \nabla_{\mathbf{V}}(L \circ \mathbf{v}) + \nabla_{\mathbf{Z}} L(\mathbf{v}) \\ =& \nabla_{\mathbf{V}}(E \circ \mathbf{v}) + \nabla_{\mathbf{Z}} L(\mathbf{v}) = \langle \mathbf{f}_{\text{DYN}}, \mathbf{v} \rangle ,\end{aligned} \tag{84}$$

where splitting Eq. (A.5) and definition Eq. (44) have been resorted to. ∎

7 LAGRANGE PRINCIPLE

The formal structure of an action principle, as defined by Eq. (2), is not respected in HAMILTON principle Eq. (67), since a pair of 1-forms on $\mathscr{C}$ are there involved:

- the 1-form $(L \circ \mathbf{v})\, dt_{\mathscr{C}}$ in the integral over the trajectory,
- the 1-form $\theta_L \circ \mathbf{v}$ in the integral over the trajectory boundary.

According to the nomenclature in Rem. 2.1, HAMILTON principle is then an *hybrid* action principle. An equivalent *faithful* action principle will however be enunciated in Prop. 7.1 by introducing of the following item.[8]

Definition 7.1 (Lagrange action form). *The* LAGRANGE *action* 1*-form on the trajectory manifold* $\omega_L^1 \circ \mathbf{v} : \Gamma \mapsto (T\mathscr{C})^*_\Gamma$*, is induced by the map* $\omega_L^1 : (T\mathscr{C})_\Gamma \mapsto (T\mathscr{C})^*_\Gamma$ *defined by*

$$\boxed{\omega_L^1(\mathbf{v}) := \theta_L(\mathbf{v}) - E(\mathbf{v})\, dt_{\mathscr{C}}\,.} \tag{85}$$

Lemma 7.1 (Equality between path integrals). *On a time parameterised path* Γ *we have the equalities*

$$\int_\Gamma L(\mathbf{v})\, dt_{\mathscr{C}} = \int_\Gamma \omega_L^1(\mathbf{v})\,. \tag{86}$$

$$\oint_{\partial\Gamma} \langle\, \theta_L(\mathbf{v}), \delta\mathbf{v} \rangle = \oint_{\partial\Gamma} \langle\, \omega_L^1(\mathbf{v}), \delta\mathbf{v} \rangle\,. \tag{87}$$

Moreover, by synchronicity of virtual flows, Eq. (86) *holds also on dragged paths*

$$\int_{\delta\varphi_\lambda^{\mathscr{C}}(\Gamma)} L(\mathbf{v})\, dt_{\mathscr{C}} = \int_{\delta\varphi_\lambda^{\mathscr{C}}(\Gamma)} \omega_L^1(\mathbf{v})\,. \tag{88}$$

Proof. By EULER-LEGENDRE transform, the evaluation $\langle dt_{\mathscr{C}}, \mathbf{V} \rangle = 1$ gives

$$\langle\, \omega_L^1(\mathbf{v}), \mathbf{V} \rangle = \langle\, \theta_L(\mathbf{v}), \mathbf{V} \rangle - (E(\mathbf{v}))\langle dt_{\mathscr{C}}, \mathbf{V} \rangle = L(\mathbf{v}) = \langle L(\mathbf{v})\, dt_{\mathscr{C}}, \mathbf{V} \rangle\,, \tag{89}$$

and the evaluation $\langle dt_{\mathscr{C}}, \delta\mathbf{v} \rangle = 0$ yields

$$\langle\, \omega_L^1(\mathbf{v}), \delta\mathbf{v} \rangle = \langle\, \theta_L(\mathbf{v}), \delta\mathbf{v} \rangle - (E(\mathbf{v}))\langle dt_{\mathscr{C}}, \delta\mathbf{v} \rangle = \langle\, \theta_L(\mathbf{v}), \delta\mathbf{v} \rangle\,. \tag{90}$$

This proves Eq. (86) and Eq. (87). Eq. (88) holds since $\langle dt_{\mathscr{C}}, \delta\varphi_\lambda^{\mathscr{C}} \uparrow \mathbf{V} \rangle = 1$ due to synchronicity Eq. (64). ■

[8] In (Arnold, 1974)) is said: *the form* θ_L *seems here to appear out of thin air. In the following paragraph we will see how the idea of using this form arose form optics.* A formal motivation is suggested by Lemma 7.1.

Proposition 7.1 (Lagrange action principle). *The motion along the trajectory* Γ *in the control manifold* $\mathscr{C}$*, is characterized by the extremality condition*

$$\boxed{\partial_{\lambda=0}\int_{\delta\varphi_\lambda^{\mathscr{C}}(\Gamma)}\omega_L^1(\mathbf{v})-\oint_{\partial\Gamma}\langle\omega_L^1(\mathbf{v}),\delta\mathbf{v}\rangle=\int_\Gamma(dt_{\mathscr{C}}\wedge\mathbf{f}_{\mathrm{DYN}})\cdot\delta\mathbf{v},} \tag{91}$$

for all synchronous virtual flows with velocity $\delta\mathbf{v}=\partial_{\lambda=0}\delta\varphi_\lambda^{\mathscr{C}}\in\mathscr{H}_{\mathscr{C}}$*. The corresponding* EULER *differential condition writes*

$$\boxed{\langle d(\theta_L\circ\mathbf{v})\cdot\mathbf{V}+d(E\circ\mathbf{v}),\delta\mathbf{v}\rangle=\langle\mathbf{f}_{\mathrm{DYN}},\delta\mathbf{v}\rangle,} \tag{92}$$

which, in terms of a linear connection ∇*, is expressed by*

$$\boxed{\langle\nabla_{\mathbf{V}}(\theta_L\circ\mathbf{v})-\nabla L(\mathbf{v})+\theta_L(\mathbf{v})\cdot\mathbf{T}(\mathbf{V}),\delta\mathbf{v}\rangle=\langle\mathbf{f}_{\mathrm{DYN}},\delta\mathbf{v}\rangle.} \tag{93}$$

The whole expression at the l.h.s. of LAGRANGE *law of dynamics Eq.* (93) *is independent of the choice of a linear connection.*

Proof. Equivalence between action principles in Eq. (91) and Eq. (67) follows directly from the equalities Eq. (88) and (87). The proof of Eq. (93) is carried out as follows. The extrusion formula Eq. (8), applied to Eq. (91), gives

$$\int_\Gamma d(\omega_L^1\circ\mathbf{v})\cdot\delta\mathbf{v}=\int_\Gamma(dt_{\mathscr{C}}\wedge\mathbf{f}_{\mathrm{DYN}})\cdot\delta\mathbf{v}. \tag{94}$$

and hence, by Eq. (96), the EULER differential condition

$$d(\omega_L^1\circ\mathbf{v})\cdot\delta\mathbf{v}\cdot\mathbf{V}=d\Big((\theta_L\circ\mathbf{v})-(E\circ\mathbf{v})\,dt_{\mathscr{C}}\Big)\cdot\delta\mathbf{v}\cdot\mathbf{V}=-\langle\mathbf{f}_{\mathrm{DYN}},\delta\mathbf{v}\rangle, \tag{95}$$

Being $\langle dt_{\mathscr{C}},\mathbf{V}\rangle=1$ and $\langle dt_{\mathscr{C}},\delta\mathbf{v}\rangle=0$, we have that

$$\begin{aligned}
d\Big((E\circ\mathbf{v})\,dt_{\mathscr{C}}\Big)\cdot\delta\mathbf{v}\cdot\mathbf{V}&=\Big(d(E\circ\mathbf{v})\wedge dt_{\mathscr{C}}\Big)\cdot\delta\mathbf{v}\cdot\mathbf{V}=d(E\circ\mathbf{v})\cdot\delta\mathbf{v},\\
(dt_{\mathscr{C}}\wedge\mathbf{f}_{\mathrm{DYN}})\cdot\delta\mathbf{v}\cdot\mathbf{V}&=(dt_{\mathscr{C}}\cdot\delta\mathbf{v})(\mathbf{f}_{\mathrm{DYN}}\cdot\mathbf{V})-(dt_{\mathscr{C}}\cdot\mathbf{V})(\mathbf{f}_{\mathrm{DYN}}\cdot\delta\mathbf{v})\\
&=-\langle\mathbf{f}_{\mathrm{DYN}},\delta\mathbf{v}\rangle.
\end{aligned} \tag{96}$$

Moreover, from Lemma A.1 and the formula in Eq. (A.1), being

$$\begin{aligned}
\langle\theta_L(\mathbf{v}),\mathbf{V}\rangle&=\langle\theta_L(\mathbf{v}),\mathbf{v}\rangle,\\
\langle\theta_L(\mathbf{v}),\nabla_{\delta\mathbf{v}}\mathbf{V}\rangle&=\langle\theta_L(\mathbf{v}),\nabla_{\delta\mathbf{v}}\mathbf{v}\rangle,
\end{aligned} \tag{97}$$

we get

$$
\begin{cases}
d(\theta_L \circ \mathbf{v}) \cdot \mathbf{V} \cdot \delta\mathbf{v} = 2\,\mathrm{skew}\,(\nabla(\theta_L \circ \mathbf{v}) \cdot \mathbf{V} \cdot \delta\mathbf{v}) \\
\qquad\qquad + \langle \theta_L(\mathbf{v}), \mathbf{T}(\mathbf{V}, \delta\mathbf{v}) \rangle \\
\qquad\qquad = \langle \nabla_{\mathbf{V}}(\theta_L \circ \mathbf{v}), \delta\mathbf{v} \rangle - \langle \nabla_{\delta\mathbf{v}}(\theta_L \circ \mathbf{v}), \mathbf{V} \rangle \\
\qquad\qquad + \langle \theta_L(\mathbf{v}), \mathbf{T}(\mathbf{V}, \delta\mathbf{v}) \rangle, \\
\langle \nabla_{\delta\mathbf{v}}(\theta_L \circ \mathbf{v}), \mathbf{V} \rangle = \nabla_{\delta\mathbf{v}} \langle \theta_L \circ \mathbf{v}, \mathbf{V} \rangle - \langle \theta_L(\mathbf{v}), \nabla_{\delta\mathbf{v}} \mathbf{V} \rangle \\
\qquad\qquad = \nabla_{\delta\mathbf{v}}(A \circ \mathbf{v}) - \langle \theta_L(\mathbf{v}), \nabla_{\delta\mathbf{v}} \mathbf{V} \rangle, \\
\nabla_{\delta\mathbf{v}}(A \circ \mathbf{v}) = \nabla_{\delta\mathbf{v}} A(\mathbf{v}) + \langle d_F A(\mathbf{v}), \nabla_{\delta\mathbf{v}} \mathbf{v} \rangle, \\
d(E \circ \mathbf{v}) \cdot \delta\mathbf{v} = \nabla_{\delta\mathbf{v}}(E \circ \mathbf{v}) = \nabla_{\delta\mathbf{v}} E(\mathbf{v}) + \langle d_F E(\mathbf{v}), \nabla_{\delta\mathbf{v}} \mathbf{v} \rangle .
\end{cases}
\tag{98}
$$

The EULER-LEGENDRE transform gives

$$
\theta_L(\mathbf{v}) = d_F A(\mathbf{v}) - d_F E(\mathbf{v}), \qquad \nabla_{\delta\mathbf{v}} A - \nabla_{\delta\mathbf{v}} E = \nabla_{\delta\mathbf{v}} L, \tag{99}
$$

and Eq. (93) follows. ■

8 MAUPERTUIS PRINCIPLE

Attribution of the least action principle to MAUPERTUIS was at the centre of an ugly dispute with KÖNIG, who sustained that the principle was first enunciated by LEIBNIZ in a letter to HERMANN in 1707, some 37 years before. The original of the letter was however never found and its existence was even questioned by supporters of MAUPERTUIS.

The principle enunciated in (Maupertuis, 1744) was also formulated in more precise terms and in the same year in (Euler, 1744). An undiscussed parental attribution is still lacking. Therefore the principle could also be properly named LEIBNIZ-EULER-MAUPERTUIS least action principle, although the names of LAGRANGE and JACOBI should be added with full credit to the list. Following the tradition we will simply refer to it as the MAUPERTUIS least action principle.

The least action principle is also referred to in literature as stationarity principle for the *reduced action*, to underline that the 1-form $\theta_L \circ \mathbf{v}$ is got from the 1-form $\omega_L^1 \circ \mathbf{v} := \theta_L \circ \mathbf{v} - (E \circ \mathbf{v})\, dt_{\mathscr{C}}$ appearing in LAGRANGE action principle Prop. 7.1, by dropping the term $(E \circ \mathbf{v})\, dt_{\mathscr{C}}$ involving the energy (Arnold, 1974).

A proper formulation of the principle has always been reported as a challenging task in literature.

Difficulties in providing a clear statement were reported in (Jacobi, 1837a,b, 1884) and thence repeated in literature till recently, see (Goldstein, 1950; Godbillon, 1971; Arnold, 1974; Landau and Lifšits, 1976; Abraham and Marsden, 1988). In (Arnold, 1974, p. 246), it is said:

"In almost all textbooks, even the best, this principle is presented so that it is impossible to understand" (C. JACOBI, *Lectures on Dynamics). I do not choose to break with tradition. A very interesting "proof" of* MAUPERTUIS *principle is in Section 44 of the mechanics textbook of* LANDAU *and* LIFŠITS *(Mechanics, Oxford, Pergamon 1960).*

In (Abraham and Marsden, 1988, footnote on p. 249), it is written: *We thank* M. SPIVAK *for helping us to formulate this theorem correctly. The authors, like many others (we were happy to learn), were confused by the standard textbook statements. For instance the misterious variation "Δ" in* GOLDSTEIN *[1950, p. 228] corresponds to our enlargement of the variables by $c \to (\tau, c)$.*

We provide here a quite general formulation in which the power balance constraint is imposed only on test fields, as shown in the diagram Eq. (100).

Standard statements in literature are affected by an misformulation which results in the *variational crime*[9] described below:

- The natural condition, concerning balance of mechanical power along the motion, is imposed as an essential condition on admissible paths and on virtual velocities. On the contrary, balance of virtual mechanical power is an essential condition to be imposed on virtual velocities, while balance of mechanical power along the motion is a natural outcome of the variational principle and holds only under the special assumption of time independence of the LAGRANGE functional.

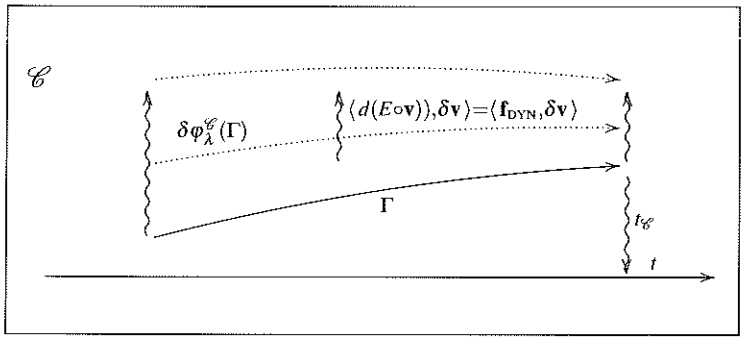

(100)

[9] We imitate here the title of an interesting chapter in a nice book on the finite element method (Strang and Fix, 1988).

Generality is achieved by the new formulation in Prop. 8.1 under two respects:

1. The end point of the trajectory segment are left free to vary, according to the assumed virtual flow in the control manifold.
2. The original constraint of energy conservation, in which both motions and virtual flows are imposed to evolve while leaving the energy functional constant, is replaced by the sole constraint that virtual velocities must fulfils balance of virtual power, with no constraints concerning the motion.

The new form of MAUPERTUIS least action principle, enunciated in Prop. 8.1 and sketched in diagram Eq. (100), is named MAUPERTUIS extremality principle in agreement with Def. 2.3, and is shown to be equivalent to HAMILTON action principle of Prop. 6.1, by performing a comparison of the ensuing EULER differential conditions.

Proposition 8.1 (Maupertuis extremality principle). *The trajectory* Γ *is characterized by an extremality condition for the path integral of the kinetic momentum*

$$\boxed{\partial_{\lambda=0} \int_{\delta\varphi^{\mathscr{C}}_{\lambda}(\Gamma)} \theta_L(\mathbf{v}) = \oint_{\partial\Gamma} \langle \theta_L(\mathbf{v}), \delta\mathbf{v} \rangle \,,} \tag{101}$$

in the class of synchronous virtual flows whose velocity $\delta\mathbf{v} \in \mathscr{H}_{\mathscr{C}}$ *fulfils the constraint of virtual power balance*

$$\boxed{\langle d(E \circ \mathbf{v}), \delta\mathbf{v} \rangle = \langle \mathbf{f}_{\text{DYN}}, \delta\mathbf{v} \rangle \,.} \tag{102}$$

By extrusion formula Eq. (8), *the variational condition Eq.* (101) *is equivalent to the differential condition*

$$\boxed{d(\theta_L \circ \mathbf{v}) \cdot \mathbf{V} \cdot \delta\mathbf{v} = 0 \,,} \tag{103}$$

for all time-vertical virtual velocity fields $\delta\mathbf{v} : \Gamma \mapsto V\mathscr{C}$ *fulfilling the virtual power balance Eq.* (102).

Proof. For notational convenience, we introduce the covector $\mathbf{f}_{\text{EQ}} : (T\mathscr{C})_\Gamma \mapsto \mathfrak{R}$ defined by $\mathbf{f}_{\text{EQ}} := \mathbf{f}_{\text{DYN}} - d(E \circ \mathbf{v})$, with dual $\mathbf{f}^*_{\text{EQ}} : \mathfrak{R} \mapsto (T\mathscr{C})^*_\Gamma$. The differential law Eq. (103), with the linear constraint Eq. (102) on the virtual velocities, may

then be expressed by the conditions

$$\begin{aligned} & d(\theta_L \circ \mathbf{v}) \cdot \mathbf{V} \in (\mathrm{Ker}\,\mathbf{f}_{\mathrm{EQ}})^{\circ} \\ \Longleftrightarrow\ & d(\theta_L \circ \mathbf{v}) \cdot \mathbf{V} \in \mathrm{Im}\,\mathbf{f}^*_{\mathrm{EQ}} \\ \Longleftrightarrow\ & d(\theta_L \circ \mathbf{v}) \cdot \mathbf{V} = \mathbf{f}^*_{\mathrm{EQ}}(\lambda) \\ \Longleftrightarrow\ & d(\theta_L \circ \mathbf{v}) \cdot \mathbf{V} \cdot \delta\mathbf{v} = \langle \mathbf{f}^*_{\mathrm{EQ}}(\lambda), \delta\mathbf{v} \rangle = \lambda \langle \mathbf{f}_{\mathrm{EQ}}, \delta\mathbf{v} \rangle . \end{aligned} \tag{104}$$

For a given space velocity $\mathbf{v} \in V\mathscr{E}$, the solutions of Eq. (103) describe a 1D manifold with the space-time velocity parameterized by

$$\mathbf{V} = \mathbf{v} + (p/p_0)\,\mathbf{Z}, \tag{105}$$

with p_0 normalizing value to be fixed so that the time component of the space-time velocity is unitary. The function $\hat{p} : \Re \mapsto \Re$ is defined by imposing equality in last of Eqs. (104):

$$d(\theta_L \circ \mathbf{v}) \cdot (\mathbf{v} + (\hat{p}(\lambda)/p_0)\,\mathbf{Z}) \cdot \delta\mathbf{v} = \lambda \langle \mathbf{f}_{\mathrm{DYN}} - d(E \circ \mathbf{v}), \delta\mathbf{v} \rangle . \tag{106}$$

Setting $p_0 = \hat{p}(1)$, the solution of the least action principle Prop. 8.1, corresponding to $\lambda = 1$, is then

$$\mathbf{V} = \mathbf{v} + (\hat{p}(1)/p_0)\,\mathbf{Z} = \mathbf{v} + \mathbf{Z}. \tag{107}$$

Hence the space-time velocity in Eq. (107) is also the solution of EULER-LAGRANGE Eq. (93). The converse statement, that the solution of Eq. (93)

$$d(\theta_L \circ \mathbf{v}) \cdot \mathbf{V} \cdot \delta\mathbf{v} = (\mathbf{f}_{\mathrm{DYN}} - d(E \circ \mathbf{v})) \cdot \delta\mathbf{v}, \tag{108}$$

is also solution of Eqs. Eq. (102), (103), is trivial. ■

Remark 8.1. *The solution of the stationarity principle Eq.* (91) *is also solution of the action principle characterized by the extremality condition in Eq.* (101) *under the integral constraint*

$$\boxed{\int_{\Gamma} \langle d(E \circ \mathbf{v}), \delta\mathbf{v} \rangle\, dt_{\mathscr{C}} = \int_{\Gamma} \langle \mathbf{f}_{\mathrm{DYN}}, \delta\mathbf{v} \rangle\, dt_{\mathscr{C}} .} \tag{109}$$

In turn the solution the extremality condition with the integral constraint Eq. (109) *is also solution of the least action principle Eq.* (101) *with the pointwise constraint Eq.* (102). *The equivalence proved in Prop. 8.1 closes the path of implications so that all these formulations are in fact equivalent one another.*

MAUPERTUIS principle was discussed in (Romano et al., 2009a) where a geometric treatment based on the lifting to the LAGRANGE bundle $V\mathscr{C}$ was provided.

9 POINCARÉ-CARTAN PRINCIPLE

The next lemma yields the basic relations for the formulation of HAMILTON canonical law of dynamics in terms of a linear connection ∇. In (Gantmacher, 1970) the analogous result in coordinates is referred to as DONKIN's theorem (Donkin, 1854).

Lemma 9.1 (Donkin theorem). *For any linear connection* ∇ *and associated parallel transport* $\Uparrow$, *parallel derivatives of* LAGRANGE *and* HAMILTON *functionals fulfil the relations*

$$\begin{cases} \nabla_{\delta\mathbf{v}} H + \nabla_{\delta\mathbf{v}} L \circ \theta_H = 0\,, \\ \nabla_{\delta\mathbf{v}} L + \nabla_{\delta\mathbf{v}} H \circ \theta_L = 0\,. \end{cases} \tag{110}$$

Proof. Recalling that, by definition, the parallel transport of a covector fulfils the invariance property

$$\langle \delta\varphi_\lambda^{\mathscr{C}} \Uparrow \mathbf{p}, \delta\varphi_\lambda^{\mathscr{C}} \Uparrow \mathbf{v} \rangle = \langle \mathbf{p}, \mathbf{v} \rangle\,, \tag{111}$$

we infer that

$$\begin{aligned} \nabla_{\delta\mathbf{v}} H(\mathbf{p}) &:= \partial_{\lambda=0} H(\delta\varphi_\lambda^{\mathscr{C}} \Uparrow \mathbf{p})\,, \\ \nabla_{\delta\mathbf{v}} L(\mathbf{v}) &:= \partial_{\lambda=0} L(\delta\varphi_\lambda^{\mathscr{C}} \Uparrow \mathbf{v})\,, \\ \nabla_{\delta\mathbf{v}} \langle \mathbf{p}, \mathbf{v} \rangle &= \partial_{\lambda=0} \langle \delta\varphi_\lambda^{\mathscr{C}} \Uparrow \mathbf{p}, \delta\varphi_\lambda^{\mathscr{C}} \Uparrow \mathbf{v} \rangle = \partial_{\lambda=0} \langle \mathbf{p}, \mathbf{v} \rangle = 0\,, \end{aligned} \tag{112}$$

and the result follows from EULER-LEGENDRE transform Eq. (56). ■

Proposition 9.1 (Hamilton law of dynamics). *The* EULER-LAGRANGE-POINCARÉ *law of motion is equivalent to* HAMILTON *law expressed, in terms of kinetic momentum, by*

$$\boxed{\begin{cases} \mathbf{p} = \theta_L(\mathbf{v})\,, \\ \langle \nabla_{\mathbf{V}} \mathbf{p} + \nabla H(\mathbf{p}) + \mathbf{p} \cdot \mathbf{T}(\mathbf{V}), \delta\mathbf{v} \rangle = \langle \mathbf{f}_{\mathrm{DYN}}, \delta\mathbf{v} \rangle\,, \end{cases}} \tag{113}$$

for all synchronous $\delta\mathbf{v} \in \mathscr{H}_{\mathscr{C}}$, *with the jump condition* $[[\langle \mathbf{p}, \delta\mathbf{v} \rangle]] = \langle \mathbf{f}_{\mathrm{SING}}, \delta\mathbf{v} \rangle$ *at singular points.*

Proof. Applying EULER-LEGENDRE transform Eq. (56) and DONKIN relation Eq. (110) to LAGRANGE law Eq. (93), we get HAMILTON law Eq. (113). ■

Proposition 9.2 (Time rate of Hamilton functional). *Let us assume that the* HAMILTON *functional is time independent that is*

$$\nabla_{\mathbf{Z}} H(\mathbf{p}) = 0 \iff \nabla_{\mathbf{V}} H(\mathbf{p}) = \nabla_{\mathbf{v}} H(\mathbf{p}) . \tag{114}$$

Then its rate along the motion is equal to the power expended by dynamical forces

$$\boxed{\nabla_{\mathbf{V}}(H \circ \mathbf{p}) = \langle \mathbf{f}_{\mathrm{DYN}}, \mathbf{v} \rangle .} \tag{115}$$

Proof. Setting $\delta \mathbf{v} = \mathbf{v}$ in Eq. (113), noting that

$$\mathbf{T}(\mathbf{V}, \mathbf{v}) = \mathbf{T}(\mathbf{v}, \mathbf{v}) = \mathbf{0} \tag{116}$$

and recalling that $\mathbf{v} = d_F H(\mathbf{p})$, the result follows from the relations

$$\begin{aligned} \langle \nabla_{\mathbf{V}} \mathbf{p}, \mathbf{v} \rangle + \langle \nabla H(\mathbf{p}), \mathbf{v} \rangle &= d_F H(\mathbf{p}) \cdot \nabla_{\mathbf{V}} \mathbf{p} + \nabla_{\mathbf{V}} H(\mathbf{p}) - \nabla_{\mathbf{Z}} H(\mathbf{p}) \\ &= \nabla_{\mathbf{V}}(H \circ \mathbf{p}) - \nabla_{\mathbf{Z}} H(\mathbf{p}) = \langle \mathbf{f}_{\mathrm{DYN}}, \mathbf{v} \rangle , \end{aligned} \tag{117}$$

where Eqs. (A.5) and (56) have been resorted to. ■

HAMILTON differential law of dynamics Eq. (113) can be derived from EULER condition of an action principle governed by a 1-form. Proof is omitted for brevity.

Definition 9.1 (Poincaré-Cartan action form). *The* POINCARÉ-CARTAN *action 1-form* $\omega_H^1 \circ \mathbf{p} : \mathscr{C} \mapsto (V\mathscr{C})_\Gamma^*$ *on the control manifold is induced by the map* $\omega_H^1 : (V\mathscr{C})_\Gamma^* \mapsto (V\mathscr{C})_\Gamma^*$ *defined by*

$$\boxed{\omega_H^1(\mathbf{p}) := \mathbf{p} - H(\mathbf{p})\, dt_{\mathscr{C}} .} \tag{118}$$

The LAGRANGE map $\omega_L^1 : (V\mathscr{C})_\Gamma \mapsto (V\mathscr{C})_\Gamma^*$ is related to the POINCARÉ-CARTAN map $\omega_H^1 : (V\mathscr{C})_\Gamma^* \mapsto (V\mathscr{C})_\Gamma^*$ by the LEGENDRE diffeomorphism $\theta_L : (V\mathscr{C})_\Gamma \mapsto (V\mathscr{C})_\Gamma^*$ with inverse $\theta_H : (V\mathscr{C})_\Gamma^* \mapsto (V\mathscr{C})_\Gamma$.

Indeed, being $E = H \circ \theta_L$, we have the commutative diagram

$$\begin{tikzcd} & (T\mathscr{C})^* & \\ T\mathscr{C} \arrow[ur, "\omega_L^1"] \arrow[rr, shift left, "\theta_L"] & & (T\mathscr{C})^* \arrow[ul, "\omega_H^1"'] \arrow[ll, shift left, "\theta_H"] \end{tikzcd} \iff \begin{cases} \omega_L^1 = \omega_H^1 \circ \theta_L , \\ \omega_H^1 = \omega_L^1 \circ \theta_H . \end{cases} \tag{119}$$

Proposition 9.3 (Poincaré-Cartan action principle). *The motion along the trajectory Γ in the control manifold $\mathscr{C}$, is characterized by the action principle governed by the* POINCARÉ-CARTAN *action form*

$$\boxed{\partial_{\lambda=0}\int_{\delta\varphi^{\mathscr{C}}_{\lambda}(\Gamma)}\omega^1_H\circ\mathbf{p}-\oint_{\partial\Gamma}\langle\omega^1_H\circ\mathbf{p},\delta\mathbf{v}\rangle=\int_{\Gamma}(dt_{\mathscr{C}}\wedge\mathbf{f}_{\mathrm{DYN}})\cdot\delta\mathbf{v},} \tag{120}$$

where $\mathbf{p}=\theta_L(\mathbf{v})\in\mathscr{H}^*_{\mathscr{C}}$ is the momentum field and the variational condition holds for all synchronous $\delta\mathbf{v}\in\mathscr{H}_{\mathscr{C}}$. The localization of Eq. (120), *resorting to Eq.* (118), *yields the differential condition*

$$\boxed{\langle d(\omega^1_H\circ\mathbf{p})\cdot\mathbf{V},\delta\mathbf{v}\rangle=\langle d\mathbf{p}\cdot\mathbf{V}-d(H\circ\mathbf{p}),\delta\mathbf{v}\rangle=\langle\mathbf{f}_{\mathrm{DYN}},\delta\mathbf{v}\rangle,} \tag{121}$$

that will be referred to as the EULER-HAMILTON *law. Expressed in terms of a linear connection, Eq.* (121) *gives* HAMILTON *law Eq.* (113) *since from Eq.* (A.1) *and Eq.* $(A.5)_2$ *we infer that*

$$\begin{aligned} d(\omega^1_H\circ\mathbf{p})\cdot\mathbf{V}\cdot\delta\mathbf{v}=&\langle\nabla_{\mathbf{V}}\mathbf{p},\delta\mathbf{v}\rangle+\nabla_{\delta\mathbf{v}}H(\mathbf{p})+\langle\mathbf{p},\mathbf{T}(\mathbf{V},\delta\mathbf{v})\rangle\\ &+\langle\theta_H(\mathbf{p})-\mathbf{v},\nabla_{\delta\mathbf{v}}\mathbf{p}\rangle, \end{aligned} \tag{122}$$

with the last term vanishing due to the assumption that $\mathbf{v}=\theta_H(\mathbf{p})$.

According to the nomenclature introduced in Rem. 2.1, both the LAGRANGE action principle of Prop. 7.1 and POINCARÉ-CARTAN action principle of Prop. 9.3, are *faithful* action principles, and such is also MAUPERTUIS least action principle Eq. (101). The HAMILTON principle enunciated by Eq. (67) is instead a *hybrid* variational principle.

In a finite dimensional control manifold, with $\dim\mathscr{C}=m+1$, let us consider a coordinate system $\phi:\mathscr{Z}\times\Re^m\mapsto\mathscr{C}$ adapted to the time-fibration, composed by the time parameterization map $\gamma:\mathscr{Z}\mapsto\mathscr{C}$ of the control trajectory line $\Gamma\subset\mathscr{C}$ (0-th coordinate) and by a system of coordinates in the slices of isochronous placements

$$\phi=\{q_i,i=1,\dots m\}:\Re^m\mapsto\mathscr{C}. \tag{123}$$

We may then set the definitions

$$\begin{cases} \dot q=\dfrac{dp}{dt}:=\phi{\downarrow}\mathbf{v},\quad \delta q:=\phi{\downarrow}\delta\mathbf{v},\quad p:=\phi{\downarrow}\mathbf{p},\\ \delta p:=\phi{\downarrow}(\nabla_{\delta\mathbf{v}}\mathbf{p}),\\ \delta\dot q:=\phi{\downarrow}(\nabla_{\delta\mathbf{v}}\mathbf{v}),\quad (\delta q)^{\cdot}:=\phi{\downarrow}(\nabla_{\mathbf{V}}\delta\mathbf{v}). \end{cases} \tag{124}$$

By extension Eq. (66) we have that $[\mathbf{V}, \delta\mathbf{v}] = \mathbf{0}$ and hence

$$\mathbf{T}(\mathbf{V}, \delta\mathbf{v}) = \nabla_{\delta\mathbf{v}}\mathbf{V} - \nabla_{\mathbf{V}}\delta\mathbf{v} - [\mathbf{V}, \delta\mathbf{v}] = \nabla_{\delta\mathbf{v}}\mathbf{V} - \nabla_{\mathbf{V}}\delta\mathbf{v}. \tag{125}$$

Adopting a symmetric connection ($\mathbf{T} = \mathbf{0}$), $\delta\dot{q}$ will be equal to $(\delta q)^{\cdot}$ since

$$\delta\dot{q} = \phi{\downarrow}(\nabla_{\delta\mathbf{v}}\mathbf{v}) = \phi{\downarrow}(\nabla_{\delta\mathbf{v}}\mathbf{V}) = \phi{\downarrow}(\nabla_{\mathbf{V}}\delta\mathbf{v}) = (\delta q)^{\cdot}. \tag{126}$$

The time-vertical 1-form $\mathbf{p} \in (V\mathscr{C})^*_\Gamma$ is then expressed, in the coordinates introduced in Remark 6.4, as a linear combination of the covectors of the dual frame:

$$\mathbf{p} = p\,dq := \sum_{k=1,n} p_k\,dq^k, \tag{127}$$

and its exterior derivative is given by [10]

$$d\mathbf{p} = dp \wedge dq := \sum_{k=1,n} dp_k \wedge dq^k. \tag{128}$$

The POINCARÉ-CARTAN action 1-form of Eq. (118) is then written as

$$\omega^1_H \circ \mathbf{p} := \mathbf{p} - H(\mathbf{p})\,dt_{\mathscr{C}} = p\,dq - H(q,p)\,dt_{\mathscr{C}}, \tag{129}$$

and HAMILTON law Eq. (113) takes the standard expression

$$\begin{cases} \dfrac{dq}{dt} = \dfrac{dH}{dp} & \Longleftrightarrow \quad \mathbf{v} = d_F H(\mathbf{p}), \\ -\dfrac{dp}{dt} = \dfrac{dH}{dq} - Q & \Longleftrightarrow \quad -\nabla_{\mathbf{V}}\mathbf{p} = \nabla H(\mathbf{p}) - \mathbf{f}_{\text{DYN}}. \end{cases} \tag{130}$$

10 VARIATIONAL PRINCIPLES WITH VERTICAL VARIATIONS

The present status of proposed formulations is the following.

1. In (Gantmacher, 1970, 3.17, p. 96) a *second form of* HAMILTON *principle* in *phase space* is enunciated without proof. Analogous statements are the *principle of least action in phase space* in (Arnold, 1974, 9.45 C, p. 244) and the HAMILTON principle in *phase space* in (Marsden and Ratiu, 1998, 8.1.6, p. 224) and (Yoshimura and Marsden, 2006, 3.9). In these statements, the POINCARÉ-CARTAN action principle Eq. (120) of the present paper, is modified by dropping the fiberwise relation $\mathbf{v} = d_F H(\mathbf{p})$ so that the covector $\mathbf{p} \in (V\mathscr{C})^*_\Gamma$ is free to vary in the relevant time-vertical cotangent fiber, that is with the base point kept fixed.

[10] In literature the expressions in components Eq. (127) and Eq. (128) are improperly attributed to the canonical 1-form on the cotangent bundle and to its exterior derivative.

2. In (Yoshimura and Marsden, 2006, 3.1) a HAMILTON-PONTRYAGIN principle in *phase space* is also enunciated by introducing a pair of tangent-cotangent vectors $(\mathbf{u},\mathbf{p}) \in V\mathscr{C} \times_\Gamma (V\mathscr{C})^*$ with $\mathbf{u} \in (V\mathscr{C})_\Gamma$ related to the time-vertical velocity field $\mathbf{v} \in (V\mathscr{C})_\Gamma$ by a fiberwise LAGRANGE constraint in which the covector field $\mathbf{p} \in (V\mathscr{C})^*_\Gamma$ plays the role of controller.

In Prop. 10.1 it will be shown that POINCARÉ-CARTAN action principle of Prop. 9.3 can be extended, by changing the 1-form to be integrated, to an equivalent hybrid principle. Therein the covector field $\mathbf{p} \in \mathscr{H}^*_\mathscr{C}$ is left free to vary in each cotangent fiber (that is at fixed base points) and the momentum relation $\mathbf{p} = \theta_L \circ \mathbf{v}$ is recovered as a natural condition stemming from the variational principle. In Prop. 10.2 the geometric formulation of the HAMILTON-PONTRYAGIN principle considered in (Yoshimura and Marsden, 2006) is provided.

To design the modifications to be brought to POINCARÉ-CARTAN action 1-form, let us preliminarily derive two integral equalities along the trajectory. The property $\langle dt_\mathscr{C}, \mathbf{V}\rangle = 1$ leads, for any $\mathbf{p} \in (V\mathscr{C})^*_\Gamma$, to the equalities

$$\langle \mathbf{p}, \mathbf{V}\rangle = \langle \mathbf{p}, \mathbf{v}\rangle = \langle \mathbf{p}, \mathbf{v}\rangle \langle dt_\mathscr{C}, \mathbf{V}\rangle = \langle \langle \mathbf{p}, \mathbf{v}\rangle dt_\mathscr{C}, \mathbf{V}\rangle . \tag{131}$$

Being $\langle dt_\mathscr{C}, \delta\mathbf{v}\rangle = 0$, the definition $\omega^1_H \circ \mathbf{p} := \mathbf{p} - H(\mathbf{p})\, dt_\mathscr{C}$ gives

$$\begin{cases} (\omega^1_H \circ \mathbf{p}) \cdot \mathbf{V} = \langle \mathbf{p}, \mathbf{v}\rangle - H(\mathbf{p}) = \Big(\langle \mathbf{p}, \mathbf{v}\rangle - H(\mathbf{p})\Big)\, dt_\mathscr{C} \cdot \mathbf{V}, \\ (\omega^1_H \circ \mathbf{p}) \cdot \delta\mathbf{v} = \langle \mathbf{p}, \delta\mathbf{v}\rangle . \end{cases} \tag{132}$$

From Eq. (131) and Eq. $(132)_1$ the following equalities are inferred

$$\int_\Gamma \mathbf{p} = \int_\Gamma \langle \mathbf{p}, \mathbf{v}\rangle\, dt_\mathscr{C} , \tag{133}$$

and

$$\int_\Gamma \omega^1_H \circ \mathbf{p} = \int_\Gamma \Big(\langle \mathbf{p}, \mathbf{v}\rangle - H(\mathbf{p})\Big)\, dt_\mathscr{C} . \tag{134}$$

The 1-forms ω^1_{PC} and ω^1_{HP} that will be adopted in POINCARÉ-CARTAN and HAMILTON-PONTRYAGIN hybrid principles, with $(\mathbf{u},\mathbf{p}) \in (V\mathscr{C})_\Gamma \times_\Gamma (V\mathscr{C})^*_\Gamma$, are given by

$$\boxed{\begin{aligned} &1) \quad \omega^1_{\mathrm{PC}} \circ (\mathbf{p},\mathbf{v}) := \Big(\langle \mathbf{p}, \mathbf{v}\rangle - H(\mathbf{p})\Big)\, dt_\mathscr{C} , \quad \forall \mathbf{p} \in (V\mathscr{C})^*_\Gamma , \\ &2) \quad \omega^1_{\mathrm{HP}} \circ (\mathbf{u},\mathbf{p},\mathbf{v}) := \Big(\langle \mathbf{p}, \mathbf{v} - \mathbf{u}\rangle + (L(\mathbf{u}))\Big)\, dt_\mathscr{C} . \end{aligned}} \tag{135}$$

Setting $\mathbf{u} = \mathbf{v}$, Eq. $(135)_2$ yields the 1-form $(L \circ \mathbf{v})\, dt_\mathscr{C}$ of HAMILTON principle, Prop. 6.1. Let us illustrate in detail the geometric treatment of the variational principles corresponding to the 1-forms ω^1_{PC} and ω^1_{HP}, omitting proofs for brevity.

The former principle is well-known but the standard formulation provided in literature does not comply with the geometric features of the variational problem whose essential ingredient is the variation of the trajectory, according to dragging virtual flows in the control manifold. The issue will be accurately commented in Sect. 11. Two distinct kinds of virtual flows are considered.

1. Virtual flows in the control manifold $\mathscr{C}$, that drag the trajectory $\Gamma \subset \mathscr{C}$, and hence the feet of all tensor fields based on it. These flows are generated by vector fields of synchronous virtual velocities $\delta\mathbf{v} \in (V\mathscr{C})_\Gamma$ in the LAGRANGE bundle over the control manifold.
2. Virtual flows in the HAMILTON bundle $(V\mathscr{C})^*_\Gamma$, that drag the covectors $\mathbf{p} \in (V\mathscr{C})^*_\Gamma$, while keeping the base points fixed. These flows are generated by vector fields $\delta\mathbf{X} \in T_\mathbf{p}(V\mathscr{C})^*_\Gamma$ tangent to HAMILTON bundle and vertical according to the cotangent bundle projection, i.e. such that

$$T\tau^*_\mathscr{C} \cdot \delta\mathbf{X} = \mathbf{0} \in T\mathscr{C}\,. \tag{136}$$

Vectors fulfilling Eq. (136) are said to be *vertical* and are univocally obtainable as vertical liftings[11] of covector fields, so that we may set

$$\delta\mathbf{X} = \text{VLIFT}(\mathbf{p}, \delta\mathbf{p})\,, \qquad \mathbf{p}, \delta\mathbf{p} \in (V\mathscr{C})^*_\Gamma\,, \tag{137}$$

where $\text{VLIFT}(\mathbf{p}, \delta\mathbf{p}) = \partial_{\lambda=0}(\mathbf{p} + \lambda\delta\mathbf{p}) = \partial_{\lambda=0}(\lambda\delta\mathbf{p}) = \delta\mathbf{p}$.

Adopting the usual identification between parallel vectors tangent to a linear space at distinct points, we will set $\delta\mathbf{X} = \text{VLIFT}(\mathbf{p}, \delta\mathbf{p}) \equiv \delta\mathbf{p}$.

The statement of Prop. 10.1 puts into evidence the manner how an intrinsic formulation is feasible without performing the lifting of the trajectory to the cotangent phase space, and how boundary terms are to be taken into account.

Proposition 10.1 (Poincaré-Cartan hybrid principle). *The motion along the trajectory Γ in the control manifold $\mathscr{C}$, is characterized by the hybrid action principle*

$$\boxed{\begin{aligned} &\partial_{\mu=0}\,\partial_{\lambda=0} \int_{\delta\varphi^\mathscr{C}_\lambda(\Gamma)} \omega^1_{\text{PC}} \circ (\mathbf{Fl}^{\delta\mathbf{p}}_\mu(\mathbf{p}), \mathbf{v}) - \oint_{\partial\Gamma} \langle \omega^1_H \circ \mathbf{p}, \delta\mathbf{v} \rangle \\ &\qquad = \int_\Gamma (dt_\mathscr{C} \wedge \mathbf{f}_{\text{DYN}}) \cdot \delta\mathbf{v}\,, \end{aligned}} \tag{138}$$

for all synchronous virtual velocity fields $\delta\mathbf{v} \in \mathscr{H}_\mathscr{C}$ and dual virtual covector fields $\delta\mathbf{p} \in \mathscr{H}^*_\mathscr{C}$.

[11] The meaning here is that the relevant virtual variations are performed while keeping fixed the base point on the trajectory.

The latter principle was considered in (Yoshimura and Marsden, 2006, 3.1), but without the boundary term.

In our treatment, the variations induced in the tangent and cotangent fields by the virtual displacement of the trajectory are properly taken into account and no boundary (end points) condition is assumed. The local conditions are coincident with the ones in (Yoshimura and Marsden, 2006) because the additional terms appearing in our result are killed by the auxiliary conditions generated by vertical variations. As usual, the identification $\mathrm{VLIFT}(\mathbf{u},\delta\mathbf{u}) \equiv \delta\mathbf{u}$ is made.

Proposition 10.2 (Hamilton-Pontryagin hybrid principle). *The motion along the trajectory Γ in the control manifold $\mathscr{C}$, is characterized by the hybrid action principle*

$$\boxed{\begin{aligned}&\partial_{\theta=0}\,\partial_{\mu=0}\,\partial_{\lambda=0}\int_{\delta\varphi^{\mathscr{C}}_{\lambda}(\Gamma)}\omega^1_{\mathrm{HP}}\circ(\mathbf{Fl}^{\delta\mathbf{u}}_{\theta}(\mathbf{u}),\mathbf{Fl}^{\delta\mathbf{p}}_{\mu}(\mathbf{p}),\mathbf{v})\\ &\qquad -\oint_{\partial\Gamma}\langle\theta_L\circ\mathbf{v},\delta\mathbf{v}\rangle=\int_{\Gamma}(dt_{\mathscr{C}}\wedge\mathbf{f}_{\mathrm{DYN}})\cdot\delta\mathbf{v},\end{aligned}} \tag{139}$$

for all synchronous virtual velocities $\delta\mathbf{v}\in\mathscr{H}_{\mathscr{C}}$, and vector fields $\delta\mathbf{u}\in\mathscr{H}_{\mathscr{C}}$ and covector fields $\delta\mathbf{p}\in\mathscr{H}^*_{\mathscr{C}}$.

11 STANDARD FORMULATIONS

It is instructive to reproduce explicitly the standard treatment of POINCARÉ-CARTAN variational principle, in order to perform a direct comparison with the intrinsic formulation provided in Eq. (138) of Prop. 10.1.

The standard expression of the principle, as reported in (Arnold, 1974, 9.45 C, p. 244), but with the addition of the boundary integral, is the following

$$\begin{aligned}\delta\int_{t_1}^{t_2}(p\dot q-H)\,dt-\oint_{t_1}^{t_2}(p\,\delta q)&=\delta\int_{t_1}^{t_2}(p\dot q-H)\,dt-\int_{t_1}^{t_2}(p\,\delta q)^{\cdot}dt\\ &=\int_{t_1}^{t_2}\Big(\dot q\,\delta p-\dot p\,\delta q-\frac{\partial H}{\partial p}\delta p-\frac{\partial H}{\partial q}\delta q\Big)dt\\ &=\int_{t_1}^{t_2}\Big((\dot q-\frac{\partial H}{\partial p})\,\delta p-(\dot p+\frac{\partial H}{\partial q})\,\delta q\Big)\,dt=0,\end{aligned} \tag{140}$$

where resort was made to the commutation property $\delta\dot q=(\delta q)^{\cdot}$ and to the product rule $(p\,\delta q)^{\cdot}=p\,\delta\dot q+\dot p\,\delta q$, with the *variations* δp and δq assumed to be independent of one another, with δq vanishing at the end points t_1,t_2.

The EULER conditions of the variational principle Eq. (140) provide HAMILTON laws of dynamics, in the form corresponding to a standard connection by translation

$$\dot{q} = \frac{\partial H}{\partial p}, \qquad -\dot{p} = \frac{\partial H}{\partial q}. \tag{141}$$

Simple as it is, the previous argument leads in fact to the correct equations of the motion. But this is really an interesting example of how a geometrically incorrect analysis may lead to correct results.

The issue is delicate and the difficulty is subtle and deserves a careful examination. The basic difference, with respect to our treatment in Prop. 9.3, is that the geometric formulation takes naturally into account the rate of variation of the covector field $\mathbf{p} \in \mathscr{H}^*_{\mathscr{C}}$ due to a virtual velocity of the trajectory.

The rate of variation of a covector field $\mathbf{p} \in \mathscr{H}^*_{\mathscr{C}}$ is composed of a vertical variation (a free variation in each fiber at fixed base point in $\mathscr{C}$) and of a non-vertical variation $\nabla_{\delta\mathbf{v}}\mathbf{p}$ linearly dependent on the virtual velocity $\delta\mathbf{v} \in \mathscr{H}_{\mathscr{C}}$, as observed in Sect. 10. Only the former vertical rate of variation is considered in standard treatments, see e.g. (Gantmacher, 1970; Arnold, 1974; Yoshimura and Marsden, 2006).

The subtle point is that evaluation of the latter, non-vertical, variation is in fact not essential for correctness of the result, since the relevant term in EULER condition vanishes by imposing that the covector field is equal to kinetic momentum. This equality is either assumed as an essential condition (in Prop. 9.3) or derived as a natural condition (in Prop. 10.1). Consequently, although the non-vertical variation $\nabla_{\delta\mathbf{v}}\mathbf{p}$ and the virtual velocity $\delta\mathbf{v} \in \mathscr{H}_{\mathscr{C}}$ are *not* independent, since the former depends linearly on the latter, the result arrived at by ignoring this dependence is, after all, the correct one.

The improper procedure of ignoring non-vertical variation was, as a matter of fact, adopted in all treatments of variational dynamics, probably due to the adoption in Eq. (140) of the δ as a variation operator acting in an unspecified manner on the time integral, with the trajectory not appearing explicitly.

Ambiguity of the variation symbol δ helps in forgetting that the trajectory, which is the manifold on which the involved dynamical objects (velocity and kinetic momentum) are based, is dragged by the virtual flow and therefore the common foot of these objects has to follow the moving ground (trajectory) where they are based on. Anyway, also in purportedly geometrical treatments, the possibly misleading δ notation is still adopted, together with formulations in coordinates.

Remark 11.1. *We emphasise that no operational meaning was given in the present treatment to the symbol δ which is here adopted just as a prefix apt to denote* test fields *in variational statements. This is a distinction from the common but*

inadvisable usage of attributing to δ the meaning of an often not explicitly defined variation operator.

The schematic diagram Eq. (142) reproduces classical pictures such as (Gantmacher, 1970, 3.17, p. 96, fig. 32), and (Arnold, 1974, 9.44 C, p. 236, fig. 182; 9.44 D, p. 238, fig. 183).

These representations are geometrically unsuitable, because the fibered structure of *phase space* is not taken into proper account.

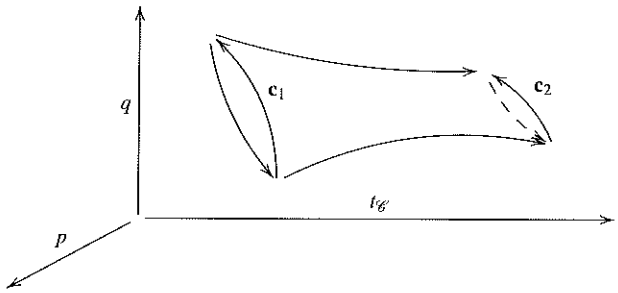

(142)

The resulting scheme, widely diffused in treatments of analytical mechanics, is eventually misleading since the variables $t_{\mathscr{C}}, q, p$ are depicted as they were just cartesian coordinates and not coordinates in a frame adapted to the nonlinear HAMILTON bundle.

In a consistent geometric analysis, coordinate variations cannot be considered as mutually independent. In the picture Eq. (142) the cotangent fibers based at distinct points of the control space are merged into a unique representative linear subspace, an identification which is not admissible since the corresponding covector fields refer to distinct placements of the body.

12 CONCLUSIONS AND RESULTS

Application of geometry to dynamics is a classical subject of investigations and has a quite long history with many brilliant contributions, well-known to scholars involved in the matter. We do not even try to provide a necessarily incomplete list of valuable contributions, but the references in the citations could help in the task. This notwithstanding, the topic is still out of the target of most scholars, even mathematically trained ones, mainly due to a discouraging complexity of notions and notations. The present contribution was focused on the task of illustrating feasibility of a proper geometric treatment of dynamics in the control manifold by resorting to simple but powerful notions and methods. The recurse to more sophisticated geometric constructions involving the second tangent bundle or the tangent

to the cotangent bundle is avoided. The theory is thus freed from unneeded complications, rendering the treatment readily addressable to a larger audience of non specialists in differential geometry. Variational principles are under the spotlight and classical treatments are revisited by basic tools of modern differential geometry, with the aim of dropping unnecessary special assumptions, while retaining or also recovering hypotheses which are basic for a proper geometrical analysis. The outcome is a new formulation of basic results, with an innovative analysis of the connections between various variational statements, and with a special care in elucidating hidden difficulties.

Main results achieved by the investigation are listed below and main topics are summarized in the synoptic table, with the *hybrid* labelling explicated in Rem. 2.1. The exterior forms included in curly braces are respectively the bulk and the boundary forms of the relevant hybrid action principle.

Synoptic table		
Tangent bundle $T\mathscr{C}$		**action forms**
HAMILTON	hybrid principle	$\begin{cases} (L\circ\mathbf{v})\,dt_{\mathscr{C}}\,, \\ \theta_L\circ\mathbf{v}\,. \end{cases}$
LAGRANGE action principle		$\omega^1_L\circ\mathbf{v}=\theta_L\circ\mathbf{v}-(E\circ\mathbf{v})\,dt_{\mathscr{C}}$
MAUPERTUIS least action principle		$\theta_L\circ\mathbf{v}$, with the constraint $\langle d(E\circ\mathbf{v})),\delta\mathbf{v}\rangle=\langle\mathbf{f}_{\mathrm{DYN}},\delta\mathbf{v}\rangle$.
Cotangent bundle $(T\mathscr{C})^*$		**action forms / loop integrals**
POINCARÉ-CARTAN action principle		$\omega^1_H\circ\mathbf{p}=\mathbf{p}-(H\circ\mathbf{p})\,dt_{\mathscr{C}}$, with $\mathbf{p}=\theta_L\circ\mathbf{v}$.
POINCARÉ-CARTAN	hybrid principle	$\begin{cases} (\langle\mathbf{p},\mathbf{v}\rangle-(H\circ\mathbf{p}))\,dt_{\mathscr{C}}\,, \\ \mathbf{p}-(H\circ\mathbf{p})\,dt_{\mathscr{C}}\,. \end{cases}$
Whitney bundle $T\mathscr{C}\times_{\mathscr{C}}(T\mathscr{C})^*$		**action form**
HAMILTON-PONTRYAGIN	hybrid principle	$\begin{cases} (\langle\mathbf{p},\mathbf{v}-\mathbf{u}\rangle+(L\circ\mathbf{u}))\,dt_{\mathscr{C}}\,, \\ \theta_L\circ\mathbf{v}\,. \end{cases}$

All variational principles listed therein are shown, after suitable and even drastic revisitation, to be equivalent statements of the law of dynamics.

- The primary target is to show that a geometric treatment of dynamics can be performed in the natural context of control manifold. This result avoids the recourse to more sophisticated geometric constructions based on considering tangent or cotangent manifolds over the control manifold and the relevant (bi-)tangent bundles. A substantial step towards popularizing geometric methods in dynamics, presently still confined to small nuclei of specialists, is thus made.

- A first issue is an appropriate presentation of what an action principle is defined to be. There are basic differences with variational statements dealing with stationarity of a functional. Action principles consider variations of the integral of an exterior form over a manifold dragged by a virtual flow, the stationarity manifold being called the trajectory. The involved exterior form is well-defined only on the trajectory and, to perform the variations, extensions along virtual flows must be explicitly declared. There is no functional for a stationarity condition to be imposed.

- Another issue is the elimination of needlessly restrictive, and even epistemologically incorrect, constraints on the variations, classically assumed to have null velocities at the trajectory end points. The adoption of unconstrained variations leads to deduce both differential and jump conditions from the action principle and plays a significant role in computational schemes.

- It is emphasised that two main procedures are available to perform comparisons and derivatives. The former procedure is naturally induced by the motion, or by the virtual flow, and consists in a pull-back operation and in the related LIE-differentiation. The latter is induced by the choice of a connection and of the related parallel transport and derivative. The specific problem at hand may suggest the convenient choice of a connection. The usual one in EUCLID spaces is parallel transport by translation, but even in EUCLID spaces other connections may be more suitable. An important instance is given by the adapted connection generated by the control.

- A general formula is contributed to evaluate exterior derivatives of differential forms in terms of parallel derivatives. The formula is a convenient tool to provide an operative expression of EULER differential condition. Arbitrary linear connections are considered and the role of the torsion form is underlined.

- HAMILTON action principle is shown to be equivalent to a constrained action principle in which virtual velocities fulfil a virtual mechanical power balance. This action principle extends and corrects standard but inappropriate definitions of MAUPERTUIS least action principle.
- POINCARÉ-CARTAN action principle for kinetic momentum is formulated in the control manifold and is shown to be equivalent to HAMILTON law of dynamics.
- A discussion, about variational principles in phase spaces as formulated in literature, witnesses the role played by geometrical notions in dynamics. These hybrid principles are reformulated in the natural context of the control manifold, with the introduction of vertical variations (i.e. variations at fixed base point) as appropriate geometric notions.

In conclusion the hope is that this innovative presentation of the geometric approach to dynamics will result into a wider acceptance of the powerful and conceptually clear framework provided by basic differential geometry.

A AUXILIARY RESULTS

The next results, contributed in (Romano G., 2007), provides the expression of the exterior derivative of a 1-form in terms of a linear connection and two split formulae that have been resorted to in the treatment of action principles.

Proposition A.1 (Exterior derivative in terms of a connection). *The exterior derivative $d\omega^1$ of a 1-form $\omega^1 \in \Lambda^1(T\mathbf{M})$ is expressed in terms of a linear connection ∇ by the formula*

$$\boxed{d\omega^1 = \nabla\omega^1 - (\nabla\omega^1)^A + \omega^1 \cdot \mathbf{T},} \tag{A.1}$$

where the 2-forms at the r.h.s. are defined by

$$\begin{aligned} (\nabla\omega^1)\cdot\mathbf{a}\cdot\mathbf{b} &= (\nabla_{\mathbf{a}}\,\omega^1)\cdot\mathbf{b}, \\ (\nabla\omega^1)^A\cdot\mathbf{a}\cdot\mathbf{b} &= (\nabla_{\mathbf{b}}\,\omega^1)\cdot\mathbf{a}, \\ (\omega^1\cdot\mathbf{T})\cdot\mathbf{a}\cdot\mathbf{b} &= \omega^1\cdot\mathbf{T}(\mathbf{a},\mathbf{b}), \quad \forall\mathbf{a},\mathbf{b}\in T\mathbf{M}. \end{aligned} \tag{A.2}$$

Let $(\phi, \mathrm{ID}_{\mathbf{M}})$ be a smooth non-linear morphism, between the tensor bundles $\mathrm{TENS}_1(T\mathbf{M})$ and $\mathrm{TENS}_2(T\mathbf{M})$, described by the commutative diagram

$$\begin{array}{ccc} \mathrm{TENS}_1(T\mathbf{M}) & \xrightarrow{\phi} & \mathrm{TENS}_2(T\mathbf{M}) \\ \pi_{\mathrm{TENS}_1}\big\downarrow & & \big\downarrow\pi_{\mathrm{TENS}_2} \\ \mathbf{M} & \xrightarrow{\mathrm{ID}_{\mathbf{M}}} & \mathbf{M} \end{array} \quad \Longleftrightarrow \quad \pi_{\mathrm{TENS}_2}\circ\phi = \pi_{\mathrm{TENS}_1}. \tag{A.3}$$

Lemma A.1 (Differential split formulae). *Let the tensor field*

$$\phi \circ \mathbf{s} : \mathbf{M} \mapsto \text{TENS}_2(T\mathbf{M}), \tag{A.4}$$

be the composition of the morphism $\phi : \text{TENS}_1(T\mathbf{M}) \mapsto \text{TENS}_2(T\mathbf{M})$ *with a tensor field* $\mathbf{s} : \mathbf{M} \mapsto \text{TENS}_1(T\mathbf{M})$. *The* LIE *and parallel derivatives along the flow* $\varphi_\alpha := \mathbf{Fl}^{\mathbf{v}}_\alpha$ *of a vector field* $\mathbf{v} : \mathbf{M} \mapsto T\mathbf{M}$, *may then be expressed by the split formulae*

$$\boxed{\begin{aligned} \mathscr{L}_{\mathbf{v}}(\phi \circ \mathbf{s}) &= (\mathscr{L}_{\mathbf{v}}\phi)(\mathbf{s}) + d_F\phi(\mathbf{s}) \cdot \mathscr{L}_{\mathbf{v}}\mathbf{s}, \\ \nabla_{\mathbf{v}}(\phi \circ \mathbf{s}) &= (\nabla_{\mathbf{v}}\phi)(\mathbf{s}) + d_F\phi(\mathbf{s}) \cdot \nabla_{\mathbf{v}}\mathbf{s}. \end{aligned}} \tag{A.5}$$

REFERENCES

Abraham, R., Marsden, J.E., 1978. Foundations of Mechanics. Benjamin/Cummings, Reading Massachusetts.

Abraham, R., Marsden, J.E., Ratiu, T.S., 2002. Manifolds, Tensor Analysis, and Applications. Springer, New York.

Ambrosio, L., Fusco, N., Pallara, D., 2000. Functions of Bounded Variation and Free Discontinuity Problems. Oxford Univ. Press, Oxford.

Arnold, V.I., 1974. Mathematical methods of classical mechanics. Nauka, Moscow. Springer-Verlag, New York (1989).

Arnold, V.I., Kozlov, V.V., and Neishtadt, A.I., 1988. Dynamical Systems III, Encyclopaedia of Mathematical Sciences. V.I. Arnold (Ed.) Springer-Verlag, New York.

Bailey, C.D., 1975. A New Look at Hamilton's Principle. Foundations of Physics, **5** (3).

Bertrand, J., 1852. Mémoire sur l'integration des équations différentielles de la Mécanique. Liouville J. **17**, 393-436.

Borri, M., Ghiringhelli, G.L., Lanz, M., Mantegazza, P., Merlini, T., 1985. Dynamic response of mechanical systems by a weak Hamiltonian formulation. Comp. & Struct. **20** (1-3) 495-508.

Borri, M., Bottasso, C., Mantegazza, P., 1992. Basic features of the time finite element approach for dynamics. Meccanica **27**, 119-130.

Borri, M., Bottasso, C., 1993. A general framework for interpreting time finite element formulations. Comp. Mech. **13**, 133-142.

Cartan, É., 1922. Leçons sur les invariants intégraux. Hermann, Paris.

Cartan, É., 1937. La théorie des groupes finis et continus et la géométrie différentielle traitées par la méthode du repère mobile. Gauthier-Villars, Paris.

Cartan, H., 1967. Forme différentielles - Applications Élémentaires au Calcul des Variations et a la Théorie des Courbes et des Surfaces. Hermann, Paris.

Choquet-Bruhat, Y., 1970. Gèométrie Différentielle et Systèmes extérieurs. Travaux et recherches matématiques, Collège de France. Dunod, Paris.

Choquet-Bruhat, Y., DeWitt-Morette, C., Dillard-Bleick, M., 1982. Analysis, Manifolds and Physics. North-Holland Publishing Company, New York.

d'Alembert, J-B., 1743. Traité de dynamique. J-B. Coignard, Paris.

Donkin, W.F., 1854. On a Class of Differential Equations, Including Those Which Occur in Dynamical Problems. Part I. Phil. Trans. R. Soc. Lond. **144**, 71-113. doi: 10.1098/rstl.1854. 0006

Deschamps, G.A., 1970. Exterior differential forms. In: Mathematics Applied to Physics, Roubine É. (Ed.) Springer-Verlag, Berlin.

Dieudonné, J., 1969-1974. Treatise on Analysis. Vol I-IV, Academic Press, New York.

Eliasson, H.I., 1967. Geometry of Manifolds of Maps. J. Diff. Geom. **1** 169-194.

Euler, L., 1744. Methodus inveniendi lineas curvas maximi minimive proprietate gaudentes, sive solutio problematis isoperimetrici latissimo sensu accepti, additamentum II. In: C. Carathéodory (ed.), Opera Omnia, Fussli, Zürich, Switzerland, LII-LV, 298-308 (1952).

Euler, L., 1761. Principia Motus Fluidorum. Novi Comm. Acad. Sci. Petrop. **6** 271-311.

Fonseca, I., Leoni G., 2007. Modern Methods in the Calculus of Variations: L^p Spaces. Springer, New York.

Gantmacher, F., 1970. Lectures in Analytical Mechanics. Mir, Moscow.

Godbillon, C., 1969. Géométrie différentielle et mécanique analytique. Collection Méthodes, Hermann, Paris.

Godbillon, C., 1971. The Principle of Maupertuis. In: D. Chillingworth (ed.), Lee. Notes Math., Springer, New York 91-94.

Goldstein, H., 1950. Classical Mechanics. Addison Wesley, Reading, Mass.

Hamilton, W.R., 1834. On a General Method in Dynamics. Philosophical Transactions, Part 2, 247-308.

Hamilton, W.R., 1940. The Mathematical Papers of Sir William Rowan Hamilton, Volume II: Dynamics. Cambridge University Press.

Jacobi, C.G.J., 1837a. Zur Theorie der Variations-Rechnung und der Differential-Gleichungen. J. Reine Angew. Math. **17** 68-82 = Werke **4** 39-55.

Jacobi, C.G.J., 1837b. Über die Reduction der Integration der partiellen Differentialgleichungen erster Ordnung zwischen irgend einer Zahl Variabeln auf die Integration eines einzigen Systems gewöhnlicher Differentialgleichungen. J. Reine Angew. Math. **17** 97-162 = Werke **4** 57-127.

Jacobi, C.G.J., 1884. Vorlesungen über Dynamik. Königsberg 1842-1843. G. Reimer, Berlin.

Klein, F., 1926. Vorlesungen über die Entwicklung der Mathematik im 19 Jahrhundert, I. Mechanik, Ch. 5. Springer-Verlag, Berlin.

Klein, J., 1962. Espaces variationnels et Mécanique. Ann. Inst. Fourier **12**, 1-124.

Lagrange, J.L., 1788. Mechanique Analytique. In: Serret J.A. (ed.), Ouvres, Gauthiers-Villars, Paris (1867).

Landau, L.D., Lifšits E.M., 1976. Mechanika, Mir Ed., Moscow.

Lie, M.S., Engel, F., 1888-1890-1893. Theorie der Transformationsgruppen. Vol. 1-3, BG Teubner, Leipzig (1888-1890-1893) 2nd edn. Chelsea, New York (1970).

Marsden, J.E., Hughes, T.J.R., 1983. Mathematical Foundations of Elasticity. Prentice-Hall, Redwood City, Cal.

Marsden, J.E., Ratiu, T.S., 1998. Introduction to Mechanics and Symmetry - A Basic Exposition of Classical Mechanical Systems. Texts in Applied Mathematics, Vol. 17, 2nd ed. Springer, Berlin.

Marsden, J.E., Patrick, G., Shkoller, S., 1998. Multisymplectic geometry, variational integrators, and nonlinear PDEs. Comm. Math. Phys. **199** 351-391

Maupertuis de, P.L.M., 1744. Accord de différentes loix de la nature qui avoient jusqu'ici paru incompatibles, Mém. As. Sc. Paris, **417**.

Noether, E.A., 1918. Invariante Variationsprobleme. Nachr. d. König. Gesellsch. d. Wiss. zu Göttingen. Math-Phys. Klasse, 235-257.

Peters, D.A., Izadpanah, A.P., 1988. hp-version finite elements for the space-time domain. Comp. Mech. **3**, 73-88.

Poisson, S.D., 1811. Traité de Mécanique, Tome I-II, Courcier, Paris.

Oliva, W.M., 1798. Geometric Mechanics. Lecture Notes in Mathematics. Springer (2002). `http://www.springerlink.com/home/main.mpx`

Palais, R.S., 1968. Foundations of Global Non-Linear Analysis. Benjamin, New York.

Poincaré, H., 1892-1893-1899. Les méthodes nouvelles de la mécanique céleste, vol 1-3. Gauthiers-Villars, Paris.

Poincaré, H., 1901. Sur une forme nouvelle des équations de la méchanique. C.R. Acad. Sci. **132** 369-371.

Riff, R., Baruch, M., 1984. Time Finite Element Discretization of Hamilton's Law of Varying Action. AIAA Journal **22** (9) 1310-1318.

Romano, G., 2007. Continuum Mechanics on Manifolds. Lecture notes, University of Naples Federico II, Naples, Italy 1-695. `http://wpage.unina.it/romano`

Romano, G., Barretta, R., Barretta, A., 2009a. On Maupertuis principle in dynamics. Rep. Math. Phys. **63** (3) 331-346.

Romano, G., Barretta, R., Diaco, M., 2009b. On Continuum Dynamics. J. Math. Phys. **50**, 102903-1-26.

Romano, G., Barretta, R., 2011. Covariant hypo-elasticity. Eur. J. Mech. A-Solids **30**, 1012-1023.

Romano, G., Barretta, R., 2013. Geometric Constitutive Theory and Frame Invariance. Int. J. Non-Linear Mech. **51**, 75-86.

Romano, G., Barretta, R., Diaco, M., 2014a. Geometric Continuum Mechanics. Meccanica **49**, 111-133.

Romano, G., Barretta, R., Diaco, M., 2014b. Rate formulations in nonlinear continuum mechanics. Acta Mech. **225** (6) 1625-1648.

Romano, G., Barretta, R., Diaco, M., 2014c. The Geometry of Non-Linear Elasticity. Acta Mech. **225**, 3199-3235.

Souriau, J.-M., 1970. Structure des systèmes dynamiques. Dunod, Paris.

Spivak, M., 1970. A comprehensive Introduction to Differential Geometry. Vol.I-V. 3rd edn. Publish or Perish, Inc., Houston (2005).

Strang, G., Fix, G.J., 1988. An Analysis of the Finite Element Method. Wellesley-Cambridge Press.

Terra, G., Kobayashi, M.H., 2004a. On classical mechanical systems with non-linear constraints. J. Geom. Phys. **49**, 385-417.

Terra, G., Kobayashi, M.H., 2004b. On the variational mechanics with non-linear constraints. J. Math. Pures Appl. **83**, 629-671.

Yoshimura, H., Marsden, J.E., 2006. Dirac structures in Lagrangian mechanics Part II: Variational structures. J. Geom. Phys. **57**, 209-250.

Rend. Acc. Sc. fis. mat. Napoli
Vol. LXXXII, (2015) pp. 47-60

Qualitative estimates for a nonlinear fourth order P.D.E. modeling physical phenomena

Paolo Fergola[1], Salvatore Rionero[2*]

Presentata dai soci Paolo Fergola e Salvatore Rionero
(Adunanza del 20 Marzo 2015)

Key words: Stability; boundedness; Asymptotic behavior of solutions.

Abstract. Qualitative estimates for solutions of a nonlinear fourth order P.D.E. are investigated. Ultimately boundedness and stability conditions of the null solution are obtained. The equation at stake, in the context of Musical Acoustic, is studied as Physical Model in order to build analogical or digital synthesizers.

Riassunto. Si studia una equazione non lineare a derivate parziali di tipo iperbolico, del quarto ordine. Si studia la definitiva limitatezza delle soluzioni e la stabilità della soluzione nulla. L'equazione in esame, nel contesto dell'acustica musicale, è studiata come Modello Fisico per sintetizzatori analogici o digitali.

1 - INTRODUCTION

The present paper is essentially constituted by two parts. The first one (Sect. 2–5) is devoted to study the long time behaviour (stability and ultimate boundedness)

[1]R.I.S.M.A. University of Naples Federico II, Complesso Universitario di Monte Sant'Angelo, Via Cintia, 80126 Naples-Italy. Società Nazionale di Scienze, Lettere e Arti, Accademia di Scienze Fisiche e Matematiche, Via Mezzocannone, 8 80134 , Napoli , Italia. **email**:pfergola@unina.it

[2]University of Naples "Federico II". Department of Mathematics And Applications "R.Caccioppoli". Via Cinthia 80126 Naples-Italy. **email**:rionero@unina.it. Accademia Nazionale dei Lincei, via della Lungara, 10. 00165 (Roma).**email**:rionero@lincei.it

[*]Author to whom correspondence should be addressed

of solutions of Initial Boundary Value Problem (I.B.V.P.)

$$u_{tt} = c^2 u_{xx} - K^2 u_{xxxx} - 2b_1 u_t + 2b_2 u_{xxt} + F(u, u_t)u, \tag{1}$$

$$\begin{cases} u(0,t) = u(1,t) = 0, \\ u(x,0) = u_0(x), \quad u_t(x,0) = \nu_1(x), \end{cases} \tag{2}$$

with u_0, ν_1 regular functions such that

$$u_0 = \nu_1 = 0, \qquad x = 0, 1, \tag{3}$$

c, K, b_1, b_2 positive constants and where the term F, generally non-linear, denoting possible perturbations to the system, is such that

$$uF = 0, \qquad \text{for } u = 0. \tag{4}$$

The second part (Sect.6) is devoted to the application of the results obtained in the first part to a problem of Musical Acoustics concerning with the propagation equation of vibrations in a struck, stiff string of a piano.

First of all we observe that equation (1), deprived of term containing the fourth order derivative, formally coincides with equation (1.1) of Rionero, 2012a, in the autonomous case

$$u_{tt} = Cu_{xx} - au_t + \varepsilon u_{xxt} + F(u) \tag{5}$$

if we set

$$C = c^2, \quad a = 2b_1, \quad \varepsilon = 2b_2, \tag{6}$$

where $F(u)$ also represents, generally, a non-linear perturbation such that $F(0) = 0$. According to (Rionero, 2012a), the interest in this equation derives by the fact that it can suitably model various and important viscoelastic fluids (Joseph et al., 1985), the propagation of plane waves in M.H.D. (Nardini, 1953), the sound propagation in viscous gases Lamb, 1959, and the classical Josephson effect in the superconductors theory (Barone and Paternò, 1982).

From a physical point of view what is interesting about equation (1) is the fact that it is the equation used by (Bensa et al., 2003), and by (Bensa et al., 2005) (Sect.6) to study the propagation of piano-vibrations in a struck stiff string with pinned ends, if we assume that

$$c^2 = \frac{T}{\mu}, \qquad K^2 = k^2(ES/TL^2), \tag{7}$$

where k is the radius of gyration of string, E is the Young's modulus, S the cross sectional area, L the length of string and the two positive constants b_1 and b_2 in (6) are identified with the values of two physical parameters derived from experiments, appearing in some empirical laws accounting globally for the losses in the air and in the string material, as well as for those due to the coupling to soundboard.

In this equation the term containing the fourth order partial derivative mathematically represents the "stiffness of strings" (Fletcher and Rossing, 1998). Of course (1) is more general than the autonomous version of (5) because it is a P.D.E. of fourth order and its perturbation term may depend not only on u but also on u_t.

2 – PRELIMINARIES

In view of the boundary conditions, we embed the problem in the space L_2^* such that $\Phi \in L_2^*$ requires

i) $\Phi = 0$, for $x = 0, 1$;

ii) $\Phi \in W^{2,4}(0,1)$;

iii) $\Phi, \Phi_t, \Phi_{xx}, \Phi_{xxxx}, \Phi_{xxt}$ can be expanded in Fourier series absolutely uniformly convergent in $(0,1)$, $\forall t \in \mathbb{R}^+$.

Further we denote by

- $\|\cdot\|$ the norm in $L_2^*(0,1)$;
- $<\cdot,\cdot>$ the scalar product in $L_2^*(0,1)$.

Since $\{\sin n\pi x\}_{n=1,2,\ldots}$ is a complete orthogonal system in $L_2^*(0,1)$, $iii)$ implies

$$\begin{cases} u = \displaystyle\sum_{n=1}^{\infty} u_n, \quad u_n(t) = X_n(t)\sin n\pi x, \\ u_t = \displaystyle\sum_{n=1}^{\infty} v_n, \; v_n(t) = Y_n(t)\sin n\pi x, \quad Y_n(t) = \dfrac{dX_n}{dt}. \end{cases} \tag{8}$$

Setting

$$u_t = v, \tag{9}$$

it follows that

$$\begin{cases} u_t = v, \\ v_t = -2b_1 v + 2b_2 v_{xx} + c^2 u_{xx} - k^2 u_{xxxx} + F(u, u_t)u \end{cases} \tag{10}$$

under the i.b.c.

$$\begin{cases} u(x,0) = u_0(x), \quad v(x,0) = v_0(x), \\ u = v = 0, \qquad x = 0, 1. \end{cases} \tag{11}$$

3 – LINEAR STABILITY

In the absence of $F(u, u_t)u$, (10) gives us

$$\begin{cases} u_t = v, \\ v_t = -2b_1 v + 2b_2 v_{xx} + c^2 u_{xx} - k^2 u_{xxxx} \end{cases} \tag{12}$$

and hence

$$\begin{cases} (u_n)_t = v_n, \\ (v_n)_t = -2b_1 v_n + 2b_2 n^2\pi^2 v_n - c^2 n^2 \pi^2 u_n - k^2 n^4 \pi^4 u_n \end{cases} \tag{13}$$

i.e.

$$\begin{cases} (u_n)_t = v_n, \\ (v_n)_t = -2(b_1 + 2b_2 n^2\pi^2) v_n - n^2\pi^2 (c^2 + k^2 n^2 \pi^2) u_n. \end{cases} \tag{14}$$

And hence

$$\begin{cases} (u_n)_t = 0 u_n + v_n, \\ (v_n)_t = -A_n u_n + \mathrm{I}_n v_n, \end{cases} \tag{15}$$

with

$$A_n = n^2\pi^2(c^2 + k^2 n^2 \pi^2), \qquad \mathrm{I}_n = -2(b_1 + b_2 n^2 \pi^2). \tag{16}$$

Introducing the Rionero's functional (Rionero, 2012a)

$$V_n = \frac{1}{2}\int_0^1 [A_n(u_n^2 + v_n^2) + A_n^2 u_n + (v_n + \mathrm{I}_n u_n)^2] dx \tag{17}$$

it follows that, along the solutions of (15), one obtains

$$\begin{aligned} \dot{V}_n &= \mathrm{I}_n A_n \int_0^1 (u_n^2 + v_n^2)\, dx \leq \\ &\leq -2\pi^2(b_1+b_2\pi^2)(c^2+k^2\pi^2) \int_0^1 (u_n^2 + v_n^2) dx \leq 0 \end{aligned} \tag{18}$$

that implies the asymptotic linear stability of the null solution.

We end by remarking that since one easily can show that there exist two positive constants α_n and β_n such that

$$\alpha_n \int_0^1 (u_n^2 + v_n^2)\, dx \leq V_n \leq \beta_n \int_0^1 (u_n^2 + v_n^2) dx \tag{19}$$

from (18) and (19) one obtains

$$\dot{V}_n \leq -\delta_n V_n, \tag{20}$$

with

$$\delta_n = \frac{|\mathrm{I}_n| A_n}{\beta_n} \tag{21}$$

and hence

$$V_n \leq V_n(0) e^{-\delta_n t} \tag{22}$$

i.e. the function V_n decreases exponentially.

Remark 1. *We observe that the eigenvalues of (15) are given by*

$$\lambda_{1n}\lambda_{2n} = A_n > 0, \qquad \lambda_{1n} + \lambda_{2n} = I_n < 0. \tag{23}$$

Further, because

$$V_n > A_n E_n, \qquad E_n = \frac{1}{2} \int_0^1 (u_n^2 + v_n^2) dx \tag{24}$$

one, in view of (22), obtains

$$E_n < \frac{V_n(0)}{A_n} e^{-\delta_n t} \leq \frac{\beta_n}{A_n} E_n(0) e^{-\delta_n t} \tag{25}$$

i.e. the energy decreases exponentially along the solutions of the linear system (15).

4 – AUXILIARY SYSTEM

(10), (11) can be written as

$$\begin{cases} u_t = \sum_{n=1}^{\infty} v_n, \\ v_t = -2\sum_{n=1}^{\infty}(b_1 + b_2 n^2\pi^2)v_n - \pi^2 \sum_{n=1}^{\infty}(c^2 + k^2 n^2 \pi^2)u_n + F(u, u_t)u \end{cases} \tag{26}$$

under the conditions

$$\begin{cases} u(x,0) = \sum_{n=1}^{\infty} u_n(x,0) = u_0(x) = \sum_{n=1}^{\infty} u_{0n}(x,0), \\ v(x,0) = \sum_{n=1}^{\infty} v_n(x,0) = v_0(x) = \sum_{n=1}^{\infty} v_{0n}(x,0), \\ u_n(0) = u_n(1) = v_n(0) = v_n(1) = 0. \end{cases} \tag{27}$$

Following (Rionero, 2012b, 2013, 2014), we call *Auxiliary Evolution System of the nth Fourier component of (u,v) associated to (u,v)*, the system

$$\begin{cases} \frac{\partial}{\partial t} u_n^* = v_n^*, \\ \frac{\partial}{\partial t} v_n^* = -2(b_1 + b_2 n^2\pi^2)v_n^* - \pi^2 \sum_{n=1}^{\infty}(c^2 + k^2 n^2 \pi^2)u_n^* + F(u, u_t)u_n^* \end{cases} \tag{28}$$

under the conditions

$$\begin{cases} (v_n^*)_{(t=0)} = v_{0n}, \\ u_n^* = v_n^* = 0, \quad \text{for} \quad x = 0, 1. \end{cases} \tag{29}$$

Theorem 1. *Let (u, v) be solution of (26)-(27) $\in L_2^*(0,1)$ and let (u_n^*, v_n^*) be solution of (28)-(29) $\forall n \in \mathbb{N}$. Then the series $\sum_{n=1}^{\infty} u_n^*$, $\sum_{n=1}^{\infty} v_n^*$ are a.e. convergent in Ω and it follows that*

$$\sum_{n=1}^{\infty} u_n^* = u, \quad \sum_{n=1}^{\infty} v_n^* = v. \tag{30}$$

Proof. Setting

$$S_m = \sum_{n=1}^{m} u, \quad S_m^* = \sum_{n=1}^{m} v_n^*, \tag{31}$$

the following I.B.V.P. holds

$$\frac{\partial}{\partial t}\begin{pmatrix} S_m \\ S_m^* \end{pmatrix} = \sum_{n=1}^{m} L_n \begin{pmatrix} u_n^* \\ v_n^* \end{pmatrix} + F(u, u_t)\begin{pmatrix} 0 \\ S_m \end{pmatrix}, \tag{32}$$

with

$$(S_m)_{(t=0)} = \sum_{n=1}^{m} u_{0n}, \qquad (S_m^*)_{(t=0)} = \sum_{n=1}^{m} v_{0n},$$

and

$$S_m = S_m^* = 0, \quad \text{for } x = 0, 1$$

$$L_n = \begin{pmatrix} 0 & 1 \\ \alpha_n & \beta_n \end{pmatrix} \tag{33}$$

$$\alpha_n = -\pi^2(c^2 + k^2 n^2 \pi^2), \qquad \beta_n = -2(b_1 + b_2 n^2 \pi^2).$$

Setting

$$\Psi_n = \begin{cases} u_n - u_n^*, & \text{for } n = 1, 2, ..., m, \\ u_n, & \text{for } n > m, \end{cases} \qquad \Psi = \sum_{n=1}^{\infty} \Psi_n \tag{34}$$

$$\Psi_n^* = \begin{cases} v_n - v_n^*, & \text{for } n = 1, 2, ..., m, \\ v_n, & \text{for } n > m, \end{cases} \qquad \Psi^* = \sum_{n=1}^{\infty} \Psi_n^* \tag{35}$$

by virtue of (28) and (32) one obtains

$$\frac{\partial}{\partial t}\begin{pmatrix} \Psi \\ \Psi^* \end{pmatrix} = \sum_{n=1}^{\infty} L_n \begin{pmatrix} \Psi_n \\ \Psi_n^* \end{pmatrix} + F(u, u_t)\Psi \tag{36}$$

under the conditions

$$\begin{cases} (\Psi)_{(t=0)} = \sum_{n=m+1}^{\infty} u_{0n}, \quad (\Psi^*)_{(t=0)} = \sum_{n=m+1}^{\infty} v_{0n}, \\ \Psi = \Psi^* = 0, \quad \text{for } x = 0, 1. \end{cases} \tag{37}$$

Since

$$\lim_{m\to\infty}\sum_{n=m+1}^{\infty} u_{0n} = \lim_{m\to\infty}\sum_{n=m+1}^{\infty} v_{0n} = 0, \tag{38}$$

it follows that

$$\lim_{m\to\infty}(u - S_m) = \lim_{m\to\infty}(v - S_m^*) = 0 \tag{39}$$

under the condition that (26) admits only the null solution under zero I.B.V.

Remark 2. *We remark that, since the Fourier components are uniquely determined, (30) implies*

$$u_n^* = u_n, \quad v_n^* = v_n \tag{40}$$

and (28) can be written in the following form

$$\begin{cases} \dfrac{\partial}{\partial t}u_n^* = v_n^*, \\[2ex] \dfrac{\partial}{\partial t}v_n^* = -2(b_1 + b_2 n^2\pi^2)v_n^* - \pi^2\displaystyle\sum_{n=1}^{\infty}(c^2 + k^2n^2\pi^2)u_n^* + F(u, u_t)u_n^* \end{cases} \tag{41}$$

that is an evolutionary system for each Fourier component of the solution (u, v).

Remark 3. *We remark that properties of the solutions of (41), holding for any* n, *produce analogous properties for (26)-(27).*

5 – ULTIMATE BOUNDEDNESS OF SOLUTIONS

Introducing the Rionero's positive definite functional (Rionero, 2012a, 2013)

$$V_n = \int_0^1 [A_n(u_n^2 + v_n^2) + A_n^2 v_n^2 + (v_n - \mathrm{I}_n u_n)^2]dx \tag{42}$$

along (41), it follows that

$$\dot{V}_n = A_n \mathrm{I}_n \int_0^1 A_n(u_n^2 + v_n^2)dx + \varphi_n, \tag{43}$$

with

$$\begin{cases} A_n = -\alpha_n = \pi^2(c^2 + k^2 n^2 \pi^2), \\ \mathtt{I}_n = \beta_n = -2(b_1 + b_2 n^2 \pi^2), \\ \varphi_n = < A_{2n} v_n - A_{3n} u_n, F(u, u_t), u_n >, \\ A_{2n} = A_{n+1}, \quad A_{3n} = \mathtt{I}_n. \end{cases} \tag{44}$$

Assuming

$$\begin{cases} < F(u, u_t) u_n, v_n > < m, \\ < F(u, u_t) u_n, u_n > < m, \end{cases} \tag{45}$$

with m positive constant, it follows that

$$\dot{V}_n < -A_n |\mathtt{I}_n| \int_0^1 A_n (u_n^2 + v_n^2) dx + m(A_n + 1 + |\mathtt{I}_n|). \tag{46}$$

On the other hand

$$V_n < \int_0^1 \left[A_n + \mathtt{I}_n^2 + |\mathtt{I}_n|/2] u_n^2 + +(A_n + A_n^2 + 3/2) v_n^2 \right] dx \leq$$

$$\leq m^* \int_0^1 (u_n^2 + v_n^2) dx, \tag{47}$$

$$m^* = \max \left\{ A_n + \mathtt{I}_n^2 + |\mathtt{I}_n|/2, A_n + A_n^2 + 3/2 \right\}$$

and hence

$$-\int_0^1 (u_n^2 + v_n^2) dx \leq -1/m^* V_n. \tag{48}$$

Then in view of (46) and (48) one obtains

$$\dot{V}_n \leq -\delta_n V_n + \gamma_n, \tag{49}$$

with

$$\delta_n = \frac{A_n |\mathtt{I}_n|}{m^*}, \qquad \gamma_n = m(A_n + 1 + \mathtt{I}_n). \tag{50}$$

Theorem 2. *Let (45) hold. Then the set $S_{n\sigma}$ of the phase plan (u_n, v_n) such that*

$$S_{n\sigma} := \left\{ (u_n, v_n) \in S_{n\sigma} \Rightarrow V_n < (1+\sigma) \frac{\gamma_n}{\delta_n} \right\} \tag{51}$$

with $\sigma > 0$, is an absorbing set for (u_n, v_n).
Furthermore if

$$\sup_{n\in\mathbb{N}} \frac{\gamma_n}{\delta_n} = \gamma < \infty \tag{52}$$

then the set

$$S_\sigma^* := \{(u_n, v_n) \in S_\sigma^* \Rightarrow V_n < (1+\sigma)\gamma\}, \tag{53}$$

is an absorbing set for any (u_n, v_n).

Proof. By virtue of (49), the proof is obtained easily via standard procedure (see, for instance, Rionero, 2012a, 2013).

Remark 4. *We observe that (45) are verified for*

i) $F(u, u_t) \leq \dfrac{m}{a + u^2 + u_t}$, *with* $\alpha \geq 0$;

ii) the obtained results continue to hold in the case of a forcing term of type

$$F(u, u_t)(au + bu_t)$$

with

$$F(u, u_t) \leq \frac{m}{a_1 + b_1(u^2 + u_t^2)}, \quad a_1, b_1 > 0.$$

For the sake of simplicity we refer to the case i). Then

$$< F(u, u_t)u_n, v_n > \leq m \int_0^1 \frac{|u_n||v_n|}{a + u^2 + v^2} dx \leq$$

$$\leq m \int_0^1 \frac{1/2(u_n^2 + v_n^2)}{a + u^2 + v^2} dx \leq \frac{m}{2} \int_0^1 \frac{(u_n^2 + v_n^2)}{a + u^2 + v^2} dx \leq$$

$$\leq m \int_0^1 \frac{(u_n^2 + v_n^2)}{a + \sum_{m=1}^{\infty} u_m^2 + \sum_{m=1}^{\infty} v_m^2} dx \leq m.$$

6 – AN APPLICATION OF THE AUXILIARY SYSTEM METHOD TO THE PROBLEM OF VIBRATIONS IN A STRUCK STIFF STRING WITH FIXED ENDS

People working in Musical Acoustics often use Physical Models[3] as basis to build analogical as well digital synthesizers of sounds, able to simulate real sounds of

[3] We recall that in the context of Musical Acoustic "Physical Model means a mathematical model representing the various physical features related to the considered phenomenology".

musical instruments (see, for instance, Bensa et al., 2005). Almost always, the associated I.B.V.P. are studied by using numerical methods of approximation as, for instance, the Finite Difference Method. Very often in these years the results of the simulations performed by using this type of approach have produced sounds very close to those generated by real pianos. Further and wide References can be found in the papers by (Fletcher and Rossing, 1998), (Hiller and Ruiz, 1971), (Chaigne and Askenfelt, 1994), (Bank and Sujbert, 2005), where other models have been suggested. In this Section we will apply the Auxiliary System Method of previous Section to prove two qualitative results concerning with the long-time behaviour of solutions of well posed I.B.V.P. (1)-(4) with (6) used in (Bensa et al., 2003) and in (Bensa et al., 2005), to study the propagation of vibrations in a struck stiff string of a piano. Here, for the convenience of readers, we rewrite the equation:

$$u_{tt} = \frac{T}{\mu} u_{xx} - k^2(ES/TL^2)u_{xxxx} - 2b_1 u_t + 2b_2 u_{xxt} + F(u, u_t)u, \tag{54}$$

$$u(x,0) = u_0(x), \qquad u_t(x,0) = \nu_1(x), \tag{55}$$

with u_0, ν_1 regular functions such that

$$(u_0)_{x=0} = (\nu_1)_{x=L} = 0, \qquad (u_{xx})_{x=0} = (u_{xx})_{x=L} = 0 \tag{56}$$

c, k, b_1, b_2 positive constants and the perturbation term F, generally non-linear and such that

$$uF = 0, \qquad \text{for } u = 0, \tag{57}$$

where T represents the tension of string, μ its linear density, k is the radius of gyration of string, E is the Young's modulus, S the cross sectional areas, L the length of string and identify b_1 and b_2 two positive constants with values derived fro experiments, appearing in some empirical laws accounting globally for the losses in the air and in the string material, as well as for those due to the coupling to soundboard. We are ready now to prove *the existence of an absorbing set* for the solutions of our I.B.V.P., i.e. the existence of a compact and invariant set of the phase space ultimately attracting overall solutions of the problem (i.e. in which they enter after a finite time τ). The proof is obtained on the basis of Theorem 5.1 of Section 5. First of all we observe that the validity of this Theorem depends on the determination of the two numbers m^* and γ^* defined through the two following definitions

$$m^* = \max\left\{A_n + I_n^2 + |I_n|/2, A_n + A_n^2 + 3/2\right\}, \tag{58}$$

$$\gamma^* = \sup_{n\in\mathbb{N}} \frac{\gamma_n}{\delta_n} < \infty. \tag{59}$$

As concerns m^*, we know from (16) that

$$A_n = n^2\pi^2(c^2 + k^2n^2\pi^2), \qquad \mathtt{I}_n = -2(b_1 + b_2n^2\pi^2). \tag{60}$$

This means that if we are able to obtain, through several suitable experimentations on piano string vibrations of real pianos, the values of the main parameters appearing in (54), we can easily know the value of m^*. According to (Nardini, 1953), we assume the following approximate values for those parameters

$$b_1 \simeq 1, \quad b_2 \simeq 10^{-4}, \quad c \simeq 200, \quad k \simeq 1, \quad \omega \simeq 400 \tag{61}$$

and this implies that

$$m^* = A_n + A_n^2 + 3/2. \tag{62}$$

As concerns γ^*, first we recall that (50) gives us

$$\delta_n = \frac{A_n|\mathtt{I}_n|}{m^*}, \qquad \gamma_n = m(A_n + 1 + |\mathtt{I}_n|)$$

therefore we obtain

$$\delta_n = (A_n|\mathtt{I}_n|)/A_n + A_n^2 + 3/2 \tag{63}$$

and

$$\gamma_n/\delta_n = m(A_n + 1 + |\mathtt{I}_n|)(A_n + A_n^2 + 3/2)/(A_n|\mathtt{I}_n|). \tag{64}$$

Now we observe that n indicates the nth harmonic in the Fourier series representing the string vibration, solution of our problem. Then, in order to find a γ^* independent of n it is sufficient in the applications to compute the sup of the ratio (64) not in $\mathbb{N}$ but in one of its finite subsets, as, for instance, in this way

$$\sup_{n\in(1,100)} \frac{\gamma_n}{\delta_n} = \gamma^*. \tag{65}$$

Of course the representation of a sound through a finite number of harmonics is necessary and, on the other hand, sufficient in many physical and computer applications. Furthermore, the choice of the number of harmonics generally depends on the type of the application. In our case, 100 seems to be more than sufficient, taking into account that, generally, *due to the limits of human auditory apparatus*, we are not able to perceive the influence (on the sounds) of harmonics with frequency too far from the fundamental one.

7 - CONCLUSION

A qualitative analysis of the long-time behaviour of the solutions of (1)-(4), (6) modeling physical phenomena, has been performed. Two are the main results of such analysis: i) the uniform asymptotic stability (u.a.s.) of the null solution of the considered problem; ii) the ultimate boundedness of overall solutions, in the context of the Direct Method of Liapunov. Both these results may be of interest in several physical applications. The first result gives a relevant information because it implies that the null solution is actually exponentially asymptotically stable. The second result, obtained by means of the so called Auxiliary system Method, also gives a meaningful information in the physical applications (see, as an example, Sect.6), because it implies the existence of an absorbing set, i.e. of a compact and invariant attractor in the Phase Space in which overall solutions of the problem enter in a finite time τ. This set is completely defined in terms of the used Liapunov functional and of overall parameters of the problem.

REFERENCES

[1] Rionero S. (2012) Asymptotic Behavior of Solutions to a Nonlinear Third Order P.D.E Modeling Physical Phenomena. Boll. U.M.I., **V**, (9), 451-468.

[2] Joseph D.D., Renardy M. and Saut J.C. (1985) Hyperbolicity and change of type in the flow of viscoelastic fluid. Arch. Rational Mech. anal. **87**, 213-251.

[3] Nardini R. (1953) Soluzione di un problema al contorno della magneto-idrodinamica. Ann. Mat. Pura Appl. **35**, 269-290 (in italian).

[4] Lamb H. (1959) Hydrodynamics. Cambridge University Press, Cambridge.

[5] Barone A. and Paternò G. (1982) Physics and Applications of the Josephson effect. Wiley Interscience, New York.

[6] Bensa J., Kronland-Martinet R., Bilbao S. and Smith J.O. (2003) A power-normalized non-linear lossy piano hammer. In Proceedings of the Stockholm Musical Acoustics Conference (SMAC-03), http://www.speech.kth.se/smac03/, (Stockholm), pp. 365-368, Royal Swedish Academy of Music.

[7] Bensa J., Bilbao S., Kronland-Martinet R., Smith J.O., and Voinier T. (2005) Computational modeling of stiff piano strings using digital waveguides and finite differences, Acta Acustica united with Acustica, **91** (2), pp.289-298.

[8] Rionero S. (2013) Multicomponent diffusive-convective fluid motions in porous layers: Ultimately boundedness, absence of subcritical instabilities, and global nonlinear stability for any number of salts. Phys. Fluids **25**, 054104.

[9] Rionero S. (2014) Heat and mass transfer by convection in multicomponent Navier-Stokes mixtures: absence of subcritical instabilities and global nonlinear stability via the Auxiliary System Method. Rend. Mat. Lincei. **25**, 1-44.

[10] Rionero S. (2012) Absence of subcritical instabilities and global nonlinear stability for porous ternary diffusive-convective fluid mixtures. Physics of Fluids, **24**, 104101.

[11] Fletcher N.H. and Rossing T.D. (1998) The Physics of Musical Instruments. Second Edition, Springer, USA.

[12] Hiller L. and Ruiz P. (1971) Synthesizing musical sounds by solving the wave equation for vibrating objects. Part I, Journal of the Audio Engineering Society, **19**, 462-470. Part II, **19** (7), 542-551.

[13] Chaigne A. and Askenfelt A.(1994) Numerical simulations of piano strings. I. A physical model for a struck string using finite difference methods. Journal of the Acoustical Society of America, **95** (2), 1112-1118.

[14] Bank B. and Sujbert L. (2005) Generation of longitudinal vibrations in piano strings: From physics sound synthesis. J. Acoust. Soc. Am., **117** (4).

[15] Chabassier J., Chaigne A. and Joly P. (2012) Modeling and simulation of a grand piano. RR (Research Report) RR-8181, p.29, ¡hal-00768234v2¿.

Rend. Acc. Sc. fis. mat. Napoli
Vol. LXXXII, (2015) pp. 61-64

Newly synthesized DNA in squid nerve terminals

Carolina Cefaliello[1], Marina Prisco[1], Marianna Crispino[1] and Antonio Giuditta[*]

Presentata dal socio Antonio Giuditta
(Adunanza del 19 giugno 2015)

Key words: brain metabolic DNA, synaptosomes, presynaptic terminals

Abstract – By incubating squid optic lobe slices with BrdU, newly synthesized DNA has been identified by immunofluorescence methods in the large synaptosomes derived from the nerve terminals of retinal photoreceptor neurons.

Riassunto – L'incubazione di fettine del lobo ottico di calamaro con BrdU ha permesso di dimostrare la presenza di DNA neosintetizzato nei grandi sinaptosomi derivati dai terminali dei fotocettori retinici.

1 - INTRODUCTION

For a long time in the past the biosynthesis of DNA was believed to be limited to the DNA replication occurring during cell division or to the DNA repair that followed DNA damage. At variance with this view, a number of observations on dividing and non-dividing cellular systems demonstrated that DNA synthesis could also be induced by cell activity (Pelc, 1968). In addition, later experiments of [^{3}H]thimidine incorporation in the adult rodent demonstrated that brain DNA undergoes a marked turnover (Perrone Capano et al., 1982) and is markedly modulated by learning (Reinis and Lamble, 1972; Ashapkin et al., 1983; Scaroni et al., 1983; Giuditta et al,. 1986). Comparable effects also occurred in brain nuclear and mitochondrial fractions (Giuditta et al,. 1986). Since the learning effect was much larger in the mitochondrial fraction than in the nuclear fraction, its possible origin from contaminating nuclear particles was excluded but the problem of the identification of the responsible subcellular particle remained.

Indeed, in addition to free mitochondria, brain mitochondrial fractions also contain the majority of synaptosomes and relatively minor amounts of other contaminants. Hence, their learning effect could be due to synaptosomes rather than mitochondria. This possibility was in agreement with the relatively short incubation time allotted for DNA synthesis (60 min) and with the comparably larger effect exhibited by isolated neuronal bodies. The former feature was at odds with the slow turnover of mitochondrial DNA, while the latter behavior could be reflecting the presence of nerve terminals still attached to the neuronal

[1]Biology Department, Federico II University, Naples Italy; *corresponding author: giuditta@unina.it.

plasma membrane that had been exposed to organic solvents (Satake and Abe, 1966).

To approach the problem and verify the presence of newly synthesized DNA in synaptosomes we decided to take advantage of the unusually large synaptosomes of squid optic lobes that originate from the nerve terminals of retinal photoreceptor neurons (Crispino et al., 1993).

2 - METHODS

Living squid (Loligo vulgaris) obtained from the Naples Zoological Station were quickly decapitated and their optic lobes dissected and immersed in cold filtered sea water. Slices with a thickness of 300 μm were prepared using a tissue slicer equipped with a vibrating razor blade. They were placed, two at a time, in a small Petri dish containing 2 ml artificial sea water (ASW: 460 mM Na, 10 mM K, 11 mM Ca, 55 mM Mg, 0.6 mM $KHCO_3$, 10 mM Tris-Cl pH 7.8) and were incubated with 20 μM bromodeoxyuridine (BrdU) at a about 18° for 2 h. Separate slices were incubated with 25 μg/ml actinomycin D. Control slices were incubated without BrdU. Following incubation, slices were homogenized with 1.5 ml 0.7 M sucrose, 20 mM Tris pH 7.4 (homogenizing medium or HM) and the homogenate was centrifuged in an Eppendorf table centrifuge (13,000 rpm for 30 min). The synaptosomal fraction floating as a thin layer over the top of the centrifuge tube (Eyman et al., 2007) was washed twice with HM, gently resuspended in 0.25 ml HM, and fixed for 15 min with 4% formaldeide in 0.5 M NaCl, 10 mM PBS. Smears of the fixed suspension on a glass slide were treated with anti-BrdU specific antibodies labeled with Alexafluor 488 (green fluorescent).

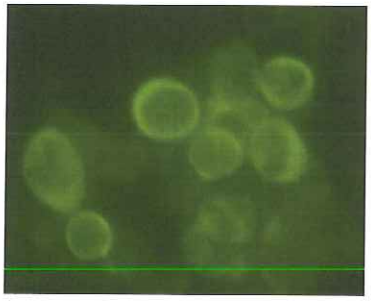

Figure 1 – Synaptosomes from optic lobe slices incubated with 20 μM BrdU

3 - RESULTS

Figure 1 shows synaptosomes prepared from slices incubated with BrdU. Several round bodies with an apparent diameter of 6-8 μm are present that contain a peripheral ring of green fluorescence indicative of incorporated BrdU. Numerous non fluorescent round bodies of comparable size are also present, as it occurs in the synaptosomal fraction of slices incubated without BrdU (not shown).

The biological origin of the BrdU-containing DNA was confirmed by experiments in which optic lobe slices incubated with BrdU were exposed to

actinomycin D, an inhibitor of DNA polymerase. Under these conditions a marked disappearance of the green fluorescence due to newly synthesized DNA was observed (not shown).

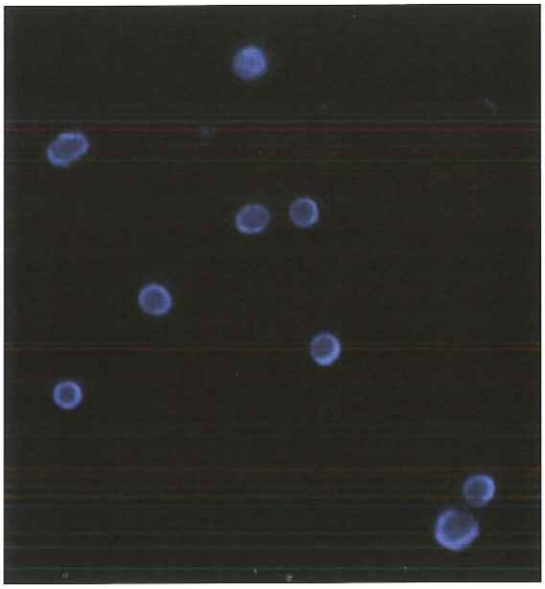

Figure 2 - Synaptosomes from optic lobe slices stained with DAPI.

The presence of DNA in the large synaptosomes of squid optic lobe was confirmed by treating the synaptosomal fraction prepared from slices incubated with BrdU with DAPI, a DNA specific fluorescent stain. As shown in Figure 2, under these conditions all round bodies exhibiting a diameter of about 5 μm exhibited peripheral rings of blue DAPI fluorescence. They were sometimes closed rings but more frequently interrupted rings.

4 - DISCUSSION

DAPI analyses show that the large squid synaptosomes derived from the terminals of retinal photoreceptors contain DNA. Indeed, DAPI blue fluorescence is selectively present in round bodies of the synaptosomal fraction which display a diameter of about 5 μm that correspond in size and shape to the synaptosomes derived from the large nerve terminals of retinal photoreceptor neurons (Giuditta et al., 2008). Phase contrast observations have identified round bodies of similar size (data not shown). The blue fluorescence localized in the peripheral ring of the large synaptosomes is unlikely to derive from mitochondrial DNA since its diffused distribution is at odds with the small punctuated appearance expected from mitochondrial DNA.

Larger round bodies with a peripheral distribution of the green fluorescence exhibited by the Alexafluor 488-labeled anti-BrdU antibodies are present in a minority of the synaptosomal population. These features suggest their correspondence to the large synaptosomes visualized by DAPI. On the other hand, their larger size appears to be in contrast with this interpretation.

Nonetheless, it should be noted that the procedure adopted for the visualization of the BrdU-related green fluorescence was considerably longer and more complex than that required for DAPI fluorescence. Notably, it required the permeabilization of synaptosomes that was required to allow the interaction of the antibody with the BrdU-containing DNA. This difference might possibly account for the size difference of the round bodies. The marked inhibition of newly synthesized DNA induced by actinomycin D emphasizes the biological nature of the incorporation process.

The occurrence of DNA and newly synthesized DNA in the large presynaptic synaptosomes of the optic lobe should be considered in the light of the anatomy of the nerve terminals that give rise to these synaptosomes. Since they derive from retinal photoreceptor neurons, in similar studies with optic lobe slices incubated with [^{3}H]uridine, the presence of radiolabeled RNA in the same synaptosomes indicated its origin from perisynaptic glial cells (Eyman et al., 2007; Giuditta et al., 2008). A comparable interpretation might be proposed with regard to the newly synthesized presynaptic DNA.

5 - REFERENCES

Ashapkin V.V., Romanov G.A., Tushmalova N.A., and Vanyushin B.F. (1983) Selective DNA synthesis in the rat brain induced by learning. Biokhimija. **48**, 355-362.

Crispino M., Castigli E., Perrone Capano C., Martin R., Menichini E., Kaplan B. B., and Giuditta A. (1993) Protein synthesis in a synaptosomal fraction from squid brain. Mol. Cell. Neurosci. **4**, 366-374.

Giuditta A., Perrone Capano C., D'Onofrio G., Toniatti C., Menna T., and Hydèn H. (1986) Synthesis of rat brain DNA during acquisition of an appetitive task. Pharmacol. Biochem. Behav. **25**, 651-658.

A. Giuditta, Chun J.T., Eyman M., Cefaliello C. and Crispino M. (2008) Local gene expression in axons and nerve endings: the glia-neuron unit. Physiol. Rev. **88**, 515-555,.

Eyman M., Cefaliello C., Ferrara E., De Stefano R., Scotto Lavina Z., Crispino M., Squillace A., van Minnen J., Kaplan B. B. and Giuditta A. (2007) Local synthesis of axonal and presynaptic RNA in squid model systems. Eur. J. Neurosci. **25**, 341-350,.

Pelc, S.R. (1968) Turnover of DNA and function. Nature **219**, 162-163.

Perrone Capano C., D'Onofrio G., and Giuditta A. (1982) DNA turnover in rat cerebral cortex. J.Neurochem. **38**, 52-56,.

Reinis, S., and Lamble, R.W. (1972) Labeling of brain DNA by ^{3}H-thymidine during learning. Physiol. Chem. Phys. **4**, 335-338.

Satake M. and Abe S. (1966) Preparation and characterization of nerve cell perikaryon from rat cerebral cortex. J. Biochem. 59, 72-75

Scaroni R., Ambrosini M. V., Principato G. B., Federici F., Ambrosi G., and Giuditta A. (1983) Synthesis of brain DNA during acquisition of an active avoidance task. Physiol. Behav. **30**, 577-582.

Rend. Acc. Sc. fis. mat. Napoli
Vol. LXXXII, (2015) pp. 65-83

The Higgs Boson Discovery at the Large Hadron Collider

Francesco A. Conventi[1], Leonardo Merola[2], Elvira Rossi[3]

Presentata dal socio Leonardo Merola
(Adunanza del 20 Novembre, 2015)

Keywords: High Energy Physics, Higgs boson, LHC, ATLAS, CMS.

Abstract - The Higgs boson was postulated in 1964, and phenomenological studies of its possible production and decays started in the early 1970s, followed by studies of its possible production in e^+e^-, $\bar{p}p$ and pp collisions. Until recently, the most sensitive searches for the Higgs boson were done at the CERN LEP (Large Electron Positron collider) between 1989 and 2000, which were complemented by searches at the Fermilab Tevatron. Then the CERN LHC (Large hadron Collider) experiments ATLAS and CMS entered the hunt, announcing on July 4, 2012 the discovery of a "Higgs-like" particle with a mass of about 125 GeV[4]. This identification has been supported by subsequent measurements of its spin, parity and coupling properties. It was widely anticipated that the Higgs boson would be accompanied by supersymmetry, although other options, like compositeness, were not completely excluded. So far there are no signs for any new physics, and the

[1] Università degli Studi di Napoli "Parthenope" and INFN Sezione di Napoli; e-mail: francesco.conventi@uniparthenope.it; francesco.conventi@na.infn.it

[2] Università degli Studi di Napoli Federico II and INFN Sezione di Napoli; e-mail: leonardo.merola@na.infn.it

[3] Università degli Studi di Napoli "Parthenope" and INFN Sezione di Napoli; e-mail: elvira.rossi@uniparthenope.it; elly@na.infn.it

[4] It should be GeV/c^2 but here the natural units are used so c=1.

measured properties of the Higgs boson are consistent with the predictions of the minimal Standard Model.

Riassunto - Il bosone di Higgs è stato teorizzato nel 1964, e studi fenomenologici sui suoi meccanismi di produzione e decadimento sono cominciati solo negli anni 70. Di poco successivi sono stati i primi studi sulla possibilità di produrre un bosone di Higgs da collisioni e^+e^-, $\bar{p}p$ and pp collisions. Fino a poco tempo fa, le ricerche con maggiore potenzialità di scoperta del bosone di Higgs sono state quelle al CERN LEP (Large Electron Positron collider) tra il 1989 e il 2000, completate dalle ricerche al Fermilab Tevatron. Successivamente, il 4 Luglio 2012, gli esperimenti ATLAS e CMS al CERN LHC (Large hadron Collider) hanno annunciato la scoperta di una nuova particelle candidata ad essere il bosone di Higgs con una massa di circa 125 GeV. L'identificazione della nuova particella con il bosone di Higgs è stata supportata dalle misure delle sue proprietà, quali spin, parità e proprietà di accoppaimento, effettuate in seguito. Era già stato ampiamente anticipato che il bosone di Higgs poteva essere inserito nella teoria della supersimmetria e anche in altre teorie che non sono ancora state completamente escluse. Al momento non ci sono segni di nuova fisica e le proprietà del bosone di Higgs sono consistenti con le predizioni del Modello Standard minimale.

1 - INTRODUCTION

The Standard Model of Particle Physics [2,3] provides the best description of three out of the four forces which occur in nature: the electromagnetic force, the weak interactions and the strong nuclear force. The aim of the Standard Model (SM) is to provide a unified theoretical description of these three forces, using the language of Quantum Field Theory (QFT).

The basic constituents of the Standard Model are quarks and leptons, spin-$\frac{1}{2}$ particles that are structureless at the current limits of resolution, about 10^{-19} m. Leptons and quarks are grouped in doublets and organised in three families as shown in Figure 1.

Interactions between quark and leptons are mediated by the exchange of integer spin particles (bosons) and lead to a rich phenomenology that is described on a wide range of energy scale (from few electronvolt to teraelectronvolt) by the Standard Model with outstanding precision. The structure of all fundamental interactions allowed in the Standard Model arise from the symmetry of the theory and the gauge paradigm. As a major consequence the local gauge symmetries of the theory lead to the presence of

boson particles [6].

The symmetry group of electroweak sector of the Standard Model [7], [8], [9] foresees four (spin-1) gauge bosons that are the electromagnetic photon and the weak bosons $W^{\pm}$ and Z^0. The electroweak symmetry group requires these gauge bosons to be massless which is not problematic for the photon due to the long-range electromagnetic interaction but it is in striking conflict to the short range of the weak force (10^{-17}m) and the known masses of the Z^0 and $W^{\pm}$ bosons ($m_{Z^0} = 91.1876 \pm 0.0021\ GeV$ and $m_W = 80.385 \pm 0.015\ GeV$). Moreover since the coupling between fermions and the W bosons involve only left-handed quarks and leptons, any fermion mass term would violate the gauge symmetry.

The Standard Model is thus able to capture and describe the non-trivial structure of the interaction but does not describe the real world and this represent the well-know problem of the massive particles inside the Standard Model.

The proposed solution for the Standard Model mass problem is the mechanism of *spontaneous symmetry breaking* (or hidden symmetry) for which the lowest energy state may not possess all the symmetries of the theory. This mechanism was originally used to describe the phenomenon of superconductivity in the theory of Bardeen, Cooper and Shrieffer [10] where for the Meissner effect the photon acquires mass when it propagates through the superconductive medium. Here of special relevance to the challenge of the mass problem inside the Standard Model is that the superconductor has a well defined reference frame so the symmetry of the theory is broken but still present by the condensation of Cooper pairs of electrons in the lowest energy state. It was shown [11] that the interactions with the photon of the Cooper pairs inside the superconductor medium led the photon itself to acquire a mass.

The analogues of the original idea of hidden symmetry was firstly introduced in particle physics by Nambu in 1960 [12] and the spontaneous breaking of gauge symmetry was carried out in 1964 by Peter Higgs, Francois Englert and Robert Brout [13–15] known as the Higgs mechanism. In the context of the Quantum Field Theory the Higgs mechanism introduces an additional doublet of complex scalar fields with a potential term that leads to non unique energy ground state (see Figure 2).

Three out the four additional degrees of freedom introduced by the doublet of complex scalar fields can be translated into longitudinal polarization degrees of freedom of the massive gauge bosons Z^0 (often referred as Z) and $W^{\pm}$ while the fourth one still survives and leads to the introduction of a new particle, the Higgs boson of the electroweak theory.

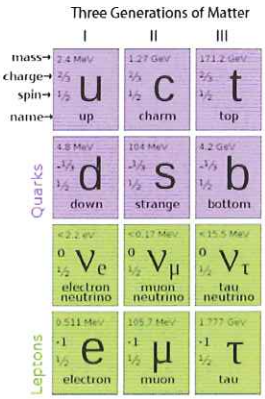

Figure 1: *Three generations of quarks and leptons in the Standard Model.*

The gauge bosons and fermions acquire their masses dynamically through the interaction with the Higgs field and their couplings are predicted to be proportional to the mass (squared mass) of the fermions (gauge bosons). The Higgs boson is the only elementary particle in the Standard Model with spin 0 but the electroweak theory does not predict its mass value.

The Higgs boson was postulated in 1964 but phenomenological studies of its possible production and decays started in the early 1970s. At that time there were only few suggestions on how to constrain or exclude the possible existence of a physical Higgs boson both from the experimental and theoretical side [16–20]. One of the first systematic study of possible Higgs phenomenology was written in the 1975 [1]. Further studies carried out that even if the mass of the Higgs boson is a priori undetermined, its range is not completely unconstrained in the SM. For example, from the partial wave analysis of the elastic W^+W^- scattering it is possible to set an upper limit on the Higgs boson mass of about 1 TeV, otherwise the Standard Model would be not longer valid at TeV scale [24]. Subsequently a comprehensive guide to the physics of Higgs bosons was written [21].

The most extensive Higgs searches were carried out at the Large Electron–Positron Collider at CERN, in studies of the reaction $e^+e^- \to HZ^0$ [25], which established a lower-bound on the mass of a standard-model Higgs boson, $M_H > 114.4$ GeV at 95% confidence level [26]. The Tevatron Collider experiments at Fermilab, in which protons and antiprotons collided at center-of-mass energy $\sqrt{s} = 1.96$ TeV, conducted searches in a large number of physical decay channels. The CDF and D0 experiments were particularly sensitive to decays into pairs of weak gauge bosons. By July

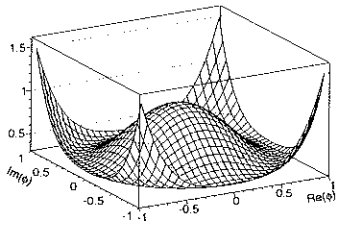

Figure 2: *Higgs potential: the lowest energy state is described by a randomly chosen state at the bottom of such potential.*

2012, their joint analysis excluded the mass range 145 GeV $\leq M_H \leq$ 180 GeV at 95% CL [27].

On 4th July 2012 both the ATLAS and CMS Collaborations [4] announced the discovery of a Higgs-like particle with mass around 125 GeV [5]. As more data were collected, the properties (spin, parity, couplings, cross section) of the discovered particle were measured. As members of the ATLAS collaboration, we actively participated in the Higgs boson discovery and now we are continuing efforts to measure its properties. LHC has been operated at center-of-mass energies ($\sqrt{s}$) of 7 TeV in 2011 and of 8 TeV in 2012 (Run I). After a period dedicated to the upgrade of the detectors and the experimental settings, now the Run II phase is operational at $\sqrt{s} = 13$ TeV. The ATLAS detector has performed very efficiently during Run I, having collected data corresponding to an integrated luminosity of 20.4 fb^{-1} at $\sqrt{s} = 8$ TeV and 4.6 fb^{-1} at $\sqrt{s} = 7$ TeV. During the Run II phase LHC will reach the center-of-mass energy of 14 TeV and a luminosity of 300 fb^{-1}. To extend its discovery potential, the LHC will need a major upgrade around 2020 to increase its luminosity by a factor of 10 beyond the original design value (from 300 to 3000 fb^{-1}).

2 - HIGGS BOSON SEARCH AT LARGE HADRON COLLIDER

The Large Hadron Collider (LHC) is a hadron hadron collider and is the world's largest and most powerful particle collider designed to accelerate beams of protons (or heavy ions) to energies up to 7 TeV each, thus reaching out center-of-mass energies of the proton proton collisions up to 14 TeV.

ATLAS [28] and CMS [29] are two large, broad-acceptance, general-purpose detectors located about 100 meters below the earth surface, in the Large Hadron Collider tunnel centered at two nominal interaction points of the LHC accelerator (see Figure 4). At LHC the Higgs boson can be produced through four different

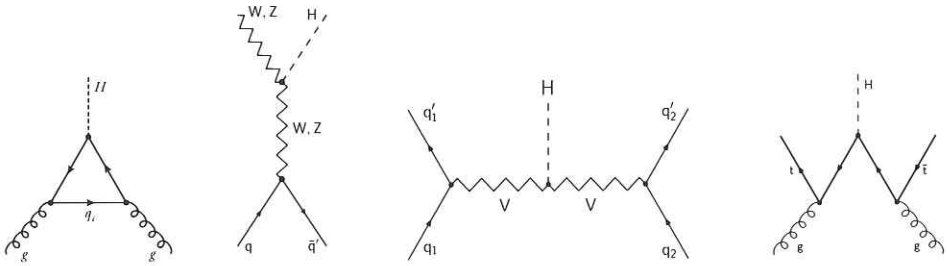

Figure 3: *Principal Higgs-boson production mechanisms at the Large Hadron Collider.*

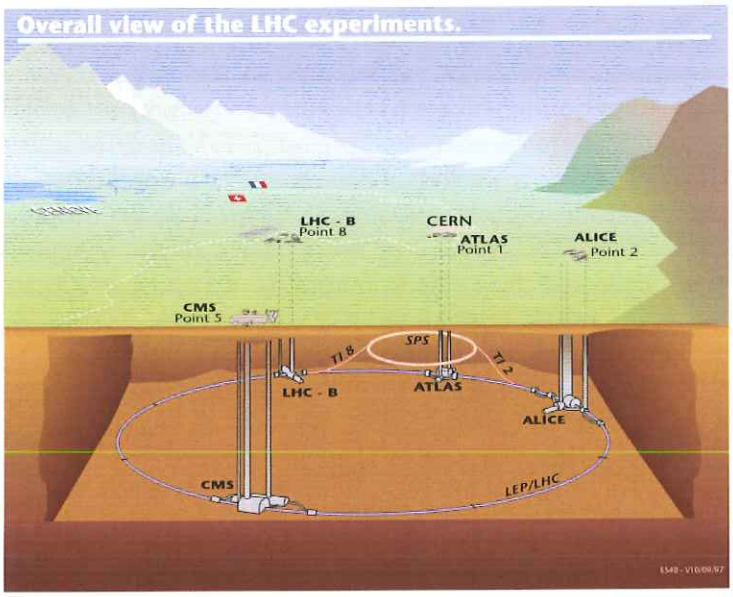

Figure 4: *The LHC accelerator and the four main experiments: ATLAS, CMS, LHCb and ALICE.*

mechanisms (Figure 3): gluon fusion through heavy-quark (top) loops, associated production with weak gauge bosons, vector-boson fusion and associated production with top quarks.

The gluon fusion, although due to loop quantum effect, is largely dominant over the other three mechanism representing about the 90% of the total events produced at the LHC.

The Higgs boson couldn't be detected directly but of course only through its decay products. Since the Higgs boson coupling is proportional to the mass of the decay products the decay width grows with increasing values of m_H , as the decay into successively heavier particles becomes energetically accessible. In Figure 5 the Higgs boson decay fractions as derived from the total and partial decay widths are shown. It illustrates a rich phenomenology with several competing decay channels for lower values of the Higgs boson mass.

The clearest signals with narrow invariant mass peaks arise from the the $\gamma\gamma$ and four-lepton ($Z^0Z^0 \rightarrow \ell^+\ell^-\ell'^+\ell'^-$) "golden" channels that have been used for the first observation of the production and decay of a new particle with a mass around 125 GeV. ATLAS and CMS have also observed the new particle in the W^+W^- decay channel [30, 31], and have given evidence for the $b\bar{b}$ [32] and $\tau^+\tau^-$ [33, 34] decay modes.

Although the new observed particle was widely expected to be the Higgs boson, and a mass value around 125 GeV is certainly consistent with the previous indications from precision electroweak data, it was important to check its properties and exclude possible alternatives. For this reason, a number of relevant properties of the new discovered particle needed to be verified with highest priority. The Higgs boson is the only scalar elementary particle with spin 0: this is consistent with its observation in the $\gamma\gamma$ final state, which excludes spin 1. However, integer spins ≥ 2 remained a possibility, albeit unexpected. Moreover, many theories beyond the Standard Model theories, for example the Supersimmetry, contain more than just one Higgs boson, with at least one being a pseudoscalar. These new degrees of freedom could mix in the presence of CP violation[5]. As already stated, the Higgs boson couples to other particles proportionally to their masses. So the measurement of the couplings represents a further proof for the new particle's connection with the origin of the particle masses.

The following sections summarise recent experimental results by ATLAS and CMS on the search of a SM-like Higgs boson and the determination of its properties.

3 - HIGGS SEARCHES IN BOSONIC DECAY MODES: $H \rightarrow ZZ^*$, $H \rightarrow \gamma\gamma$ AND $H \rightarrow WW^*$

In July 2012 both experiments ATLAS and CMS had analysed the first 5 fb^{-1}

[5]Charge conjugation and Parity invariance are treated in modern introductory textbooks, such as Refs. [36]

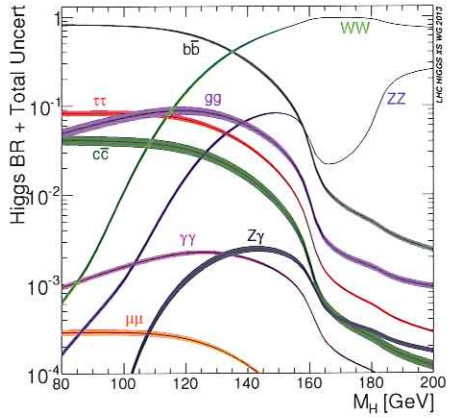

Figure 5: *Higgs-boson decay channels at the Large Hadron Collider.*

of proton-proton collision data at the highest center-of-mass energy of 8 TeV. The excess had shown up in two independent decay channels: $H \to ZZ^*$, $H \to \gamma\gamma$ and in both ATLAS and CMS experiments at approximately the same value of $m_H \simeq 125$ GeV.

Several updated results with increasing luminosity have been presented at conferences, investigating the development of the excess and the first properties of the new boson. The first data taking period of the LHC (Run I) was completed by the end of 2012 with a total amount of 5 fb^{-1} taken at 7 TeV, and 20 fb^{-1}, taken at 8 TeV center-of-mass energy.

The Higgs bosonic decay modes are: $H \to ZZ^*$, $H \to \gamma\gamma$ and $H \to WW^*$. Since the Higgs boson couples to other particles proportionally to their masses the WW and ZZ decay channels allow to extract direct information on the role of the new particle in the electroweak symmetry breaking while the $\gamma\gamma$ mode is a higher order decay (i.e. it happens only through quantum loop effects) and so it is sensitive to the presence of hypothetical new particles beyond the Standard Model. The bosonic decay modes were used as a tool for the Higgs boson discovery at the initial stage and subsequently as a tool for the measurement of the properties and the confirmation of the discovery. In all the channels the production is studied both inclusively and with events categorised according to the characteristics of the different production mechanism shown in Figure 3 .

The $H \to ZZ^* \to 4\ell$ channel, called "the Golden Channel", has a small rate but produces a very clean final state with low background contamination. The final state with four isolated leptons (electrons or muons) can be reconstructed with high accuracy; it preserves all kinematic information of the decay in the reconstructed final state, which allows the Golden Channel to be ideal for studies concerning the Higgs boson properties. The main backgrounds are the non-resonant ZZ^* production ("irreducible background"), the inclusive production ofZ^0 boson plus

hadronic jets and quark t pair production ("reducible backgrounds"). Figure 6(a) shows the four-lepton invariant mass distribution of the candidate events. Details of the final Run I ATLAS results can be found in Ref. [37].

The branching ratio of the $H \to \gamma\gamma$ channel is small, but produces a clean final state with full reconstruction of the Higgs boson and a signal $m_{\gamma\gamma}$ peak on top of a large but smooth background distribution. It is therefore an excellent channel to measure the mass and couplings of the Higgs boson. The final state consists of two isolated photons originating from the primary vertex. The diphoton continuum production constitutes the dominant (80%) background. Figure 6(b) shows the diphoton invariant mass distribution of the candidate events. The solid red curve shows the fitted signal plus expected background contribution when the Higgs boson mass is fixed at 125.4 GeV. The background component of the fit is shown with the dotted blue curve. The signal component of the fit is shown with the solid black curve. The bottom plot shows the data relative to the background component. Final ATLAS Run I analysis is summarised in Ref. [38].

The $H \to WW^*$ decay mode has a large branching ratio. However, the cleanest way to observe this channel is through the final state $H \to WW^* \to \ell\nu\ell\nu$, where both the W bosons decay leptonically to electrons or muons. Therefore, due to the two missing neutrinos the Higgs final state cannot be reconstructed completely and the signal appears as a broad peak in the transverse mass distribution (m_T). The signal consists of two isolated, high transverse momentum (p_T), opposite-sign leptons and missing energy due to the missing neutrinos. The main background is the WW^* continuum production. Figure 6 (c) shows the transverse mass distributions for $n_j \leq 1$ for the three lepton-flavour samples. The bottom plot shows the residuals of the data with respect to the estimated background compared to the expected distribution for a SM Higgs boson with $m_H = 125$ GeV.

4 - HIGGS SEARCHES IN FERMIONIC DECAY MODES AND ASSOCIATED TOP HIGGS PRODUCTION

The Higgs fermionic decay modes are: $H \to b\bar{b}$, $H \to \tau^+\tau^-$ and $H \to \mu^+\mu^-$. Since the Higgs boson coupling is predicted to be proportional to the mass of the quarks, the decay $H \to t\bar{t}$ should be the one with the highest branching ratio. However, this decay is not kinematically allowed for $m_H = 125$ GeV, thus the only way to probe the Higgs boson top quark Yukawa coupling is through its associated production with t quark pairs.

The $H \to b\bar{b}$ decay has the largest branching ratio of 58% at $m_H = 125$ GeV but suffers from huge backgrounds contaminations, making it impossible to tag this final state alone. The only feasible way for this measurement is through the use of associated production with a vector boson (VH production mechanism, V=Z,W gauge boson). Figure 7(a) shows the event yields as a function of signal to background ratio and an excess is observed at the 1.4σ level over the background-only hypothesis. Details of the search for $H \to b\bar{b}$ decays can be found in Ref. [40].

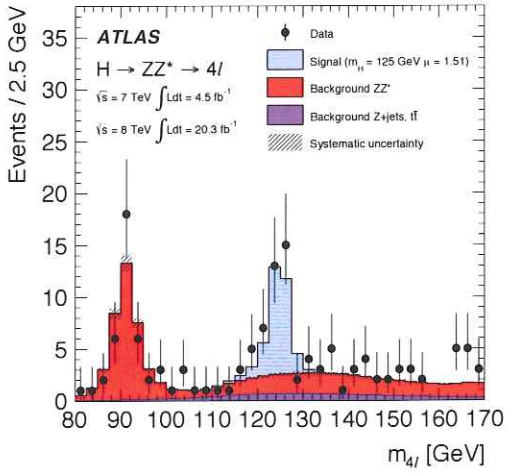

(a)

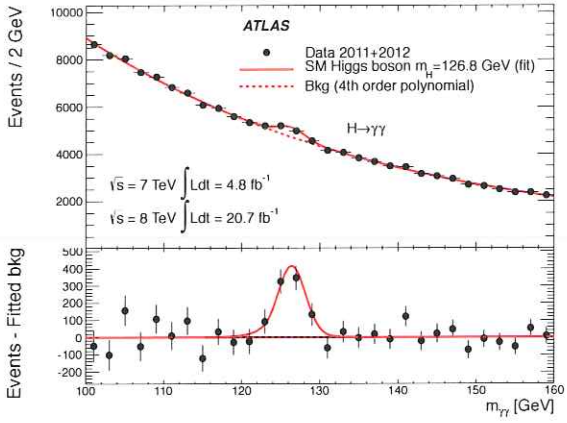

(b)

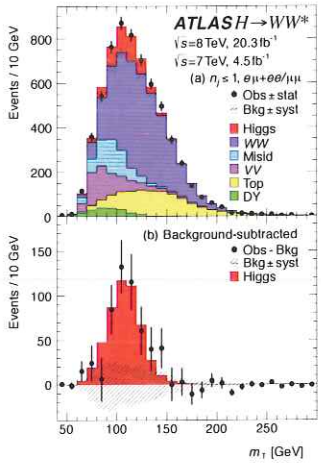

(c)

Figure 6: *(a) Four-lepton invariant mass distribution for the $H \to ZZ^*$ channel; (b) diphoton invariant mass distribution (top) and the residuals of the data with respect to the estimated background (bottom) for the $H \to \gamma\gamma$ channel; (c) transverse mass distributions for $n_j \leq 1$ for the three lepton-flavour samples (top) and the residuals of the data respect to background in $H \to WW^*$ (bottom).*

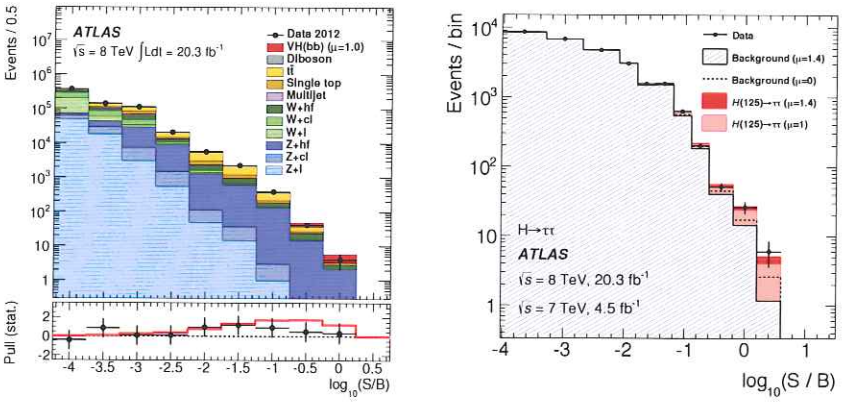

(a) (b)

Figure 7: *Event yields as a function of log(S/B) for data, background and Higgs boson signal with $m_H = 125$ GeV for the 8 TeV data for $H \to b\bar{b}$ [40] (a) and for $H \to \tau^+\tau^-$ analysis [41] (b).*

More favourable signal to background conditions are expected for $H \to \tau^+\tau^-$ decays that has a branching ratio of 6.3% at $m_H = 125$ GeV, due to the relatively high mass of the τ lepton ($m = 1.78$ GeV). Figure 7 (b) shows the event yields as a function of signal to background ratio and an excess over the SM background prediction is observed. This observation correspond to a 4.5σ deviation from the background-only hypothesis. This provides evidence for $H \to \tau^+\tau^-$ at $m_H =$ 125.36 GeV. Details of the search for $H \to \tau^+\tau^-$ decays can be found in Ref. [41].

The branching ratio for $H \to \mu^+\mu^-$ is very small ($\sim 2 \cdot 10^{-4}$) but the dimuon spectrum provides a very clean signature with a very good mass resolution and at the same time is the only means of measuring the second generation fermionic couplings. The signal is given by exactly two isolated opposite sign muons, while there is a huge irreducible background from Drell-Yan processes. No excess of events over the background is observed. Details of the search for this analysis can be found in Ref. [42].

The production of the Higgs boson in association with a pair of top quarks ($t\bar{t}H$) provides direct sensitivity to the large Yukawa coupling between the top quark and the Higgs boson. This is in contrast to the gluon fusion production mode, where the sensitivity to the top quark coupling is only via quantum loop effects. The decay modes of the Higgs boson, $H \to b\bar{b}$, $H \to W^+W^-$, $H \to ZZ$, $H \to \tau^+\tau^-$ and $H \to \gamma\gamma$ give a range of different final states in which to search for $t\bar{t}H$ production. No significant excess of events over the background has been observed in the associated top Higgs production. Details for these analyses can be found in Ref. [43].

5 - HIGGS BOSON PROPERTIES

After the discovery, the ATLAS collaboration has put great effort to study the properties of the newly discovered boson. There are properties related to the characteristics of the particle itself like its mass, charge, spin-parity, lifetime. There are also properties related to the interaction of the Higgs boson with other particles like the production and decay modes, the coupling with other particles and the cross section. In order to verify the SM origin or not of the Higgs boson, detailed measurements of all its properties have been performed.

In the SM, the Higgs boson mass is not predicted, so its measurement is therefore required for precise calculations of electroweak observables, including the production and decay properties of the Higgs boson itself. The two channels that are the most sensitive to the Higgs boson mass measurement are $H \to \gamma\gamma$ and $H \to ZZ^* \to 4\ell$. The Higgs boson manifest itself as a narrow invariant mass peak with a typical experimental resolution of 1.6 GeV to 2 GeV over a smooth background.

The ATLAS mass measurement result with full Run-I dataset is: $m_H = 125.36 \pm 0.37(stat) \pm 0.18(syst)$ GeV. More details on the measurement can be found in the reference [44]. A combined mass measurement with CMS data has been performed and recently published [45]. The combined ATLAS and CMS mass measurement result is: $m_H = 125.09 \pm 0.21(stat) \pm 0.11(syst)$ GeV.

In the SM, the electroweak symmetry breaking is achieved through the introduction of a complex doublet scalar field. This leads to the prediction of the existence of one physical neutral scalar particle, the Higgs boson. Through Yukawa interactions, the Higgs scalar field can also account for fermion masses. While the SM does not predict the value of the Higgs boson mass, the production cross sections and decay branching ratios of the Higgs boson can be precisely calculated once the mass is known. To estimate the Higgs boson production and decay rates as well as its coupling strengths to vector bosons and fermions, all the Higgs analyses have been combined. The signal strength parameter μ, defined as the ratio between the measured Higgs boson rate and its SM expectation, has been extensively used to characterise the Higgs boson yields. Figure 8 (a) shows the measurements of the signal-strength parameter from a simultaneous fit to all decay channels that were analysed. The overall signal strength of each analysis is the combined result of the measurements for different production processes. They have been combined to result in a global signal strength value of [46]: $\mu = 1.18^{+0.15}_{-0.14} = 1.18 \pm 0.10(stat) \pm 0.07(expt)^{+0.08}_{-0.07}(theo)$ consistent with the SM expectation of $\mu = 1$ with a probability of 18%. The uncertainty on the combination has comparable statistical and systematic components. Details of the combined analyses of the Higgs boson production and decay rates as well as its coupling strengths to vector bosons and fermions can be found at Ref. [46].

Recently combined ATLAS and CMS measurements of the Higgs boson production and decay rates, as well as constraints on its couplings to vector bosons and fermions were published using all the Run I data [47]. The combined signal yield

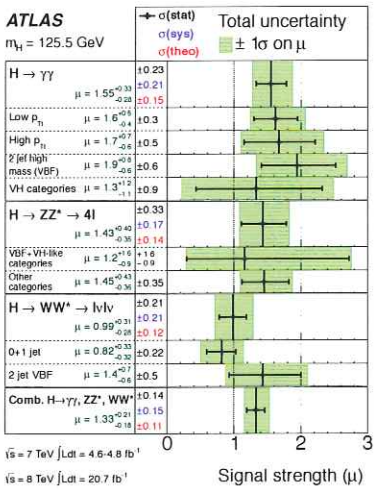

(a)

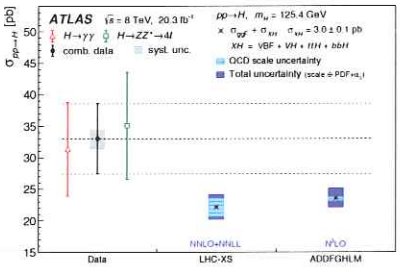

(b)

Figure 8: *(a) Summary of the signal strength measurements from all the bosonic decay modes; (b) Measured total cross section of Higgs boson production compared to two calculations of the ggF cross section [49].*

relative to the Standard Model expectation is measured to be 1.09 ± 0.11. Several interpretations of the results with more model-dependent parameterisations were attempted but the data are consistent with the absence of beyond Standard Model couplings, for all parameterisations considered.

ATLAS measured total and differential cross sections for Higgs boson production using the $H \to \gamma\gamma$ and $H \to ZZ^* \to 4\ell$ events at $\sqrt{s} = 8$ TeV [49]. The measured cross sections take into account detector efficiency, fiducial acceptances and branching fractions. Figure 8 (b) shows the measured total cross section of Higgs boson production compared to two calculations of the ggF cross section. The measured total cross section is $33.0 \pm 5.3(stat) \pm 1.6(sys)$ pb which is higher than theoretical calculations [48], but still consistent with the theory predictions. Details of this analysis can be found in Ref. [49].

In the SM, the Higgs boson is the only scalar particle with spin 0 and even parity quantum number ($J^P = 0^+$). Three possible scenarios for the spin and parity of the boson are considered: the hypothesis that the observed resonance is a spin-2 resonance, a pure spin-0 scalar or pseudo-scalar Higgs boson (non Standard Model Higgs Boson), or a mixture of spin-0 states. The latter case would imply CP-violation in the Higgs sector. In the case of CP mixing, the Higgs boson would be a mass eigenstate, but not a CP eigenstate. The study of the spin and parity properties of the Higgs boson in ATLAS is based on the $H \to \gamma\gamma$, $H \to ZZ^* \to 4\ell$ and $H \to WW^* \to \ell\nu\ell\nu$ decay channels and their combination. It relies on discriminant observables chosen to be sensitive to the spin and parity of the signal while preserving the discrimination against the various backgrounds. Recent ATLAS studies can be found in Ref. [50]. An example of distributions of the test statistic used to derive the results is presented in Figure 9 (a). In this figure, the observed value is indicated by the vertical solid line and the expected medians by the dashed lines. The signal strengths per decay channel are treated as independent parameters during each fit. Their values are compatible with the SM predictions. The combination of the three decay processes allow the exclusion of all considered non-SM spin models at more then 99% CL in favour of the SM spin-0 hypothesis.

For spin 0 models, some CP mixing scenarios in the Higgs sector have been considered using the $H \to ZZ^* \to 4\ell$ and $H \to WW^* \to \ell\nu\ell\nu$ events. Figures 9 (b) and (c) show likelihood scan as a function of the scalar and pseudo scalar coupling parameters. The observed results are consistent with no beyond Standard Model coupling, and no CP violation in the Higgs sector is observed within the current precision.

6 - CONCLUSIONS

The discovery of the Higgs boson at the Large Hadron Collider announced at CERN in 2012 represents a milestone in particle physics. This discovery confirms the original idea of the electroweak spontaneous symmetry breaking as postulated

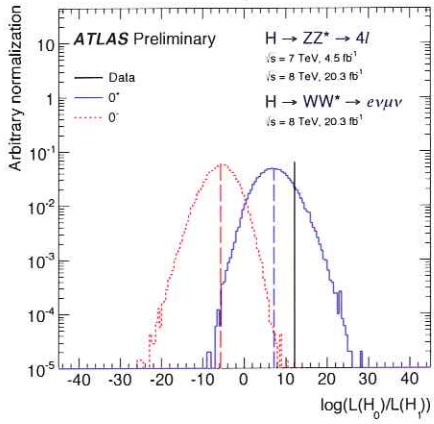

(a)

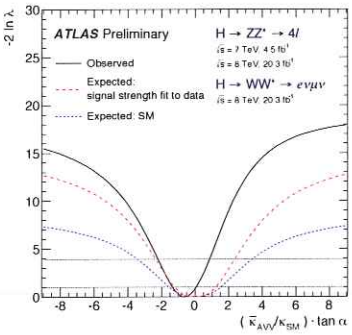

(b)

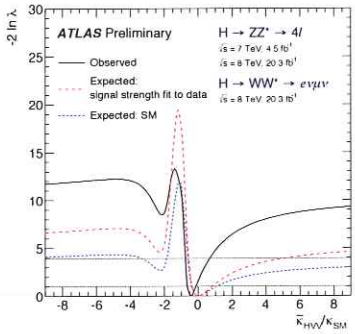

(c)

Figure 9: *(a) Example of distribution of the test statistic in the pseudoscalar hypothesis [50]; Likelihood scan as a function of non Standard Model CP-odd (b) and CP-even (c) coupling parameters [50].*

roughly 50 years ago which led to the introduction of a complete new hidden sector spanned by an extra doublet of quantum fields which has a dedicated coupling structure to gauge bosons and fermions.

The discovery at LHC was driven by the bosonic $H \to \gamma\gamma$, $H \to ZZ^* \to 4\ell$ and $H \to WW^* \to \ell\nu\ell\nu$ decay channels and it has been followed by the evidence that the new particle indeed couples to fermions.The analysis carried out by the ATLAS and CMS collaborations show that the new discovered particle is a boson with spin 0 and CP eigenvalue of +1 with high level of statistical confidence. Moreover it has a non-universal coupling structure across the fermion flavour generations.

Finally the compatibility of the coupling structure will prove that the new particle with the expectation for the Standard Model Higgs boson could be confirmed within the experimental resolution reached with full Run-I LHC dataset. However only deeper studies of the coupling structure will prove that the new particle is the Standard Model Higgs boson.

7 - ACKNOWLEDGEMENTS

We would like to thank our institutions and INFN (Istituto Nazionale di Fisica Nucleare) for the support. We would like also to thank CERN, the ATLAS and CMS collaborations for the very successful operation of the LHC.

8 - REFERENCES

[1] J. R. Ellis, M. K. Gaillard and D. V. Nanopoulos, *A phenomenological profile of the Higgs boson,* CERN preprint Nov. 1975, published in Nucl. Phys. B **106** (1976) 292.

[2] S. Weinberg, *A model of leptons,* Phys. Rev. Lett. **19**, 1264 (1967). This seems to be the first paper in which it is shown that matter particles can also acquire their masses from 'spontaneous' symmetry breaking.

[3] A. Salam, *Weak and electromagnetic interactions,* in the *Proceedings of 8th Nobel Symposium*, Lerum, Sweden, 19-25 May 1968, pp 367-377.

[4] ATLAS Collaboration, JINST 3 (2008) S08003; CMS Collaboration, JINST 3 (2008) S08004.

[5] ATLAS Collaboration, Phys. Lett. B 716 (2012) 1; CMS Collaboration, Phys. Lett. B 716 (2012) 30.

[6] C. N. Yang, Symmetry in physics, in *The Oskar Klein Memorial Lectures*, edited by G. Ekspong Vol. I, pp. 11–33, World Scientific, Singapore, 1991.

[7] S. Glashow, Nucl. Phys. **22**, 579 (1961).

[8] S. Weinberg, Phys. Rev. Lett. **19**, 1264 (1967).

[9] A. Salam, Weak and Electromagnetic Interactions, in *Elementary Particle Theory: Relativistic Groups and Analyticity* (Nobel Symposium No. 8), edited by N. Svartholm, Almqvist and Wiksell, Stockholm, 1968, p. 367.

[10] J. Bardeen, L. N. Cooper and J. R. Schrieffer, *Microscopic theory of superconductivity,* Phys. Rev. **106** (1957) 162.

[11] L. N. Cooper, *Bound electron pairs in a degenerate Fermi gas,* Phys. Rev. **104** (1956) 1189.

[12] Y. Nambu, *Axial vector current conservation in weak interactions,* Phys. Rev. Lett. **4** (1960) 380.

[13] F. Englert and R. Brout, Phys. Rev. Lett. **13**, 321 (1964).

[14] P. W. Higgs, Phys. Lett. **12**, 132 (1964).

[15] P. W. Higgs, Phys. Rev. Lett. **13**, 508 (1964).

[16] S. L. Adler, R. F. Dashen and S. B. Treiman, *Comments on proposed explanations for the mu-mesic atom X-ray discrepancy,* Phys. Rev. D **10** (1974) 3728.

[17] K. Sato and H. Sato, *Higgs meson emission from a star and a constraint on its mass,* Prog. Theor. Phys. **54** (1975) 1564.

[18] L. Resnick, M. K. Sundaresan and P. J. S. Watson, *Is there a light scalar boson?,* Phys. Rev. D **8** (1973) 172.

[19] D. Kohler, B. A. Watson and J. A. Becker, *Experimental search for a low-mass scalar boson,* Phys. Rev. Lett. **33** (1974) 1628.

[20] R. Barbieri and T. E. O. Ericson, *Evidence against the existence of a low mass scalar boson from neutron-nucleus scattering,* Phys. Lett. B **57** (1975) 270.

[21] John F. Gunion, Howard Haber, Gordon Kane, Sally Dawson, Howard E. Haber "The Higgs Hunter's Guide", http://cds.cern.ch/record/425736

[22] LHC Higgs cross section working group, arXiv:1101.0593; Anastasiou et al. Phys. Rev. Lett. 114, 212001 (2015).

[23] ATLAS Collaboration, arXiv:1504.05833, submitted to PRL.

[24] B. W. Lee, C. Quigg, and H. B. Thacker, Phys. Rev. D **16**, 1519 (1977).

[25] M. M. Kado and C. G. Tully, Ann. Rev. Nucl. Part. Sci. **52**, 65 (2002).

[26] LEP Working Group for Higgs boson searches, ALEPH, DELPHI, L3, OPAL, R. Barate *et al.*, Phys. Lett. **B565**, 61 (2003), arXiv:hep-ex/0306033.

[27] Tevatron New Physics and Higgs Working Group, CDF and D0 Collaborations, Updated Combination of CDF and D0 Searches for Standard Model Higgs Boson Production with up to 10.0 fb^{-1} of Data, 2012, arXiv:1207.0449.

[28] ATLAS Collaboration, JINST **3**, S08003 (2008).

[29] CMS Collaboration, JINST **3**, S08004 (2008).

[30] CMS Collaboration, S. Chatrchyan *et al.*, JHEP **1401**, 096 (2014), arXiv:1312.1129.

[31] ATLAS Collaboration, G. Aad *et al.*, (2014), arXiv:1412.2641, Observation and measurement of Higgs boson decays to WW^* with the ATLAS detector.

[32] CMS Collaboration, V. Khachatryan *et al.*, (2015), arXiv:1506.01010, Search for the standard model Higgs boson produced through vector boson fusion and decaying to $b\bar{b}$.

[33] CMS Collaboration, S. Chatrchyan *et al.*, JHEP **1405**, 104 (2014), arXiv:1401.5041.

[34] ATLAS Collaboration, G. Aad *et al.*, JHEP **1504**, 117 (2015), arXiv:1501.04943.

[35] ATLAS Collaboration, G. Aad *et al.*, (2015), arXiv:1507.04548, Measurements of the Higgs boson production and decay rates and coupling strengths using pp collision data at $\sqrt{s} = 7$ and 8 TeV in the ATLAS experiment. ATLAS Collaboration, Phys. Lett. B 726 (2013) 120.

[36] Yorikiyo Nagashima, Yoichiro Nambu Elementary Particle Physics: Quantum Field Theory and Particles Wiley ISBN: 978-3-527-40962-4 August 2010

[37] ATLAS Collaboration, Phys. Rev. D. 91, 012006 (2015).

[38] ATLAS Collaboration, Phys. Rev. D. 90, 112015 (2014).

[39] ATLAS Collaboration, arXiv:1412.2641 (submitted to Phys. Rev. D).

[40] ATLAS Collaboration, JHEP 01 (2015) 069.

[41] ATLAS Collaboration, JHEP 04 (2015) 117.

[42] ATLAS Collaboration, Phys. Lett. B 738 (2014) 68-86.

[43] ATLAS Collaboration, Phys. Lett. B 740 (2015) 222-242; ATLAS-CONF-2015-006 http://cds.cern.ch/record/2002125; arXiv:1503.05066 (accepted by EPJ).

[44] ATLAS Collaboration, Phys. Rev. D. 90, 052004 (2014).

[45] ATLAS and CMS Collaborations, Phys. Rev. Lett. 114, 191803.

[46] ATLAS collaboration, ATLAS-CONF-2015-007, http://cds.cern.ch/record/2002212.

[47] ATLAS and CMS Collaborations, ATLAS-CONF-2015-044, http://inspirehep.net/record/1393544

[48] LHC Higgs cross section working group, arXiv:1101.0593; Anastasiou et al. Phys. Rev. Lett. 114, 212001 (2015).

[49] ATLAS Collaboration, Phys. Rev. Lett. 115 (2015) 09180.

[50] ATLAS Collaboration, ATLAS-CONF-2015-008 (2015), http://cds.cern.ch/record/2002414.

Rend. Acc. Sc. fis. mat. Napoli
Vol. LXXXII, (2015) pp. 85-98

Neutrino cosmology: the universe at the time of Primordial Nucleosynthesis

Nota di Marco Chianese[1] e Gennaro Miele[1]

Presentata dal socio Leonardo Merola
(Adunanza del 20 novembre 2015)

Key words: neutrinos, Big Bang Nucleosynthesis, cosmology

Abstract - In the last decades, the Cosmology has become a new laboratory to study and constrain the properties of neutrinos, which are fundamental ingredients during the early phases of the Universe evolution. We provide a brief review of one of these phases, the Primordial Nucleosynthesis, paying specific attention to the crucial role played by neutrinos. The latest astrophysical and cosmological observations confirm once more the precision of Big Bang Nucleosynthesis predictions.

1 INTRODUCTION

When neutrinos first came on the scene in 1930, their father Wolfgang Pauli confessed to his colleague, the astronomer Walter Baade, that to save energy conservation in β decays (quoted in (Hoyle, 1967)):

[1]Dipartimento di Fisica, Universitá di Napoli Federico II & INFN, Sezione di Napoli, Complesso Univ. Monte S. Angelo, Via Cintia, I-80126 Napoli, Italy

"I have done a terrible thing today, something which no theoretical physicist should ever do. I have suggested something that can never be verified experimentally."

That time Pauli was mistaken, and less than thirty years later neutrinos were discovered by Reines and Cowan. Since then many interesting features of neutrino physics have been discovered, but what has been constantly true along this story is that the understanding of neutrino properties has always brought new insights on fundamental interactions, and more recently on cosmology and astrophysics as well. We know now that the Standard Model of electroweak interactions (SM) accurately describes the neutrino feeble interactions with matter. The experimental study of neutrino interactions has been mainly pursued at accelerators and reactors, where we got the first confirmation that there are only three generations of light neutrinos (3 neutrino flavors) which are weakly interacting. However, in the last decades a main breakthrough in neutrino physics has come from a different environment: astrophysics. The first indication of neutrino physics beyond the SM was the so-called *solar neutrino problem* (Davis, 1964), namely an observed deficit of neutrino flux from the Sun. Sequently, the atmospheric neutrino anomaly, first pointed out by the Kamiokande collaboration (Hirata et al., 1988), led to the definite discovery that neutrinos are massive particles. Unfortunately, due to the small values of neutrino masses and to their elusive nature a complete knowledge of the neutrino mass spectrum is far to be obtained. This is not an irrelevant question since it is strongly linked with the understanding of the real *nature* of neutrinos as Dirac or Majorana particles.

Nevertheless, a not vanishing mass for neutrinos has a spectacular implication. As first suggested by Bruno Pontecorvo, in view of their masses, neutrinos exhibit oscillations among different flavors during their time evolution. This leads to an incredibly rich phenomenology very well studied by a wide range of experimental apparatus that have eventually led to the assignment of Nobel Prize for Physics in 2015 to T. Kajita (SuperKamiokande collaboration) and A.B. McDonald (SNO collaboration) "*for the discovery of neutrino oscillations, which shows that neutrinos have mass*". The parameters characterizing this oscillatory behavior, namely squared mass differences and mixing angles are presently quite well-known, where the last missing piece of the puzzle is the CP violation phase only.

The most notable example of the relevant role played by neutrinos in cosmology is perhaps related to the synthesis of light nuclei in the so-called Big

Bang model. From the late forties, it was clear that neutrinos cannot be considered as simple passive spectators during the expansion of the Universe. Due to both their weak interactions with other particles and to *gravity* they influence the early stages of the Universe evolution. This provides an indirect way to constrain neutrino properties. In fact, by using observations of astrophysical quantities specially related to particular phases of the Universe expansion, and comparing them with the theoretical predictions deduced assuming definite neutrino characteristics one can constrain them in a quite precise way. This was the case of the Cowsik – McClelland bound that implies, on pure cosmological grounds, that the sum of the masses of stable neutrinos could not overcome $94h^2$ eV ($h = H_0/100\,\mathrm{km\,s^{-1}\,Mpc^{-1}} = 0.6711$ being H_0 the Hubble constant), and that was obtain when the corresponding limits from the accelerator physics were orders of magnitude larger. A further example, are the constraints on the number of light weakly interacting neutrinos and on their mass scale obtained using observations of primordial Helium-4 (^{4}He) and Deuterium (Big Bang Nucleosynthesis).

This vaste arena where to test neutrino properties is usually referred to as *Neutrino Cosmology*, and it represents the topic of a recent book published by Cambridge University Press (Lesgourgues et al., 2013) to which the present paper is inspired. Neutrino Cosmology is a multidisciplinary research field, where knowledge coming from theoretical and experimental particle physicists, astrophysicists and cosmologists mixes to provide a unitary description of the physical processes.

In the present paper we briefly review a particular topic of neutrino Cosmology, namely the role played by these particle at the time of Primordial Nucleosynthesis. Using the temperature of the photons as a measure of cosmological time, in the stage of the early Universe when the electromagnetic plasma had a temperature in the interval between few MeV and few tens of KeV (from 1 s to few hours after Big Bang), the primordial plasma made of nucleons, electrons and positrons, gammas and neutrinos synthesized the lightest nuclides, namely Hydrogen, Deuterium, Helium–3 and 4 and Lithium–6 and 7. The stellar/galactic evolution in the $\sim$ 13 Gy from Big Bang has then produced the heavier elements now present in the Universe and modified the pristine abundances of the lighter ones. Note that in the Big Bang Nucleosynthesis phase (BBN), the cosmic neutrino background played a relevant role in shaping the chemical composition of present Universe.

2 NEUTRINO WEAK INTERACTIONS

Neutrino interactions were initially described by the theory of β-decay, proposed by Enrico Fermi in 1934. Now they are successfully encoded in the unified picture of Standard Model of electroweak interactions. Let us restrict our review to the neutrino-matter interaction terms of the SM Lagrangian. It consists of two terms: the charged-current, and neutral-current weak interaction Lagrangian densities, denoted by $\mathcal{L}_I^{(CC)}$ and $\mathcal{L}_I^{(NC)}$. In particular, one gets

$$\mathcal{L}_I^{(CC)} = -\frac{g}{2\sqrt{2}} J_W^\mu W_\mu + h.c. \tag{1}$$

where $J_W^\mu = J_{W,Q}^\mu + J_{W,L}^\mu$ and[2]

$$\begin{aligned} J_{W,Q}^\mu &= 2\overline{q_{\alpha L}^U}\gamma^\mu V_{\alpha\beta} q_{\beta L}^D \\ J_{W,L}^\mu &= 2\overline{\nu_{kL}}\,\gamma^\mu\, U_{k\beta}^\dagger\, l_{\beta L} \end{aligned} \tag{2}$$

In the previous expressions two unitary matrices intervene: the Cabibbo–Kobayashi–Maskawa (CKM) mixing matrix of quarks (Cabibbo, 1963; Kobayashi and Maskawa, 1973), V, and the corresponding Pontecorvo–Maki–Nakagawa–Sakata matrix (Pontecorvo, 1957; Pontecorvo, 1958) U for leptons. The matrix U contains three angles and a phase if neutrinos are Dirac particles, whereas two more phases have to be considered for Majorana neutrinos. The gauge boson field W^μ by definition annihilates a W^+ boson and creates a W^- boson. The neutral current $\mathcal{L}_I^{(NC)}$ reads

$$\mathcal{L}_I^{(NC)} = -\frac{g}{2\cos\theta_W} J_Z^\mu Z_\mu + h.c. \tag{3}$$

where $J_Z^\mu = J_{Z,Q}^\mu + J_{Z,L}^\mu$ and

$$\begin{aligned} J_{Z,Q}^\mu &= 2\Big(g_L^U\,\overline{q_{\alpha L}^U}\gamma^\mu q_{\alpha L}^U + g_R^U\,\overline{q_{\alpha R}^U}\gamma^\mu q_{\alpha R}^U \\ &+ g_L^D\,\overline{q_{\alpha L}^D}\gamma^\mu q_{\alpha L}^D + g_R^D\,\overline{q_{\alpha R}^D}\gamma^\mu q_{\alpha R}^D\Big) \\ J_{Z,L}^\mu &= 2\Big(g_L^\nu\overline{\nu_{\alpha L}}\gamma^\mu\nu_{\alpha L} + g_L^l\,\overline{l_{\alpha L}}\gamma^\mu l_{\alpha L} + g_R^l\,\overline{l_{\alpha R}}\gamma^\mu l_{\alpha R}\Big) \end{aligned} \tag{4}$$

Note that $\tan\theta_W = g'/g$ and $e = g\sin\theta_W$. Finally, the couplings $g_L^{\nu,l,U,D}$ and $g_R^{l,U,D}$ are given by the relations

$$g_L^f = I_3^f - Q_f\sin^2\theta_W \qquad g_R^f = -Q_f\sin^2\theta_W \tag{5}$$

[2]Note that ν_{kL} denote mass eigenstates.

where I^f stands for the weak-isospin quantum number of the fermion f, and Q_f its electric charge (Lesgourgues et al., 2013). Remarkably, the neutral currents (4) are not affected by flavor mixing.

The two terms in the SM Lagrangian density $\mathcal{L}_I^{(CC)}$ and $\mathcal{L}_I^{(NC)}$ (see (1) and (3) respectively) describe a three-body process involving two fermions and $W^\pm$ and Z gauge bosons, whose mass is of the order of 100 GeV. In the low energy limit, namely for energies much smaller than the mass of gauge bosons produced, the gauge propagators become

$$G^W_{\mu\nu}(x-x') \overset{p^\mu \ll m_W}{\longrightarrow} i\frac{g_{\mu\nu}}{m_W^2}\,\delta^4(x-x') \tag{6}$$

$$G^Z_{\mu\nu}(x-x') \overset{p^\mu \ll m_Z}{\longrightarrow} i\frac{g_{\mu\nu}}{m_Z^2}\,\delta^4(x-x') \tag{7}$$

Hence, the weak charged-current and neutral-current processes at tree level in the low energy limit are described by the effective Lagrangians

$$\mathcal{L}_{\text{eff}}^{(CC)} = -\frac{g^2}{8m_W^2} J_W^{\mu\dagger} J_{\mu W} = -\frac{G_F}{\sqrt{2}} J_W^{\mu\dagger} J_{\mu W} \tag{8}$$

$$\mathcal{L}_{\text{eff}}^{(NC)} = -\frac{g^2}{4\cos^2\theta_W m_Z^2} J_Z^{\mu\dagger} J_{\mu Z} = -2\frac{G_F}{\sqrt{2}}\rho J_Z^{\mu\dagger} J_{\mu Z} \tag{9}$$

where $G_F \equiv \sqrt{2}g^2/(8m_W^2) = 1.166 \times 10^{-5}$ GeV^{-2} is the Fermi constant and $\rho \equiv m_W^2/(m_Z^2\cos^2\theta_W)$, which is equal to unity in the SM.

Flavor oscillations can be certainly defined as the most astonishing properties of neutrinos. They are due to the fact that neutrinos are produced *via* charged current interaction as flavour states, which are a linear superposition of mass eigenstates (U matrix). If differences among neutrino masses are exceedingly small, energy and momentum resolutions are typically not good enough to distinguish among neutrino mass eigenstates. In this case the outgoing wave–packet is a linear superposition of different mass states and the effect of interference (oscillations) can be observed. Let us consider for simplicity neutrinos as plane waves. A particular flavour *ket* state, $|\nu_\alpha\rangle$, can be written as a superposition of mass eigenstates, $|\nu_k\rangle$, as

$$|\nu_\alpha\rangle = \sum_{k=1}^{3} \mathcal{U}^*_{\alpha k}\,|\nu_k\rangle \quad \text{with} \quad \alpha = e, \mu, \tau \tag{10}$$

Since massive neutrinos are Hamiltonian eigenstates, a generic $|\nu_\alpha\rangle$ produced at

$t = 0$ evolves in time as

$$|\nu_\alpha(t)\rangle = \sum_\beta \left(\sum_{k=1}^{3} \mathcal{U}^*_{\alpha k}\, e^{-iE_k t}\, \mathcal{U}_{\beta k} \right) |\nu_\beta\rangle \tag{11}$$

From this expression, and in the relativistic limit, one gets the probability that performing a measurement of neutrino flavour at the time t one detects a flavour β

$$P_{\nu_\alpha \to \nu_\beta}(t) = |\langle \nu_\beta | \nu_\alpha(t)\rangle|^2 = \sum_{k,j=1}^{3} U^*_{\alpha k}\, U_{\beta k} U_{\alpha j}\, U^*_{\beta j}\, \exp\left\{ -i \frac{\Delta m^2_{kj}}{2|\vec{p}|} t \right\} \tag{12}$$

where $\Delta m^2_{kj} \equiv m^2_k - m^2_j$. In a neutrino experiment the time dependence of the flavour transition probability cannot be followed, but rather one can measure how the probabilities depend on L, the distance of the detection point from the origin of the neutrino beam. The probability that starting with a ν_α one still detects the same flavour at a distance L is called *survival probability* and it is obtained from the previous expression for $\alpha = \beta$

$$P_{\nu_\alpha \to \nu_\alpha}(L) = 1 - 4 \sum_{k>j} |U_{\alpha k}|^2\, |U_{\alpha j}|^2 \sin^2 \left[\frac{\Delta m^2_{kj}}{2|\vec{p}|} L \right] \tag{13}$$

The total transition probability, namely the probability to observe a change in flavour is given by $1 - P_{\nu_\alpha \to \nu_\alpha}$, from unitarity. A fully analogous treatment can be applied to antineutrinos which are produced by weak charged current via positive charged lepton transitions, $l^+_\alpha \to \overline{\nu}_\alpha$, pair creation, $l^-_\alpha \overline{\nu}_\alpha$, and neutrino–antineutrino pair creation $\nu_\alpha \overline{\nu}_\alpha$ mediated by weak neutral current.

From a global 3ν oscillation analysis (Capozzi et al., 2014), in the case of normal hierarchy the neutrino oscillation parameters are at 68% CL

$$\begin{aligned} &\delta m^2/10^{-5}\mathrm{eV}^2 = 7.54^{+0.26}_{-0.22} && \sin^2\theta_{12}/10^{-1} = 3.08 \pm 0.17 \\ &\Delta m^2/10^{-3}\mathrm{eV}^2 = 2.43 \pm 0.06 && \sin^2\theta_{13}/10^{-2} = 2.34^{+0.20}_{-0.19} \\ &\sin^3\theta_{23}/10^{-1} = 4.37^{+0.33}_{-0.23} && \delta/\pi = 1.39^{+0.33}_{-0.27} \end{aligned} \tag{14}$$

where θ_{12}, θ_{13}, θ_{23} and δ parametrize the PMNS matrix, while δm^2 and Δm^2 are the following combinations of neutrino masses.

$$\delta m^2 = m^2_2 - m^2_1 \qquad \Delta m^2 = m^2_3 - \frac{m^2_2 + m^2_1}{2} \tag{15}$$

The formalism here presented for vacuum oscillations can be extended in presence of medium. In this case resonant oscillation phenomena can occur, and this is the basis of famous MSW effect (Wolfenstein, 1978; Mikheev and Smirnov, 1985) which represents the generally accepted explanation for deficit in solar neutrino flux.

3 THE COSMIC NEUTRINO BACKGROUND

At the time of BBN the active left-handed neutrinos ν_e, ν_μ and ν_τ and the corresponding CP conjugated states were present in the primordial plasma, where all particles were kept in thermodynamical equilibrium (kinetic and chemical) by weak interactions. Hence all fermions, including neutrinos, were characterized by a Fermi-Dirac distribution. With the expansion of the Universe the temperature decreased as the inverse of scale factor, a^{-1}, with the exception of the interval of temperature when degrees of freedom (particle species) disappeared releasing their entropy to lighter species.

With the decreasing of temperature, T, the neutrino interaction rate became less and less effective dropping down the Hubble rate $H(T)$, namely the expansion rate. Hence weak rates were no more capable to maintain neutrinos in equilibrium, and they decoupled from the electromagnetic plasma (baryons, leptons, photons).

A detailed description of neutrino decoupling requires the solution of a set of Boltzmann equations. However, an estimate of the value of T at the decoupling can be simply performed by comparing the interaction rate with $H(T)$. For a temperature in the MeV range the rate of charged and neutral current interactions can be fixed by dimensional considerations only and results to be

$$\Gamma_\nu \sim G_F^2 T^2 n_e \sim G_F^2 T^5 \tag{16}$$

where n_e is the electron/positron (target) density, of the order of T^3 for relativistic electrons. The Hubble parameter in the radiation dominated epoch is then given by

$$H(T) = \sqrt{\frac{8\pi G}{3} g_* \frac{\pi^2}{30} T^4} \sim \sqrt{g_*} \frac{T^2}{m_{Pl}} \tag{17}$$

where g_* denotes the effective d.o.f. of the plasma at that temperature. The decoupling temperature $T_{\nu D}$ is then simply obtained by equating

$$G_F^2 T_{\nu D}^5 = \sqrt{g_*} \frac{T_{\nu D}^2}{m_{Pl}} \quad \Rightarrow \quad T_{\nu D} = \left(\frac{\sqrt{g_*}}{G_F^2 m_{Pl}} \right)^{1/3} \sim g_*^{1/6}\,\mathrm{MeV} \tag{18}$$

Around this temperature, only photons, electron/positron and neutrinos themselves contribute to g_* (the factor $7/8$ is the statistical weight for fermions), and one gets

$$g_* = 2 + \frac{7}{8}4 + \frac{7}{8}6 = \frac{43}{4} = 10.75 \tag{19}$$

To obtain a more refined computation of the decoupling temperature one has to solve the kinetic equation (Dolgov, 2002), that in terms of the variables $x = ma$ and $y = pa$, with m some mass scale (usually taken 1 MeV) read

$$Hx\frac{\partial f_{\nu_e}}{\partial x} = -\frac{80G_F^2(\tilde{g}_L^{l2} + g_R^{l2})m^9}{3\pi^3 x^5} y f_{\nu_e} \tag{20}$$

$$Hx\frac{\partial f_{\nu_{\mu,\tau}}}{\partial x} = -\frac{80G_F^2(g_L^{l2} + g_R^{l2})m^9}{3\pi^3 x^5} y f_{\nu_{\mu,\tau}} \tag{21}$$

where $\tilde{g}_L^l = 1 + g_L^l$. The solution of the previous set of equations yields $T_{\nu_e D} =$ 1.87 MeV and $T_{\nu_\mu,\nu_\tau D} = 3.12$ MeV, see also (Dolgov and Zeldovich, 1981; Enqvist et al., 1992).

Interesting conclusions can be derived in the limit in which we consider neutrino decoupling instantaneously occurring at $T_{\nu D}$, the so-called *instantaneous decoupling limit*. After decoupling, neutrinos propagate freely, and their distribution remains unchanged but for the effect of redshift of physical momentum

$$f_{\nu_\alpha}(p) = \left[\exp\left(\frac{p\,a}{T_{\nu D} a_D}\right) + 1\right]^{-1} \tag{22}$$

In particular, the distribution is completely specified by a "temperature" parameter scaling as $T_{\nu D} a_D / a$. This temperature scaling is equivalent to the conservation of the neutrino entropy per comoving volume, $s_{\nu,\overline{\nu}_\alpha} a^3 =$ constant.

Under the above approximation, the neutrino to photon temperature ratio after neutrino decoupling can be derived by simply applying the conservation of entropy for the electromagnetic plasma of $e^\pm$ and photons. As long as electron/positron pairs are relativistic, the photon temperature simply scales as a^{-1} since the number of degrees of freedom remains constant. When the temperature drops below a value $T_{ann} \sim m_e$ the $e^\pm$ pair annihilations in photons cannot be efficiently compensated by the inverse pair production. As a result, photons get heated, and their temperature in this phase is not decreasing as the inverse scale factor. Neutrinos are basically left undisturbed by pair annihilations.

To compute the evolution of the photon temperature during this stage, let us consider the entropy density of coupled $e^{\pm}$ and photons

$$s_{e^{\pm},\gamma} = \frac{2\pi^2}{45} T^3 g_s(T) \tag{23}$$

where for $T \gg m_e$, electrons and positrons are still relativistic, and $g_s \to 2 + 7/8(2+2) = 11/2$. In the opposite limit, $T \ll m_e$, electrons and positrons have a negligible entropy and $g_s \to 2$. Since the entropy per comoving volume $s_{e^{\pm},\gamma} a^3$ is conserved, and $T_\nu \sim a^{-1}$, we have

$$g_s(T) \frac{T^3}{T_\nu^3} = \text{constant} \tag{24}$$

At neutrino decoupling $T_\nu = T$. After the $e^{\pm}$ annihilation stage, when $T \ll m_e$, g_s drops and we get

$$\frac{11}{2} = 2\frac{T^3}{T_\nu^3} \Rightarrow \frac{T_\nu}{T} = \left(\frac{4}{11}\right)^{1/3}, \quad T << m_e \tag{25}$$

By reminding that the CMB temperature today is $T_0 = 2.725\,\mathrm{K}$, we get for neutrinos $T_{\nu,0} = 1.945\,\mathrm{K}$, or $1.676 \cdot 10^{-4}$ eV in natural units. This leads, in absence of relevant chemical potentials, to a density of neutrinos that at present is

$$n_{\nu,0} = n_{\overline{\nu},0} \sim 56\,\mathrm{cm}^{-3} \tag{26}$$

Unfortunately their energy is so small to make almost impossible or at least very challenging a direct detection.

After $e^{\pm}$ annihilation, the radiation energy density can be written as

$$\rho_R = \rho_\gamma \left(1 + \frac{7}{8} N_{\text{eff}} \left(\frac{4}{11}\right)^{4/3}\right) \tag{27}$$

where N_{eff} is the effective number of relativistic degrees of freedom in addition to photons. In an Universe populated by photons and three standard neutrinos only, under the approximation of instantaneous neutrino decoupling we have $N_{\text{eff}} = 3$. Such a value is very close to the one obtained solving the kinetic equations which is $N_{\text{eff}} = 3.046$ (Mangano et al., 2005).

4 BIG BANG NUCLEOSYNTHESIS

The main idea of the BBN arised few years after the seminal paper (Alpher et al., 1948) and since then it has become one of the observational pillars of the Big Bang model, providing one of the most robust evidences of it.

At neutrino decoupling ($\sim 2-3$ MeV), the densities of all nuclei were set by Nuclear Statistical Equilibrium (NSE), namely by the general laws of Thermodynamics. Fast nuclear and electromagnetic interactions kept nuclear species in kinetic and chemical equilibrium. Since there were too many photons per baryons, $\eta_B^{-1} \sim 10^9$, for temperatures of the typical order of magnitude of nuclear binding energy per nucleon (few MeV), baryon matter still remained in the form of free neutrons and protons.

Consider for example the case of Deuterium, which is formed via proton neutron fusion reaction $n + p \leftrightarrow {}^2\mathrm{H} + \gamma$. Applying NSE (Saha equation) to this process we get

$$\frac{n_{^2\mathrm{H}}}{n_p n_n} = \frac{3}{4}\left(\frac{2\pi\left(m_n + m_p - B_{^2\mathrm{H}}\right)}{m_n m_p T}\right)^{3/2} \exp\left(\frac{B_{^2\mathrm{H}}}{T}\right) \tag{28}$$

Observing that $B_{^2\mathrm{H}} \sim 2.2$ MeV (Deuterium binding energy), it follows that

$$\frac{n_{^2\mathrm{H}}}{n_B} \sim \eta_B \left(\frac{T}{m_N}\right)^{3/2} \exp\left(\frac{B_{^2\mathrm{H}}}{T}\right) \tag{29}$$

with m_N the average nucleon mass. From this expression one finds that at $T \sim B_{^2\mathrm{H}}$ only a fraction of order 10^{-12} of baryons is in the form of Deuterium. Higher mass nuclei are even less abundant.

Soon after neutrinos decoupling, charged-current weak interactions involving neutrons and protons, namely

$$\begin{array}{llll} (a) & \nu_e + n \to e^- + p & (d) & \overline{\nu}_e + p \to e^+ + n \\ (b) & e^- + p \to \nu_e + n & (e) & n \to e^- + \overline{\nu}_e + p \\ (c) & e^+ + n \to \overline{\nu}_e + p & (f) & e^- + \overline{\nu}_e + p \to n \end{array} \tag{30}$$

also became too slow to guarantee $n - p$ chemical equilibrium. When the temperatures went below $T_D \sim 0.7$ MeV, the n/p density ratio departed from its equilibrium value and freezed out at the value $n/p = \exp(-\Delta m/T_D) \sim 1/6$, with $\Delta m = 1.29$ MeV the neutron–proton mass difference, and was then reduced only by neutron decays. At this stage, the photon temperature was already

below the Deuterium binding energy but Deuterium synthesis started only when the photodissociation process became ineffective. This is the so-called *Deuterium bottleneck*, which was overcome at $T_{\rm BBN} \sim 0.07$ MeV, for which the ratio in (29) is of order one.

The onset of ^{2}H formation leads to a whole chain of nuclear processes that eventually produces heavier nuclei. As soon as Deuterium formed, it was almost immediately burned into ^{4}He, which has the largest binding energy per nucleon among light nuclei. This nucleus represents the main BBN outcome, and its abundance can be quite accurately obtained by very simple arguments.

The final value $n_{^4\rm He}$, is almost insensitive to the details of the nuclear network, hence one can simply assume that all neutrons, not yet decayed at $T_{\rm BBN}$ are bound into Helium nuclei. This leads to the famous result for the Helium mass fraction $Y_p \equiv 4\, n_{^4\rm He}/n_B$

$$Y_p \sim \frac{2}{1+\exp(\Delta m/T_D)\exp(t(T_{\rm BBN})/\tau_n)} \sim 0.25 \tag{31}$$

where $t(T_{\rm BBN})$ denotes the value of time at $T_{\rm BBN}$ and τ_n the neutron lifetime. It is worth noticing that enlarging the number of neutrinos forming the cosmic neutrino background, namely $N_{\rm eff}$, would lead to a faster expansion rate so decreasing the time necessary to reach *Deuterium bottleneck*, and hence more neutrons would survive to β-decay. This would lead to an increase of Y_p. For this reason the Helium-4 mass fraction predicted by BBN is very sensitive to the presence of neutrinos in the cosmic background.

A more accurate determination of the primordial abundances of all light nuclei requires the solution of a set of coupled kinetic equations, supplemented by Einstein equations, covariant conservation of total stress–energy tensor, as well as conservation of baryon number and electric charge. This is typically obtained from numerical codes. More recently our group in Naples has released the very precise and updated code `PArthENoPE` (Pisanti et al., 2008).

Let us consider N_{nuc} species of nuclides, whose number densities, n_i, are normalized with respect to the total number density of baryons n_B, $X_i = \frac{n_i}{n_B}$ with $i = p$, n, ^{2}H, ^{3}He, ... The list of nuclides considered for BBN in `PArthENoPE` is made of more than twenty elements, ranging from free neutron up to ^{16}O. The most interesting abundances, those of ^{2}H, ^{3}He, ^{4}He and ^{7}Li, are usually expressed as

$$\frac{^2\rm H}{\rm H} = \frac{X_{^2\rm H}}{X_p}\,, \qquad \frac{^3\rm He}{\rm H} = \frac{X_{^3\rm He}}{X_p}\,, \qquad Y_p = 4X_{^4\rm He}\,, \qquad \frac{^7\rm Li}{\rm H} = \frac{X_{^7\rm Li}}{X_p} \tag{32}$$

In terms of these quantities a set of ordinary non–linear differential equations has to be solved. Fortunately in the temperature range of interest for BBN, few MeV $\gtrsim T \gtrsim 10\,\mathrm{keV}$, electrons and positrons are kept in thermodynamical equilibrium with photons. Their distribution is a Fermi-Dirac function with a small chemical potential, due to the charge neutrality of the Universe, $\mu_e/T \simeq \eta_B$. On the other hand, to follow the neutrino–antineutrino distribution in details, it is necessary to write down evolution equations for their distribution in phase space and this can be done separately since baryons are too few to modify neutrino distributions. Once neutrinos distributions are known as a function of time one can substitute them in the BBN equations.

The standard BBN depends only on two parameters, which are the baryonic cosmological parameter $\omega_B \equiv \Omega_B h^2$ (related to the baryon–to–photon density ratio η_B), and the effective number of relativistic degrees of freedom N_{eff} (see (27)). Once the predictions of BBN are obtained they have to be compared with inferred primordial abundances derived by astrophysical observations.

The astrophysical environments which seem most appropriate to obtain reliable measurements of the primordial deuterium fraction are the hydrogen-rich clouds absorbing the light of background QSOs at high redshifts. On the other hand, the key data for inferring Helium-4 primordial abundance are provided by observations of helium and hydrogen emission lines generated from the recombination of ionized hydrogen and helium in low-metallicity extragalactic HII regions. The estimate for Helium-3 and Lithium-6 and 7 are more complicate due to galactic and stellar evolution, and show a relevant level of disagreement with BBN predictions.

Nevertheless, it is of particular relevance to observe that the values of $\omega_B \equiv \Omega_B h^2$ and N_{eff} needed to obtain the observed abundances of primordial Deuterium and Helium-4 (with Hydrogen the most abundant elements among the lighter ones) are in good agreement with the independent estimates coming from CMB. Combining CMB observations with other astrophysical data, the Planck Collaboration (Ade et al., 2015) finds $\omega_B = 0.02222 \pm 0.00023$ (*Planck* TT+lowP) and $N_{\mathrm{eff}} = 3.15 \pm 0.23$ (*Planck* TT+lowP+BAO), which are consistent with the BBN predictions $\omega_B = 0.021 \pm 0.002$ and $N_{\mathrm{eff}} = 3.046$.

5 CONCLUSIONS

As it was clear from the late forties, neutrinos are fundamental ingredients in understanding the early stages of the Universe evolution. Following a chronolog-

ical order, neutrinos can be related to the production of the baryon–antibaryon asymmetry of the Universe in the elegant scenario of *baryogenesis through leptogenesis*, they considerably influence the primordial synthesis of light nuclei, and finally they provide a direct impact on matter perturbations through gravity during the phase of structure formation in the Universe.

In the present paper we have analyzed the role played by neutrinos during the Big Bang Nucleosynthesis phase. In this epoch, the weak interactions involving neutrinos maintain the baryonic matter (protons and neutrons) in chemical equilibrium, and after neutrino decoupling they are crucial to define the value of neutron–to–proton number density ratio, which sets the initial condition for the nuclear reactions producing light nuclei. Moreover, neutrinos give a considerable contribution to the radiation energy density, which defines the expansion rate of the Universe.

Astrophysical and cosmological observations provide important information on the BBN, and consequently constrain the neutrino properties. In particular, the latest result of Planck are in good agreement with the predictions for ω_b and $N_{\rm eff}$ obtained by numerical calculations of primordial abundances, confirming the power of the standard BBN model.

6 REFERENCES

Ade P.A.R. et al. [Planck Collaboration] (2015) "*Planck 2015 results. XIII. Cosmological parameters*". arXiv:1502.01589 [astro-ph.CO].

Alpher R.A., Bethe H. and Gamow W. (1948) "*The origin of chemical elements*". Phys. Rev. **73**, 803-804.

Cabibbo N. (1963) "*Unitary symmetry and leptonic decay*". Phys. Rev. Lett. **10**, 531-533.

Capozzi F. et al. (2014) "*Status of three-neutrino oscillation parameters, circa 2013*". Phys. Rev. D **89**, 093018.

Davis R. Jr. (1964) "*Solar neutrinos. II. Experimental*". Phys. Rev. Lett. **12**, 303-305.

Dolgov A.D. (2002) "*Neutrinos in cosmology*". Phys. Rep. **370**, 333-535.

Dolgov A.D. and Zeldovich Ya.B. (1981) "*Cosmology and elementary particles*". Rev. Mod. Phys. **53**, 1-41.

Enqvist K., Kainulainen K. and Semikoz V. (1992) "*Neutrino annihilation in hot plasma*". Nucl. Phys. B **374**, 392-404.

Hirata K.S. et al. (1988) "*Experimental study of the atmospheric neutrino flux*". Phys. Lett. **B205** 416.

Hoyle F. (1967) "*Concluding remarks*". Proc. Royal Soc. (London) **A 301**, 171.

Kobayashi M. and Maskawa T. (1973) "*CP violation in the renormalizable theory of weak interaction*". Prog. Theor. Phys. **49**, 652-657.

Lesgourgues J., Mangano G., Miele G. and Pastor S. (2013) "*Neutrino Cosmology*". Cambridge University Press, New York, USA.

Mangano G. et al. (2005) "*Relic neutrino decoupling including flavor oscillations*". Nucl. Phys. **B729** 221-234.

Mikheev S.P. and Smirnov A.Yu. (1985) "*Resonance enhancement of oscillations in matter and solar neutrino spectroscopy*". Sov. J. Nucl. Phys. **42**, 913-917.

Pisanti O. et al. (2008) "*PArthENoPE: Public Algorithm Evaluating the Nucleosynthesis of Primordial Elements*". Comput. Phys. Commun. **178** 956-971.

Pontecorvo B. (1957) "*Mesonium and anti-mesonium*". Sov. Phys. JETP **6**, 429.

Pontecorvo B. (1958) "*Inverse beta processes and nonconservation of lepton charge*". Sov. Phys. JETP **7**, 172-173.

Wolfenstein L. (1978) "*Neutrino oscillation in matter*". Phys. Rev. D **17**, 2369.

Rend. Acc. Sc. fis. mat. Napoli
Vol. LXXXII, (2015) pp. 99-106

The unexpected recovery of misplaced data on brain metabolic DNA

Bruno Rutigliano[1] and Antonio Giuditta*

Nota presentata dal socio Antonio Giuditta
(Adunanza del 20 novembre 2015)

Key words: DNA synthesis, brain, reverse transcription, synaptosomes

Abstract – Newly synthesized DNA from rat brain is mostly present in cytoplasmic organelles sedimenting in the mitochondrial fraction but differing from mitochondria. At early incorporation times a considerable fraction of radiolabeled DNA is associated with putative RNA-DNA hybrids detected by their behavior in cesium gradients.

Riassunto – Gran parte del DNA sintetizzato nel cervello di ratto è presente in organelli citoplasmatici che sedimentano con la frazione mitocondriale ma differiscono dai mitocondri. Con tempi di incorporazione molto brevi una notevole frazione di tale DNA risulta associata a presumibili ibridi RNA-DNA identificati dal loro comportamento in gradienti di cesio.

1 - INTRODUCTION

In the early eighties I moved from the International Laboratory of Genetics and Biophysics (ILGB) to the Institute of General Physiology of the Federico II University in Naples. During the move or at somewhat later time one of my notebooks containing experimental data on brain metabolic DNA could not be located despite repeated attempts. The loss was relevant since it occurred at a time I was debating whether to continue investing my research resources to that intriguing project (Perrone Capano et al., 1982) or rather commit them to a

---

[1]deceased on December 3, 1991; *corresponding author, giuditta@unina.it.

promising investigation on the controversial presence of a local system of protein synthesis in the squid giant axon (Cutillo et al., 1983; Ingoglia et al., 1983). For a number of reasons that also included the apparent loss of the missing notebook the latter issue became my primary research interest (Giuditta et al., 2002; 2008), and consequently the study of brain metabolic DNA became progressively less relevant and was eventually abandoned (Grassi Zucconi and Giuditta, 2002). Memories of that unfinished project came back to my mind in the last few years when by a survey of the literature I realized that no additional study had concerned the modulation of brain metabolic DNA by learning (Reinis, 1972; Ashapkin et al., 1983; Scaroni et al., 1983; Giuditta et al., 1986), by post-trial sleep (Giuditta et al., 1985), and by circadian oscillations (Grassi Zucconi et al., 1988; 1990). This was surprising since experimental data indicated that newly synthesized brain DNA was involved in memory processing and could possibly be conditioning brain evolution. The latter possibility was suggested by a study of DNA mutations in the brain of psychiatric patients which demonstrated their non random nature but rather their mostly regarding well known metabolic pathways. The data were interpreted to support the view that brain evolution had been conditioned by a neoLamarckian mechanism (Barry, 2013). This possibility markedly strengthened my desire to resume studies on brain metabolic DNA since they might eventually support my previous neoLamarckian view (Giuditta, 1982).

Having recently set my mind to this task, the impending retirement from the University made this objective considerably hard to be attained. I was supposed to leave my lab and free my office of the scientific papers that had been piling up during the last forty years. The situation was far from being satisfactory but it was hiding a very pleasant surprise: during the clearing of my lab and office the misplaced notebook suddenly popped up. Its contents revealed an unexpected long list of experiments aiming to elucidate the basic features of brain metabolic DNA.

This brief note describes data obtained in my ILGB laboratory in the seventies and subsequently forgotten. They regard the demonstration of newly synthesized brain DNA in nuclear and cytoplasmic fractions and its initial time-dependent appearance in association with putative DNA-RNA hybrids that were identified by their behavior in cesium gradients. It is hoped that these preliminary results might eventually prompt additional investigations.

2 – METHODS

All experiments were made with adult male Wistar rats that received [^{3}H]methythymidine in the olfactory bulbs. This injection route insured a satisfactory distribution of the DNA precursor in brain while minimizing damage to the neocortical tissue. At the end of the incorporation period rats were decapitated with a guillotine and brain was isolated at ice temperature.

Hemispheres were cleaned of major blood vessels and membranes and homogenized in a Dounce homogenizer with 9 volumes 0.32 M sucrose, 10 mM Tris-Cl pH 7.4 (homogenizing medium or HM).

The homogenate was subjected to progressively increasing centrifugal forces to obtain three subcellular fractions (P1, P2, and P3). The P1 fraction (also known as the nuclear fraction) was sedimented at 800g for 15 min. The resulting supernatant fraction was centrifugation at a higher speed (15.000g, 15 min) to yield the P2 fraction (also known as the mitochondrial fraction), and the further centrifugation of the resulting supernatant fraction (100,000g, 60 min) produced the P3 fraction (also known as the microsomal fraction). It should be noted that these fractions, in addition to the subcellular particles designating each fraction, also contain several additional particles. Indeed, the P1 fraction also contains synaptosomes, mitochondria and cell debris; the P2 fraction also contains synaptosomes and microsomes, and the P3 fraction also contains synaptosomes and free and membrane-bound polysomes.

Purified nuclei characterized by their large or small size were also prepared by homogenizing the brain in 2 M sucrose, 1 mM $CaCl_2$, 1 mM potassium phosphate buffer pH 6.5. The homogenate was centrifuged in the Spinco rotor SW-25 (22,000 rpm, 75 min) on a discontinuous sucrose gradient consisting of 2.2 M, 2.4 M, and 2.7 M layers. Large nuclei derived from astrocytes and large neurons were recovered over the 2.4 M sucrose layer, while small nuclei originating from small neurons and oligodendrocytes sedimented over the 2.7 M sucrose layer.

3 - RESULTS

Experiments of March 17-20, 1972

The well known localization of DNA in nuclei and the possibility to separate large nuclei from small nuclei (Giuditta et al., 1972) suggested the determination of newly synthesized DNA in those nuclear classes. In rats of 100 g the concentration of radiolabeled DNA was consistently 2-3-fold larger in the small nuclei than in the large nuclei. After an incorporation period of 15 min the DNA specific activity was 20 cpm/μg in the large nuclei and 66 cpm/μg in the small nuclei. Likewise, after an incorporation period of 20 min the DNA specific activity was respectively 37 cpm/μg and 74 cpm/μg in the large and small nuclei. Comparable data were obtained in several additional analyses made after longer incorporation times. The prevalent synthesis of DNA in the small nuclei was in agreement with the marked DNA synthesis observed in white matter oligodendrocytes by autoradiographic analyses (Reinis, 1972).

Experiments of January 20 to March 20, 1972

In additional experiments (n=7) in which incorporation time ranged from 15 min to 120 min, the content of newly synthesized DNA was examined in the

Table 1

Time (min)	[^{3}H]DNA/cyt. oxid. (%/%)		
	P2	post-P2	post-P2/P2
15	0.32	2.50	7.8
20	0.28	0.74	2.6
20	0.46	7.41	16.1
40	0.24	0.62	2.6
60	0.40	1.48	3.7
120	0.48	2.50	5.2
120	0.34	8.00	23.5

subcellular fractions of isotonic brain homogenates. As expected, most radiolabeled DNA was recovered from the P1 fraction but conspicuous amounts were also unexpectedly present in the P2 fraction and in the post-P2 supernatant. The prevalence of mitochondria in the P2 fraction suggested that the newly synthesized DNA was presumably mitochondrial DNA. This possibility appeared at odds with the low turnover of mitochondrial DNA but was nevertheless examined. Accordingly, the percent content of newly synthesized DNA present in the P2 fraction and in the post-P2 supernatant was determined and referred to the percent content of cytochrome oxidase activity that was considered a reliable index of the mitochondrial content.

As shown in Table 1, the consistently low ratios between radiolabeled DNA and cytochrome oxidase exhibited by the P2 fraction clearly reflected its high content of mitochondria. However comparable values were not reproduced in the post-P2 fraction in which ratios were consistently much higher. Comparable results were provided by an additional experiment in which the incorporation time was 120 min and P2 mitochondria were separated from a synaptosomal/myelin fraction. The ratios in free mitochondria and in the latter fraction were respectively 0.21 and 0.73, that is 3.5-fold larger in the latter fraction. Hence, the data excluded that newly synthesized brain DNA was mitochondrial DNA.

Experiment of April 24, 1972

The latter conclusion left open the possibility that newly synthesized DNA present in the P2 and post-P2 fractions originated from contaminating nuclei or nuclear fragments. This possibility prompted further analyses of newly synthesized DNA with a view that its properties might eventually be used to compare the nuclear P1 fraction with the cytoplasmic P2 and P3 fractions. Our attention specifically regarded the modifications displayed by newly synthesized DNA with increasing incorporation time (from 30 min to 60 and 180 min). In these experiments neocortical tissue homogenized in physiological saline (0.9%

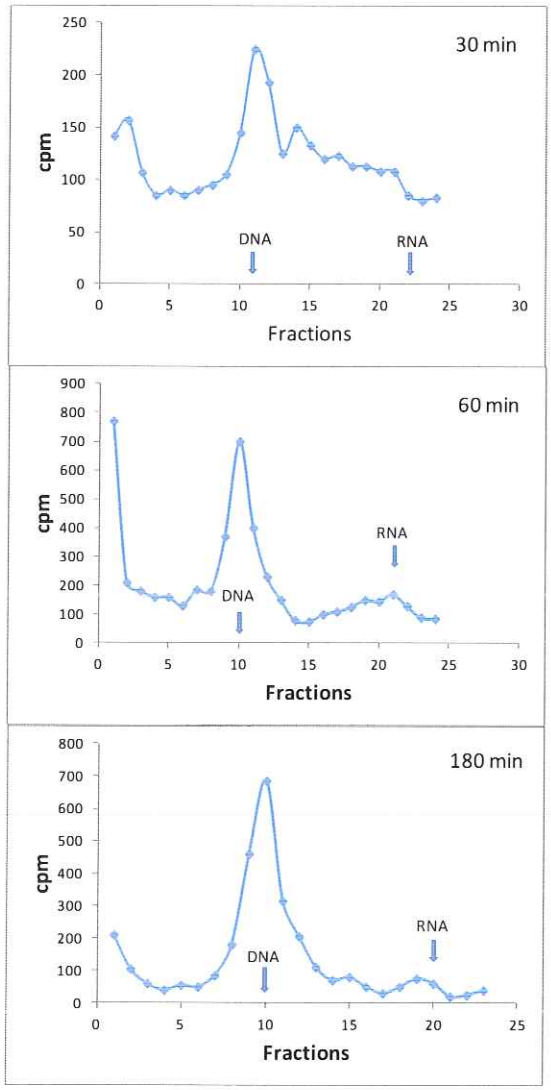

Figure 1

NaCl) was brought to 1% sarcosil and to a density very close to 1.5 g/ml by $CsSO_4$ addition. Following centrifugation in Spinco SW39 rotor (36,000 rpm, 46 h, 20°) gradient fractions were collected and analyzed for OD_{260} absorbance and radiolabeled DNA content. Results are presented in Figure 1 in which the thick arrows indicate the position of native DNA and RNA determined by OD_{260} readings.

In all gradients most newly synthesized DNA coincided with the peak of native DNA but some of it was present in different gradient regions. The fraction

localized in lower density regions was likely associated with protein while that present in regions denser than native DNA appeared associated with RNA. Interestingly, the content of the latter fraction underwent a progressive decrement with longer incorporation times. At an early time (30 min) it represented 47% of the total gradient content of newly synthesized DNA , at 60 min it decreased to 28%, and at 180 min was less than 20%. The results suggested that a large amount of newly synthesized DNA initially behaved as an RNA-DNA hybrid which progressively decreased with longer incorporation

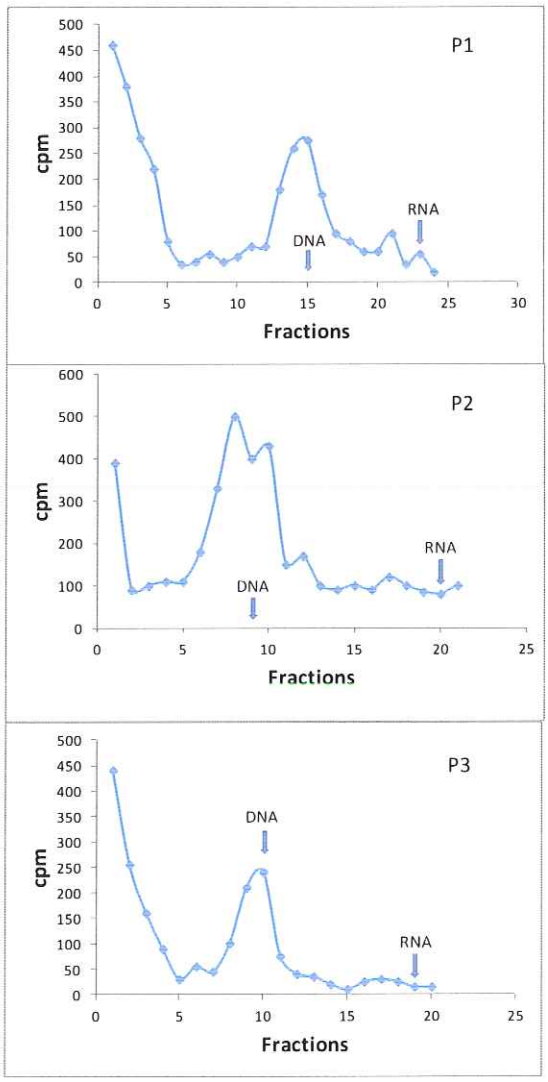

Figure 2

times.

Since these data were assumed to be largely due to nuclear DNA we examined the presence of the putative RNA-DNA hybrid in nuclear and cytoplasmic fractions. Accordingly, in an additional experiment in which the incorporation time was 30 min, brain tissue was homogenized in isotonic HM, P1, P2 and P3 fractions were prepared and they were treated with 1% sarcosil and $CsSO_4$ to be centrifuged as described above. Figure 2 shows that the fraction of newly synthesized DNA localized in gradient regions denser than native DNA was present in P1 and P2 fractions but not in the P3 fraction. Its content represented 17% of the total radiolabeled DNA in the P1 gradient and almost twice as much (31%) in the P2 gradient. The latter data confirmed previous results (Figure 1).

Since the majority of the putative DNA-RNA hybrid was present in the P2 fraction, the lower amount of the P1 fraction could not be considered a contaminant of the P2 fraction. Indeed, it was more likely that a non mitochondrial component of the P2 fraction contaminated the P1 fraction. In other words, the putative hybrid between RNA and newly synthesized DNA was likely to be present in a non mitochondrial component of the P2 fraction.

The data of Figure 2 only allow preliminary suggestions as to the apparent densities of newly synthesized DNA. They regard i) the apparent difference between either one of the two P2 peaks and the single P1 peak; and ii) the correspondence of the denser P2 peak with the single P1 peak.

4 - CONCLUSION

The data support the conclusion that brain metabolic DNA is synthesized in cytoplasmic organelles sedimenting in the crude mitochondrial fraction but not attributable to mitochondria. Data obtained in the experiments of January-March 1972 and in those described in the note of June 19, 2015 suggest that these organelles may be synaptosomes.

5 - REFERENCES

Ashapkin V.V., Romanov G.A., Tushmalova N.A., Vanyushin B.F. (1983) Selective DNA synthesis in the rat brain induced by learning. Biokhimija **48**: 355-362.

Barry, G. (2013) Lamarckian evolution explains human brain evolution and psychiatric disorders. Front. Neurosci. 7: 224. doi: 10.3389/fnins.2013.00224.

Cutillo V., Montagnese P., Gremo F., Casola L., and Giuditta A. (1983) Origin of axoplasmic RNA in the squid giant fibre. Neurochem. Res. **8**: 1621-1634.

Giuditta A., Rutigliano B., Casola L., and Romano M.. Biosynthesis of RNA in two nuclear classes separated from rat cerebral cortex. *Brain.Res.* 46:313-328, 1972.

Giuditta A. (1982) Proposal of a "spiral" mechanism of evolution. Riv. Biol. **75**: 13-31.

Giuditta A., Ambrosini M. V., Scaroni R., Chiurulla C., and Sadile A. (1985) Effect of sleep on cerebral DNA synthesized during shuttle-box avoidance training. Physiol.Behav. **34**: 769-778.

Giuditta A., Perrone Capano C., D'Onofrio G., Toniatti C., Menna T., and Hydèn H. (1986) Synthesis of rat brain DNA during acquisition of an appetitive task. Pharmacol.Biochem.Behav. **25**: 651-658.

Giuditta A., Kaplan B. B., van Minnen J., Alvarez J., and Koenig E. (2002) Axonal and presynaptic protein synthesis: new insights into the biology of the neuron. Trends Neurosci. **25**: 400-404.

Giuditta A., Chun J.T., Eyman M., Cefaliello C.and Crispino M. (2008). Local gene expression in axons and nerve endings: the glia-neuron unit. Physiol. Rev. **88**: 515-555.

Grassi Zucconi G., Menichini E., Castigli E., Belia S., and Giuditta A. (1988) Circadian oscillations of DNA synthesis in rat brain. Brain.Res. **447**: 253-261.

Grassi Zucconi G., Crognale M. C., Bassetti M. A., and Giuditta A. (1990) Environmental stimuli modulate the circadian rhythm of [3H- methyl] thymidine incorporation into brain DNA of male rats. Behav.Brain Res. **41**: 103-110.

Grassi Zucconi G. and Giuditta A. (2002) Is it only neurogenesis? Rev. Neurosci. **13**: 375-382.

Ingoglia N. A., Giuditta A., Zanakis M. F., Babigian A., Tasaki I., Chakraborty G., and Sturman J. (1983) Incorporation of ^{3}H-amino acids into proteins in a partially purified fraction of axoplasm: evidence for transfer RNA mediated, post-translational protein modification in squid giant axon. J. Neurosci. **3**: 2463-2473.

Perrone Capano C., D'Onofrio G., and Giuditta A. (1982) DNA turnover in rat cerebral cortex. J. Neurochem. **38**: 52-56,.

Reinis S. (1972) Autoradiographic study of 3H-thymidine incorporation into brain DNA during learning. Physiol. Chem. Phys. **4**: 391-397.

Scaroni R., Ambrosini M. V., Principato G. B., Federici F., Ambrosi G., and Giuditta A. (1983) Synthesis of brain DNA during acquisition of an active avoidance task. Physiol. Behav. **30**: 577-582.

Rend. Acc. Sc. fis. mat. Napoli
Vol. LXXXII, (2015) pp. 107-114

Duality for borderline A_p–weights and G_q–weights on $\mathbb{R}$

Antonio Esposito[1], Teresa Radice [2], Roberta Schiattarella [3]

Presentata dal socio Carlo Sbordone
(Adunanza del 18 dicembre, 2015)

Key words: Muckenhoupt weights, Gehring classes.

Abstract - In this note we find the sharp G_q–constant, $1 \leq q < \infty$, for weights $v : [a,b] \subset \mathbb{R} \to [0,\infty[$ in the borderline G_∞–class, i.e. for $v \in L^1_{\text{loc}}$ such that

$$\operatorname{ess\,sup}_I v \leq G \fint_I v$$

for any interval $I \subset [a,b]$, in terms of $G > 1$. This result was missing in recent works concerning sharp results on reverse Hölder inequalities. Moreover, we are able to deduce the link between the Muckenhoupt class A_1 and the Gehring class G_q as in (BSW) from the relation between G_∞–class and A_p– class as in (BDS) and conversely.

Riassunto - In questa nota determiniamo la costante G_q ottimale, $1 \leq q < \infty$, per pesi $v : [a,b] \subset \mathbb{R} \to [0,\infty[$ appartenenti alla classe G_∞, i.e. per $v \in L^1_{\text{loc}}$ tale che

$$\operatorname{ess\,sup}_I v \leq G \fint_I v$$

per ogni intervallo $I \subset [a,b]$. Tale risultato non era stato ancora ottenuto nei recenti lavori che trattano dei risultati ottimali sulla disuguaglianza inversa di Hölder. Deduciamo inoltre la relazione

[1]Dipartimento di Ingegneria e Scienze dell'Informazione e Matematica Università di L'Aquila, 67100 L'Aquila, Italy.

[2]Dipartimento di Matematica e Applicazioni "R. Caccioppoli". Università degli Studi di Napoli "Federico II" Via Cintia, Complesso Universitario Monte S. Angelo 80126 Napoli, Italy.
E-mail: teresa.radice@unina.it

[3]Author to whom correspondence should be addressed
Dipartimento di Matematica e Applicazioni "R. Caccioppoli". Università degli Studi di Napoli "Federico II", Via Cintia, Complesso Universitario Monte S. Angelo 80126 Napoli, Italy.
E-mail: roberta.schiattarella@unina.it

tra la classe di Muckenhoupt A_1 e la classe di Gehring G_q come in (BSW) attraverso la relazione tra la classe G_∞ e la classe A_p come in (BDS) e viceversa.

1 - INTRODUCTION

In this note we consider borderline classes of weights $w : J_0 \subset \mathbb{R} \to [0, \infty[$ and $v : I_0 \subset \mathbb{R} \to [0, \infty[$ where I_0 and J_0 are intervals: the A_1- class of weights w verifying the condition (M)

$$A_1(w) = \sup_{J \subset J_0} \frac{\fint_J w}{\operatorname{ess\,inf}_J w} < \infty \tag{1.1}$$

and the G_∞- class of weights v verifying the condition ((F), (CN))

$$G_\infty(v) = \sup_{I \subset I_0} \frac{\operatorname{ess\,sup}_I v}{\fint_I v} < \infty \tag{1.2}$$

where the suprema are taken over all intervals $I \subset I_0$, $J \subset J_0$.
We complement some known results due to (BSW) and (BDS) which consider the self improvement of summability exponents for weights $w \in A_1$ or $v \in G_\infty$, which involve A_p-classes of Muckenhoupt or G_q-classes of Gehring.
For a weight w (a nonnegative locally integrable function) on an interval $J_0 \subset \mathbb{R}$ we define the A_p-constant of w, $p > 1$, as

$$A_p(w) = \sup_{J \subset J_0} \fint_J w \left(\fint_J w^{-\frac{1}{p-1}} \right)^{p-1} \tag{1.3}$$

where the supremum is taken over all intervals $J \subset J_0$. Similarly, for a weight v on $I_0 \subset \mathbb{R}$ we define the G_q- constant of v, $q > 1$, as

$$G_q(v) = \sup_{I \subset I_0} \left[\frac{\left(\fint_I v^q \right)^{\frac{1}{q}}}{\fint_I v} \right]^{\frac{q}{q-1}} . \tag{1.4}$$

The class A_p of weights w such that $A_p(w) < \infty$ was introduced in 1972 by Muckenhoupt (M) for a characterization of weighted L^p- maximal inequalities (see also (DS)). The author proved that, for $w \in A_p$ such that $A_p(w) \leqslant A$, there exists $\rho < p$ such that $w \in A_\rho$ with $\rho = \rho(p, A)$ and $A_\rho(w) \leqslant C(\rho, p, A)$.
The class G_q of weights v such that $G_q(v) < \infty$ was introduced in 1973 by F.W.Gehring in the study of L^q-integrability of gradient of quasiconformal mappings (see (G)). The author proved that, for $v \in G_q$ with $G_q(v) \leqslant G$, there exists $r > q$ such that $v \in G_r$ with $r = r(q, G)$ and $G_r(v) \leqslant C(q, r, G)$.
Note that, by Hölder inequality

$$\text{if } 1 \leqslant p \leqslant \rho < \infty, \text{ then } A_p \subset A_\rho \text{ and } 1 \leqslant A_\rho(w) \leqslant A_p(w) \tag{1.5}$$

and

$$\text{if } 1 \leqslant q \leqslant r < \infty, \text{ then } G_r \subset G_q \text{ and } 1 \leqslant G_q(v) \leqslant G_r(v). \tag{1.6}$$

Define also the A_∞- class of weights given by

$$A_\infty = \bigcup_{p>1} A_p, \tag{1.7}$$

and the G_1- class of weights given by

$$G_1 = \bigcup_{q>1} G_q. \tag{1.8}$$

A relation between Muckenhoupt and Gehring class was established by R. Coifman and C. Fefferman in 1974 (CF). Namely they proved that

$$A_\infty = G_1. \tag{1.9}$$

In (BSW) the following sharp self-improvement of A_1-condition was proved:

Theorem 1.1. *If $A_1(w) \leqslant A$, then for $1 < q < \frac{A}{A-1}$*

$$G_q(w) \leqslant \frac{1}{A}\left[\frac{1}{q - A(q-1)}\right]^{\frac{1}{q-1}} \tag{1.10}$$

(see for a recent approach (N1), (N2)).
In (BDS), the Authors proved the following sharp self-improvement result:

Theorem 1.2. *If $G_\infty(v) \leqslant G$, then for $p > G$*

$$A_p(v) \leqslant \frac{1}{G}\left(\frac{p-1}{p-G}\right)^{p-1}. \tag{1.11}$$

In a recent paper Dindoš and Wall (DW) gave the following complement to Theorem 1.2:

Theorem 1.3. *If $G_\infty(v) \leq G$, then*

$$A_\infty(v) \leqslant \frac{1}{G}\, e^{G-1}. \tag{1.12}$$

Our aim is to show first of all that the following complement to Theorem 1.1 holds true

Theorem 1.4. *If $A_1(w) \leq A$, then*

$$G_1(w) \leqslant \frac{1}{A} e^{A-1}. \tag{1.13}$$

Remark 1.1. It is obvious that

$$G_\infty \subset A_\infty,$$

and

$$A_1 \subset G_1.$$

The point of Theorem 1.3 and Theorem 1.4 is to quantify the A_∞-constant with respect to the G_∞-constant and the G_1-constant with respect to the A_1-constant.

Let us define for $A \geqslant 1$

$$q_1 = q_1(A) = \sup\{q > 1 : G_q(w) < \infty \text{ for } w \in A_1 \text{ such that } A_1(w) \leqslant A\} \tag{1.14}$$

and for $G \geqslant 1$

$$p_\infty = p_\infty(G) = \inf\{p : A_p(v) < \infty \text{ for } v \in G_\infty \text{ such that } G_\infty(v) \leqslant G\} \tag{1.15}$$

we have

$$q_1(A) = \frac{A}{A-1} \tag{1.16}$$

and

$$p_\infty(G) = G. \tag{1.17}$$

Notice that when $A = G$, $q_1(A)$ and $p_\infty(G)$ are Hölder conjugate.
Here we define the sharp improvement constants

$$\tilde{\gamma}_{1,q}(A) = \sup\ \{G_q(w) : w \in A_1 \text{ and } A_1(w) \leqslant A\} \tag{1.18}$$

$$\tilde{\alpha}_{\infty,p}(G) = \sup\ \{A_p(v) : v \in G_\infty(v) \text{ and } G_\infty \leqslant G\}. \tag{1.19}$$

We have the following:

Proposition 1.1. *If $\frac{1}{p} + \frac{1}{q} = 1$ then, for $A = G$, $q < q_1(A)$ and $p > p_\infty(G)$*

$$\tilde{\gamma}_{1,q}(A) = \tilde{\alpha}_{\infty,p}(G). \tag{1.20}$$

In order to explain that the optimal constants in (1.10) and (1.11) agree when p and q are conjugate, we use a recent result in (DPS) which states that for any weight $w : J_0 \to [0, \infty)$, $w \in A_\infty$, there exists a bi–Sobolev map $h : J_0 \to h(J_0)$, that is $h \in W^{1,1}_{loc}$, $h^{-1} \in W^{1,1}_{loc}$, such that

$$w(t) = (h^{-1})'(t) \quad \text{for a.e. } t \in J_0. \tag{1.21}$$

Moreover, if we set

$$v(s) = h'(s) \tag{1.22}$$

we have, for a couple of conjugate exponents $1 \leqslant q < \infty$ and $1 \leqslant p < \infty$,

$$A_p(w) = G_q(v). \tag{1.23}$$

In this paper we extend (1.23) to the case $p = 1$ and $q = \infty$. (see Proposition 2.1)

2 - PRELIMINARY RESULTS

In Section 1 we introduced A_p-constants for $1 \leqslant p < \infty$ and G_q-constants for $1 \leqslant q < \infty$. Here we introduce A_∞-constants and G_1-constants and describe their role for the characterization of A_∞ and G_1 classes.
Namely, we set (Hruscev (H)) for a weight $w \in L^1_{loc}(J_0)$

$$A_\infty(w) = \sup_I \left(\fint_I w \right) \cdot \exp\left(\int_I \log \frac{1}{w} \right) \tag{2.1}$$

and for a weight $v \in L^1_{loc}(I_0)$ (Fefferman (F1), (F2))

$$G_1(v) = \sup_I \exp\left(\fint_I \frac{v}{v_I} \log \frac{v}{v_I} \right), \tag{2.2}$$

where $v_I = \frac{1}{|I|} \int_I v$. In these papers it was established that

$$w \in A_\infty \quad \text{iff } A_\infty(w) < \infty \tag{2.3}$$

and

$$v \in G_1 \quad \text{iff } G_1(v) < \infty. \tag{2.4}$$

Moreover, respectively in (SW) and in (MS), the following formulas

$$A_\infty(w) = \lim_{p \to \infty} A_p(w) \tag{2.5}$$

and

$$G_1(v) = \lim_{q \to 1^+} G_q(v) \tag{2.6}$$

were proved.

Proposition 2.1. *Let I, J be intervals of $\mathbb{R}$ and $h : I \to J$ be a bi–Sobolev map. Then, $(h^{-1})' \in G_\infty$ if and only if $h' \in A_1$ and*

$$G_\infty\left((h^{-1})'\right) = A_1\left((h)'\right). \tag{2.7}$$

Proof of Proposition 2.1. If $h' \in A_1$, then for any interval $I_0 = [a, b] \subset I$, we have

$$\fint_a^b h'(x)\, dx \leq A_1(h') \operatorname*{ess\,inf}_{[a,b]} h'(x).$$

Let $h(I_0) = J_0 = [c, d]$. By the change of variables $t = h(x)$, we have

$$\begin{aligned} \frac{d-c}{h^{-1}(d) - h^{-1}(c)} = \frac{h(b) - h(a)}{b - a} &\leq A_1(h') \operatorname*{ess\,inf}_{[a,b]} h'(x) \\ &\leq A_1(h') \frac{1}{(h^{-1}(t))'}. \end{aligned} \tag{2.8}$$

Hence,

$$(h^{-1}(t))' \leq A_1(h') \frac{h^{-1}(d) - h^{-1}(c)}{d - c} = A_1(h') \fint_c^d (h^{-1}(t))' \, dt.$$

Consequently,

$$\operatorname*{ess\,sup}_{J_0} (h^{-1}(t))' \leq A_1(h') \fint_c^d (h^{-1}(t))' \, dt$$

and this gives

$$G_\infty((h^{-1})') \leq A_1(h').$$

Analogously, we deduce

$$A_1(h') \leq G_\infty((h^{-1})').$$

□

3 - SHARP CONSTANTS

In this Section we show some applications of duality formula $G_\infty\left((h^{-1})'\right) = A_1\left((h)'\right)$. In particular we are interested in a–priori bounds for sets of weights of the form $\{G_q(w) : w \in A_1 \text{ and } A_1(w) \leqslant A\}$ and $\{A_p(v) : v \in G_\infty(v) \text{ and } G_\infty \leqslant G\}$. In Proposition 1.1 we are able to show that the sharp improvement constants (1.18) and (1.19) coincide.

Proof. By definition $\tilde{\gamma}_{1,q}(A) \geqslant G_q(w)$ $\forall w \in A_1$ and $A_1(w) \leqslant A$. Now consider the constant $A_p(v)$ with $p > G = A$ and v such that $G_\infty(v) \leqslant A$. It is known that there exists an increasing bi-Sobolev map (see (DPS)), $h : \mathbb{R} \to \mathbb{R}$ such that

$$v = (h^{-1})' \quad \text{and} \quad w = h'.$$

By Lemma 2.5 in (JN) for $\frac{1}{p} + \frac{1}{q} = 1$

$$A_p(v) = G_q(w).$$

Hence:

$$\tilde{\gamma}_{1,q}(A) \geqslant A_p(v) \tag{3.1}$$

and taking the supremum we obtain

$$\tilde{\gamma}_{1,q}(A) \geqslant \tilde{\alpha}_{\infty,p}(G). \tag{3.2}$$

Similarly, it is possible to prove the reverse inequality to (3.2). □

In (V), the author find the sharp A_p–constant for weights in the A_1–class.

Theorem 3.1. *For any weight w such that $A_1(w) \leq A$ then, for any $p > 1$*

$$A_p(w) \leq A \left(\frac{A(p-1)}{pA - 1} \right)^{p-1}. \tag{3.3}$$

Here we are able to find the sharp G_q– constant for a weight $v \in G_\infty$.

Theorem 3.2. *For any weight v such that $G_\infty(v) \leq G$ then, for any $q > 1$*

$$G_q(v) \leq G\left(\frac{G}{qG - q + 1}\right)^{\frac{1}{q-1}}. \tag{3.4}$$

Proof. Let $v \in G_\infty$. By Theorem 1.5 in (DPS) we know that there exists a bi–Sobolev map h such that

$$v = h', \quad w = (h^{-1})' \tag{3.5}$$

and

$$A_p(w) = G_q(v) \tag{3.6}$$

when $\frac{1}{p} + \frac{1}{q} = 1$.

By Proposition 2.1 we know also that

$$A_1(w) = G_\infty(v) \leq G.$$

By (3.6) and by Theorem 3.1 with $A = G$ and $p = \frac{q}{q-1}$, we obtain

$$G_q(v) \leq G\left(\frac{G}{qG - q + 1}\right)^{\frac{1}{q-1}}.$$

□

Now we present the sharp A_∞– constant for weights in the borderline class A_1 and the sharp G_1– constant for weights in the borderline class G_∞.

Theorem 3.3. *Let $A_1(w) \leq A$ then,*

$$A_\infty(w) \leq Ae^{\frac{1-A}{A}}. \tag{3.7}$$

Let $G_\infty(v) \leq G$ then,

$$G_1(v) \leq Ge^{\frac{1-G}{G}}. \tag{3.8}$$

Proof. By Theorem 3.1 we know that if $A_1(w) \leq A$ then,

$$A_p(w) \leq A\left(\frac{A(p-1)}{pA - 1}\right)^{p-1}. \tag{3.9}$$

By (SW), we know that

$$A_\infty(w) = \lim_{p\to\infty} A_p(w).$$

Passing to the limit when p goes to infinity on the right hand side in (3.9), we obtain

$$A_\infty(w) \leq Ae^{\frac{1-A}{A}}.$$

Analogously we obtain (3.8), using (3.4) and that (see (MS))

$$G_1(v) = \lim_{q\to 1^+} G_q(v).$$

□

Acknowledgement: The authors have been supported by the Gruppo Nazionale per l'Analisi Matematica, la Probabilità e le loro Applicazioni (GNAMPA) of the Istituto Nazionale di Alta Matematica (INdAM).

References

[BDS] Basile L. , D'Apuzzo L. , Squillante M. , (2001) *The limit class of Gehring type G_∞ in the n-dimensional case.* Rend. Mat. Appl. (7) 21, no.1-4, 207–221.

[BSW] Bojarski B. , Sbordone C., Wik L., (1992) *The Muckenhoupt class $A_1(\mathbb{R})$,* Studia Math. 101, no.2, 155–163.

[CF] Coifman R. R. , Fefferman C., (1974) *Weighted norm inequalities for maximal functions and singular integrals*, Studia Math. 51, 241–250.

[CN] Cruz-Uribe D. , Neugebauer C. J., (1995) *The structure of the reverse Holder classes,* trans. Amer. Mat. Soc. 347, no-8, 2941–2960.

[DW] Dindoš M., Wall M., (2009) *The sharp A_p constant for weights in a reverse Hölder class*, Rev. Mat. Iberoam. 25, no. 2, 559–594.

[DPS] D'Onofrio L., Popoli A. , Schiattarella R., *Duality for A_∞– weights on the real line*, to appear.

[DS] D'Onofrio L. , Schiattarella R. , (2013), *The exact dependence on $A_2(w)$ for the $L^p(\mathbb{R}, w)$ maximal inequalities*, J. Math. Anal. Appl. 400, no. 2, 396– 405.

[F] Franchi B., (1991), *Weighted Sobolev-Poincaré inequalities and pointwise estimates for a class of degenerate elliptic equations*, Trans. Amer. Math. Soc. 327, no. 1, 125–158.

[F1] Fefferman R., (1989), *A criterion for the absolute continuity of the harmonic measure associated with an elliptic operator,* J. Amer. Math. Soc. 2, 127–135.

[F2] Fefferman R., (1993), *Large perturbations of elliptic operators and the solvability of the L^p Dirichlet problem,* J. Funct. Anal. 118, no.2, 477–510.

[G] Gehring F. W. ,(1973), *The L^p-integrability of the partial derivatives of a quasiconformal mapping*, Acta Math. 130, 265–277.

[H] Hruscev S. V., (1984)*A description of weights satisfying the A_∞ condition of Muckenhoupt,* Proc. Amer. Math. Soc. 90, 253–257.

[JN] Johnson R., Neugebauer C. J., (1987) *Homeomorphisms preserving A_p*, Rev. Mat. Iberoamericana 3, no. 2, 249-273.

[M] Muckenhoupt B., (1972) *Weighted norm inequalities for the Hardy maximal function,* Trans. Amer. Math. Soc,, 165, 207–226.

[MS] Moscariello G., Sbordone C., (1995) *A_∞ as limit case of reverse Hölder inequalities when the exponent tends to 1,* Ricerche Mat. 44, no.1, 131-144.

[N1] Nikolidakis E. N., (2004) *A sharp integral Hardy type inequality and applications to Muckenhoupt weights on* $\mathbb{R}$ Ann. Acad. Sci. Fenn. Math. 39, no.2, 887–896.

[N2] Nikolidakis E. N. , *A_1 weights on $\mathbb{R}$, an alternative approach* to appear.

[SW] Sbordone C., Wik L., (1994) *Maximal functions and related weight classes,* Publ. Mat. 38, no.1 . 127–155.

[V] Vasyunin V. , (2004) *The exact constant in the inverse Hölder inequality for Muckenhoupt weights*, (Russian) Algebra i Analiz 15 (2003), no. 1, 73–117; translation in St. Petersburg Math. J. 15, no. 1, 49-79.

Rend. Acc. Sc. fis. mat. Napoli
Vol. LXXXII, (2015) pp. 115-126

L'imaging a raggi X nella diagnosi del tumore alla mammella: dalle tecniche bidimensionali a quelle 3D

Nota di Giovanni Mettivier[1], Antonio Sarno[1], Francesca Di Lillo[1], Paolo Russo[1]

Presentata dal socio Leonardo Merola
(Adunanza del 18 dicembre 2015)

Keywords: Breast cancer, X-ray, Mammography, Tomosynthesis, Computed Tomography

Abstact – Breast cancer is the first cause of death from cancer in females, and the technique of X-ray mammography is the gold standard for its detection in asymptomatic patients. Mammography is a 2D imaging technique which permits the diagnosis of breast tumor in up to 90% of the cancers, but its performance can be much less than this in so-called dense breasts, also due to the superposition of normal glandular tissue and tumor tissue. 3D imaging techniques may overcome this limitation; in the last years, digital breast tomosyntesis has been introduced in the clinical routine in conjunction with mammography, for a more efficient diagnosis of breast cancer. Breast tomosynthesis produces a sequence of virtual slices of the compressed breast anatomy as attenuation maps of about 1-mm thickness, and it may permit a better detection and localization of massive lesions in the compressed breast. Recently, the Food and Drug Administration in USA has approved for clinical use a scanner for X-ray Computed Tomography dedicated to the breast, which produces high-contrast 3D images of the breast anatomy with an isotropic resolution of about 0.3 mm. The transition from 2D to 3D techniques for X-ray imaging of the breast represents a significant advancement in the field of breast cancer diagnosis, due to research in medical physics. Moreover, at variance with the above attenuation-based X-ray imaging techniques, new techniques are under development for 2D and 3D breast imaging which exploit the refraction and the phase shift of the X-ray electromagnetic wave traversing the breast tissues: these methods have potential of producing higher contrast images at dose levels comparable to that of two-view mammography conventionally adopted for breast cancer screening, as described in this Note.

Riassunto – Il cancro alla mammella è la prima causa di morte da cancro nella donna, e la tecnica di riferimento per la diagnosi di tali tumori nelle pazienti asintomatiche è la mammografia a raggi X. Tale tecnica di imaging bidimensionale (2D), tuttavia, permette di diagnosticare al più il 90% dei tumori alla mammella, con risultati anche peggiori nelle mammelle dense molto radio-opache, anche a causa della sovrapposizione tra tessuto ghiandolare normale e massa tumorale. Negli ultimi anni è

[1] Dipartimento di Fisica "Ettore Pancini", Università degli Studi di Napoli "Federico II", Napoli.

stata introdotta nella routine clinica una tecnica di imaging tridimensionale (3D) a raggi X, la tomosintesi digitale, da effettuare in concomitanza con la mammografia, che fornisce immagini di attenuazione di fettine virtuali di tessuto mammario dello spessore di circa 1 mm per una migliore individuazione e localizzazione della lesione. In fase di sperimentazione, e recentemente approvata per l'uso clinico in USA, è la tecnica della tomografia computerizzata a raggi X dedicata alla mammella, che permette di ottenere un'immagine 3D dell'intera anatomia dei tessuti mammari, con una risoluzione spaziale di circa 0.3 mm ed elevato contrasto radiologico. Il passaggio da tecniche 2D a tecniche 3D di imaging della mammella basate sull'attenuazione dei raggi X nei tessuti, rappresenta un notevole passo avanti, permesso dalla ricerca in fisica medica, per la diagnosi del cancro alla mammella. Ancora in fase di studio, poi, sono le tecniche di imaging che sfruttano la rifrazione e lo sfasamento della radiazione X nell'attraversamento dei tessuti, che permetteranno un miglior contrasto radiografico a dosi comparabili a quelle delle due viste mammografiche per ciascuna mammella, comunemente utilizzate nella mammografia di screening, come descritto in questa Nota.

1. INTRODUZIONE

Il cancro alla mammella è la seconda tipologia di cancro più frequentemente diagnosticata nel mondo ed è la prima causa di morte causata da cancro nelle donne; nel 2012, per il cancro alla mammella, sono stati riportati 1.67 milioni di nuovi casi (233.000 in USA e 367.000 in EU) e 522.000 morti (44.000 in USA e 92.000 in UE nel mondo) (Global Cancer Facts sheet, 2015). Il cancro alla mammella ha origine principalmente nei dotti lattiferi (la rete che permette il flusso del latte dalla mammella al capezzolo) o nei lobuli (le ghiandole mammarie che rappresentano la parte terminale del sistema dei dotti, attraverso il quale fluisce il latte). Più raramente, ha inizio in altri siti. La caratterizzazione patologica delle lesioni mammarie si basa sull'architettura, le caratteristiche citologiche ed il tipo di cellula (Siegel *et al*, 2015). Per il 2015, l'American Cancer Society stima circa 231.840 nuovi casi di cancro mammario invasivo e circa 40.290 morti per cancro alla mammella nelle donne statunitensi (Siegel *et al*, 2015). Il cancro alla mammella è una patologia multifattoriale; ci sono molti fattori di rischio conosciuti, ed altri non conosciuti: la rivelazione precoce è un fattore chiave nel trattamento e nella sconfitta della malattia. Dagli anni '80, quando è stato introdotto lo screening periodico alla mammella in molti Paesi di tutto il mondo, l'incidenza di morte dovuta al tumore al seno è diminuita. L'American Cancer Society ha stimato che, per quanto riguarda le donne statunitensi, il cancro al seno provocava la morte di una donna su 3.333 nel 1980 e che questo valore è sceso fino a 1 su 5.000 nel 2011 (fig. 1) (Siegel *et al*, 2015).

La tecnica "gold standard" per lo screening e la diagnosi al seno è rappresentata dall'esame mammografico a raggi X. Le linee guida del Ministero della Salute italiano (reperibili sul sito http://www.salute.gov.it/portale/salute) suggeriscono che *"Lo screening per la diagnosi precoce del tumore mammario si rivolge alle donne di età compresa tra i 50 e i 69 anni e si esegue con una mammografia ogni 2 anni"*. Inoltre alcune regioni italiane stanno valutando l'estensione di questo intervallo di età. A tale tecnica "convenzionale", che produce immagini bidimensionali (2D) del seno, si stanno affiancando da diversi anni altre due nuove tecniche radiologiche per l'analisi della mammella che producono immagini tridimensionali (3D): la tomosintesi digitale al seno (*digital breast tomosynthesis*, DBT) e la tomografia computerizzata dedicata al seno (*breast CT* o BCT). Queste due tecniche, presentate nei successivi paragrafi 3 e 4, sono

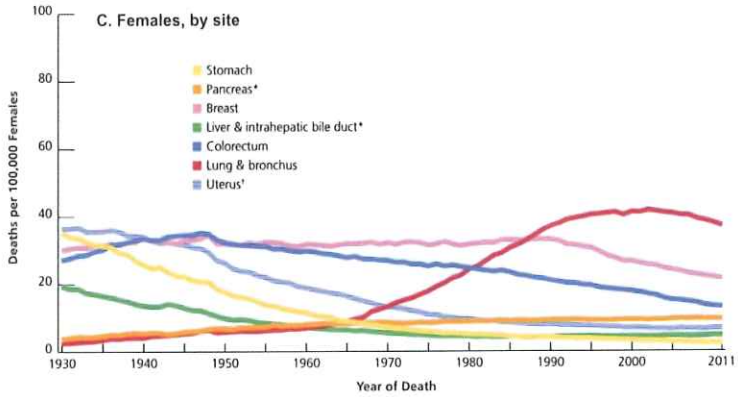

Figura 1: Mortalità correlata ad i più diffusi tipi di cancro nelle donne statunitensi dal 1930 al 2011 (Siegel *et al*, 2015).

state approvate dalla Food and Drug Administration (FDA), l'agenzia federale statunitense che si occupa di normativa e supervisione nel campo della salute umana, rispettivamente nel 2011 e nel 2015 per l'utilizzo in esami al seno di secondo livello (solo dopo aver eseguito preventivamente un esame mammografico) nel caso in cui sia necessaria una ulteriore indagine.

2 LA MAMMOGRAFIA

L'esame mammografico è un esame radiografico alla mammella. Durante l'esame di screening, effettuato sulla paziente asintomatica, esso consta di due radiografie per ogni mammella, una nella direzione cranio-caudale (vista CC) ed una seconda, ruotando il rivelatore e la sorgente di raggi X di 45°, obliqua medio-laterale (vista MLO) (fig. 2). In entrambi i casi il seno viene fortemente compresso nella direzione di irraggiamento per diminuire lo spessore che i raggi X devono attraversare per raggiungere il rivelatore, sia per "spalmare" il tessuto mammario su una area più ampia e quindi ridurne eventuali sovrapposizioni, che per aumentare il contrasto radiografico delle eventuali lesioni mammarie. La compressione del seno è effettuata con una forza di circa 100 N, che può variare in base alle caratteristiche del seno stesso o della tecnica utilizzata.

La sensibilità dell'esame mammografico (la percentuale di casi positivi che hanno una interpretazione iniziale positiva) risulta dell'84.9% e la specificità (la percentuale di soggetti sani che vengono identificati come tali) è del 90.8%; la prestazione della tecnica peggiora nell'esame delle mammografie di donne giovani (NCI-funded Breast Cancer Surveillance Consortium, 2015). Vale la pena notare che nella valutazione della sensibilità è considerato canceroso un tessuto che viene diagnosticato come carcinoma duttale *in situ* o cancro invasivo, nell'anno successivo alla prima diagnosi o comunque entro il successivo esame mammografico; se venissero considerate tutte le lesioni cancerose presenti e non diagnosticate, il valore di tale parametro potrebbe essere drasticamente ridotto. Allo stesso modo, nella valutazione della specificità sono considerati casi negativi quelle lesioni che entro un anno dall'esame diagnostico non vengono diagnosticate come tali[7]: anche in questo caso un arco di tempo maggiore potrebbe portare a stime differenti del parametro. Oltretutto, i valori di specificità e sensibilità citati denotano una prestazione non ideale dell'esame mammografico.

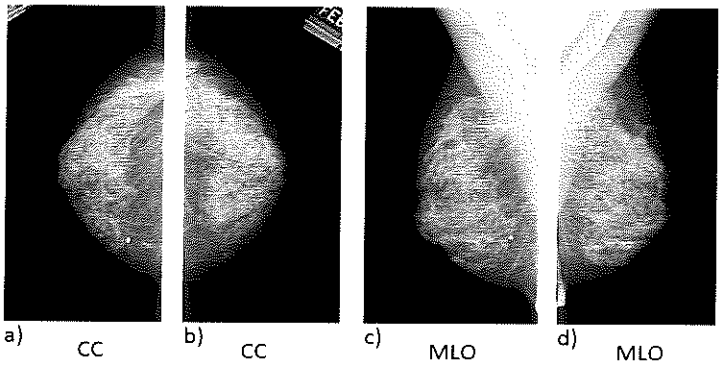

Figura 2: Mammogrammi del seno sinistro (a,c) e del seno destro (b,d) nelle viste CC (a,b) e MLO (c,d).
(dal sito: http://marathon.csee.usf.edu/Mammography/Database.html)

Una delle cause di errata diagnosi in mammografia è rappresentata dalla sovrapposizione dei tessuti. La procedura di esame mammografico prevede due (o più) immagini 2D di un volume 3D (la mammella) e quindi le strutture tissutali ghiandolari possono sovrapporsi alle lesioni tumorali e nasconderle, pur in presenza di compressione dell'organo. Tale fenomeno è accentuato dal fatto che tessuto ghiandolare e lesioni tumorali hanno coefficienti di attenuazione simili nell'intervallo energetico dei raggi X utilizzati (circa 15–32 keV), e sono facilmente confondibili, in particolar modo quando le masse tumorali sono di piccole dimensioni od agli stadi iniziali di sviluppo (diversi mm). Tecniche tridimensionali di imaging come la DBT e la BCT discusse in seguito si propongono di superare tali limitazioni.

Un ruolo importante nell'esame mammografico gioca la dose di radiazione rilasciata nel seno: da una parte, una dose maggiore permette una migliore qualità dell'immagine e dall'altra, la risultante energia impartita al tessuto ghiandolare mammario, molto radiosensibile, può essere causa di tumore indotto da radiazione, nel seguito della vita successiva della paziente. Essendo il tessuto ghiandolare la parte radiosensibile del seno, la grandezza dosimetrica riportata negli esami mammografici è la dose rilasciata in media in tale tessuto (dose ghiandolare media o MGD, misurata in mGy, dove 1 Gy = 1 J/kg). Le linee guida europee per la mammografia digitale fissano a 2.5 mGy la MGD massima ammissibile per l'esame di una mammella di dimensioni e caratteristiche "standard", per ciascuna vista, mentre indicano un valore di 2 mGy come valore di MGD ragionevolmente ottenibile in una singola mammografia, per tale mammella standard.

3. TOMOSINTESI DIGITALE DELLA MAMMELLA (DIGITAL BREAST TOMOSYNTHESYS, DBT)

Nonostante la convenzionale tecnica mammografica sia considerata il "gold standard" per la diagnosi del tumore al seno, la sua natura di tecnica bidimensionale può rappresentare un limite per la diagnosi. Questo è vero soprattutto nel caso di mammelle con un'alta frazione di tessuto fibroghiandolare (mammelle cosiddette dense), a causa della sovrapposizione dei tessuti che può oscurare eventuali strutture patologiche. Per superare questo limite, è necessario recuperare l'informazione sulla terza dimensione (ossia la

profondità delle strutture anatomiche nella mammella compressa). A questo scopo, negli ultimi anni, la mammografia convenzionale è stata affiancata nella pratica clinica da una nuova tecnica diagnostica tridimensionale denominata Tomosintesi digitale della mammella (Digital Breast Tomosynthesis, DBT) (Reiser *et al*, 2014). I diversi studi condotti principalmente negli USA, ma che hanno interessato negli ultimi anni anche l'Europa, hanno mostrato risultati incoraggianti sulla combinazione mammografia/tomosintesi riscontrando una maggiore efficacia nel diagnosticare lesioni al seno.

La tomosintesi mammaria è una tecnica diagnostica a raggi X di ultima generazione che permette di ricostruire immagini quasi tridimensionali del seno a partire dall'acquisizione di un numero finito di proiezioni bidimensionali dell'organo, ottenute con differenti angolazioni del tubo radiogeno rispetto alla mammella compressa (fig. 3). Con riferimento alla nota tecnica di tomografia computerizzata a raggi X (*Computed Tomography*, CT) per il corpo intero, nel quale l'apparato di acquisizione radiografica ruota a 360° attorno al corpo del paziente, concettualmente la DBT può essere considerata come una CT ad angolo limitato; essa offre la possibilità di visualizzare separatamente strutture posizionate a diverse profondità nella mammella, con una potenziale riduzione od eliminazione dell'effetto di sovrapposizione dei tessuti presente nelle mammografie. Il principio radio-geometrico della DBT è simile a quello utilizzato nella tecnica stratigrafica introdotta dal radiologo italiano Vallebona nel 1931, in cui la sorgente e la lastra radiografica compiono un movimento rotatorio intorno ad un punto fisso, detto fulcro, che determina lo strato di mammella "messo a fuoco". Mentre la stratigrafia richiede di acquisire per ogni strato una diversa sequenza di proiezioni bidimensionali, la DBT permette di ricostruire un numero arbitrario di piani utilizzando un'unica sequenza.

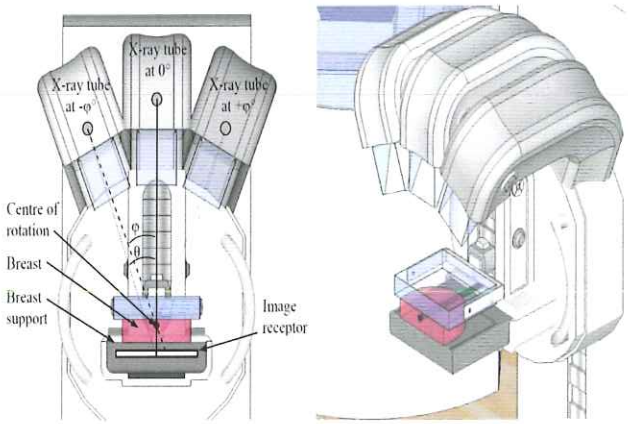

Figura 3: Geometria utilizzata per un sistema di tomosintesi digitale mammaria (DBT). Sono mostrate tre differenti posizioni del tubo radiogeno, dell'angolo di rotazione φ e dell'angolo di proiezione θ. (Immagine da: "Protocol for the Quality Control of the Physical and Technical Aspects of Digital Breast Tomosynthesis Systems", disponibile all'indirizzo web http://www.euref.org/european-guidelines/physico-technical-protocol#breasttomo).

Il sistema utilizzato per effettuare l'esame DBT è sostanzialmente un sistema mammografico modificato per consentire alla sorgente radiogena di ruotare attorno ad un asse orizzontale passante per il piano centrale della mammella compressa. La fig. 3 mostra la tipica geometria utilizzata: mentre la

mammella, posta su di un supporto contenente un rivelatore per mammografia digitale, viene immobilizzata e compressa con un piatto compressore come in mammografia, il tubo a raggi X viene ruotato in un limitato campo angolare (di estensione totale variabile da 15° a 50° a seconda del produttore) per un tempo totale di scansione tipicamente compreso tra i 4 e i 25 s. Esposizioni a bassa dose vengono eseguite a fissati intervalli angolari per acquisire le immagini digitali, chiamate viste, utilizzate poi per la ricostruzione tridimensionale, effettuata mediante elaborazione digitale. La rotazione della sorgente radiogena può avvenire con continuità, con fascio di raggi X continuo o pulsato, o in maniera discreta, a piccoli passi; quest'ultima modalità evita l'effetto di degrado nell'immagine di proiezione prodotto dal movimento della macchia focale del tubo radiogeno durante una singola esposizione, ma richiede tempi più lunghi per l'esame. Durante le acquisizioni il rivelatore può essere fisso o ruotare all'interno del supporto per mantenere la sua superficie di rivelazione sempre perpendicolare all'asse centrale del fascio di raggi X. I sistemi commerciali impiegano generalmente rivelatori radiografici di tipo *flat panel* (dimensioni circa 24 cm × 30 cm, dimensioni dei pixel tra i 70 μm e i 100 μm) a rivelazione diretta (rivelatore a Selenio amorfo) oppure indiretta (rivelatore a matrice di fotodiodi accoppiata ad uno strato di scintillatore che converte la radiazione X in radiazione visibile, rivelata dai fotodiodi), ma sono in corso ricerche da parte di vari gruppi internazionali per testare l'utilizzo dei rivelatori a conteggio di singolo fotone a rivelazione diretta, che presentano prestazioni eccellenti nelle applicazioni con basso rateo di flusso di radiazione, come in DBT. La scelta delle dimensioni del campo angolare e del numero di viste risulta essere cruciale per ottimizzare la qualità dell'immagine di tomosintesi e la dose di radiazione all'organo; tale scelta dipende sia dalle caratteristiche fisiche delle componenti del sistema sia dall'algoritmo di ricostruzione utilizzato, generalmente di tipo retroproiezione filtrata (FBP) o di tipo iterativo. L'algoritmo FBP, normalmente adoperato nella CT al corpo intero, risulta più semplice da utilizzare e richiede tempi di ricostruzione brevi, ma produce artefatti dovuti al limitato campo angolare che non permette un completo campionamento del volume dell'organo; tuttavia, l'utilizzo di nuovi tipi di filtraggio ha permesso di ottimizzarne l'utilizzo nel campo della tomosintesi[9].

4. LA TOMOGRAFIA COMPUTERIZZA DEDICATA ALLA MAMMELLA[10]

Il primo prototipo di Tomografia Computerizzata a raggi X dedicato alla mammella fu presentato nel 1975, al LXXVI Annual Meeting dell'American Roentgen Ray Society. Questo prototipo della General Electric denominato CT/M era composto da un tubo a raggi X (GE Maxiray 75) e da un rivelatore contenente gas Xenon. La paziente era posta in una posizione prona su un tavolo in cui era presente un foro in cui poter inserire il seno. Per l'esame, la tensione e la corrente del tubo erano impostati a 120 kVp e 20mA. La scansione su 360 gradi era effettuata in 10 s. L'immagine finale era una matrice di 127×127 voxels. Ogni voxel aveva una dimensione di 1.56×1.56×1.00 cm^3 e ogni fetta tomografica aveva uno spessore di 1 cm. Ogni seno era ispezionato singolarmente e durante l'esame era mantenuto in un contenitore in cui veniva fatta scorrere continuamente dell'acqua calda. La dose media per produrre un'immagine di 6 fette di 10 mm di spessore era di 1.75 mGy. Gli studi con tale scanner avevano mostrato che il CT/M era capace di rivelare lesioni maligne, se veniva utilizzato con un agente di contrasto iniettato per via endovenosa. In molti studi condotti senza l'uso di un agente di contrasto, le lesioni benigne sembravano essere maligne, e la risoluzione spaziale del CT/M era peggiore della risoluzione spaziale della mammografia basata su film. Inoltre, la dose

necessaria per fare un singolo esame era maggiore di quella della singola mammografia. A causa di questi problemi, la ricerca sui sistemi CT per l'imaging del tumore al seno fu abbandonata.

Nel 2001, in un articolo pioneristico, il Prof. J. Boone all'Università della California a Davis (UC Davis) (Boone *et al*, 2001) presentò uno studio di fattibilità per un sistema CT al seno con sistemi dedicati (*breast* CT, o BCT). Grazie agli avanzamenti tecnologici (lo sviluppo dei rivelatori *flat panel* per radiografia digitale introdotti nel 1999) e l'uso della geometria di irraggiamento con fascio di raggi X a cono (*cone beam geometry*) invece della geometria a ventaglio (*fan beam geometry*) comunemente adottata negli scanner CT al corpo intero, Boone propose (e poi sviluppò) una tecnologia capace di produrre immagini CT dell'intera mammella non compressa usando dosi di radiazione dell'ordine della MGD fornita alla stessa mammella compressa nel caso di in una mammografia a doppia vista (CC + MLO).

Il valore di MGD per una singola vista in mammografia è diminuito negli anni, con valori della MGD che attualmente sono, in media, tra 1.4 e 2.0 mGy, per tutti gli spessori delle mammelle compresse. Per un esame mammografico in doppia vista, per una mammella "standard" si stima un valore di MGD di circa 3–4 mGy. Nello studio di Boone del 2001, per una BCT eseguita con una tensione del tubo radiogeno di 80 kV per una mammella compressa di 5 cm, è stato previsto un valore di circa 4.5 mGy per la MGD.

Il prototipo e lo schema geometrico proposto da Boone (fig. 4) hanno ispirato differenti gruppi di ricerca (incluso quello degli autori) nello sviluppare altri sistemi BCT dedicati all'imaging della mammella (Sarno *et al*, 2015). Una linea di ricerca parallela è stata condotta, indipendentemente, da un gruppo di ricerca dalla University of Rochester in USA. Entrambi i gruppi (UC Davis e U Rochester) hanno già iniziato *trials* clinici nei loro rispettivi centri medici universitari (dal 2004 a UC Davis, e dal 2006 a U Rochester). Studi addizionali in questo campo stanno arrivando anche dalla Duke University (Duke U), dove M. P. Tornai ed il suo gruppo di ricerca hanno iniziato studi clinici con uno scanner prototipo da loro assemblato. Studi per valutare le prestazioni della tecnica BCT attraverso scanner BCT dedicati sono stati condotti all'Università del Texas M.D. Anderson Cancer Center (C. Shaw) e dalla University of Massachusetts, Worcester (A. Karellas, S. J. Glick). In Germania, nel 2008–2010, il gruppo del prof. W. A. Kalender alla Friedrich-Alexander University Erlangen-Nürnberg, ha condotto un progetto europeo dedicato alla valutazione della BCT ed ha recentemente presentato (in collaborazione con una Ditta *spinoff* dell'Università di Erlangen) uno scanner BCT con scansione a spirale, impiegante un rivelatore a conteggio di singolo fotone.

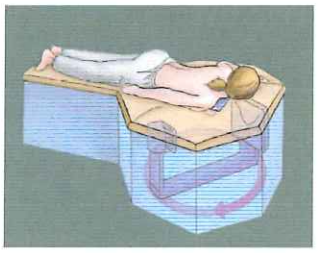

Figura 4: Schema del prototipo di CT dedicato al seno sviluppato dal gruppo del Prof. J. Boone presso l'Università della California a Davis. Il gruppo (tubo a raggi X - rivelatore per radiografia digitale) ruota a 360 gradi attorno alla mammella della paziente, pendente liberamente da un foro nel lettino.

In Italia, dal 2007, il gruppo degli autori presso il Laboratorio di Fisica Medica del Dipartimento di Fisica "Ettore Pancini" dell'Università di Napoli Federico II sta sviluppando prototipi di laboratorio di *cone beam* micro-CT dedicati alla mammella. Presso l'Università di Trieste ed al laboratorio di luce di sincrotrone ELETTRA (Trieste), è in fase di sviluppo una tecnica BCT a contrasto di fase con un fascio monocromatico di luce di sincrotrone ed un rivelatore a conteggio di singolo fotone ad alta risoluzione spaziale, nell'ambito del progetto di ricerca SYRMA-CT dell'Istituto Nazionale di Fisica Nucleare (INFN). All'Università della California a Irvine, il gruppo di S. Molloi ha investigato la BCT spettrale per l'imaging della mammella ad alta risoluzione usando rivelatori a conteggio di singolo fotone basati su substrati a semiconduttore Si oppure CdZnTe.

I codici di calcolo per la ricostruzione delle immagini tipicamente utilizzati in BCT impiegano l'algoritmo Feldkamp-Davis-Kress (FDK) per la ricostruzione 3D partendo dalle proiezioni acquisite in geometria con fascio a cono, come una approssimazione 3D dell'algoritmo 2D di *filtered backprojection* (FBP) utilizzato nell'imaging convenzionale CT al corpo intero con geometria *fan beam*. Differentemente dalla DBT, l'immagine digitale finale in BCT è rappresentata da una matrice immagine 3D con voxel cubici, che fornisce una risoluzione spaziale isotropica nell'intero volume della mammella non compressa.

La ben nota eccellente risoluzione di contrasto radiografico della CT a raggi X rispetto all'imaging planare con raggi X per tessuti soffici, è un *plus* addizionale di un esame BCT: infatti, una migliore qualità dell'immagine può produrre una migliore diagnosi. Vantaggi addizionali della BCT includono il suo possibile utilizzo con agente di contrasto allo iodio, o in combinazione con la Positron Emission Tomography (PET) o la Single Photon Emission Computed Tomography (SPECT) per imaging ibrido, nonchè la radioterapia a raggi X rotazionale al kilovoltaggio e/o con un sistema robotico per la biopsia ad ago aspirato con imaging stereotassico a raggi X. Di seguito viene descritto lo scanner che si sta sviluppando nel Laboratorio di Fisica Medica dell'Università di Napoli "Federico II".

5. PROTOTIPO DI CT DEDICATO ALLA MAMMELLA PRESSO L'UNIVERSITA' DI NAPOLI FEDERICO II

I tre prototipi da laboratorio per BCT ad alta risoluzione sviluppati presso il laboratorio di Fisica Medica del Dipartimento di Fisica "Ettore Pancini" dell'Università degli Studi di Napoli "Federico II" (fig. 5) includono una sorgente X a microfuoco, un rivelatore *flat panel* CMOS con pixel da 50 μm di lato, e motori passo-passo per il movimento verticale, orizzontale e per la rotazione del rivelatore e del *gantry*, con la possibilità di ottenere un ingrandimento ed una geometria di acquisizione variabili.

Nei primi due prototipi realizzati, a partire dal 2006, il tubo raggi X aveva una macchia focale di 40 μm, mentre il terzo prototipo comprende un tubo a raggi X a microfuoco con una macchia focale variabile da 50 μm, a 20 μm oppure 5 μm. Con il secondo sistema è stata ottenuta una risoluzione spaziale di 3 mm^{-1} nella direzione radiale. Questo secondo prototipo comprende, inoltre, una gamma camera compatta, con piccolo campo di vista per investigare l'imaging ibrido SPECT/CT, dove l'imaging medico-nucleare SPECT (*Single Photon Emission Computed Tomography*) fornisce informazioni fisiologiche di captazione del tracciante radioattivo da parte di lesioni mammarie, complementari alle informazioni anatomiche fornite dalla CT. L'uso di una sorgente X di alta coerenza spaziale (conseguenza delle limitate dimensioni

della macchia focale) e di un rivelatore *flat panel* ad alta risoluzione spaziale, permette la visibilità di effetti di contrasto di fase anche con una distanza sorgente-immagine di solo 1 m (vedi par. 4 di seguito). Questo scanner micro-CT da laboratorio ha prodotto immagini BCT a contrasto di fase in fantocci 3D di mammella. Le piccole dimensioni della macchia focale pongono, però, severi limiti alla corrente massima del tubo a raggi X: questo implicherebbe, in un tipico esame clinico, un lungo tempo di scansione (1–2 min) per visualizzare una intera mammella non compressa, con la conseguente possibilità di artefatti da movimento. A causa di ciò, il gruppo dell'Università di Napoli ha sviluppato dei supporti per la mammella, di quattro dimensioni standard, fissati al di sotto del lettino in modo da fissare la posizione della mammella durante lunghe acquisizioni e ridurre gli artefatti da movimento. La loro forma è stata disegnata sulla base delle forme anatomiche ricavate dalla scansione di pazienti con la BCT, ottenute dal gruppo del Prof. Boone che nel settembre 2009 ha inaugurato il prototipo dell'equipe napoletana durante una visita al Dipartimento di Fisica della Federico II. Questi supporti permettono anche un'autocentratura della mammella rispetto all'asse di rotazione dello scanner, e offrono una protezione meccanica per la mammella durante la rotazione del *gantry*. Una volta fissati sotto il letto del paziente, forniscono anche un volume di riferimento per il riposizionamento della mammella e per l'inclusione di bracci robotici per biopsia con ago aspirato, avendo previsto delle aperture mobili nel supporto. Il sostegno per la mammella è presente anche durante le acquisizioni SPECT.

Figura 5: La seconda a) e terza versione b) del prototipo di microCT dedicato al seno sviluppato dal gruppo di Fisica Medica presso il Dipartimento di Fisica "Ettore Pancini" dell'Università di Napoli Federico II. 1) Tubo a raggi X a microfuoco 2) Rivelatore radiografico digitale del tipo CMOS *flat panel*; 3) sistema di rotazione dell'apparato attorno ad un asse verticale; 4) Gamma camera a piccolo campo di vista basata su rivelatore a semiconduttore CdTe, sviluppata presso il Dipartimento di Fisica nell'ambito di una collaborazione europea; 5) fantoccio di plexiglas simulante la mammella pendula durante l'esame CT.

6. TOMOGRAFIA COMPUTERIZZATA A CONTRASTO DI FASE

L'uso dell'imaging a contrasto di fase (Bravin *et al*, 2013) in BCT potrebbe fornire un modo per aumentare il contrasto nelle immagini 3D della mammella, per senza utilizzare agenti di contrasto. La tecnica a contrasto di fase (basata sulla propagazione delle onde elettromagnetiche X) produce un fenomeno di esaltazione dei contorni delle strutture (*edge enhancement*), in modo che i contorni dei tessuti normali e tumorali sono meglio delineati rispetto allo stesso mammogramma acquisito con la mammella a contatto con il rivelatore.

E' utile qui introdurre alcuni concetti di base dell'imaging radiografico a contrasto di fase. Le onde elettromagnetiche di lunghezza d'onda λ ad un'energia dei raggi X pari a $E = hc/\lambda$ subiscono sia un assorbimento che una variazione di fase nell'attraversare uno spessore di tessuto caratterizzato da un indice di rifrazione complesso spazialmente variabile $n(x,y,z;\ \lambda) = 1 - \delta(x,y,z;\ \lambda) + i\beta(x,y,z;\ \lambda)$. Qui, β è l'indice di assorbimento del tessuto (il coefficiente di attenuazione lineare è $\mu = 4\pi\beta/\lambda$) e $\delta > 0$ è il decremento della parte reale di n (responsabile della variazione di fase, ϕ, lungo un cammino di lunghezza l, secondo la relazione $\phi = -(2\pi/\lambda)\int\delta(l)dl$). Nell'intervallo di energia di interesse dell'imaging mammografico, δ assume valori circa 3 ordini di grandezza maggiori di quelli del parametro β per il tessuto mammario, il che indica che potenzialmente l'imaging dello sfasamento dei raggi X nell'attraversamento tissutale produce maggiore contrasto rispetto all'imaging radiografico convenzionale basato sull'assorbimento dei raggi X nel tessuto. I cambiamenti di fase nel tessuto implicano effetti di rifrazione dei raggi X al bordo delle disomogeneità presenti nel tessuto, come risultato della diffusione coerente e a piccolissimi angoli nel tessuto.

Vari metodi per l'imaging CT in contrasto di fase sono stati sviluppati negli ultimi anni per recuperare la mappa di fase 3D nei tessuti attraverso la misura della variazione di fase ϕ (ad esempio usando interferometria X con reticoli), o gradienti di variazione di fase $\nabla\phi$ (come nella tecnica di imaging *diffraction-enhanced*) o il laplaciano della fase $\nabla^2\phi$ (come nella tecnica *propagation based imaging*) lungo il cammino dei raggi dalla sorgente all'oggetto. Infatti, il contrasto di fase nel tessuto può essere più alto che nell'imaging basato sull'attenuazione.

Esistono limitazioni pratiche della mammografia a contrasto di fase basata su interferometria X: in particolare vengono impiegate dosi ghiandolari relativamente più elevate di quelle della mammografia digitale convenzionale, e complessi apparati ottici a raggi X. Un approccio semplice e clinicamente efficace alla tecnica BCT a contrasto di fase consiste nell'acquisire proiezioni con la tecnica basata sulla propagazione nello spazio libero, che non richiede elementi ottici interposti lungo il fascio di raggi X.

L'imaging in contrasto di fase basato sulla propagazione in BCT è stato studiato da molti gruppi. Esso richiede una alta coerenza laterale del fascio di raggi X: infatti, la potenziale superiorità del contrato di fase sul contrasto in assorbimento dipende dal grado di coerenza spaziale laterale del fascio X utilizzato. Nei sistemi CT clinici che impiegano radiazione emessa da un tubo radiogeno con macchie focali dell'ordine di 0.6 – 1 mm e con piccole distanze di propagazione, la coerenza spaziale della radiazione è molto limitata. Un fascio di raggi X di sufficiente coerenza può essere realizzato utilizzando tubi a raggi X con una macchia focale dalle dimensioni dell'ordine dei millesimi di millimetro (microfuoco) e/o con una sufficientemente grande distanza sorgente-oggetto. Alternativamente, fasci parzialmente coerenti possono essere prodotti usando una sorgente X incoerente ed un opportuno insieme di fessure ed aperture a griglia, secondo una tecnica messa a punto dal gruppo di Fisica Medica del Prof. A. Olivo presso lo University College London (Londra, UK).

Le immagini acquisite in condizioni di contrasto di fase basate sulla propagazione vengono poi retro-proiettate con un algoritmo FDK, in modo da ottenere una scansione BCT 3D a contrasto di fase. Se, successivamente, le viste angolari BCT sono prima processate per recuperare le mappe di variazione di fase proiettate (assumendo che il rapporto δ/β sia spazialmente uniforme nel volume del tessuto ed usando, ad esempio, l'approccio cosiddetto della *transport-of-intensity equation*), allora una mappa di fase dell'organo può essere ottenuta per retroproiezione attraverso l'algoritmo FDK. Questo processo

può generare immagini di fase un contrasto tra i tessuti dovuto alle disomogeneità locali di densità elettronica dei tessuti.

E' prevedibile che in mammografia digitale o in BCT, l'uso di una sorgente altamente coerente possa mostrare benefici in tecniche di imaging basate sul recupero della mappa di fase. Nell'ambito di progetti dell'INFN, alla linea di fascio SYRMEP del laboratorio di luce di sincrotrone ELETTRA (Trieste), è stato completato uno studio clinico per la mammografia in contrasto di fase con un fascio di raggi X monocromatico laminare e coerente; nel 2005 è stato anche riportato uno studio CT su un campione di mammella da cadavere, ma l'uso di un rivelatore di non elevata risoluzione spaziale non permise di evidenziare effetti di fase.

Il progetto SYRMA-CT (guidato dal gruppo dell'Università e INFN Trieste e comprendente, tra gli altri, il gruppo di Fisica Medica presso il Dipartimento di Fisica dell'Ateneo Federico II) per l'imaging tomografico a contrasto di fase dedicato alla mammella, mediante luce di sincrotrone e un rivelatore ad alta risoluzione spaziale, prevede di effettuare la prima scansione *in vivo* su paziente entro il 2017. I primi studi su oggetti di test sono stati recentemente completati e pubblicati (Longo *et al* 2016, Mettivier *et al* 2016). La fig. 6 mostra un'immagine di un campione di tessuto mammario (immerso in agarosio) ottenuta con radiazione monocromatica di luce di sincrotrone ad energia di 38 keV e con una dose ghiandolare dell'ordine di quella impiegata nella mammografia a doppia vista. In fig. 6a è riportata la ricostruzione tomografica della mappa dei coefficienti di attenuazione del campione, mentre la fig. 6b rappresenta una fettina tomografica ottenuta recuperando il segnale di fase in proiezione prima della ricostruzione tridimensionale. Il contrasto dell'immagine tra il tessuto canceroso (porzione chiara al centro dell'immagine) e tessuto adiposo (porzione di tessuto più scura che circonda il tessuto canceroso), grazie al recupero del segnale di fase, risulta maggiore rispetto all'immagine ottenuta senza il recupero di fase (fig. 6a).

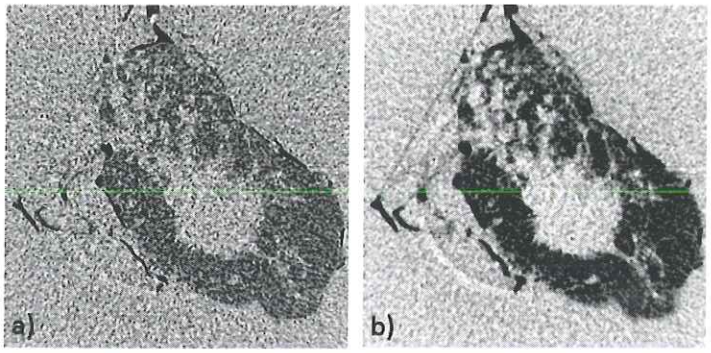

Figura 6: Fetta tomografica di un campione di tessuto mammario senza il recupero del segnale di fase (a) e con il recupero del segnale di fase (b): la scansione CT è stata effettuata presso il laboratorio di luce di sincrotrone ELETTRA (Trieste), con un fascio monocromatico di raggi X di energia pari a 38 keV ed un rivelatore a conteggio di singolo fotone, prodotto dalla Ditta PIXIRAD spin-off della Sezione di Pisa dell'Istituto Nazionale di Fisica Nucleare (INFN). La dimensione del voxel è di $120\times120\times120\ \mu m^3$ e la ricostruzione tomografica è stata effettuata da 600 viste angolari equispaziate su un intervallo di scansione angolare di 180°. Immagine acquisita nell'ambito del progetto SYRMA-CT dell'INFN.

7. CONCLUSIONI

La diagnosi del tumore alla mammella mediante imaging a raggi X, sia nella paziente asintomatica (per studi di screening sulla popolazione) che in studi diagnostici clinici, sta attraversando un periodo di grande evoluzione tecnologica, con il passaggio da tecniche 2D (mammografia convenzionale) alle nuove tecniche 3D di tomosintesi digitale e di tomografia con scanner dedicati. Queste tecniche 3D permettono di eliminare la sovrapposizione dei tessuti che si verifica nella tecnica mammografica bidimensionale, permettendo una migliore localizzazione delle lesioni mammarie e diagnosi più efficaci. La dose di radiazione necessaria per tali esami è paragonabile a quella delle due viste mammografiche tipicamente utilizzate nello screening del cancro al seno, per ciascuna mammella.

Rispetto alla mammografia convenzionale, la tomosintesi mammaria è stata introdotta nella pratica clinica negli ultimi quattro anni mentre uno scanner CT commerciale dedicato al seno è disponibile solo dall'inizio del 2015. A queste tecniche, basate sull'attenuazione che i raggi X subiscono nell'attraversare il tessuto, si aggiungono – per il momento in fase solo sperimentale in laboratorio – tecniche 2D e 3D di imaging a raggi X basate sulla rivelazione delle differenze nello sfasamento subito dall'onda elettromagnetica nell'attraversamento dei vari tessuti, aventi diversa densità elettronica. Una delle caratteristiche dell'imaging CT è che la mammella non viene compressa (a differenza della mammografia e della tomosintesi). Presso l'Università Federico II sono in corso studi sperimentali per lo sviluppo di tecniche tomografiche di imaging a raggi X della mammella sia in attenuazione che in contrasto di fase. La descrizione qui presentata illustra il fervore di attività di ricerca in questo settore, per una sempre più efficace lotta al cancro al seno con i metodi della Fisica applicata alla Medicina.

8. BIBLIOGRAFIA

Global Cancer Facts sheet: Breast cancer. Lyon, France. International agency for research on cancer. (2015) http://globocan.iarc.fr/Pages/fact_sheets_cancer.aspx. Accessed on-line 24/11/2015.

Siegel R. L., Miller K. D., Jemal A. (2015) Cancer Statistics, 2015, CA CANCER J CLIN **65**, 5–29.

NCI-funded Breast Cancer Surveillance Consortium (HHSN261201100031C). Breast Cancer Surveillance Consortium Web site - http://breastscreening.cancer.gov/. Accessed on-line 30/11/2015.

Reiser I., Sechopoulos I. (2014) A review of breast tomoshyntesis. Med. Phys. Int. **2**, 57–66.

Sechopoulos I. (2013) A review of breast tomoshyntesis. Part I. The image acquisition process, Med. Phys. **40**, 014301.

Sarno A., Mettivier G., Russo P. (2015) Dedicated breast computed tomography: Basic aspects, Med. Phys. **42**, 2786-2804.

Boone J.M., Nelson T.R., Lindfors K.K., Seibert J.A. (2001) Dedicated Breast CT: Radiation Dose and Image Quality Evaluation, Radiology **221**, 657–667.

Bravin A., Coan P., Suortti P. (2013) X-ray phase-contrast imaging: from pre-clinical applications towards clinics, Phys. Med. Biol. **58**, R1–R35.

Longo R. et al. (2016) Low dose phase-contrast breast tomography with synchrotron radiation at Elettra: first images, Phys. Med. Biol. 61, 1634-1641.

Mettivier G. et al. (2016) Glandular dose in breast computed tomography with synchrotron radiation, Phys. Med. Biol. **61**, 569-587.

Rend. Acc. Sc. fis. mat. Napoli
Vol. LXXXII, (2015) pp. 127-142

Advanced Raman Spectroscopies for Exploring Bio-systems

Giulia Rusciano[1] and Antonio Sasso[1*]

Presentata dal socio Leonardo Merola
(Adunanza del 18 dicembre, 2015)

Keywords: Raman spectroscopy, Surface- and Tip-Enhanced Raman Scattering, Biophotonics

ABSTRACT - Raman spectroscopy has experienced a renewed development for the huge potentiality offered by the plasmonics, a new area of nano-physics concerning the enhanced response of metal nanostructures to optical fields. Here we review the basic principles of these novel Raman spectroscopies focusing on a selection of experiments performed in our laboratories during the last recent years.

RIASSUNTO - La spettroscopia Raman ha ricevuto un rinnovato sviluppo per le potenzialità offerte dalle plasmonica, una nuova area della nano-fisica che riguarda la risposta di nanostrutture metalliche irradiate a campi ottici. In questa nota intendiamo riportare una breve rassegna sui principi di base di queste nuove tecniche Raman concentrandosi su una selezione di esperimenti condotti nel corso degli ultimi anni nei nostri laboratori.

[1]Universita' di Napoli *"Federico II"*, Dipartimento di Fisica "*Ettore Pancini*", Via Cintia, 80126 Napoli.
*To whom correspondence should be addressed: sasso@na.infn.it

1- INTRODUCTION

Biophotonics is an emerging area of scientific research, involving the use of light to detect and manipulate biological materials [Pavesi and Fauchet, 2008]. Its mission is to understand the inner workings of single microorganisms, or even single bio-macromolecules, in a non-invasive way. This approach has recently allowed to shed light on the peculiar function of single proteins, DNA and other important molecules. In medicine, the advent of biophotonics has introduced new ways to image and analyze living microorganisms, in order to detect, diagnose and treat diseases.

For biological samples, confocal, laser-based fluorescence microscopy has been traditionally considered as the golden standard for optical imaging due to its high sensitivity and facile preparation of samples (staining). Generally, fluorescence imaging is achieved by using fluorophores that selectively bind to target molecules. However, all fluorescence-based techniques present several shortcomings, such as photobleaching and photoblinking of the fluorescent labels, interference of fluorophores with the marked molecules and, most importantly, the quite poor chemical selectivity of fluorescence spectra.

Raman Spectroscopy (RS) has recently emerged as a formidable alternative to fluorescence, potentially capable to overcome fluorescence's drawbacks, as demonstrated by the increasing number of applications in many fields of life sciences. Raman Spectroscopy assesses the chemical composition of a sample by exploiting the inherent and unique vibrational structure of molecular bonds in the sample (chemical fingerprinting).

In this brief review we present some applications of RS to biological systems. We start from the conventional RS, discussing the basic principle and the main limits. Afterwards, we discuss recent variants of this spectroscopic technique based on the excitation of plasmon resonances in metal nanostructures (Surface Enhanced Raman Scattering, SERS). Finally, we present the frontiers of modern Raman-based techniques, which allows to acquire a spatial resolution that is outside of the diffraction-limited regime of the conventional optical techniques. plasmonics-based Raman discussing of a novel technique which combine the nanometric resolution of the Atomic Force Microscopy with the plasmonics resonance localized at the tip itself of the AFM.

2. BASIC PRINCIPLES OF RAMAN SPECTROSCOPY

In the photon picture, scattering of light can be seen as an elastic or inelastic collision between an incident photon and a molecule (see Fig.1): the molecule undergoes an excitation to a virtual state followed by a nearly

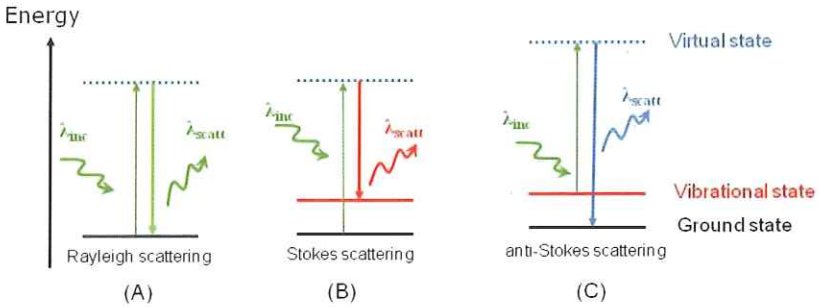

Figure 1: Energy level diagram for Rayleigh, Stokes, and anti-Stokes Raman scattering.

simultaneous de-excitation towards the initial energy level (elastic) or a vibrational level different from the initial one (inelastic). The scattering event duration is of the order of an optical cycle, i.e. it occurs in 10^{-14} s or less. Moreover, since virtual states are created only when photons interact with electrons, the energy of these states is determined by the frequency itself of the incident photons. From the virtual state, molecules may decay following three different paths. Most of them return back to the initial state through the emission of a photon having the same energy of the incident photon (see Fig.1A). This process, named Rayleigh scattering, is, for instance, the reason for the blue colour of the sky caused by the scattering of sunlight in the atmosphere. Another possibility is that the molecule decays toward an excited vibrational level (see Fig.1B): in this case the energy photon is lower than the incident one and the energy defect is released to the internal (vibrational) energy of the molecule. This process is called Stokes scattering. Hence the energy difference between the initial and final vibrational levels (Raman shift) expressed in wavenumbers $\tilde{\nu}$ (cm^{-1}), is given through the relation:

$$\tilde{\nu} = \frac{1}{\lambda_{inc}} - \frac{1}{\lambda_{scat}} \qquad (1)$$

in which λ_{inc} and λ_{scat} are the wavelengths of the incident and Raman scattered photons, respectively. Finally, a third process can take place when we consider molecules in an excited vibrational level. In this case a molecule excited in a virtual state can decay in the ground state (see Fig.1C). This process, called anti-Stokes scattering, produces photons with energy higher that the incident ones: the energy defect is now transferred from the molecules to the photons. Nevertheless, since the number of molecules in an excited vibrational level decreases as $e^{-\frac{\Delta E}{kT}}$ (Boltzmann statistic), anti-Stokes scattering is much less probable than the Stokes scattering (typically by a factor around 1000). For this

reason, Raman analysis is usually limited to the observation of the Stokes scattering.

From an experimental point of view, a Raman spectrum is obtained by dispersing the scattered photons by means of diffraction gratings, rejecting the intense elastic scattered light by a notch filter, and recording the several peaks by means of a sensitive CCD camera. Since different molecules have bonds vibrating at well-defined frequencies, it turns out that the Raman spectrum consists of quite sharp peaks representing the actual "*chemical fingerprint*" of the molecule.

When RS is combined with confocal optical microscopy (*micro-RS*) a spatial resolution of ~300 nm in the transverse x-y plane and of ~1.2 μm in the axial direction can be achieved. Clearly, for extended samples, it is possible to acquire the Raman spectra on a two- or three-dimensional array of points, with a step comparable with the spatial resolution (*Raman imaging*). Therefore, the information carried by the acquired spectra can be represented by 2D images (or 3D profiles), reporting the spatial variation of a given Raman parameter. This parameter is usually the intensity of a particular Raman band, but sometimes it derives it from a more complicated analysis of the whole Raman spectrum.

Nowadays *Raman imaging* is becoming a tool for a patchwork of interdisciplinary researches, involving physicists, chemists and biologists, as well as molecular biologists and clinicians.

The Raman spectrum provides essentially the same type of information as the infrared (IR) absorption spectrum, i.e. the vibrational energies of molecular normal modes of vibration. However, the two techniques have experienced a quite different fortune for biological applications. This is mainly due to the strong IR-absorption cross section of water, which usually mask the contribution of species in aqueous environment. In contrast, water interferes only poorly with Raman spectra of aqueous solutions, due to the quite low water Raman activity. The other side of the coin of RS is its very low efficiency caused by the small cross-section of the inelastic scattering process, up to 12 orders of magnitude smaller than fluorescence. This makes Raman detection of molecules at sub micro-molar concentration prohibitive.

3. RESONANT RAMAN SPECTROSCOPY OF SINGLE RED BLOOD CELL MANIPULATED BY OPTICAL TWEEZERS

When the frequency of the Raman probe is close to the frequency of an electronic transition, the Raman scattering cross section is enhanced by 3-6 order of magnitude. This effect, which greatly improves the sensitivity of RS, is referred to Resonance Raman Scattering (RRS). RRS has been observed for several classes of biologically important molecules, such as metalloporphyrins

and carotenoids, which exhibit strongly allowed electronic transitions in the visible region due to the presence of a chromophor. The enhanced contribution from selected chromophoric moieties can be used to selectively pick out and positively identify a molecule in a matrix. This is the lucky case of haemoglobin (Hb), the main component of Red Blood Cells (RBC).

As a matter of facts, the chromophoric structure of the heme, the functional group of Hb which links oxygen in lungs and realises it throughout the body, results in a strong enhancement of the Raman Scattering using laser wavelengths close to the heme electronic absorption bands. This allows the investigation of Hb within erythrocytes without interference by the scattering from other cellular component.

The Hb structure is characterized by two states: an oxygenated, relaxed structure (R or oxy state) and a de-oxygenated or tense structure (T or de-oxy state). Intriguingly, these two state are well distinguishable by RRS, due to the presence of specific Raman bands which are quite sensitive to spin state of iron according if this atom is bond to oxygen or to carbon dioxide, as shown in Fig. 2 [Rusciano, 2010]. This feature has expired numerous studies, aimed at shedding light on the response of Hb to external stimuli and/or to reveal Hb-related disorders, even at level of single cell.

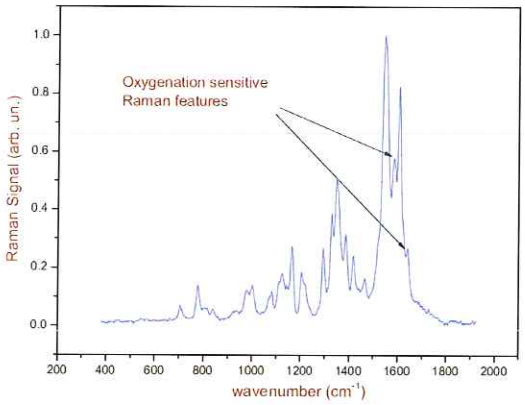

Figure 2: Raman spectra of Hemoglobin.
The peaks in the range 1500-1700 cm^{-1} are sensitive to the oxy- or deoxy state. In particular, the two peaks highlighted by the arrows represent two significant vibrational modes of Hb used in our analysis.

Recently, we have demonstrated that RRS is able to investigate the process of oxygen release from Hb occurring in the body circulatory system [De Luca et al., 2008]. Historically, the deformation of RBCs when they pass through small microcapillaries has been thought as the main channel where Hb oxy-deoxy

transition occurs. In particular, numerical simulations show that Hb deoxigenation under RBC stretching is due to the necessity to pack Hb in a smaller volume and the contemporary enhanced hemoglobin-membrane interactions. However, the strict connection between RBCs deformation and Hb de-oxygenation was never proven before. RRS, combined with the use of an Optical Tweezers (OT), gave us the opportunity to reach this goal. OTs are based on the use of strongly focused laser beams, allowing manipulation of single cells in absence of any mechanical contact. A sketch of our experimental approach is shown in Fig. 3A where a single RBC is immobilized at two its ends by two OTs, used as handles to manipulate the cell.

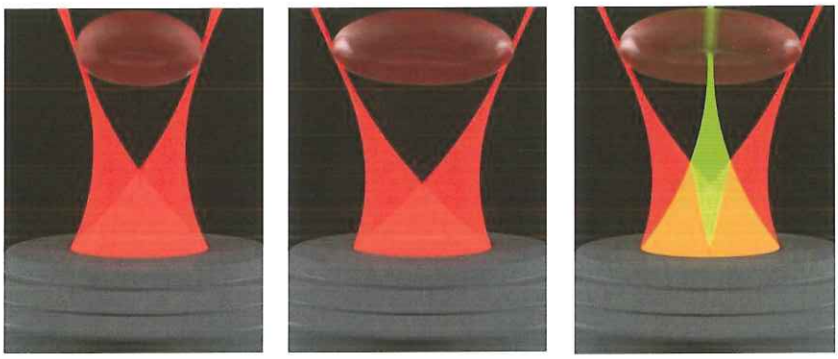

A) B) C)

Figure 3: Manipulation and stretching of a single RBC

A single red blood cell is handle by two optical traps at its two ends using a near infrared laser, λ=1064 nm (part A). By translating the traps the cell is stretched (part B). A third laser, emitting at 532 nm, is used as Raman probe (part C).

Afterwards, the RBC is stretched by increasing the distance between the traps (Fig.3B). Finally, RBC was relaxed by reporting the cell to its natural, un-stretched state. Besides the two laser traps (emitting in the near infrared, λ=1064 nm), a third laser (emitting in the visible, λ=532 nm) is employed as Raman probe (Fig.3C). At each step of the cell elongation, Hb oxygenation state is monitored by recording the Raman spectrum collected from the same region of the trapped cell. From the analysis of the resulting spectra, it turns out that, under stretching, Hb undergoes transition to the deoxygenated state. After stretching, RBC recovers its initial shape together with its initial oxygenation state. Although optical stretching of a floating RBC is only a poor simulation of folded-elongated RBCs within capillaries, our study constitutes the first experimental evidence of the de-oxygenation of Hb inside RBCs under the

application of a mechanical deformation. This result is quite interesting from a physiological point of view, contributing to understand how oxygen transfer occurs in human body.

Deficiency in Hb oxygenation capability are common to many blood disorder, including thalassemia. Thalassemia is a disease of RBC inherited as a semidominant trait, quite diffuse in the populations of the Mediterranean sea. In thalassemia, the genetic defect results in reduced rate of synthesis of one of the globin chains composing the heme group.

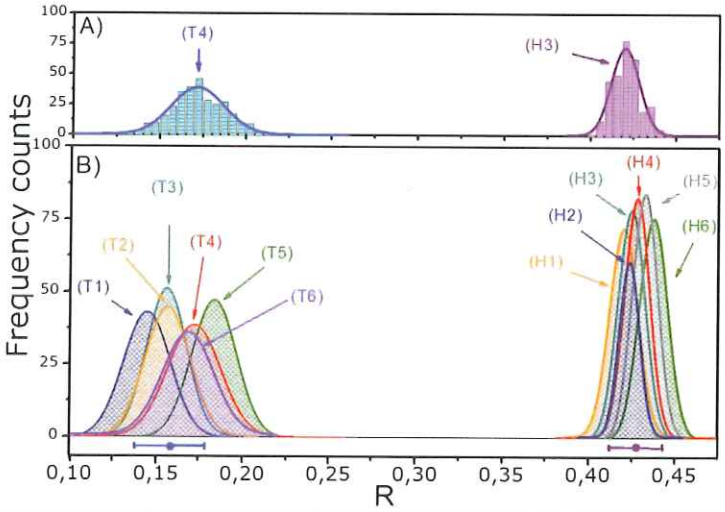

Figure 4: Analysis of healthy and thalassemic RBCs.
Statistical distributions of the ratio $R=I_{37}/I_{11}$ obtained by analyzing 300 RBCs from a single normal (pink histogram) and thalassemic (blue histogram) donor. The fitting of these distributions with Gaussian profile is also shown. B: Gaussian profiles obtained by fitting the experimental distributions relative to 6 normal (Hi) and 6 thalassemic (Ti) volunteers. The weighted-mean and the standard deviation for the two kinds of cells are evidenced by horizontal bars.

So far, we have investigated the effects of thalassemia, at single cell level, using a Raman system. By resonant excitation of hemoglobin Raman bands, we have examined the oxygenation capability of β-thalassemic erythrocytes. Fig. 4, part a, shows the statistical distributions (over 300 measurements) of the ratio $R=I_{37}/I_{11}$ between two selected Hb Raman bands, the first being sensitive to Hb oxygenation.

As it is possible to note, this ratio completely differentiates RBCs from obtained by analyzing 300 RBCs from a single normal (pink histogram) and thalassemic (blue histogram) donor. Part b of Fig. 4, instead, shows the Gaussian profiles obtained by fitting the experimental distributions relative to 6 normal (Hi) and 6

thalassemic (Ti) volunteers. These results demonstrate that our approach may have potential for the monitoring of blood diseases.

4. BASIC PRINCIPLE OF SURFACE ENHANCED RAMAN SCATTERING

A huge step forward to the concrete use of Raman spectroscopy in biosciences is due to the discovery of the huge enhancement (up to 12 orders of magnitudes) of the Raman signal when the analyte under investigation is close to proper nano-sized metallic particles (NPs). This phenomenon is called Surface-Enhanced Raman Scattering (SERS) and, since its discovery, its use as analytical technique has grown exponentially [Rusciano et al., 2011].
Historically, SERS birth dates backs to 1974 when Fleishmann and co-workers [Fleischmann et al, 1974] observed an anomalous enhancement of the Raman signal for pyridine molecules adsorbed over a roughened silver surfaces. Few years later two independent papers [Jeanmaire and Van Duyne, 1977, Albrecht and Creighton, 1977] provided the first physical interpretation based on Localized Plasmon Resonance (LPR) induced by the laser radiation shining the nanostructured metal surface.

As the simplest model to describe LPR we can assume a small metal sphere illuminated by the light. The time-varying electromagnetic (EM) field of the illuminating light can sustain collective oscillating surface plasmonic multipoles. If the size of the metallic structure is small compared to wavelength of incident light, the plasmonic wavepacket will remain confined in the nanostructure and it will give rise to a surface plasmon (SP). Moreover, if the frequency of incident EM field is close to the SP oscillation frequency, the field extinction, i.e. absorption and scattering, will reach a maximum. It is not difficult to image that the SP resonance depends critically not only by the NPs size and shape but also by the dielectric function of the bulk metal and by the surrounding material. This is the reason for which, although the gold bulk plasma frequency is in the UV region, the SP frequency for a gold NP lies in the green region (near 520 nm). This scattering property have attracted considerable interest since historical times when metallic NPs were used as decorative pigments in stained glasses and artworks. The most famous example of such application is the famous Lycurgus Cup is a 4th-century Roman glass cage cup, which exhibits a different colour depending on whether or not light is passing through it. To get an idea into the origin of SP resonances in metallic nanostructures, we have no other options but to actually solve Maxwell's equations with appropriate boundary conditions. A useful approximation scheme for this purpose is the so called electrostatic approximation, in which the electric field of the light is considered to be constant over distances comparable to the object size so that any phase delay of the field is neglected. In

practice, for visible radiation, the electrostatic approximation works well for objects of typical sizes up to ~10 nm. Fully analytical solutions of Maxwell equations exist in a few selected simple geometries (Mie theory). The sphere is one of these cases. In such case, it is possible to demonstrate that the electrostatic boundary conditions on the sphere can be satisfied by considering the total EM field as the superposition of that produced by an induced dipole at the origin (p) with the external applied field (E). The induced dipole is given by:

$$\alpha = \varepsilon_m V \frac{\varepsilon - \varepsilon_m}{\epsilon + 2\varepsilon_m} \qquad (2)$$

where V is the particle volume, $\varepsilon = \varepsilon_r + i\varepsilon_{im}$ is the complex frequency-dependent dielectric function of the metal, and ε_m is the dielectric constant of the surrounding medium. Starting from Eq. (1), SERS enhancement mechanism can be simply described with the diagram of Fig. 5.

As a matter of facts, a molecule in proximity of the sphere (at distance d) is exposed to a field E_{tot}, which is the superposition of the incoming field E_0 and the field of the dipole, E_{dip}, induced in the metal nanosphere. This field assumes the form:

$$E_{tot} = E_0 + E_{dip} = E_0 + r^3 \frac{\varepsilon - \varepsilon_m}{\varepsilon + 2\varepsilon_m} E_0 \frac{1}{(r+d)^3} \qquad (3)$$

It is possible to define an enhancement factor (EF) as ratio of the total field E_{tot} at the molecule position and the incoming field E_0:

$$A(\nu_L) = \frac{E_{tot}}{E_0} \sim \frac{\varepsilon - \varepsilon_m}{\varepsilon + 2\varepsilon_m} E_0 \left(\frac{r}{r+d}\right)^3 \qquad (4)$$

The most important feature of the previous equation is the presence of the denominator $\varepsilon + 2\varepsilon_m$. In fact, assuming $\varepsilon_{im} \sim 0$ (low metal absorption), a strong resonance occurs when at the laser frequency ν_L the condition $\varepsilon_r = -2\varepsilon_m$ is satisfied. In an analogous fashion, the Stokes and anti-Stokes fields

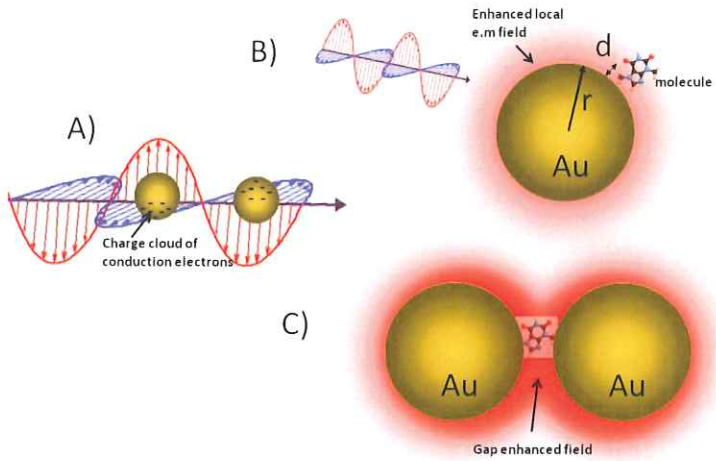

Figure 5: Cartoon of SERS mechanism.
Simple description of SERS: a) a metal nanoparticle illuminated by light gives place to oscillation of the free electrons of the surface; b) a molecule placed at nanometric distance d from the NP surface is affected by an amplified optical field; c) amplification if further increased (hot-spot) in the gap region in dimer structure.

will be enhanced too, if they are in resonance with surface plasmons of the sphere. Therefore, taking into account both effects, the electromagnetic enhancement factor for the Stokes signal is:

$$G = |A|^2|A|^2 \sim E_0^4 \left|\frac{\varepsilon(\nu_L) - \varepsilon_m}{\varepsilon(\nu_L) + 2\varepsilon_m}\right|^2 \left|\frac{\varepsilon(\nu_S) - \varepsilon_m}{\varepsilon(\nu_S) + 2\varepsilon_m}\right|^2 \left(\frac{r}{r+d}\right)^{12} \qquad (5)$$

being ν_S the frequency of the inelastically scattered photon. This formula shows that the EM enhancement factor scales as the forth power of the local field and reaches its maximum when both excitation and Stokes field are in resonance with the plasmons. Moreover, electromagnetic enhancement is effective when the analyte is very close to the nanostructure, as G decreases as $(1/d)^{12}$, which is responsible of the local character of SERS enhancement.

For noble metals (gold, silver, and copper) the resonance condition can be satisfied at visible frequencies, where they exhibit a negative dielectric function and low absorption. It is worth noticing that, in the electrostatic approximation, the plasmon frequency of a nanosphere does not depend by its actual size. Nevertheless, the conditions under which the electrostatic approximation represent the real solution of the problem (the solution of Maxwell's equations)

is limited by applicability range of the electrostatic approximation. For larger NPs, the size effect on the resonances can be observed. As general rule, as the size increases, the NPs resonances (i) shift to the red, (ii) are strongly damped and spectrally broadened, and (iii) new resonances appear, which are typically related to the activation of multipolar resonances (such as quadrupolar resonance). An additional level of complexity, but also of great interest, of the plasmonic resonances arises from the existence of coupled plasmon resonances for two or more closely spaced objects. Considering, for instance, the very simple case of two metallic nanobeads, it is possible to demonstrate that resonance coupling produces a red shift of the plasmon resonance, with its intensity mainly concentrated in the middle of the two beads. This gap effect is illustrated in Fig.5c.

The enhancement effect just described is commonly referred as "electromagnetic enhancement". However, SERS effect has also a strong molecular selectivity and a clear dependence on the chemical nature of the Raman molecule. This suggests the existence of an additional chemical SERS enhancement mechanism. Among the different mechanisms proposed to explain this chemical effect, the charge transfer mechanism is the most reliable. In particular, it is described as a four steps process, involving the transfer of a charge from the metallic nanostructure and back. In general, the chemical SERS enhancement mechanisms contribute to the enhancement by a factor of $10 - 10^3$.

5. SERS SUBSTRATES OF HIGH SPATIAL REPRODUCIBILITY FOR IMAGING OF CELL MEMBRANES

Label-free chemical imaging of live cell membranes can shed light on the molecular basis of cell membrane functionalities and their alterations under membrane-related diseases. In principle, this can be done by surface-enhanced Raman scattering (SERS) in confocal microscopy, but requires engineering plasmonic architectures with a spatially invariant SERS enhancement factor G. This requirement has opened new research area in nanoplasmonic, aimed at producing nano-structured surface showing high efficiency and reproducibility. SERS substrates can be grouped in three main categories: i) metal NPs in suspension; ii) metal NPs immobilized on solid substrates; iii) nanostructures fabricated directly on solid substrates, which includes nanolithography and template synthesis of nanostructures. The variety of SERS substrates reported in recent years is enormous and obviously it is not possible to review the whole field herein. Rather, we prefer to discuss a method developed in our laboratory that seems to combine the main expectations for realistic application of SERS to bio-system. We took advantage of the use of the so-called block-copolymer (BCP), polymers made up of blocks of different monomeric components.

Intriguingly, BCP tend to self-assemble on nanoscale, in a way which strongly depends by the relative concentration of their different polymeric components. In our case, starting from polystyrene-block-poly-4-vinylpyridine (PS-b-P4VP) BCP we produced micelles loaded with silver nano-particles (Ag-NPs). Through a spin-coating deposition over a glass substrate we obtained a self-assembled isotropic nanostructure with characteristics of homogeneity typical of the so-called near-hyperuniform disorder [Zito et al, 2015]. The resulting highly dense, homogeneous and isotropic random pattern consists of clusters of silver nanoparticles with limited size dispersion.

A typical TEM image of the resulting SERS substrate is shown in Fig. 6. Each nano-island consisted of nearly touching (or in contact) nanoparticles of size in the range ~1–12 nm. The average nano-island diameter was D ~26 nm, the cluster height was h ~ 14 nm, and the hexagonal pattern is characterized by a gap g ~ 2-3 nm between the NP-islands.

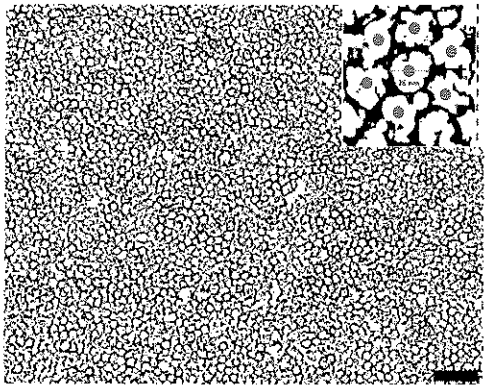

Figure 6: Transmission Electron Microscopy image of self-assembled SERS substrates.
TEM micrograph of the final random pattern obtained by applying our protocol: the filling fraction is highly increased inducing nanoisland gaps of 2–3 nm, as shown in the close-up. Scale bar is 150 nm.

We took advantages of the high spatial reproducibility of our SERS substrates to analyse the RBC membrane. Since the SERS substrate is actually localized only at the cell surface our method is able to discriminate the bio-chemistry composition of the cell membrane. Remarkably, SERS spectra resulted to be characterized by glycoprotein and glycolipid contributions not masked by the resonant membrane-bound Hb (see Fig.7). We are currently expanding the study on red blood cells to discriminate the molecular variation induced at the membrane during the life cycle of the cell and under mechanical stress induced into a microfluidic channel. The same approach will be also used

to study the expression of specific proteins on cancer cells membranes, an information that can be helpful for early diagnosis.

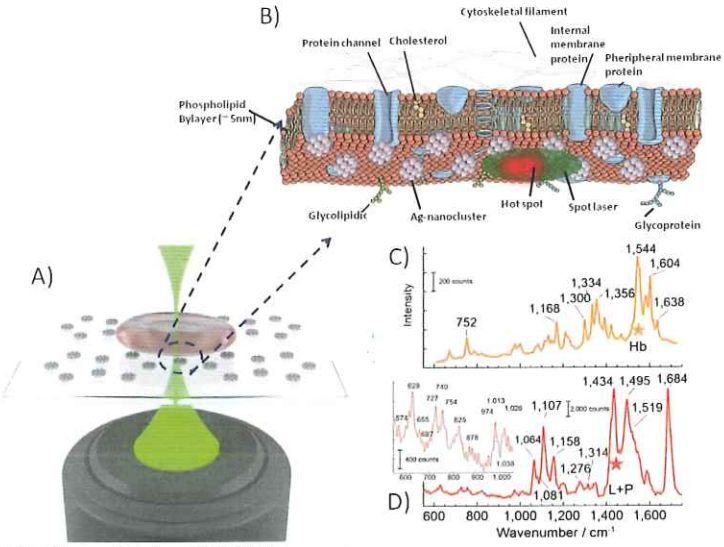

Figure 7: SERS analysis of RBC membrane.
A) the laser beam is focused on a single RBC adhered on a SERS coated or uncoated (not shown in figure) coverslips; B) Zoom on the interface between the SERS substrates and the RBC membrane; C) Spontaneous Raman spectrum of RBC, which shows typical spectral features of hemoglobin; D) Typical SERS spectrum measured at z = 0, which clearly presents spectral markers of membrane lipids and proteins. Inset in D) shows a magnified view of the smaller spectral features.

6. TIP-ENHANCED RAMAN SCATTERING FOR STUDYING BACTERIA SURFACE

Many problems at the frontiers of materials science and biotechnology require a spatial resolution that is outside of the diffraction-limited regime of the conventional optical techniques. Very recently, a new research field has emerged that seems to offer the potential to bridge this gap. This new technique is termed Tip-Enhanced Raman Scattering (TERS). TERS relies on the combination of near-field scanning probe microscopy and enhanced Raman spectroscopy. In TERS, in fact, the near field scanning probe (e.g. the tip of an Atomic Force Microscope, AFM) is covered by metal NPs. In this way, the tip behaves as a sort of optical nano-antenna that gives place to huge amplification

of the optical field as for SERS but only in proximity of the tip apex. Therefore, due the short-range character of plasmon resonance, the enhanced Raman signal can be acquired with a spatial resolution only limited by the tip geometry. Since the radius of curvature of scanning probe tips is of the order of tens of nm, the obtained spatial resolution is well below the light diffraction limit. Hence, TERS acquires simultaneously the topographic structure of the scanned surface but also its bio-chemistry composition, revealed by the tip-enhanced spectrum. A sketch of TERS mechanism is shown in Fig. 8.

Figure 8: Basic idea of Tip Enhanced Raman Scattering.
A sketch of the basic principle of TERS. A very thin tip of an Atomic Force Microscope is coated with metal nanoparticles and shined by a proper laser wavelength. When the tip approaches the surface of the sample the enhanced optical field allows the detection of also few molecules in the short range of the nano-antenna.

Historically, the first TERS realization dates to 2000 by Kawata and co-workers [Hayazawa et al., 2000], shortly followed by Zenobi's group [Stockle et al., 2000]. These pioneering studies have well elucidated the main TERS features: a very high sensitivity (due to the near-field plasmonic enhancement) combined with an elevated spatial resolution, obtained by the scanning probe-based approach. Both these characteristics make TERS a unique tool, for instance, to directly localize and identify proteins and their conformation in a complex (e.g., native) environment. In addition, it represents an excellent tool for detecting biomolecules that are adsorbed, layered, or assembled on a large variety of surfaces and interfaces, included the outer side of cell membranes.

The simultaneous recording of both topographical and chemical structure achievable by TERS has, over the last years, allowed to reach a deeper insight into the surface properties of many complex systems at the nanoscale, opening

new opportunities for their use as concrete *living biotechnological tools*. Spores, the "dormant" state of bacteria, own to this family.

Recently, we applied TERS spectroscopy for surface analysis of *Bacillus subtilis* spores, a very attractive bio-system for a wide range of applications regulated by the spore surface properties. In particular, these spores have been proposed as mucosal vaccines and proposed as carriers for drug delivery applications.

The observed TERS spectra reflect the complex and heterogeneous environment explored by the plasmonic tip, therefore exhibiting significant point-to-point variations at the nanoscale (see Fig. 9).

Given such molecular complexity, a robust correlative imaging was necessary for eliciting the spore surface chemical information. In particular, by taking advantage of advanced statistical tools such as Principal Components Analysis (PCA), we demonstrated the existence of a denser arrangement of both proteins and carbohydrates on specific spore surface regions (the spore "ridges", see Fig. 9a) simultaneously revealed by AFM imaging [Rusciano et al., 2014]. Intriguingly, the ridge might act as a sort of chemical reservoir for bacteria after sporulation of the dormant cell. Successful TERS analysis of spores' surface constitutes an essential step toward the use of spores for drug delivery applications.

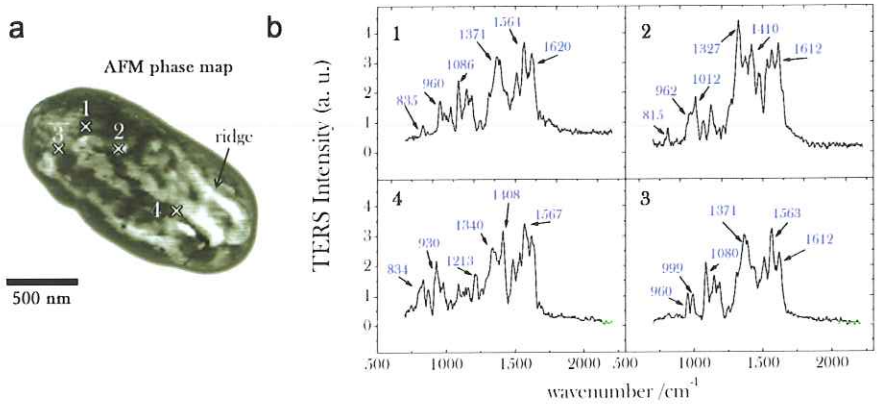

Figure 9: TERS analysis of bacteria spore surface.
(a) AFM phase map of a whole spore acquired in tapping mode (scale bar = 500 nm, step-size = 20 nm).
(b) Near-field (normalized) TERS spectra acquired in four selected positions over the spore coat, corresponding to the cross-marks in (a).

7. REFERENCES

[1] *Biophotonics,* Pavesi L. and Fauchet P. M. (Eds.), Springer-Verlag Berlin Heidelberg (2008).

[2] Rusciano G. (2010) *"Experimental analysis of Hb oxy-deoxy transition in single optically stretched red-blood cells"* Physica Medica: European Journal of Medical Physics **26**, 233-239.

[3] De Luca A.C., Rusciano G., Ciancia R., Martinelli V., Pesce G., Rotoli B. and Sasso A. (2008) "*Spectroscopical and Mechanical Characterization of Normal and Thalassemic Red Blood Cells by Raman Tweezers*" , Opt. Express **16**, 7943.

[4] Rusciano G., De Luca A.C., Pesce G., Oliviero G., Amato J., Borbone N., D'Errico S., Piccialli V., Piccialli G., Mayol L. (2011)*"Label-Free Probing of G-Quadruplex Formation by Surface-Enhanced Raman Scattering"* Anal. Chem. **83**, 6849-6855.

[5] Fleischmann M., Hendra P. J. and McQuillan A. J. (1974) "*Raman spectra of pyridine adsorbed at a silver electrode"* Chem. Phys.Lett., 1974, **26**, 163–166.

[6] Jeanmaire D. L. and Van Duyne R. P. (1977) *"Surface Raman Spectro electrochemistry Part I. Heterocyclic, Aromatic, and Aliphatic Amines Adsorbed on the Anodized Silver Electrode"* J. Electroanal. Chem., **84**, 1–20.

[7] Albrecht M. G. and Creighton J. A. (1977) *"Anomalously intense Raman spectra of pyridine at a silver electrode"* J. Am. Chem. Soc. **99**, 5215–5217.

[8] Zito G., Rusciano G., Pesce G., Dochshanov A., Sasso A. (2015) "*Surface-enhanced Raman imaging of cell membrane by a highly homogeneous and isotropic silver nanostructure*" Nanoscale **7**, 8593-8606.

[9] Hayazawa N., Inouye Y., Sekkat Z., Kawata S. (2000) "*Metallized Tip amplification of near-field Raman scattering*", Opt. Commun.; **183**, 333–6.

[10] Stockle R.M., Suh Y.D., Deckert V., Zenobi R. (2000) "*Nanoscale chemical analysis by tip-enhanced Raman spectroscopy*", Chem. Phys. Lett. **318**, 131–6.

[11] Rusciano G., Zito G., Isticato R., Sirec T., Ricca E., Bailo E., Sasso A. (2014) "*Nanoscale chemical imaging of bacillus subtilis spores by combining Tip-Enhanced Raman Scattering and advanced statistical tools*" ACS Nano **8,** 12300-12309.

Rend. Acc. Sc. fis. mat. Napoli
Vol. LXXXII, (2015) pp. 143-147

Experiments on gravity in Firenze: From Galileo to quantum sensors with ultracold atoms

Nota di Guglielmo M. Tino[1]

Presentata dal socio Leonardo Merola
(Adunanza del 18 dicembre, 2015)

Keywords: Atom interferometry, atomic clocks, cold atoms, gravitational physics.

Abstract - About 450 years since the birth of Galileo Galilei, some of the experiments he performed or discussed as conceptual experiments to investigategravity are repeated with advanced quantum systems based on atoms brought to temperatures near absolute zero using laser light.

Riassunto - A 450 anni dalla nascita di Galileo Galilei, alcuni degli esperimenti sulla gravità da lui eseguiti o immaginati come esperimenti concettuali per studiare la gravità, vengono ripetuti con sistemi quantistici avanzatissimi basati su atomi portati a temperature vicine allo zero assoluto utilizzando la luce laser.

1 – INTRODUCTION

New quantum sensors based on laser cooled atoms (Nobel Lectures, 1997) allow us to measure gravitational effects with high precision. Atom interferometers (Tino, 2014), for example, are used to test the equivalence principle underlying the general theory of relativity of Einstein. Optical atomic clocks (Poli, 2013), which use the oscillation of light field as a pendulum, measure the passage of time with a precision that was unimaginable until a few years ago and allow us to detect in the laboratory the effect of gravity on time.

Many are also the possible applications in fields such as geophysics, space physics, telecommunications.

2 – TESTING GENERAL RELATIVITY USING ULTRACOLD STRONTIUM ATOMS AND SEARCH FOR SPIN-GRAVITY COUPLING

Recently, we reported the results of an experiment we performed at the LENS laboratory in Firenze in which we tested for the first time the validity of the equivalence principle of general relativity for atoms with spin and without spin and with different characteristics, namely bosons and fermions, showing that they fall in the same way in the presence of gravity (Tarallo, 2014). This experiment is conceptually analogous to the one conceived by Galileo Galilei to show that different objects fall in the same way: "... cascai in opinione, che se si levasse totalmente la resistenza

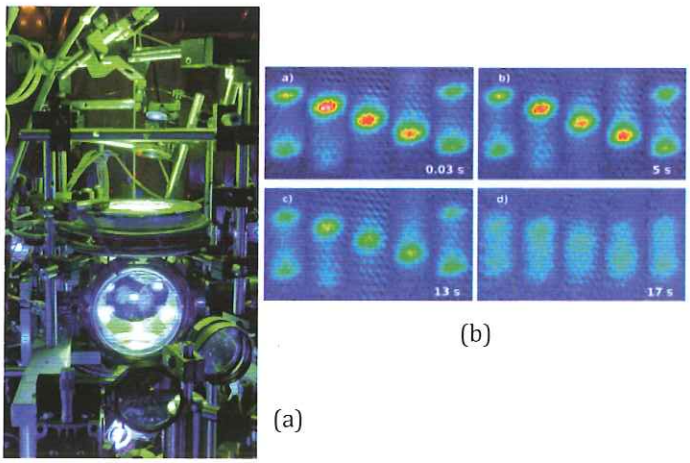

Fig. 1. Gravity measurement with Bloch oscillations of cold Sr atoms in a vertical optical lattice.
a) Picture showing the ultra-high-vacuum cell and the apparatus to cool and trap Sr atoms using laser light. Three orthogonal couples of counterpropagating laser beams with a wavelength of 461 nm (blue light) intersect at the center of the cell where a quadrupole magnetic field is produced by two anti-Helmholtz coils (one is visible in the picture). The atoms are trapped at the center of the cell in the region around the zero of the magnetic field where the laser beams overlap. The trapped atoms can be seen from the light they scatter as fluorescence. The vertical green laser beam is retroreflected by a mirror thus producing a standing wave; the cold Sr atoms are trapped in the regions corresponding to the anti-nodes.
b) Bloch oscillations for Sr atoms in the vertical optical lattice under the influence of gravity. Each picture shows one Bloch cycle in successive time-of-flight absorption images giving the momentum distribution at the time of release from the lattice (Poli, 2011).

del mezzo, tutte le materie discenderebbero con eguali velocità" (... I was convinced, that if the resistance of the medium was completely eliminated, all materials would fall with equal velocity) (Galileo, 1638).

Our experiment was based on the quantum phenomenon known as Bloch oscillations in condensed matter physics since it was predicted by Bloch in 1928 for electrons in the periodic potential of a crystal in the presence of the external force produced by an electric field. In our experiment, the role of the electrons is played by ultracold Sr atoms, the force is produced by gravity and the standing wave produced by a retroreflected laser beam corresponds to a "perfect crystal" in which the atoms are confined. It can be shown that the frequency of the Bloch oscillations is proportional to the force, that is in our experiment, to gravity acceleration.

By measuring the frequency of the Bloch oscillations for ^{87}Sr and ^{88}Sr isotopes of strontium atoms in a vertical optical lattice, we set an upper limit to a possible difference in the acceleration for the two isotopes. Strontium atoms have no electronic angular momentum in the ground state; ^{88}Sr has no nuclear spin (I=0) and is a boson while ^{87}Sr has a half-

integer nuclear spin (I=9/2) and is a fermion. Therefore this experiment can be considered as the first test comparing gravitational interaction for bosonic and fermionic particles and it can also be interpreted as a search for a possible coupling between spin and gravity that is predicted in different theoretical models (Capozziello, 2011).

For its unique features, the atom interferometer with strontium atoms that we developed will enable also the investigation of the gravitational field produced by a microscopic source mass. This will make it possible to study the force of gravity at a distance of a few micrometers and place limits on the existence and extent of extra dimensions in our universe (Ferrari, 2006).

Strontium atoms cooled and trapped with laser light also provide the frequency reference for the new optical atomic clocks that, using as the pendulum the oscillation of the field of laser light, allow us to measure the passage of time with such a high precision that the general relativity effects, as the gravitational time dilation, can now be observed in the laboratory (Poli, 2013). Optical clocks have already shown levels of precision that are hundred times better than the best atomic clocks based on microwave transitions. Therefore they will likely lead to a new definition of the second. Compact and transportable Sr optical clocks, as the one first developed by our group in Firenze (Poli, 2014), are being considered for future experiments in space in which it will be possible to operate the clocks in a well characterized gravitational environment and to perform extremely precise measurements of the gravitational red shift predicted by general relativity (Tino, 2013).

3 – PRECISION MEASUREMENT OF THE NEWTONIAN GRAVITATIONAL CONSTANT USING COLD ATOMS

We recently reported the results of a 10-year experiment named MAGIA (which stands for Accurate Measurement of G by Atom Interferometry) and funded by Istituto Nazionale di Fisica Nucleare (INFN), in which for the first time the value of the Newtonian gravitational constant G was measured using an atom interferometer as a probe (Rosi, 2014). The measurement of G is still, after more than two hundred years after the first experiment by Cavendish in 1798, a challenge for experimental physics. About 300 experiments have tried to accurately

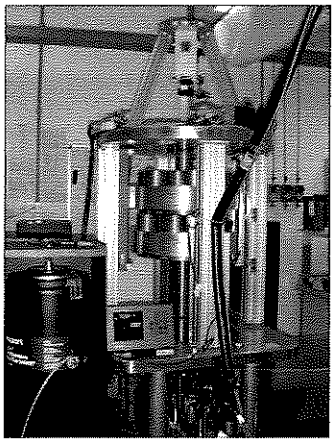

Fig. 2. Apparatus for the MAGIA experiment. The magnetically-shielded vertical tube in which the cold atoms are launched in a fountain from the magneto-optical trap can be seen at the center. The source mass surrounding the tube is composed of 24 tungsten cylinders which are placed on a mount that allows to precisely position them with respect to the position of the atom interferometry sensors.

determine its value but the results of different experiments are inconsistent with each other. Most of the experiments conducted to date were based on the torsion balance, as in the experiment of Cavendish, and in all cases macroscopic masses had been used.

In the MAGIA experiment, we used for the first time a microscopic probe consisting of rubidium atoms cooled by laser light at a temperature of about two microKelvin and vertically launched in an atomic fountain. A mass of about 500 kg of tungsten, placed at a distance of a few centimeters from the atoms, generates a variation of the acceleration of the atoms around ten million times smaller than the acceleration of gravity g due to the Earth. Although this effect is minimal, it was measured with high accuracy by means of an atom interferometry method called Raman pulse interferometry first demonstrated by S. Chu (Nobel Lectures, 1997).

In order to subtract common-mode systematic effects, two vertically displaced atom interferometers were interrogated simultaneously and the source masses could be placed in different positions with respect to the atomic sensors to modulate the relevant effect.

From the measurement of the gravitational field produced by the source mass and the precise characterization of the mass distribution, it was possible to determine the value of $G = 6.67191\ (99) \times 10^{-11} m^3\ kg^{-1}\ s^{-2}$ with a relative uncertainty of 150 parts per million. The value obtained differs by about 1.5 standard deviations from the currently accepted value.

Other laboratories are now trying to reproduce our experiment and test the result. One can hope that the new method we demonstrated will lead to a better control of systematic errors, compared to previous experiments performed with classical apparatus, and eventually provide a precise value for this fundamental constant.

4 – CONCLUSIONS

The ability to control the internal and external degrees of freedom of atoms opened the way to new experiments in gravitational physics and for the precision measurement of fundamental physical quantities. I discussed experiments we performed recently using atom interferometers and optical atomic clocks. These new quantum devices based on cold atoms will enable in the future new fundamental physics experiments as, for example, the investigation of quantum gravity effects (Amelino-Camelia, 2009), the detection of gravitational waves at frequencies not reached by optical interferometers (Tino, 2011), and other stringent tests of general relativity in space (Tino, 2013). They will be used also for applications in fields such as geophysics, underground prospecting for mineral resources, and for the prediction of volcanic eruptions (de Angelis 2009).

5 - REFERENCES

(Nobel Lectures, 1997) S. Chu, C. N. Cohen-Tannoudji, W. D. Phillips, 1997 Nobel Lectures in Physics, Rev. Mod. Phys., Vol. 70, No. 3 (1998).

(Tino, 2014) G. M. Tino and M. A. Kasevich (Eds.), *Atom Interferometry*, SIF and IOS Press (2014).

(Poli, 2013) N. Poli, C. W. Oates, P. Gill, G. M. Tino, Optical Atomic Clocks, La Rivista del Nuovo Cimento vol. 36 n. 12, p. 555 (2013).

(Tarallo, 2014) M. G. Tarallo, T. Mazzoni, N. Poli, D.V. Sutyrin, X. Zhang, G. M. Tino, Test of Einstein Equivalence Principle for 0-Spin and

Half-Integer-Spin Atoms: Search for Spin-Gravity Coupling Effects, Physical Review Letters vol. 113, p. 023005 (2014).

(Poli, 2011) N. Poli, F.-Y. Wang, M. G. Tarallo, A. Alberti, M. Prevedelli, G. M. Tino, Precision Measurement of Gravity with Cold Atoms in an Optical Lattice and Comparison with a Classical Gravimeter, Physical Review Letters vol. 106, p. 038501 (2011).

(Galileo, 1638) Galileo Galilei, Discorsi e Dimostrazioni Matematiche Intorno a Due Nuove Scienze, 1638.

(Capozziello, 2011) S. Capozziello and M. De Laurentis, Extended Theories of Gravity, Phys. Rep. vol. 509, p. 167 (2011).

(Ferrari, 2006) G. Ferrari, N. Poli, F. Sorrentino, G. M. Tino, Long-lived Bloch oscillations with Bosonic Sr Atoms and Application to Gravity Measurement at the Micrometer Scale, Physical Review Letters vol. 97, p. 060402 (2006).

(Poli, 2014) N. Poli, M. Schioppo, S. Vogt, St. Falke, U. Sterr, Ch. Lisdat, G. M. Tino, A transportable strontium optical lattice clock, Appl. Phys. B vol. 117, p. 1107 (2014).

(Tino, 2013) G. M. Tino et al., Precision Gravity Tests with Atom Interferometry in Space, Nuclear Physics B vol. 243–244, p. 203 (2013).

(Rosi, 2014) G. Rosi, F. Sorrentino, L. Cacciapuoti, M. Prevedelli, G. M. Tino, Precision Measurement of the Newtonian Gravitational Constant Using Cold Atoms, Nature vol. 510, p. 518 (2014).

(Amelino-Camelia, 2009) G. Amelino-Camelia, C. Laemmerzahl, F. Mercati, G. M. Tino, Constraining the Energy-Momentum Dispersion Relation with Planck-Scale Sensitivity Using Cold Atoms, Phys. Rev. Lett. vol. 103, p. 171302 (2009).

(Tino, 2011) G. M. Tino, F. Vetrano, C. Lämmerzahl (Eds.), Gravitational Waves Detection with Atom Interferometry, Proceedings of the Workshop held in 2009 at Galileo Galilei Institute in Arcetri, General Relativity and Gravitation vol. 43, p. 1901 (2011).

(de Angelis, 2009) M. de Angelis, A. Bertoldi, L. Cacciapuoti, A. Giorgini, G. Lamporesi, M. Prevedelli, G. Saccorotti, F. Sorrentino, G. M. Tino, Precision Gravimetry with Atomic Sensors, Measurement Science and Technology vol. 20, p. 022001 (2009).

Rend. Acc. Sc. fis. mat. Napoli
Vol. LXXXII, (2015) pp. 149-152

DNA synthesis in mouse brain cytoplasm

Marina Prisco[1], Joyce Casalino[1], Carolina Cefaliello[1]
and Antonio Giuditta*

Nota presentata dal socio Antonio Giuditta
(Adunanza del 18 dicembre 2015)

Key words: metabolic DNA, brain, DNA synthesis, cytoplasm

Abstract – Previous data have indicated that newly synthesized DNA is localized in the presynaptic terminals of squid optic lobes and in cytoplasmic particles from rat brain. The latter localization has been confirmed by immunofluorence analyses of subcellular particles from mouse brain following the incorporation of BrdU into DNA.

Riassunto – Dati precedenti hanno indicato la presenza di DNA appena sintetizzato nei terminali presinaptici dei lobi ottici del calamaro e nel particolato citoplasmatico del cervello di ratto. Quest'ultima localizzazione è stata confermata da analisi di immunofluorescenza dei componenti subcellulari del cervello di topo successive all'incorporazione di BrdU nel DNA.

1 – INTRODUCTION

Previous experiments have shown that brain DNA is actively synthesized and degraded in the adult rat (Perrone Capano et al., 1982) and that its turnover is modulated by learning (Reinis, 1972; Ashapkin et al., 1983; Scaroni et al., 1983; Giuditta et al., 1986), post-trial sleep (Giuditta et al., 1985) and circadian oscillations (Grassi Zucconi et al., 1988; 1990; for a review, see Grassi Zucconi and Giuditta, 2002). These data were recently enriched by the unexpected recovery of a notebook that contained interesting observations on brain newly synthesized DNA. The experiments were made in the seventies but they had remained hidden in the lost notebook. The data suggested that most newly synthesized DNA was associated with cytoplasmic organelles exhibiting different features from nuclei and mitochondria (Rutigliano and Giuditta, 2015).

Additional data in agreement with these results (Giuditta et al., 1986) were recently interpreted to suggest that newly synthesized DNA could be associated with synaptosomes that are also present in the brain mitochondrial fraction. This possibility was examined by analyzing the large synaptosomes of squid optic lobes that originate from the nerve terminals of retinal photoreceptors. In previous experiments with optic lobe slices incubated with [^{3}H]uridine they were shown to contain newly synthesized RNA that in view of the different

[1]Biology Department, Federico II University, Naples Italy; *corresponding author: giuditta@unina.it.

location of their cognate perikarya could only derive from nearby cells of a presumably glial nature (Eyman et al., 2007). Comparable experiments were performed by incubating optic lobe slices with the DNA precursor BrdU and visualizing the newly synthesized BudR-DNA using a fluorescent anti-BrdU antibody. The experiments demonstrated that newly synthesized DNA was indeed present in the terminals of squid photoreceptor neurons (Cefaliello et al., 2015).

We now report data extending comparable observations to mouse brain. They indicate that most newly synthesized DNA is not present in nuclei but in cytoplasmic organelles of a presumably synaptosomal nature.

2 - Methods

A male 2 month old CD1 mouse was injected subcutaneously with 150 µl of 5 mM BrdU and was decapitated 2 h later. Brain freed from large vessels and extraneous material at ice temperature was homogenized in a Dounce homogenizer and brought to 15 ml 0.32 M sucrose, 10 mM Tris-Cl pH 7.4 (homogenizing medium or HM). A 0.5 ml sample of the homogenate was diluted with an equal volume of HM and centrifuged at 1000 g for 2 minutes. The sediment was resuspended in 1 ml HM (the nuclear fraction) and the supernatant fraction was centrifuged at 10,000 g for 20 minutes to obtain the mitochondrial fraction that was also resuspended in 1 ml HM. Both fractions and 1 ml aliquot of the homogenate were incubated with equal volumes HM containing 8% paraformaldehyde and kept 20 min at room temperature. The precipitated material collected by centrifugation (5000 g, 2 minutes) was washed 3 times with 2 ml HM by centrifugation and resuspended in 1 ml HM. The samples were kept at 4 °C.

30 µl of samples were spotted on Superfrost slides and dried at 37°C. After blocking with 5% bovine serum albumine (BSA) in phosphate buffer (PB) the slides were incubated with anti-BrdU antibody Alexa Fluor 488 conjugate (Merck Millipore) diluted 1:5 in 1% BSA in PB for 1 h at room temperature and then with Hoechst 33258 (Sigma Aldrich) 5 µg/ml for 10 min at room temperature. The fluorescent signal was analyzed with Zeiss Axioskop microscope and images were acquired with an AxioCam MRc5 camera and analyzed with AxioVision 4.7 software Axioskop System (Zeiss, Germany).

3 – RESULTS

As shown by Figure 1, the green fluorescence of the anti-BrdU antibody is conspicuously present in the nuclear fraction in round bodies of variable size that tend to form clusters. Most of them are not associated with isolated or aggregated blue-fluorescent nuclei stained with the dsDNA-specific DAPI reagent.

Green fluorescent round bodies of variable size of somewhat smaller dimension are also present in the mitochondrial fraction (Figure 2) in which nuclei are essentially absent. A large number of blue fluorescent nuclei and of isolated and clustered green fluorescent round bodies are present in the homogenate (Figure 3). The clustered formations are larger than those present in the nuclear fraction presumably because they had not been compressed by the gravitational force. They more clearly appear as resulting from the association of round bodies of variable size. Notably, as in the nuclear and mitochondrial fractions, the green fluorescent round bodies present in the homogenate are fully separated from the blue fluorescent nuclei.

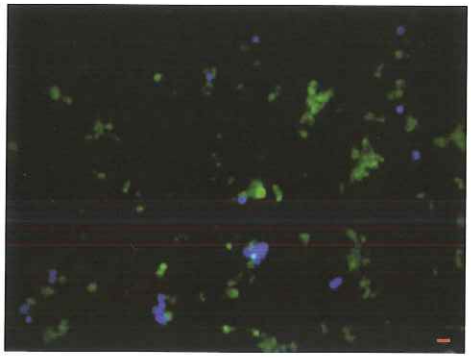

Figure 1. The nuclear fraction
Scale bar, 10 μm

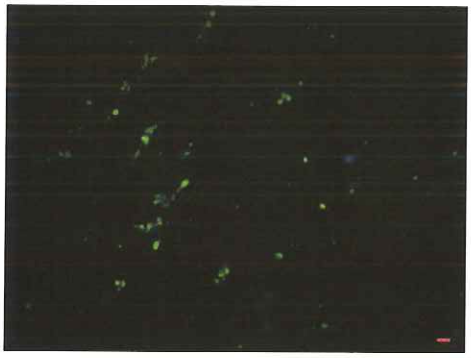

Figure 2. The mitochondrial fraction.
Scale bar, 10 μm

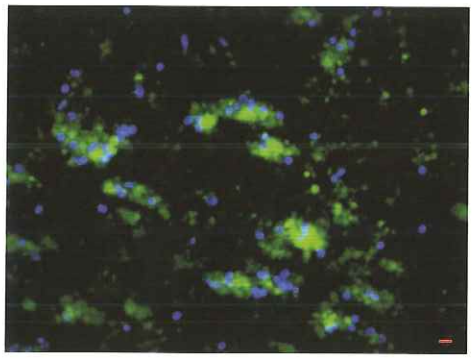

Figure 3. The homogenate.
Scale bar, 10 μm

4 – DISCUSSION

The early data indicating that most newly synthesized DNA from rat brain was not localized in nuclei or mitochondria were based on the following two sets of observations: i) the [^{3}H]thymidine-labeled DNA exhibited a different subcellular distribution than the cytochrome oxidase activity that reflected the presence of mitochondria; and ii) the putative hybrids between [^{3}H]thymidine-labeled DNA and RNA that were detected by cesium gradient centrifugation after a 30 min incorporation were more prevalent in the mitochondrial fraction than in the nuclear fraction (Rutigliano and Giuditta, 2015). These observations are to be considered by keeping in mind that brain subcellular fractions obtained by differential centrifugation are not only containing nuclei or mitochondria but are also heavily contaminated with other cellular organelles, notably synaptosomes.

The present morphological analysis of the comparable subcellular fractions from mouse brain confirms that newly synthesized BrdU-labeled DNA is largely located in subcellular particles that are clearly distinguished from nuclei and may resemble synaptosomes for their general round shape and for their smaller size in the mitochondrial fraction. Such tentative interpretation is also in line with data demonstrating the presence of newly synthesized BrdU-labeled DNA in the large presynaptic synaptosomes of the optic lobes (Cefaliello et al., 2015).

5 - REFERENCES

Ashapkin V.V., Romanov G.A., Tushmalova N.A., Vanyushin B.F. (1983) Selective DNA synthesis in the rat brain induced by learning. Biokhimija **48**: 355-362.

Cefaliello C., Prisco M., Crispino M. and Giuditta A. (2015) Newly synthesized DNA in squid nerve terminals. Rendiconto dell'Accademia delle Scienze Fisiche e Matematiche, Serie IV – Vol. LXXXII – Anno CLIV, giugno 2015 (in press).

Eyman M., Cefaliello C., Ferrara E., De Stefano R., Scotto Lavina Z., Crispino M., Squillace A., van Minnen J., Kaplan B. B. and Giuditta A. (2007) Local synthesis of axonal and presynaptic RNA in squid model systems. Eur. J. Neurosci. **25**: 341-350.

Giuditta A., Ambrosini M. V., Scaroni R., Chiurulla C., and Sadile A. (1985) Effect of sleep on cerebral DNA synthesized during shuttle-box avoidance training. Physiol.Behav. **34**: 769-778.

Giuditta A., Perrone Capano C., D'Onofrio G., Toniatti C., Menna T., and Hydèn H. (1986) Synthesis of rat brain DNA during acquisition of an appetitive task. Pharmacol.Biochem.Behav. **25**: 651-658.

Grassi Zucconi G., Menichini E., Castigli E., Belia S., and Giuditta A. (1988) Circadian oscillations of DNA synthesis in rat brain. Brain.Res. **447**: 253-261.

Grassi Zucconi G., Crognale M. C., Bassetti M. A., and Giuditta A. (1990) Environmental stimuli modulate the circadian rhythm of [3H- methyl] thymidine incorporation into brain DNA of male rats. Behav.Brain Res. **41**: 103-110.

Grassi Zucconi G. and Giuditta A. (2002) Is it only neurogenesis? Rev. Neurosci. **13**: 375-382.

Perrone Capano C., D'Onofrio G., and Giuditta A. (1982) DNA turnover in rat cerebral cortex. J. Neurochem. **38**: 52-56,.

Reinis S. (1972) Autoradiographic study of 3H-thymidine incorporation into brain DNA during learning. Physiol. Chem. Phys. **4**: 391-397.

Rutigliano B. and Giuditta A. (2015) Rendiconto dell'Accademia delle Scienze Fisiche e Matematiche, Serie IV – Vol. LXXXII – Anno CLIV, novembre 2015 (in press).

Scaroni R., Ambrosini M. V., Principato G. B., Federici F., Ambrosi G., and Giuditta A. (1983) Synthesis of brain DNA during acquisition of an active avoidance task. Physiol. Behav. **30**: 577-582.

Appendice

Rend. Acc. Sc. fis. mat. Napoli
Vol. LXXXII, (2015) pp. 155-200

L'Osservatorio Meteorologico di *San Marcellino* - Napoli Centro: i dati dell'anno 2015

Nota di Adriano Mazzarella[1]*, Raffaele Di Cristo[1], RaffaeleViola[1]

Presentata dal socio Giuseppe Luongo
(Adunanza del 15 gennaio, 2016)

Key words: Air temperature, atmospheric pressure, rainfall, solar radiation, wind intensity-direction, UV index

Abstract - The analysis of all meteorological parameters of the year 2015 shows that:

• The monthly mean pressure ranges between 1012.8 hPa of February and 1031.6 hPa of December, with an annual mean of 1017.4 hPa, with an absolute minimum of 984.5 hPa measured on 30 January at 15:10 and with an absolute maximum of 1037.4 hPa measured on December 6 at 23:20.

• The monthly mean air temperature ranges from 10.4 °C of February and 28.4 °C of July, with an annual mean of 18.5 °C, with an absolute minimum of 2.2 °C measured on 9 February at 13:30 and with an absolute maximum of 37.1 °C measured on 8 August at 15:00.

• The monthly mean relative humidity ranges from 62.7% of June and 73.7% of January, with an annual mean of 69.3%, with an absolute minimum of 22.0% measured on May 12 at 14:20 and with an absolute maximum of 95.0% measured on 31 January at 19:40.

• The mean monthly global solar radiation ranges between 160.5 W/m^2 of January and 454.5 W/m^2 in July, with an annual mean of 315.8 W/m^2 and with an absolute

[1]Osservatorio Meteorologico -Dipartimento di Scienze della Terra, dell'Ambiente e delle Risorse
Largo San Marcellino 10 80122 Napoli Università degli Studi di Napoli Federico II
*Author to whom correspondence should be addressed

maximum of 1285.0 W/m^2 measured on 24 May at 14:20.

• The mean monthly UV Index ranges from 2.6 of January to 5.9 of August, with an annual average of 5.2 and with an absolute maximum of 12.5 measured on 27 July at 13:30.

• The monthly mean wind intensity ranges between 1.0 m/s of July and 1.8 m/s of March, with an annual mean of 1.3 m/s and with most intense gust of 22.4 m/s measured on 4 February at 00:40.

• The wind direction shows a mode from the North, North-East in the months of January, February, November, December, from South, South-West in the months of March, April, May, June, July, August.

•The monthly cumulate rainfall ranges from 0 mm of December to 189.3 mm of February, with a cumulate annual value of 840.7 mm and with an absolute maximum of 189.3 mm measured on 22 February.

Riassunto - Dall'analisi di tutti i parametri meteo dell'anno 2015 emerge quanto segue:

• La pressione atmosferica media mensile oscilla fra 1012.8 hPa di febbraio e 1031.6 hPa di dicembre, con una media annua di 1017.4 hPa, con un minimo assoluto di 984.5 hPa registrato il 30 gennaio alle ore 15:10 e con un massimo assoluto di 1037.4 hPa registrato il 6 dicembre alle ore 23:20.
• La temperatura dell'aria media mensile oscilla fra 10.4°C di febbraio e 28.4°C di luglio, con una media annua di 18.5°C, con un minimo assoluto di 2.2°C registrato il 9 febbraio alle ore 13:30 e con un massimo assoluto di 37.1°C registrato il 31 gennaio alle ore 19:40.
• L'umidità relativa media mensile oscilla fra 62.7% di giugno e 73.7% di gennaio, con una media annua di 69.3%, con un minimo assoluto del 22.0% registrato il 12 maggio aprile alle ore 14:20 e con un massimo assoluto di 95.0% registrato il 31 gennaio alle ore 19:40.
• La radiazione solare globale media mensile oscilla fra 160.5 W/m^2 di gennaio e 454.5 W/m^2 di luglio, con una media annua di 315.8 W/m^2 e con un massimo assoluto di 1285.0 W/m^2 registrato il 24 maggio alle ore 14:20.
• L'indice UV medio mensile oscilla fra 2.6 di gennaio e 5.9 di agosto, con una media annua di 5.2 e con un massimo assoluto di 12.5 registrato il 27 luglio alle ore 13:30.
• L'intensità media mensile del vento oscilla tra 1.0 m/s di luglio e 1.8 m/s di marzo, con una media annua di 1.3 m/s e con la raffica più intensa di 22.4 m/s registrata il 4 febbraio alle ore 13:50.
• La direzione del vento presenta una moda da Nord, Nord-Est nei mesi di gennaio, febbraio, novembre, dicembre, da Sud, Sud-Ovest nei mesi di marzo, aprile, maggio, giugno, luglio, agosto.
• La pioggia cumulata mensile oscilla tra il valore 0 mm di dicembre e i 189.3 mm di

febbraio, con un valore annuale cumulato di 840.7 mm e con un massimo giornaliero assoluto di 189.3 mm registrato il 22 febbraio.

1 – INTRODUZIONE

I dati meteo sono attualmente rilevati da una centralina automatica sita sulla torretta dell'edificio di San Marcellino (lat. 40°50'50" N; long. 14°15'29" E; quota 50 m slm), sede attuale del Dipartimento di Scienze della Terra, dell'Ambiente e delle Risorse a meno di 50 m dall'Accademia di Scienze Fisiche e Matematiche della Società Nazionale di Scienze, Lettere ed Arti in Napoli.

La stazione gestisce i seguenti sensori: temperatura dell'aria (°C), pressione atmosferica (hPa) (normalizzata a livello del mare), umidità relativa (%), velocità del vento (m/s), direzione del vento (°Nord), precipitazione (mm), radiazione solare globale (W/m^2), indice UV (scala da 0 a 16).

Per ogni mese i valori estremi giornalieri sono evidenziati in grassetto.

I dati sono acquisiti con cadenza di 10 minuti ed i valori, fatta eccezione per la pioggia che viene registrata come cumulata, sono quelli istantanei; i dati giornalieri di radiazione globale ed indice UV sono mediati sulla loro effettiva durata.

Sono stati analizzati anche i dati giornalieri della temperatura del mare (°C) misurati nel golfo di Napoli (lat. 40°50'23"; long. 14° 16'09") presso il molo del Carmine, gentilmente forniti dall'Istituto Superiore per la Protezione e la Ricerca Ambientale (ISPRA). Per novembre e dicembre c'è indisponibilità del dato.

La direzione del vento è calcolata come moda sia a scala di 10 minuti per i grafici orari che a scala giornaliera per i grafici mensili. E' considerata variabile (var.) quando la direzione non è stata registrata su uno stesso quadrante per più di 8 ore.

L'assenza del dato indica sensore fuori uso

2- MATERIALI E METODI

Il bollettino meteorologico dell'anno 2015 è così organizzato:

- Un breve rapporto meteorologico per ogni mese;
- Una catalogazione delle medie orarie mensili (00 -23 h) e dei relativi grafici per ogni mese;
- Una catalogazione dei valori medi giornalieri e dei relativi grafici, per ogni

mese, con l'indicazione dei valori estremi registrati;

- Un riepilogo mensile di tutti i parametri meteo relativo all'anno in corso;
- Un riepilogo mensile delle frequenze di precipitazione, temperature minime e massime distinte per soglia.

E' possibile accedere via web alla consultazione dei dati rilevati in tempo reale all'indirizzo:

http ://www.meteo.unina.it

RAPPORTI METEO MENSILI

GENNAIO 2015

Il mese di gennaio 2015 è stato caratterizzato da una notevole variabilità atmosferica: con la temperatura al di sotto della media nei primi 3 giorni, al di sopra fino all'inizio della terza decade e ancora al di sotto e con piogge fino alla fine del mese. Le medie delle temperature minime e massime sono state così, rispettivamente, di 8.5 °C (un grado e mezzo in più delle media stagionale) e di 13.3 °C (mezzo grado in più); la quantità di pioggia caduta è stata di 177.7 mm, quasi il doppio della media stagionale. Tale scenario è dipeso dall'alternanza sul Mediterraneo prima di masse d'aria fredda siberiana, poi atlantica ed infine polare, con neve sul Vesuvio il 25, il 26 e il 28 e freddo accentuato dall'effetto del vento da Nord. I "giorni della merla", 29, 30 e 31 gennaio, sono stati all'insegna della pioggia e di un forte libeccio che ha messo a dura prova la navigazione nel golfo.

FEBBRAIO 2015

Il mese di febbraio 2015 è stato caratterizzato da valori di temperatura dell'aria quasi sempre al di sotto o in linea con le medie stagionali e il cono del Vesuvio sistematicamente imbiancato di neve per tutti i primi 17 giorni. Le medie delle temperature minime e massime dell'intero mese sono state, rispettivamente, di 7.9 °C, mezzo grado in più della media stagionale, e di 13.3°C, mezzo grado in meno; il giorno più freddo è stato il 9 febbraio con 2.2 °C. La quantità di pioggia è stata di 189.3 mm, due volte e mezzo quella che cade normalmente a febbraio, con 15 giorni di pioggia di cui 8 consecutivi; la quantità è stata di poco inferiore ai 229 mm del 1996 e ai 195 mm del 1873 e del 1906. Il freddo continuo, anche se non intenso, di questo febbraio è stato causato dalle numerose incursioni di aria fredda polare che hanno colpito intensamente il Nord dell'Italia e in maniera più attenuata il Sud.

MARZO 2015

Il mese di marzo 2015 sarà ricordato come un mese molto ventoso, con raffiche di 80 km orari nei giorni 6 e 25 che hanno causato la caduta di alberi secolari e messo a dura

prova la navigazione nel golfo. La temperatura dell'aria è stata molto variabile, con valori distribuiti al di sopra e al di sotto della media in maniera omogenea così come è da aspettarsi per un mese di passaggio dall'inverno alla primavera quando miti masse d'aria atlantica tendono a sostituire masse d'aria fredde preesistenti. La media delle temperature massime è stata così di 15.9 °C, in linea con la media del periodo, mentre la media delle minime è stata di 10.5 °C, più alta di 1.5 °C e questo perché la temperatura minima, diversamente dalla massima, risente molto dell'influenza dell'isola di calore urbana. La pioggia caduta è stata di 34.3 mm, circa la metà di quella che cade normalmente a marzo, e il cono del Vesuvio è stato ammantato di neve nei giorni 5,6 e 12.

APRILE 2015

La temperatura dell'aria di aprile è stata molto variabile con la prima decade più bassa di circa 3°C rispetto alla media stagionale e con la rimanente parte del mese più alta di circa 2 °C. Le medie delle temperature minime e massime dell'intero mese sono state, rispettivamente, di 12.8 °C, un grado e mezzo in più della media stagionale, e di 18.8°C, mezzo grado in meno. Il giorno più caldo è stato il 22 aprile con 23.6 °C e la pioggia è stata pari a 51.1 mm, un po' meno di quanto cade normalmente a aprile.

MAGGIO 2015

Una notevole variabilità atmosferica ha caratterizzato il mese di maggio 2015, con la temperatura dell'aria al di sotto della media stagionale nei primi 3 giorni, al di sopra fino alla fine della seconda decade e decisamente al di sotto nei rimanenti giorni. La media delle minime è stata così di 17.6 °C, più elevata di 2.5 °C della relativa media stagionale, mentre quella delle massime è stata di 24.0 °C, mezzo grado in più. Il giorno più caldo è stato il 5 maggio con 31.1 °C e le precipitazioni hanno raggiunto i 30.9 mm, il 25% in meno di quanto piove normalmente a maggio. La variabilità atmosferica di questo mese è dovuta alla prolungata presenza dell'anticiclone delle Azzorre ad Ovest del Mediterraneo e dalla depressione ligure posizionata una volta più a Sud e una volta più a Nord, in grado di attrarre prima aria calda africana e poi aria fredda polare. Ma tali improvvisi sbalzi termici sono fisiologici a maggio quando l'atmosfera si prepara al passaggio dall'inverno all'estate e i ghiacciai per sciogliersi sottraggono energia termica all'ambiente.

GIUGNO 2015

La temperatura dell'aria di giugno 2015 è stata altalenante: al di sopra della media stagionale nei primi 15 giorni, al di sotto nei successivi 10 giorni e ancora al di sopra negli ultimi giorni. Tale variabilità termica non è sorprendente ma appartiene alla fisiologia di giugno a causa dell'alternarsi sul Mediterraneo di masse d'aria fredda atlantica e masse d'aria calda subtropicale, quest'ultime in grado di determinare un notevole disagio nella popolazione per gli elevati valori di temperatura e di umidità. La media delle temperature massime e minime è stata a Napoli centro rispettivamente di 28.0 °C, mezzo grado in più di quella stagionale, e di 21.1 °C, due gradi e mezzo più elevata. Il giorno più caldo è stato il 13 giugno con 31.9 °C; le precipitazioni sono state pari a 50.8 mm, 20 mm in più del valore stagionale, e concentrate nei rovesci dei giorni 8, 9 e 17 giugno.

LUGLIO 2015

Luglio 2015 ha sorpreso i climatologi per l'assenza sul Mediterraneo del mite anticiclone delle Azzorre completamente soppiantato dal più umido e bollente anticiclone africano che è stato responsabile per tutto il mese, con l'eccezione degli ultimi giorni, di temperature elevate e situazioni di grave disagio notturno nella popolazione per valori di umidità dell'ordine dell'85%. La media delle temperature massime è stata perciò di 31.9 °C, 2 °C in più del valore stagionale. I giorni più caldi sono stati il 17, 18 e 19 luglio con 36.7, 36.9 e 35.1 °C, rispettivamente; le precipitazioni sono state pari a 27.9 mm, pari a quasi il doppio della media stagionale, e concentrate nei giorni 23 e 24 in seguito alla formazione di imponenti temporali di calore. La temperatura del mare è schizzata dai 21.5°C dell'inizio del mese ai 27.5°C della fine del mese come ha avuto modo di notare chi ha avuto la fortuna di fare i bagni in questo periodo. Tutti i mass media hanno urlato e ritenuto che la causa di tutto ciò sia esclusivamente dovuto ai cambiamenti climatici determinati dall'uomo. Basta però consultare l'archivio storico dell'Osservatorio meteorologico della Federico II per rendersi conto che valori più elevati a luglio già sono stati raggiunti nel passato intorno a gli anni '50: il 1945 con 32.4 °C, il 1946 con 32.2 °C, il 1947 con 32.7 °C, il 1950 con ben 33.2 °C e il 1953 con 33.1 °C.

AGOSTO 2015

Agosto 2015 è stato più variabile di luglio: fino al giorno 14 con valori di temperatura massima 4-5 °C al di sopra della media stagionale, nella decade successiva con valori 1-2 °C al di sotto e nell'ultima settimana ancora con 3-4 °C al di sopra La media delle temperature minime e massime è stata, rispettivamente, di 24.5 °C, tre gradi in più della media, e di 31.2 °C, un grado in più. Il giorno più caldo è stato l'8 agosto con una temperatura massima di ben 37.2 °C; la pioggia caduta è stata pari a 35.5 mm, 10 mm in più di quella che cade normalmente in agosto e quasi tutta concentrata nel rovescio del giorno 16. Tale scenario meteorologico è imputabile sostanzialmente all'anticiclone delle Azzorre che si è posizionato nella prima decade su alte latitudini ed ha agevolando la risalita del bollente ed umido anticiclone africano; nella decade successiva, spostandosi sul Mediterraneo, ha determinato un brusco abbassamento della temperatura con violenti temporali; nella settimana successiva, abbandonando il Mediterraneo, ha richiamato ancora l'anticiclone africano che ha causato un vero e proprio colpo di coda dell'estate.

SETTEMBRE 2015

Il mese di settembre 2015 è stato caratterizzato da una notevole variabilità termica con la temperatura dell'aria altalenante fra 3-4 °C al di sopra della media nella prima parte del mese e 2-3 °C al di sotto della media nell'ultima parte del mese. A livello mensile, la media delle temperature minime è stata così di 21.0 °C, due gradi in più della media stagionale, mentre quella delle temperature massime è stata di 27.2°C, in linea con la media. Scenari così diversi sono stati determinati dall'alternarsi sul Mediterraneo dell'anticiclone africano e di aree cicloniche che hanno attratto in successione aria bollente ed umida africana e aria fredda nord-orientale. Il giorno più caldo è stato il 17 settembre con 34.2 °C mentre la temperatura del mare nel golfo, vero termometro ambientale, ha raggiunto i 27 °C nella prima decade e i 25 °C a fine mese che è una temperatura ancora ideale per un bagno a mare. La pioggia è stata pari a 51.0 mm, 15

mm meno della media del periodo. Degna di nota è stata la violenta grandinata del 5 settembre che ha flagellato l'area flegrea con chicchi di grandine pesanti più di 150 grammi.

OTTOBRE 2015

La temperatura dell'aria nella prima decade di ottobre è stata al di sopra della media stagionale e, nella rimanente parte del mese, al di sotto. A livello mensile, la media delle temperature minime è stata così di 16.5 °C, un grado in più della media stagionale, mentre quella delle temperature massime è stata di 21.5 °C, un grado in meno. Il giorno più caldo è stato il 14 ottobre con 24.4 °C. Le precipitazioni sono state pari a 157.9 mm, il 35% in più di quanto piove normalmente ad ottobre e questo surplus è legato alle elevate temperature estive che hanno arricchito l'atmosfera di vapor d'acqua: quando, poi, masse d'aria fredda si incuneano al di sotto delle masse d'aria calda preesistenti si formano nubi temporalesche e piogge abbondanti come quelle che hanno colpito la città di Benevento il 15 ottobre.

NOVEMBRE 2015

I valori di temperatura dell'aria di novembre 2015 a Napoli centro sono stati 2-3 gradi al di sopra della media stagionale nelle prime due decadi e 3-4 gradi al di sotto nell'ultima decade. A livello mensile, le medie delle temperature minima e massima hanno raggiunto, rispettivamente, 13.1 °C, un grado e mezzo più della media, e 18.5 °C, un grado in più. La pioggia, caduta soltanto nell'ultima decade, è stata pari a 34.3 mm, 90 mm in meno di quella che cade normalmente a novembre. La notevole variabilità meteorologica di questo novembre trova la sua spiegazione nella presenza di una estesa ed intensa area anticiclonica sul Mediterraneo che nelle prime due decadi ha determinato cielo sereno, assenza di ventilazione, elevati tassi di umidità e di inquinamento urbano; nell'ultima decade, invece, una profonda depressione sull'Italia ha richiamato aria gelida artica che ha causato una decisa diminuzione della temperatura dell'aria con piogge e neve specie nelle zone interne.

DICEMBRE 2015

Il mese di dicembre 2015 ha sorpreso i meteorologi a causa di una inaspettata e duratura area di alta pressione che ha determinato cielo sereno, valori di temperatura dell'aria bassi di notte ed elevati di giorno, scarsa ventilazione ed una stabilità atmosferica così elevata da costringere l'amministrazione locale ad adottare limitazioni del traffico per diminuire l'inquinamento da polveri sottili. Le medie mensili sono risultate così di 10.2 °C per le temperature minime e di 16.1 per le massime, entrambe due gradi più elevate della media. La pioggia è stata assente e questo è un record per il mese di dicembre almeno sin dal 1872 cioè da quando sono iniziate le rilevazioni sistematiche presso l'Osservatorio Meteorologico della Federico II a Napoli centro. Questo perchè un vigoroso ed ampio anticiclone, rafforzato dal surriscaldamento del Pacifico tropicale (il cosiddetto El Niño), ha raggiunto valori di pressione atmosferica di 1037 hPa e bloccato la normale circolazione atmosferica alle nostre latitudini. E' curioso osservare che anticicloni così poderosi sono in grado di causare anche un abbassamento del livello del mare e che i Napoletani a via Caracciolo hanno potuto verificare attraverso l'insolito affioramento di una parte scura della scogliera normalmente sotto il livello del mare. A chiusura d'anno, risulta utile riportare il bilancio termo-pluviometrico dell'intero 2015:

la temperatura media è stata di 18.5 °C, circa un grado in più rispetto alla media annuale secolare; la quantità di pioggia annuale è stata di 840.7 mm in linea con la media annuale ma con grossi deficit in aprile, novembre e dicembre. La temperatura dell'aria del 2015 non è da record e rientra nella normale variabilità climatica: basti pensare che anni come il 1946, 1947, 2002, 2003 e 2006 sono stati più caldi di circa mezzo grado.

GENNAIO 2015

(medie orarie)

Ore	Temperatura °C	Umidità %	Pressione hPa	Vento velocità m/s	Vento direzione	Radiazione Solare W/m²	Radiazione Solare Indice UV
0	10.4	74.5	1018.6	1.5	W	0.0	0.0
1	10.1	74.6	1018.7	1.6	W	0.0	0.0
2	9.9	74.0	1018.7	1.5	W	0.0	0.0
3	9.8	73.8	1018.5	1.2	W	0.0	0.0
4	9.7	74.4	1018.2	1.3	W	0.0	0.0
5	9.6	75.3	1018.2	1.3	N	0.0	0.0
6	9.6	75.3	1018.3	1.3	N	0.0	0.0
7	9.5	76.3	1018.4	1.2	N	4.1	0.0
8	9.8	76.5	1018.7	1.1	N	51.8	0.7
9	10.5	74.3	1019.0	1.0	N	144.5	1.9
10	11.3	71.6	1019.2	1.1	N	221.6	2.4
11	11.9	70.8	1018.9	1.5	SE	282.1	2.7
12	12.4	69.4	1018.3	1.6	SE	270.8	2.8
13	12.4	69.0	1017.8	1.8	SE	223.8	2.4
14	12.4	69.1	1017.5	1.8	SE	186.3	2.1
15	12.3	70.1	1017.5	1.5	SE	107.1	1.7
16	12.1	71.5	1017.5	1.4	NW	33.0	0.5
17	11.7	72.8	1017.7	1.2	SW	0.9	0.0
18	11.4	74.1	1017.9	1.2	N	0.0	0.0
19	11.2	75.0	1018.0	1.2	W	0.0	0.0
20	11.1	75.3	1018.0	1.2	W	0.0	0.0
21	11.0	74.9	1018.0	1.5	W	0.0	0.0
22	10.8	75.1	1018.0	1.3	W	0.0	0.0
23	10.6	75.5	1017.9	1.2	W	0.0	0.0

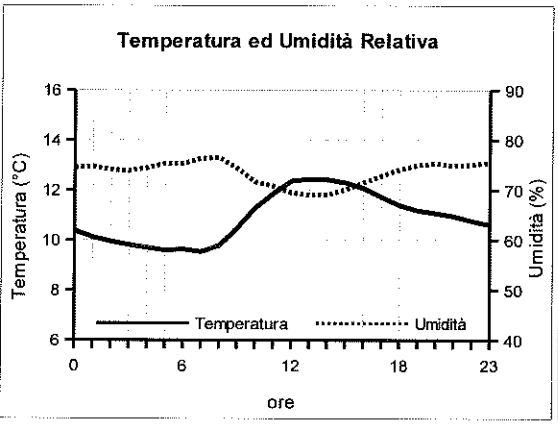

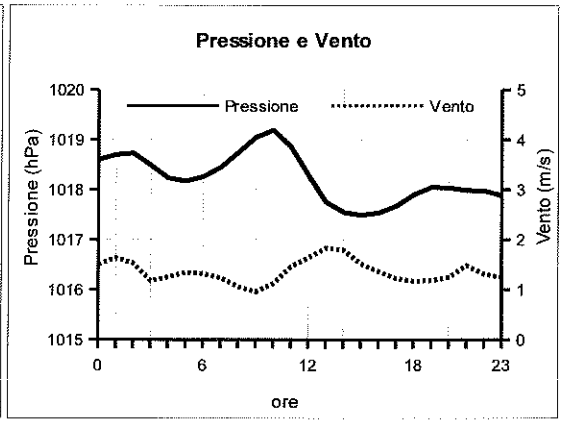

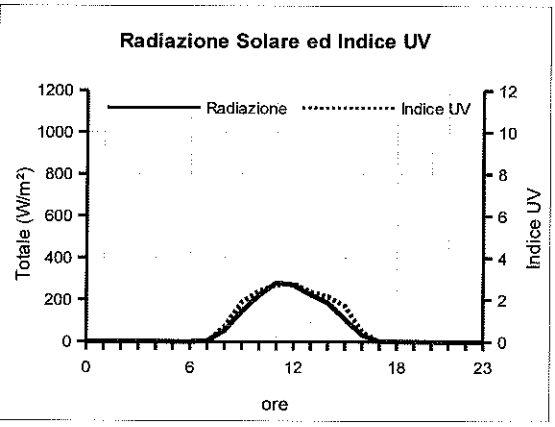

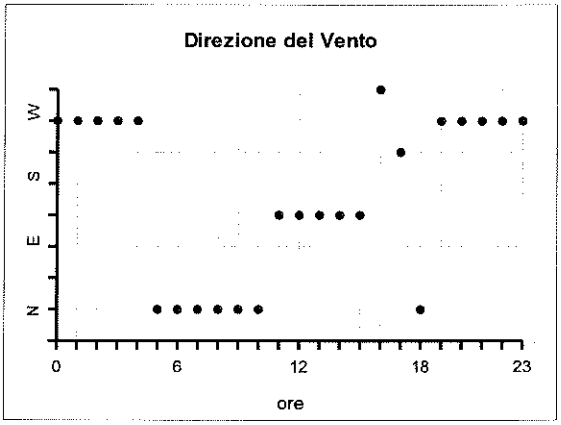

FEBBRAIO 2015

(medie orarie)

Ore	Temperatura °C	Umidità %	Pressione hPa	Vento velocità m/s	Vento direzione	Radiazione Solare W/m²	Radiazione Solare Indice UV
0	9.7	74.4	1012.7	1.7	N	0.0	0.0
1	9.5	74.8	1012.5	1.6	N	0.0	0.0
2	9.3	75.3	1012.3	1.7	N	0.0	0.0
3	9.2	75.1	1012.0	1.8	W	0.0	0.0
4	9.0	75.4	1012.0	1.8	W	0.0	0.0
5	8.9	76.0	1012.1	1.7	N	0.0	0.0
6	8.8	76.2	1012.2	1.5	N	0.1	0.0
7	8.8	76.5	1012.5	1.3	N	22.9	0.5
8	9.6	75.0	1013.0	1.4	N	124.4	2.7
9	10.4	71.9	1013.3	1.5	N	230.7	3.7
10	11.2	69.0	1013.4	1.9	SE	330.6	4.5
11	11.7	67.3	1013.5	1.9	SE	401.8	5.1
12	12.2	65.4	1013.1	2.1	E	397.7	5.1
13	12.3	65.7	1012.7	2.0	S	343.0	4.9
14	12.3	66.0	1012.4	2.3	S	271.9	4.2
15	12.1	66.2	1012.4	2.2	SE	199.9	3.4
16	11.7	68.1	1012.4	1.8	SE	91.9	2.4
17	11.3	69.6	1012.6	1.6	SE	13.8	0.2
18	10.9	71.3	1013.0	1.2	NW	0.0	0.0
19	10.6	72.3	1013.3	1.2	N	0.0	0.0
20	10.2	73.4	1013.6	1.0	N	0.0	0.0
21	10.1	73.6	1013.7	1.2	N	0.0	0.0
22	10.0	73.3	1013.8	1.2	N	0.0	0.0
23	9.9	73.8	1013.7	1.6	N	0.0	0.0

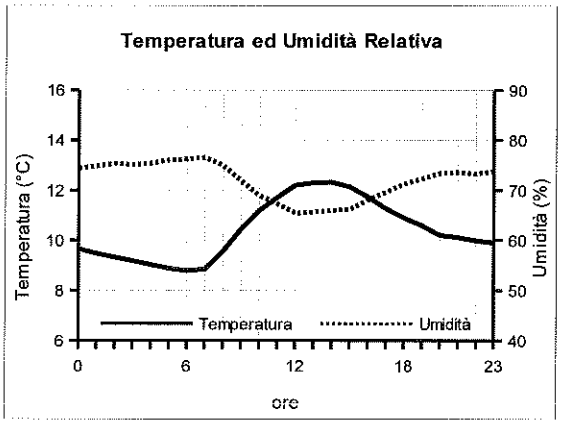

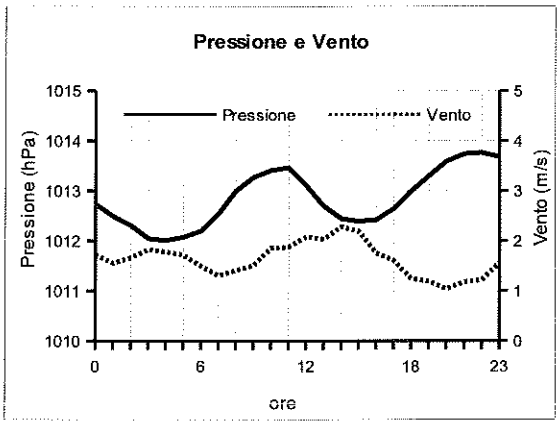

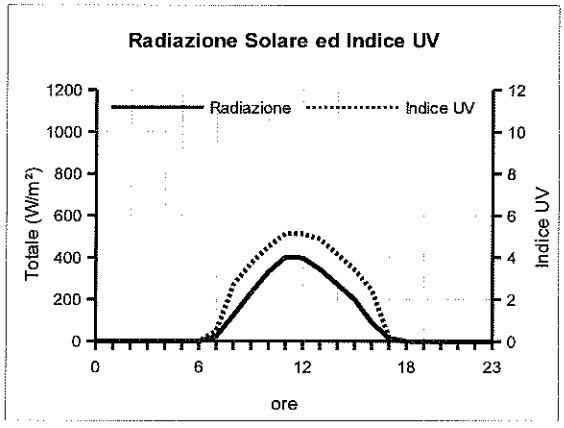

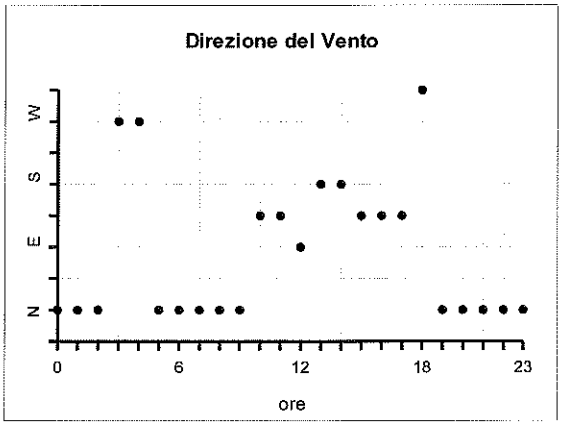

MARZO 2015

(medie orarie)

Ore	Temperatura °C	Umidità %	Pressione hPa	Vento velocità m/s	Vento direzione	Radiazione Solare W/m²	Radiazione Solare Indice UV
0	12.0	72.3	1017.1	1.2	N	0.0	0.0
1	11.9	72.6	1017.0	1.5	N	0.0	0.0
2	11.8	73.7	1016.9	1.3	N	0.0	0.0
3	11.5	73.4	1016.4	1.4	N	0.0	0.0
4	11.4	73.8	1016.2	1.6	N	0.0	0.0
5	11.2	74.4	1016.3	1.6	N	0.0	0.0
6	11.2	74.0	1016.4	1.6	W	7.7	0.0
7	11.5	73.1	1016.7	1.7	W	76.0	1.8
8	12.4	70.5	1017.1	1.6	N	201.7	3.4
9	13.4	66.8	1017.3	1.9	N	333.4	4.3
10	14.0	64.2	1017.4	2.0	SE	433.1	5.1
11	14.5	62.4	1017.3	2.3	SE	534.5	5.8
12	15.0	60.8	1017.0	2.4	SE	531.8	6.0
13	15.1	60.7	1016.6	2.3	S	478.3	5.7
14	15.0	62.3	1016.3	2.4	SW	416.8	5.2
15	14.8	63.2	1016.2	2.4	SW	296.4	4.5
16	14.6	64.2	1016.1	2.3	SW	184.2	3.6
17	14.1	66.1	1016.2	2.1	SW	70.9	1.7
18	13.7	67.8	1016.5	1.7	NW	12.2	0.2
19	13.3	68.9	1016.8	1.5	N	0.6	0.0
20	13.0	70.5	1017.0	1.4	N	0.0	0.0
21	12.6	71.8	1017.1	1.3	N	0.0	0.0
22	12.4	72.6	1017.2	1.5	N	0.0	0.0
23	12.2	72.7	1017.1	1.4	N	0.0	0.0

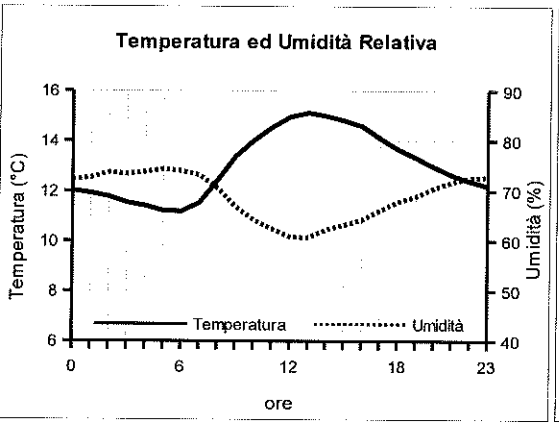

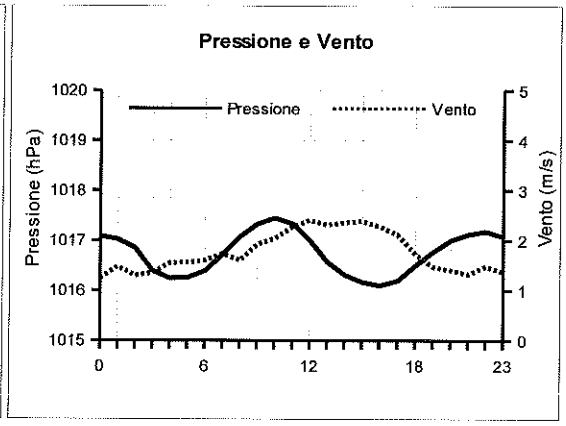

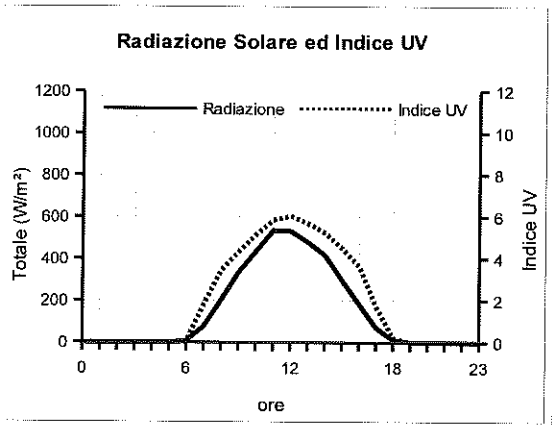

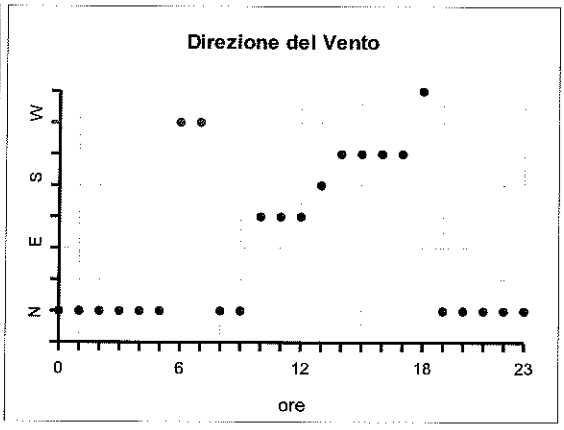

APRILE 2015

(medie orarie)

Ore	Temperatura °C	Umidità %	Pressione hPa	Vento velocità m/s	Vento direzione	Radiazione Solare W/m²	Radiazione Solare Indice UV
0	14.3	77.0	1019.6	0.9	S	0.0	0.0
1	14.0	76.8	1019.5	0.9	SW	0.0	0.0
2	13.9	76.2	1019.3	0.7	W	0.0	0.0
3	13.6	76.4	1019.1	0.6	W	0.0	0.0
4	13.4	76.0	1019.0	0.7	W	0.0	0.0
5	13.3	75.5	1019.0	0.7	W	0.0	0.0
6	13.1	75.5	1019.1	0.7	W	4.9	0.0
7	13.4	74.6	1019.4	0.7	W	73.2	1.7
8	14.5	70.9	1019.7	0.7	SW	214.7	3.5
9	15.5	67.3	1019.9	1.0	SE	375.8	4.2
10	16.1	65.3	1020.1	1.6	E	515.0	5.3
11	16.6	65.0	1020.2	2.1	E	581.0	6.1
12	17.0	64.6	1019.9	2.5	S	647.7	6.9
13	17.4	62.7	1019.6	2.6	S	656.2	7.0
14	17.5	62.4	1019.3	2.5	S	590.9	6.3
15	17.7	61.4	1018.9	2.5	S	520.9	5.4
16	17.7	61.4	1018.6	2.3	S	392.1	4.6
17	17.3	62.5	1018.5	2.3	SW	265.1	3.7
18	16.7	64.9	1018.5	2.0	S	128.2	2.9
19	16.0	68.0	1018.7	1.7	SW	22.6	0.3
20	15.4	71.0	1019.1	1.4	SW	0.1	0.0
21	15.0	73.3	1019.6	1.2	SW	0.0	0.0
22	14.7	74.7	1019.8	0.8	SW	0.0	0.0
23	14.5	76.4	1019.8	0.8	S	0.0	0.0

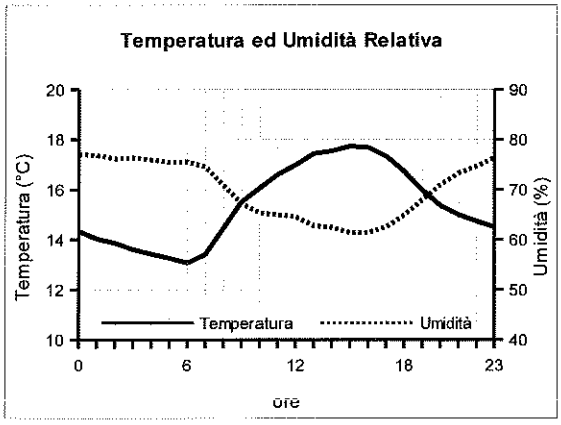

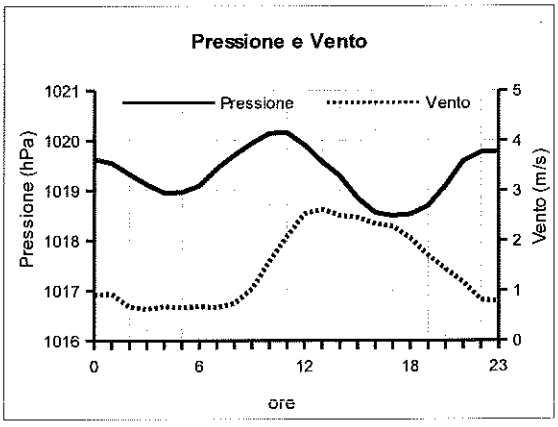

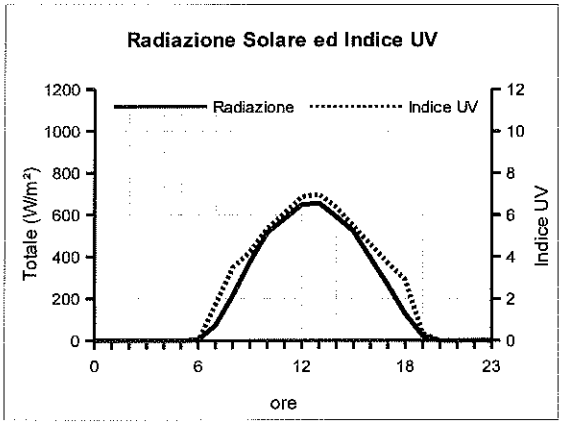

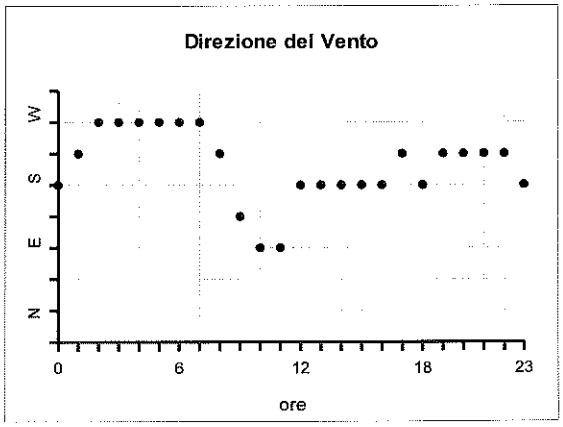

MAGGIO 2015

(medie orarie)

Ore	Temperatura °C	Umidità %	Pressione hPa	Vento velocità m/s	Vento direzione	Radiazione Solare W/m²	Radiazione Solare Indice UV
0	19.3	72.3	1015.7	0.5	S	0.0	0.0
1	19.0	72.8	1015.6	0.5	SW	0.0	0.0
2	18.8	73.0	1015.3	0.5	W	0.0	0.0
3	18.5	74.1	1015.2	0.5	W	0.0	0.0
4	18.3	75.3	1015.1	0.5	W	0.0	0.0
5	18.0	75.6	1015.1	0.3	SW	0.2	0.0
6	17.9	75.2	1015.2	0.5	W	26.8	0.5
7	18.6	72.5	1015.5	0.6	W	130.2	2.5
8	19.6	69.6	1015.7	0.7	SE	268.8	3.6
9	20.4	66.1	1015.8	1.1	E	421.1	4.6
10	21.2	63.1	1015.9	1.6	S	580.5	5.8
11	21.7	62.0	1016.0	2.0	E	649.5	6.9
12	22.1	61.0	1015.9	2.4	S	709.4	7.7
13	22.6	59.9	1015.7	2.4	S	758.1	8.1
14	22.7	60.2	1015.5	2.6	S	708.9	7.5
15	22.6	60.0	1015.3	2.5	S	630.5	6.5
16	22.7	60.5	1015.0	2.2	S	524.2	5.4
17	22.4	63.0	1014.9	2.3	S	383.8	4.3
18	21.9	64.4	1014.9	1.9	S	232.5	3.5
19	21.2	67.1	1014.9	1.7	S	94.9	1.5
20	20.6	69.6	1015.0	1.1	S	31.3	0.4
21	20.2	71.7	1015.4	0.8	W	7.2	0.2
22	20.0	71.4	1015.6	0.8	W	0.4	0.0
23	19.7	71.3	1015.7	0.8	SW	0.0	0.0

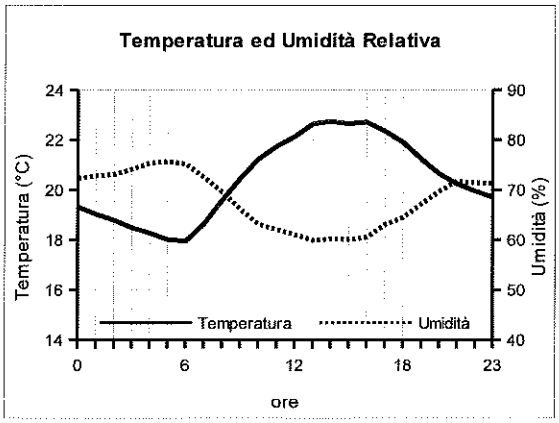

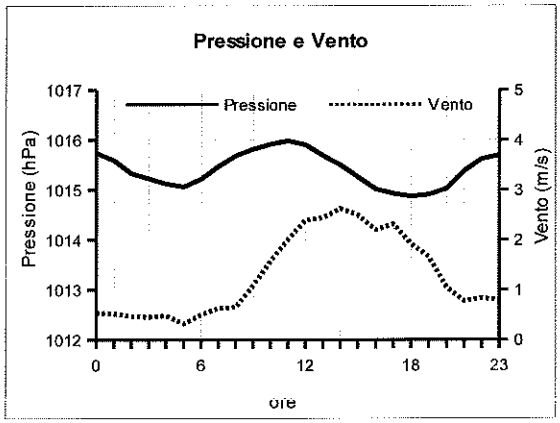

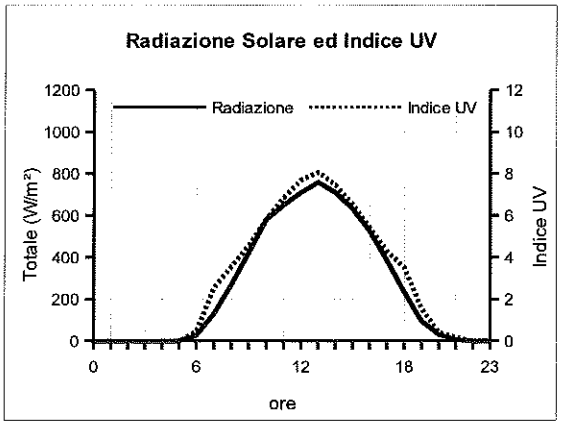

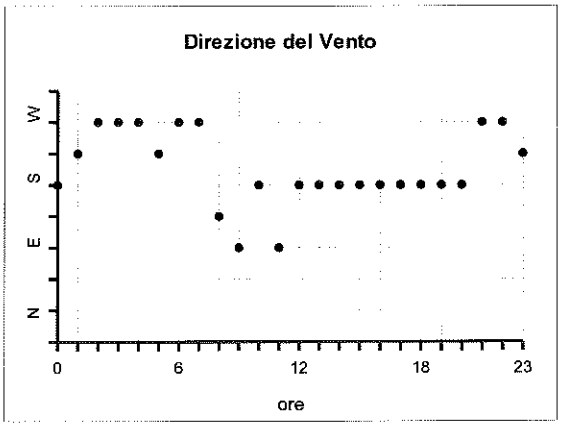

GIUGNO 2015

(medie orarie)

Ore	Temperatura °C	Umidità %	Pressione hPa	Vento velocità m/s	Vento direzione	Radiazione Solare W/m²	Radiazione Solare Indice UV
0	22.9	70.3	1017.2	0.4	N	0.5	0.0
1	22.5	71.5	1017.1	0.4	N	0.5	0.0
2	22.3	70.5	1016.9	0.3	W	0.5	0.0
3	22.0	70.8	1016.7	0.5	W	0.5	0.0
4	21.7	71.5	1016.6	0.4	N	0.5	0.0
5	21.5	71.5	1016.7	0.5	W	9.3	0.0
6	21.8	70.0	1016.8	0.5	N	82.4	0.9
7	22.9	65.8	1016.9	0.6	N	229.7	2.4
8	23.9	62.2	1017.1	0.9	SE	392.9	3.1
9	24.7	60.3	1017.2	1.3	E	533.3	4.0
10	25.2	58.4	1017.3	1.9	E	669.6	5.1
11	25.7	57.2	1017.3	2.2	S	757.1	6.3
12	26.2	56.3	1017.2	2.2	S	835.0	7.5
13	26.8	55.2	1016.8	2.3	S	872.8	7.7
14	27.0	55.7	1016.5	2.4	S	810.8	7.0
15	27.1	55.8	1016.3	2.5	S	699.0	5.9
16	26.7	57.9	1016.2	2.3	S	508.0	4.4
17	26.3	58.9	1016.1	2.1	S	345.1	3.1
18	25.5	61.3	1016.0	1.9	SW	187.6	2.4
19	24.8	64.6	1016.2	1.6	SW	77.9	1.5
20	24.4	65.4	1016.5	1.1	SW	10.7	0.0
21	24.0	66.9	1016.8	0.7	NW	0.5	0.0
22	23.6	69.2	1017.1	0.4	SW	0.5	0.0
23	23.3	69.5	1017.2	0.5	N	0.5	0.0

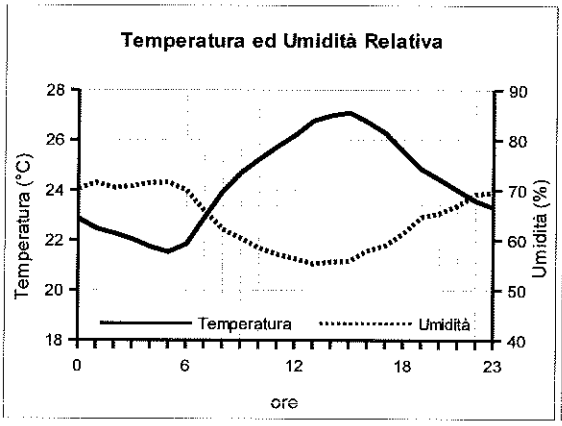

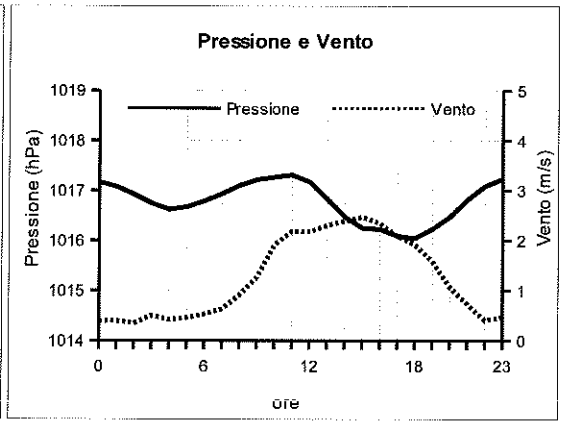

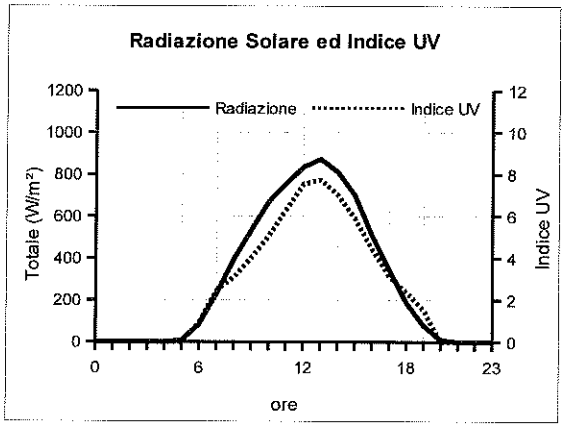

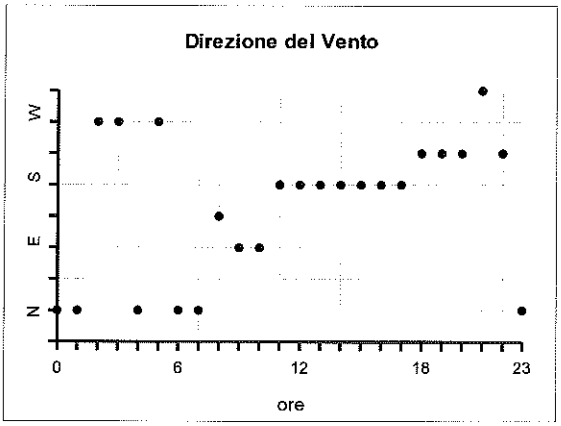

LUGLIO 2015

(medie orarie)

Ore	Temperatura °C	Umidità %	Pressione hPa	Vento velocità m/s	Vento direzione	Radiazione Solare W/m²	Radiazione Solare Indice UV
0	27.1	70.7	1015.5	0.3	W	0.0	0.0
1	26.8	70.7	1015.4	0.3	W	0.0	0.0
2	26.5	71.5	1015.2	0.3	W	0.0	0.0
3	26.2	72.7	1015.0	0.2	W	0.0	0.0
4	26.0	73.2	1014.9	0.2	N	0.0	0.0
5	25.8	73.1	1014.9	0.3	SW	0.6	0.0
6	25.9	72.0	1015.1	0.3	W	34.6	0.5
7	26.7	69.6	1015.3	0.4	N	160.3	2.7
8	27.7	67.3	1015.5	0.5	E	322.3	3.5
9	28.1	66.8	1015.5	0.8	E	451.2	4.6
10	28.7	66.0	1015.5	1.3	E	609.2	6.1
11	29.3	64.3	1015.5	1.8	E	722.7	7.5
12	29.9	62.8	1015.4	2.1	S	793.1	8.6
13	30.3	62.7	1015.2	2.2	S	813.1	8.8
14	30.8	60.8	1014.9	2.2	S	790.1	8.1
15	31.2	57.6	1014.6	1.9	S	710.3	6.9
16	31.2	57.0	1014.4	1.7	W	565.9	5.4
17	30.5	59.5	1014.3	1.9	S	397.3	4.0
18	30.3	58.7	1014.3	1.3	W	247.5	3.1
19	29.7	59.6	1014.4	1.2	W	86.8	1.9
20	28.6	63.8	1014.6	0.7	W	10.1	0.0
21	28.0	66.5	1014.9	0.4	SW	0.0	0.0
22	27.6	69.0	1015.1	0.4	SW	0.0	0.0
23	27.3	70.4	1015.3	0.3	W	0.0	0.0

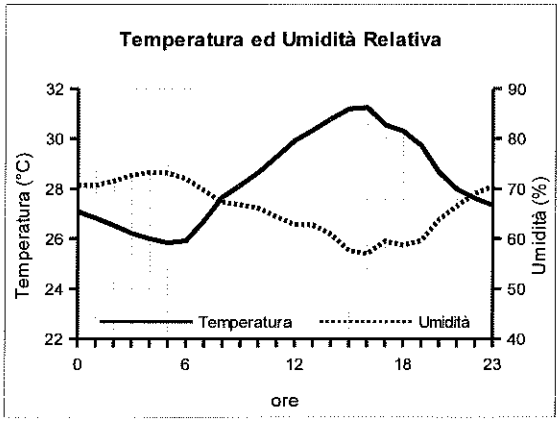

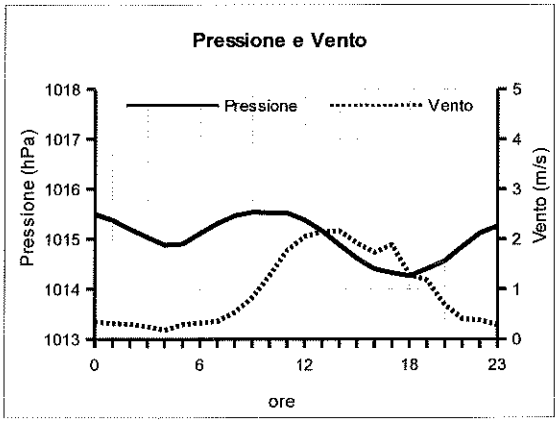

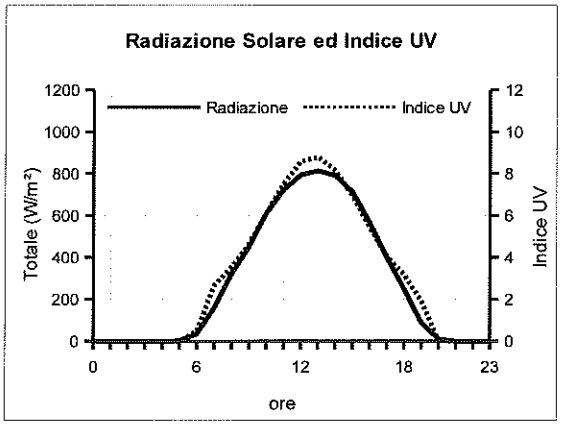

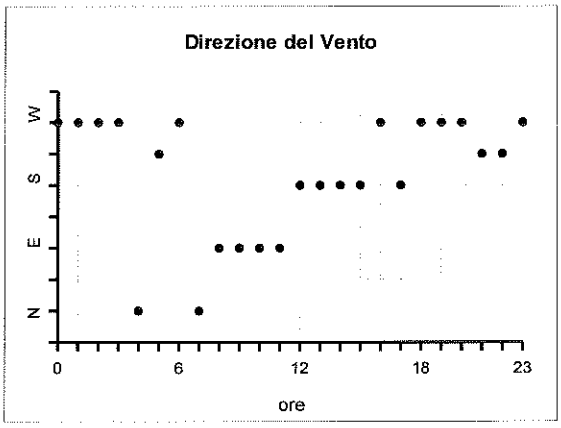

AGOSTO 2015

(medie orarie)

Ore	Temperatura °C	Umidità %	Pressione hPa	Vento velocità m/s	Vento direzione	Radiazione Solare W/m²	Radiazione Solare Indice UV
0	26.6	67.6	1015.5	0.6	N	0.0	0.0
1	26.3	68.3	1015.3	0.5	N	0.0	0.0
2	26.1	68.9	1015.1	0.6	N	0.0	0.0
3	25.8	69.9	1014.9	0.6	N	0.0	0.0
4	25.5	70.6	1014.7	0.6	N	0.0	0.0
5	25.3	71.4	1014.7	0.6	N	0.0	0.0
6	25.0	71.9	1014.9	0.8	N	13.1	0.1
7	25.7	68.7	1015.1	0.8	N	105.2	2.5
8	26.7	65.1	1015.3	0.9	N	254.4	3.7
9	27.6	63.0	1015.4	1.2	E	408.7	4.8
10	28.2	61.4	1015.6	1.6	E	549.8	6.2
11	29.0	59.4	1015.5	2.0	S	666.9	7.6
12	29.6	58.2	1015.4	2.3	S	733.2	8.4
13	29.8	58.6	1015.2	2.4	S	708.4	8.3
14	30.0	58.6	1015.0	2.4	S	665.8	7.6
15	30.2	57.0	1014.7	2.3	S	601.3	6.6
16	30.2	56.7	1014.5	2.1	W	504.4	5.5
17	29.9	58.1	1014.4	2.0	W	347.3	4.4
18	29.3	59.9	1014.4	1.8	W	169.0	3.4
19	28.4	61.8	1014.6	1.4	W	42.2	1.0
20	27.8	62.7	1014.9	0.7	SW	1.3	0.0
21	27.3	65.0	1015.4	0.7	SW	0.0	0.0
22	27.0	66.1	1015.5	0.4	N	0.0	0.0
23	26.8	67.3	1015.6	0.6	N	0.0	0.0

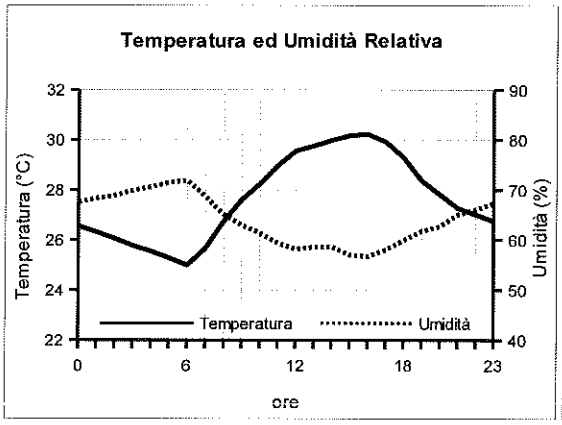

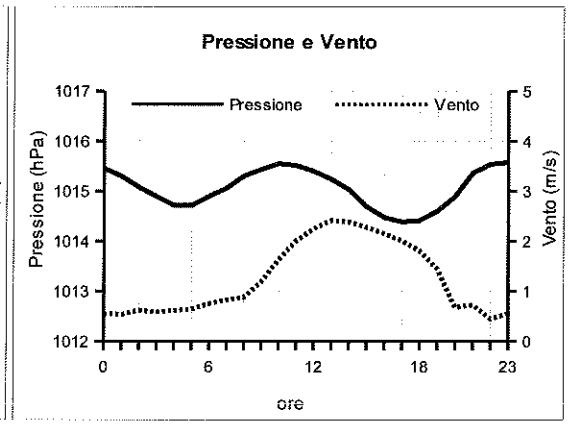

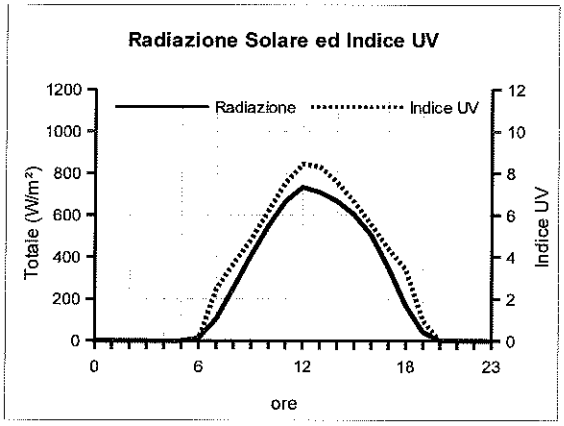

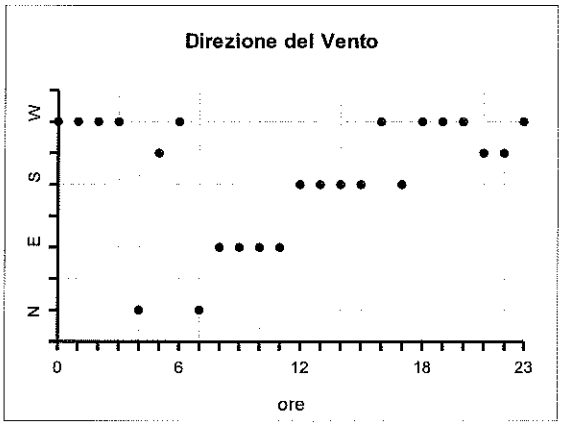

SETTEMBRE 2015

(medie orarie)

Ore	Temperatura °C	Umidità %	Pressione hPa	Vento velocità m/s	Vento direzione	Radiazione Solare W/m²	Radiazione Solare Indice UV
0	22.7	67.7	1016.0	1.2	N	0.0	0.0
1	22.4	68.4	1015.8	1.2	N	0.0	0.0
2	22.2	68.7	1015.6	1.3	N	0.0	0.0
3	21.9	69.2	1015.5	1.1	N	0.0	0.0
4	21.7	69.0	1015.4	1.2	N	0.0	0.0
5	21.6	68.8	1015.2	1.2	N	0.0	0.0
6	21.5	69.3	1015.3	1.0	N	1.1	0.0
7	21.7	68.8	1015.6	1.1	N	47.8	1.2
8	22.7	66.0	1015.7	1.1	N	186.8	3.9
9	23.9	62.2	1015.9	1.5	N	342.9	4.9
10	24.9	59.3	1016.1	1.8	E	471.9	5.7
11	25.4	57.8	1016.2	2.2	S	539.2	6.6
12	25.7	56.8	1016.0	2.3	S	603.4	7.4
13	26.2	56.0	1015.8	2.2	S	634.0	7.6
14	26.6	55.4	1015.4	2.3	S	619.7	7.1
15	26.6	55.3	1015.2	2.4	S	483.2	5.9
16	26.5	55.2	1015.1	2.3	S	355.7	4.8
17	25.9	56.2	1015.1	2.2	SW	211.0	3.9
18	25.3	57.9	1015.1	1.9	SW	68.0	1.9
19	24.4	61.1	1015.3	1.5	SW	4.4	0.0
20	23.9	63.1	1015.7	1.2	N	0.0	0.0
21	23.6	63.4	1016.0	1.2	N	0.0	0.0
22	23.3	64.1	1016.1	1.3	N	0.0	0.0
23	22.9	65.4	1016.1	1.4	N	0.0	0.0

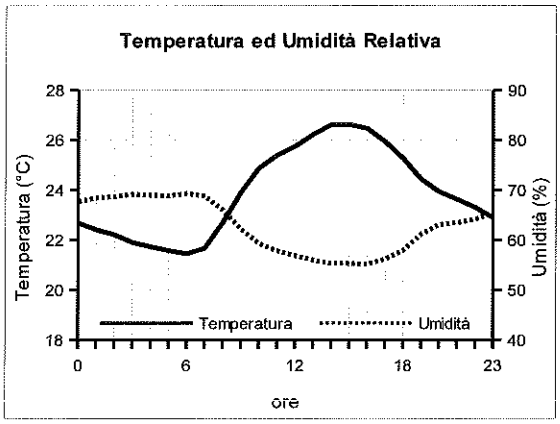

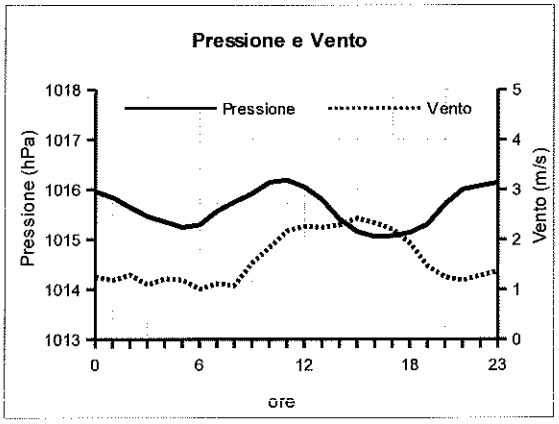

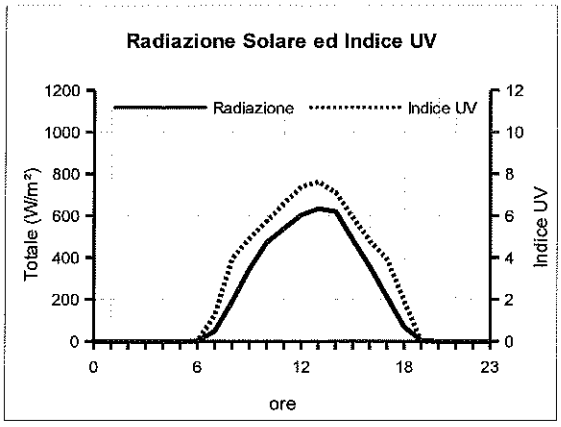

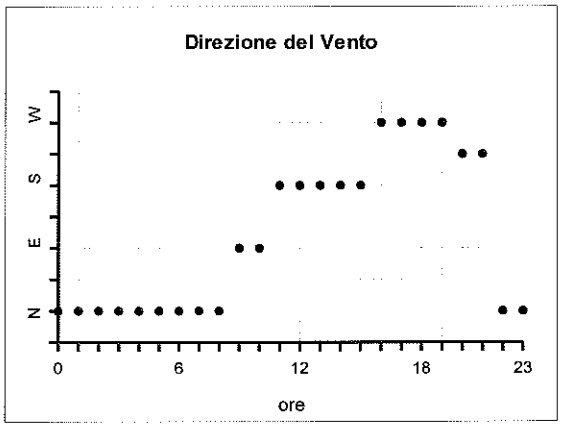

OTTOBRE 2015

(medie orarie)

Ore	Temperatura °C	Umidità %	Pressione hPa	Vento velocità m/s	Vento direzione	Radiazione Solare W/m²	Radiazione Solare Indice UV
0	18.4	78.8	1016.0	1.2	N	0.0	0.0
1	18.2	79.6	1015.8	1.3	N	0.0	0.0
2	18.1	79.9	1015.7	1.3	W	0.0	0.0
3	17.9	80.2	1015.4	1.4	N	0.0	0.0
4	17.8	80.0	1015.3	1.4	N	0.0	0.0
5	17.7	80.1	1015.3	1.3	N	0.0	0.0
6	17.5	80.2	1015.3	1.5	N	1.3	0.0
7	17.4	80.5	1015.5	1.4	N	22.5	0.6
8	17.9	79.3	1015.9	1.3	N	93.4	2.6
9	18.7	77.5	1016.2	1.4	N	178.0	4.1
10	19.4	75.3	1016.4	1.7	N	280.0	4.9
11	20.0	73.1	1016.4	1.8	N	328.6	5.5
12	20.5	70.8	1016.2	2.1	S	382.6	6.2
13	20.7	70.0	1015.9	2.2	S	361.2	6.1
14	20.7	70.5	1015.6	2.4	S	282.9	5.3
15	20.6	70.6	1015.4	2.3	S	220.8	4.4
16	20.4	71.3	1015.4	2.2	S	149.4	3.2
17	20.2	71.7	1015.4	1.9	S	58.1	1.7
18	19.8	73.5	1015.6	1.6	S	5.3	0.0
19	19.4	75.1	1015.9	1.4	S	0.0	0.0
20	19.2	76.1	1016.1	1.3	SW	0.0	0.0
21	18.9	77.1	1016.3	1.4	N	0.0	0.0
22	18.7	77.3	1016.3	1.5	SW	0.0	0.0
23	18.5	78.2	1016.2	1.3	N	0.0	0.0

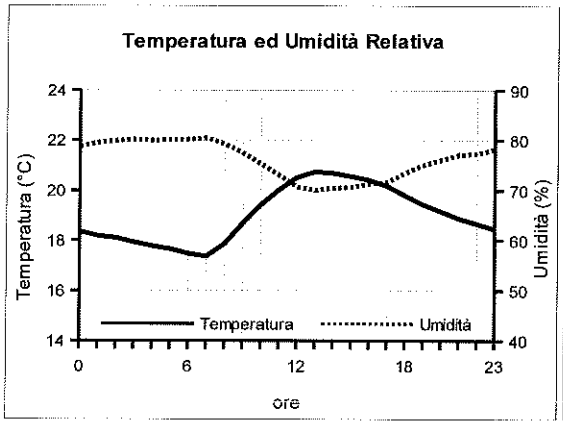

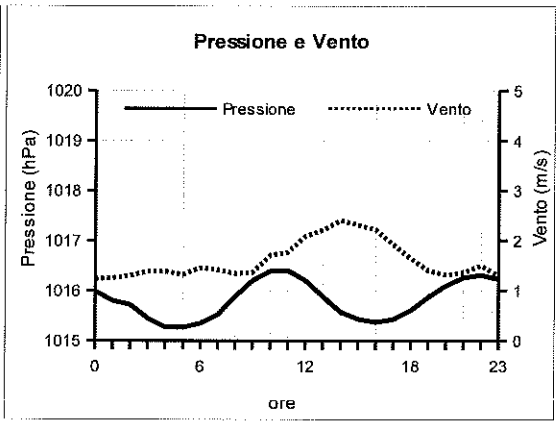

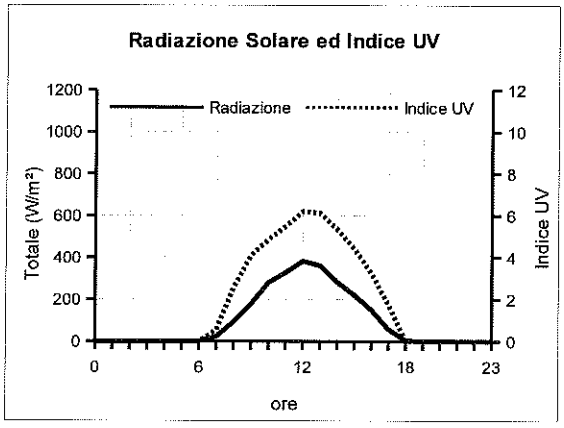

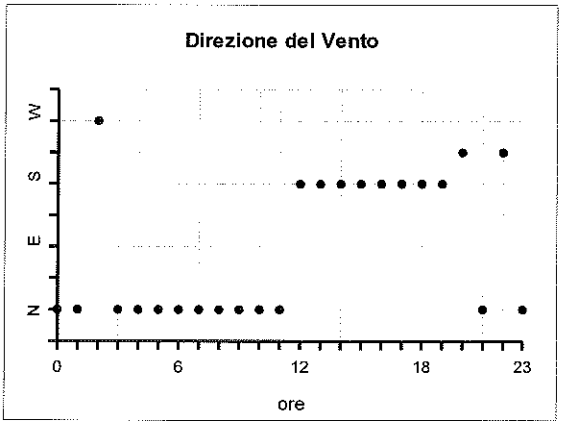

NOVEMBRE 2015

(medie orarie)

Ore	Temperatura °C	Umidità %	Pressione hPa	Vento velocità m/s	Vento direzione	Radiazione Solare W/m²	Radiazione Solare Indice UV
0	14.5	77.9	1020.5	1.0	W	0.0	0.0
1	14.4	78.0	1020.3	0.9	W	0.0	0.0
2	14.3	78.0	1020.2	1.0	W	0.0	0.0
3	14.2	78.2	1019.9	1.1	W	0.0	0.0
4	13.9	78.5	1019.8	1.3	W	0.0	0.0
5	13.8	78.0	1019.8	1.4	W	0.0	0.0
6	13.8	77.8	1020.0	1.4	W	0.8	0.0
7	13.9	77.8	1020.3	1.3	W	34.5	1.1
8	14.8	75.6	1020.7	1.1	N	140.7	4.6
9	15.9	71.8	1020.9	1.2	N	245.3	5.5
10	16.9	68.8	1021.0	1.3	N	325.6	6.1
11	17.3	68.2	1020.7	1.7	SE	341.2	6.4
12	17.6	67.9	1020.3	1.8	SE	323.7	6.3
13	17.8	67.4	1019.9	1.7	SW	295.7	5.8
14	17.9	66.5	1019.8	1.8	SW	234.2	5.5
15	17.9	66.3	1019.7	1.5	W	129.9	4.4
16	17.2	68.5	1019.7	1.3	W	24.6	0.7
17	16.5	71.4	1019.9	1.1	W	0.1	0.0
18	16.0	72.4	1020.2	0.9	W	0.0	0.0
19	15.7	73.8	1020.5	0.7	W	0.0	0.0
20	15.4	75.0	1020.6	0.7	W	0.0	0.0
21	15.2	75.9	1020.8	0.7	W	0.0	0.0
22	15.0	76.2	1020.8	0.7	W	0.0	0.0
23	14.7	77.6	1020.8	0.8	W	0.0	0.0

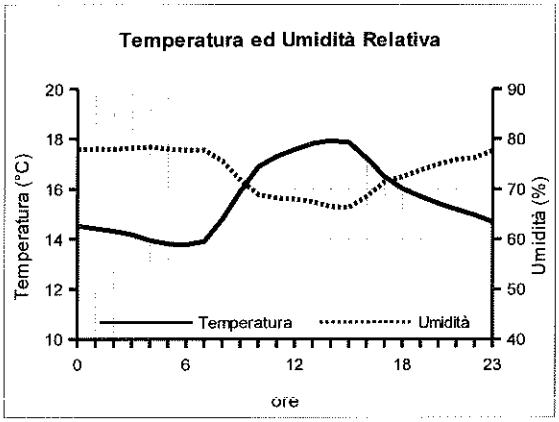

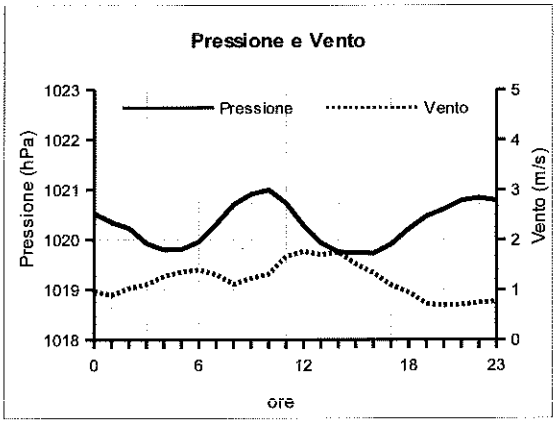

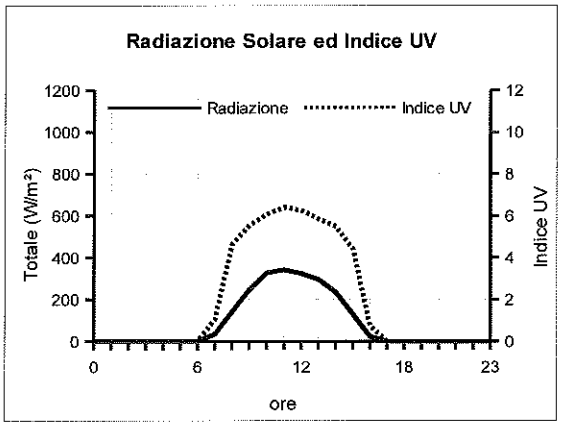

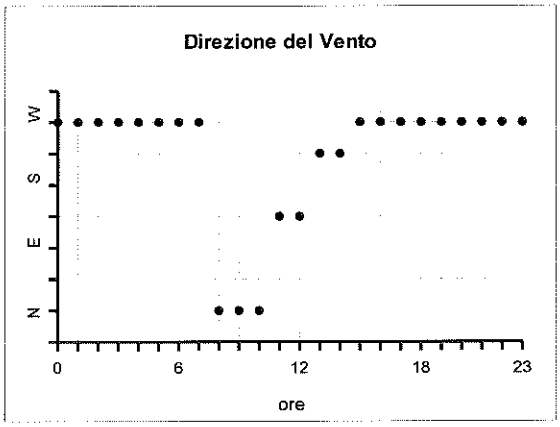

DICEMBRE 2015

(medie orarie)

Ore	Temperatura °C	Umidità %	Pressione hPa	Vento velocità m/s	Vento direzione	Radiazione Solare W/m²	Radiazione Solare Indice UV
0	11.8	77.2	1031.8	0.8	W	0.0	0.0
1	11.6	77.3	1031.7	0.8	W	0.0	0.0
2	11.3	77.8	1031.7	0.9	W	0.0	0.0
3	11.2	77.8	1031.6	1.1	W	0.0	0.0
4	11.0	78.0	1031.4	1.1	W	0.0	0.0
5	10.9	78.2	1031.4	1.1	W	0.0	0.0
6	10.8	78.0	1031.6	0.9	W	0.0	0.0
7	10.8	77.8	1031.8	1.0	W	7.8	0.0
8	11.4	75.9	1032.1	1.1	W	78.7	3.4
9	12.3	72.5	1032.4	1.1	N	188.2	5.7
10	13.6	69.0	1032.5	1.0	N	280.5	6.1
11	14.8	64.9	1032.1	1.0	E	340.1	6.3
12	15.5	62.3	1031.6	1.2	E	343.7	6.3
13	15.7	63.0	1031.1	1.4	SE	278.9	6.1
14	15.8	64.2	1030.8	1.2	S	215.2	5.7
15	15.5	64.7	1030.9	1.1	SW	98.8	4.4
16	14.9	66.5	1031.0	0.8	W	15.2	0.0
17	14.1	69.5	1031.1	0.7	W	0.0	0.0
18	13.4	72.1	1031.4	0.7	W	0.0	0.0
19	13.0	73.6	1031.6	0.7	W	0.0	0.0
20	12.6	74.7	1031.8	0.8	W	0.0	0.0
21	12.2	75.5	1031.9	0.7	W	0.0	0.0
22	12.1	75.9	1031.9	0.9	W	0.0	0.0
23	11.9	76.0	1032.0	1.0	W	0.0	0.0

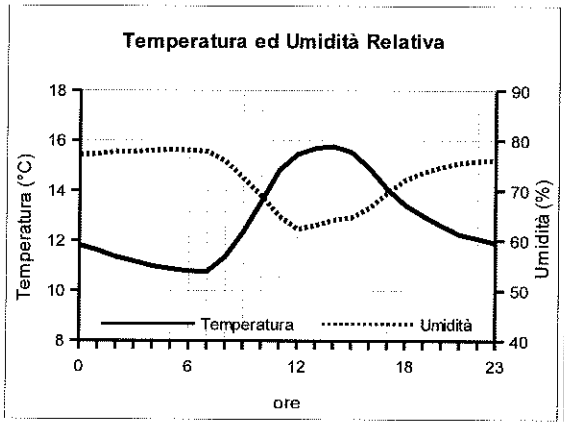

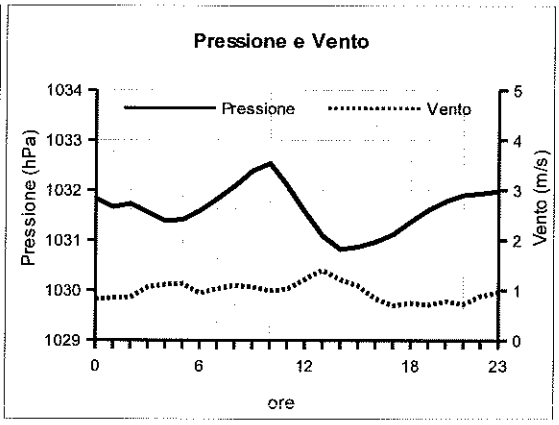

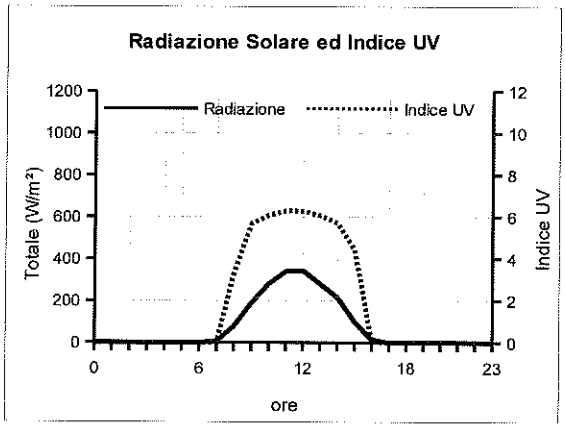

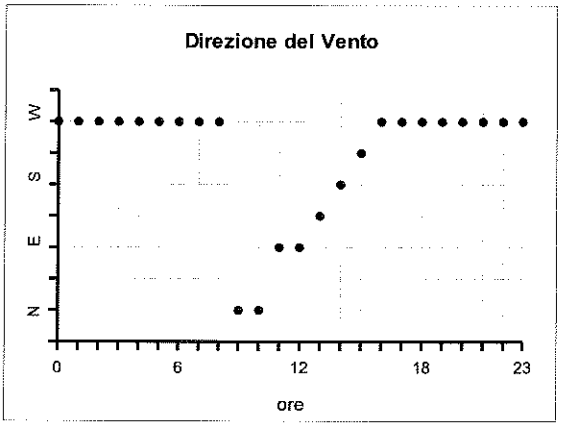

GENNAIO 2015

(medie giornaliere)

Data	Temperatura aria (°C)	Temperatura mare (°C)	Umidità %	Pressione hPa	Vento m/s	Vento direzione	Rad. Solare W/m²	Rad. Solare durata	Pioggia mm	Indice UV medio	Indice UV max	Indice UV (ore)
01/01/15	6.8	15.5	50.6	1026.6	3.7	NE	246.7	9:30	0.0	2.4	2.8	(12:10)
02/01/15	9.5	15.3	62.1	1031.1	1.5	NW	246.8	9:30	0.0	2.4	3.0	(12:00)
03/01/15	11.4	15.3	77.4	1029.6	0.3	SW	124.7	9:30	0.0	2.0	2.8	(12:00)
04/01/15	14.0	15.6	74.1	1021.1	1.1	NW	219.1	9:10	1.0	2.2	2.9	(11:40)
05/01/15	8.8	15.7	48.9	1027.5	2.6	N	234.6	9:30	0.0	2.5	3.1	(11:50)
06/01/15	8.5	15.9	53.8	1025.7	1.0	NW	253.6	9:30	0.0	2.5	3.1	(12:20)
07/01/15	9.8	16.0	65.4	1030.7	0.2	SW	178.8	9:20	0.8	2.5	3.1	(12:10)
08/01/15	11.5	16.0	81.9	1034.3	0.3	NW	166.3	9:20	0.0	2.5	3.2	(11:20)
09/01/15	12.2	16.0	83.1	1033.5	0.2	W	73.2	8:30	0.2	1.9	2.6	(11:30)
10/01/15	14.2	16.0	83.2	1026.1	1.2	S	92.2	9:30	0.0	1.9	2.8	(11:00)
11/01/15	14.7	16.0	87.5	1020.2	0.6	SW	136.5	9:00	0.4	2.1	2.8	(12:20)
12/01/15	11.7	15.9	53.8	1029.5	1.6	NE	260.2	9:40	0.4	2.5	3.1	(12:10)
13/01/15	11.1	15.9	73.7	1030.9	0.4	SW	260.2	9:40	0.0	2.4	3.8	(10:50)
14/01/15	11.9	16.0	81.6	1024.7	0.4	SW	133.9	9:30	0.0	2.3	2.9	(11:50)
15/01/15	12.6	16.0	80.5	1024.5	0.3	SW	214.1	9:40	0.0	2.4	3.0	(11:30)
16/01/15	12.4	16.1	80.1	1022.2	0.3	NW	237.9	9:40	0.0	2.5	3.1	(11:40)
17/01/15	14.7	16.0	82.3	1019.6	2.2	S	155.6	9:20	0.0	2.3	3.2	(11:50)
18/01/15	11.6	16.0	90.2	1016.3	0.9	NW	27.6	7:50	33.4	2.0	4.0	(09:20)
19/01/15	11.7	15.9	81.7	1012.9	0.1	NE	144.4	9:40	1.2	2.4	3.4	(11:50)
20/01/15	10.8	15.8	89.6	1010.6	0.5	NW	66.9	9:00	33.6	2.9	**7.1**	**(13:00)**
21/01/15	11.3	15.8	83.6	1012.3	0.5	NW	140.6	9:40	4.2	2.7	4.1	(16:00)
22/01/15	9.9	15.8	89.1	1008.8	1.9	NW	35.1	9:40	13.2	1.6	4.0	(14:20)
23/01/15	9.4	15.9	85.1	999.1	2.2	NW	61.8	9:30	10.6	3.3	4.7	(12:20)
24/01/15	10.9	15.8	69.1	1006.3	1.2	N	170.4	9:30	0.0	2.8	3.5	(12:20)
25/01/15	9.6	15.8	64.3	1011.3	2.5	NE	110.6	9:50	0.4	2.8	3.0	(11:10)
26/01/15	9.1	15.6	60.9	1017.5	3.1	NE	113.7	9:50	0.0	2.8	3.2	(12:10)
27/01/15	8.1	15.8	60.7	1014.7	1.4	NW	252.0	10:10	0.0	2.7	3.3	(11:20)
28/01/15	8.2	15.6	58.3	1011.3	2.5	NE	282.8	9:50	0.0	3.7	4.8	(11:50)
29/01/15	9.2	15.4	71.4	1007.5	1.8	SW	194.1	9:40	14.9	3.8	4.8	(12:30)
30/01/15	11.7	15.1	76.0	990.0	4.0	SW	65.1	9:10	27.9	3.4	5.0	(11:10)
31/01/15	9.8	15.2	77.1	989.3	1.3	NW	74.9	7:40	35.5	3.7	4.4	(10:40)

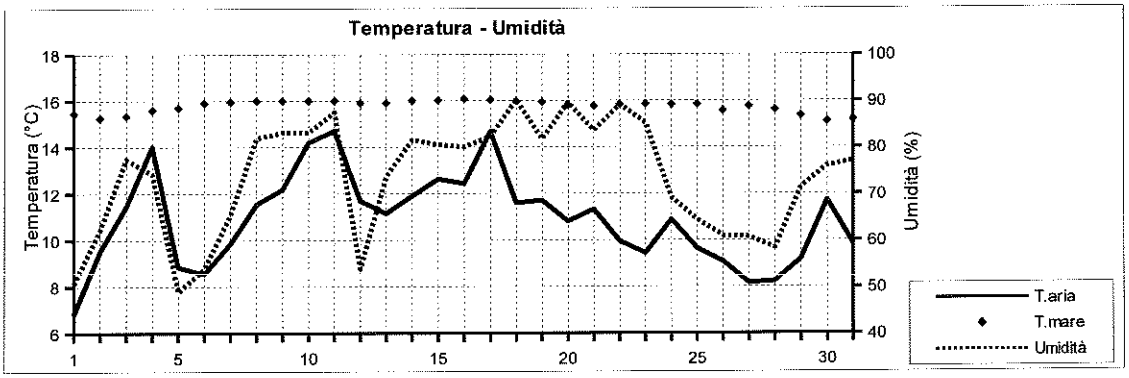

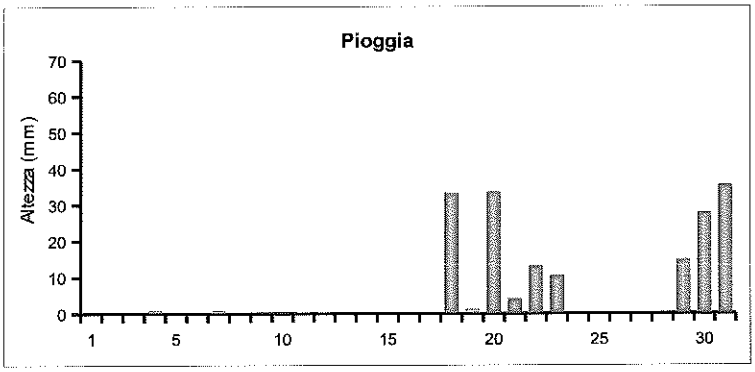

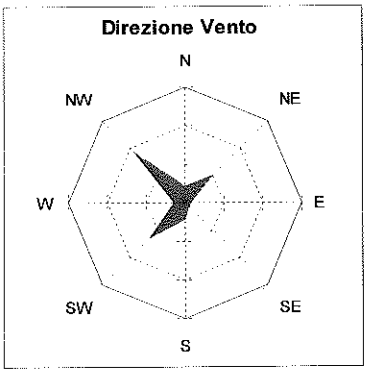

GENNAIO 2015

(estremi giornalieri)

Data	Temperatura (°C)				Umidità (%)				Pressione (hPa)				Vento (m/s)		Radiazione (W/m²)	
	min	(ore)	max	(ore)	min	(ore)	max	(ore)	min	(ore)	max	(ore)	max	(ore)	max	(ore)
01/01/15	**4.7**	**(03:50)**	9.0	(11:40)	43.0	(14:50)	61.0	(00:00)	1022.3	(00:10)	1030.1	(22:50)	13.9	(15:50)	431.0	(12:50)
02/01/15	6.2	(01:10)	13.4	(14:20)	50.0	(15:20)	74.0	(22:10)	1029.9	(00:00)	1032.2	(11:00)	8.9	(05:10)	570.0	(12:10)
03/01/15	7.5	(04:00)	13.9	(13:30)	70.0	(00:00)	83.0	(07:00)	1024.5	(00:00)	1032.1	(10:30)	5.4	(19:40)	332.0	(10:40)
04/01/15	10.3	(23:50)	**17.2**	**(14:40)**	50.0	(00:00)	86.0	(08:20)	1018.8	(15:20)	1024.5	(00:00)	11.6	(22:10)	557.0	(12:10)
05/01/15	6.2	(23:40)	11.1	(14:10)	**32.0**	**(14:00)**	70.0	(08:40)	1023.3	(00:10)	1029.6	(09:50)	14.3	(02:00)	517.0	(10:30)
06/01/15	5.2	(05:30)	12.2	(13:00)	40.0	(10:20)	61.0	(22:10)	1023.8	(04:50)	1029.0	(23:30)	9.8	(13:10)	434.0	(12:00)
07/01/15	5.9	(03:20)	12.9	(11:50)	46.0	(11:10)	87.0	(00:00)	1028.9	(00:10)	1032.7	(22:40)	4.0	(21:40)	599.0	(12:50)
08/01/15	9.0	(03:50)	14.9	(12:20)	68.0	(12:20)	88.0	(00:50)	1032.6	(00:00)	1035.3	(19:10)	3.6	(23:30)	538.0	(11:50)
09/01/15	10.7	(02:50)	13.5	(17:00)	77.0	(21:30)	87.0	(01:30)	1030.0	(23:40)	**1035.7**	**(10:20)**	5.8	(21:30)	267.0	(11:30)
10/01/15	12.7	(00:00)	15.4	(14:30)	77.0	(04:40)	88.0	(19:20)	1024.1	(16:10)	1030.2	(00:00)	7.6	(19:10)	455.0	(14:10)
11/01/15	12.6	(00:00)	16.2	(14:40)	84.0	(16:20)	90.0	(18:20)	1017.2	(16:40)	1024.3	(00:00)	9.8	(00:00)	454.0	(14:50)
12/01/15	9.6	(07:20)	14.9	(15:40)	32.0	(14:00)	87.0	(00:30)	1020.9	(00:30)	1034.3	(22:20)	10.7	(03:40)	524.0	(11:30)
13/01/15	8.1	(07:20)	13.8	(14:00)	62.0	(10:10)	84.0	(21:00)	1027.4	(23:40)	1033.6	(00:00)	4.0	(13:50)	450.0	(12:10)
14/01/15	9.1	(02:50)	13.7	(16:00)	76.0	(09:50)	87.0	(07:30)	1023.0	(15:10)	1027.4	(00:00)	4.5	(14:10)	394.0	(10:10)
15/01/15	10.0	(06:40)	15.5	(14:10)	68.0	(14:20)	87.0	(06:30)	1023.7	(15:40)	1025.9	(10:30)	4.9	(14:50)	554.0	(12:30)
16/01/15	9.8	(05:00)	15.1	(14:50)	69.0	(10:40)	88.0	(01:10)	1020.0	(23:40)	1024.5	(00:00)	4.0	(14:00)	492.0	(11:40)
17/01/15	11.4	(00:50)	16.4	(12:20)	70.0	(03:50)	90.0	(23:10)	1018.7	(15:00)	1020.3	(02:10)	10.7	(11:50)	610.0	(11:50)
18/01/15	9.7	(16:40)	14.9	(00:10)	84.0	(23:40)	94.0	(14:10)	1012.5	(22:00)	1019.6	(00:00)	12.5	(08:40)	135.0	(11:50)
19/01/15	9.6	(06:00)	13.8	(11:30)	70.0	(11:40)	89.0	(05:10)	1011.9	(23:00)	1014.5	(10:50)	3.1	(23:40)	**635.0**	**(11:10)**
20/01/15	9.8	(09:40)	11.8	(00:00)	81.0	(23:20)	94.0	(03:30)	1009.5	(15:10)	1012.0	(00:00)	5.8	(01:20)	258.0	(13:50)
21/01/15	9.7	(07:30)	13.9	(12:40)	72.0	(10:50)	90.0	(17:20)	1010.2	(04:00)	1014.6	(22:10)	8.9	(13:40)	622.0	(12:30)
22/01/15	8.9	(07:20)	11.7	(00:00)	82.0	(00:00)	93.0	(07:20)	998.3	(23:30)	1014.4	(00:10)	11.6	(22:50)	111.0	(10:10)
23/01/15	8.2	(11:20)	10.9	(20:50)	79.0	(09:40)	91.0	(11:20)	997.1	(06:00)	1003.6	(00:00)	9.4	(00:00)	204.0	(15:30)
24/01/15	9.5	(05:20)	12.7	(12:50)	59.0	(14:40)	80.0	(00:00)	1003.6	(00:00)	1008.1	(22:10)	6.7	(00:00)	555.0	(12:20)
25/01/15	8.2	(07:40)	11.0	(11:50)	56.0	(14:00)	74.0	(02:40)	1007.6	(00:40)	1016.1	(00:00)	9.4	(20:20)	248.0	(10:10)
26/01/15	6.6	(00:00)	10.9	(14:10)	54.0	(14:50)	69.0	(00:00)	1016.0	(00:10)	1018.5	(10:20)	10.7	(00:50)	353.0	(14:10)
27/01/15	5.3	(04:20)	11.8	(12:40)	47.0	(11:40)	70.0	(00:20)	1012.4	(23:40)	1018.1	(00:00)	5.8	(00:00)	624.0	(11:40)
28/01/15	6.7	(07:30)	10.7	(13:00)	48.0	(13:30)	65.0	(07:20)	1009.9	(14:40)	1012.7	(21:50)	10.3	(11:20)	603.0	(12:20)
29/01/15	5.3	(07:10)	12.7	(00:00)	51.0	(12:30)	90.0	(18:40)	999.5	(00:00)	1011.5	(00:10)	11.6	(22:30)	563.0	(12:30)
30/01/15	7.8	(19:00)	13.7	(12:20)	46.0	(17:50)	91.0	(09:10)	**984.5**	**(16:10)**	999.5	(00:00)	**20.1**	**(18:50)**	503.0	(11:00)
31/01/15	8.2	(23:40)	11.6	(05:30)	52.0	(02:50)	**95.0**	**(19:40)**	987.2	(22:30)	991.5	(09:50)	12.1	(01:30)	374.0	(11:00)

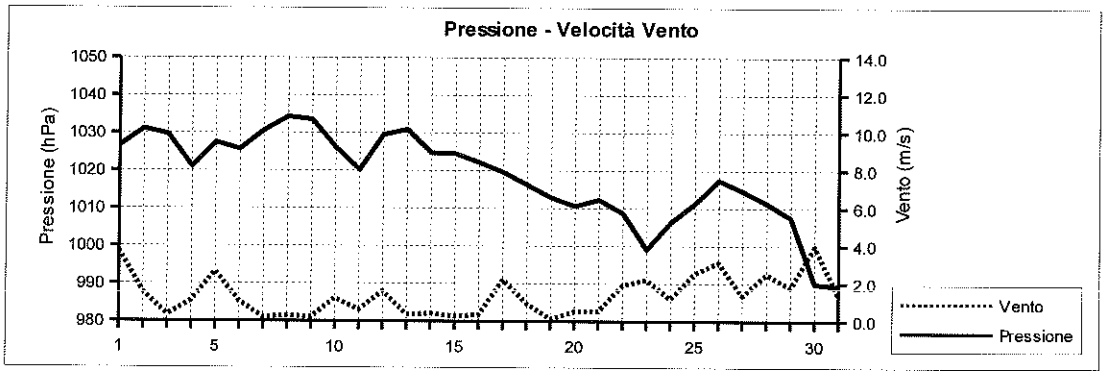

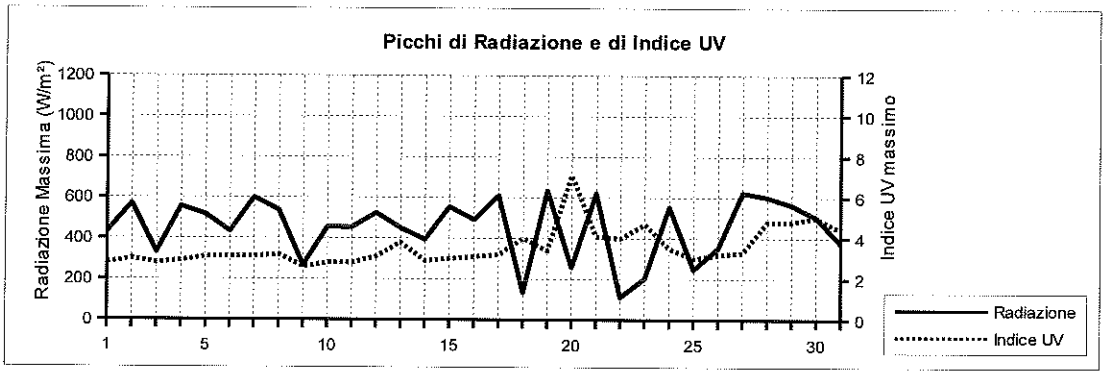

FEBBRAIO 2015

(medie giornaliere)

Data	Temperatura aria (°C)	Temperatura mare (°C)	Umidità %	Pressione hPa	Vento m/s	Vento direzione	Rad. Solare W/m²	Rad. Solare durata	Pioggia mm	Indice UV medio	Indice UV max	Indice UV (ore)
01/02/15	9.2	15.0	78.2	994.1	1.5	SW	202.9	9:40	8.9	4.4	6.2	(11:30)
02/02/15	7.5	15.2	77.7	1002.5	0.6	NW	218.7	9:10	3.8	4.2	5.4	(12:40)
03/02/15	7.9	15.0	83.6	1005.8	2.2	SE	113.1	9:40	38.0	4.0	6.3	(13:10)
04/02/15	12.7	14.4	65.7	1003.8	2.9	SW	210.9	10:10	1.5	4.4	5.7	(12:30)
05/02/15	12.6	14.4	75.7	1001.0	3.0	SE	142.1	9:40	16.4	4.0	5.2	(13:00)
06/02/15	8.9	14.2	85.3	1002.9	1.3	SE	100.9	9:40	17.7	3.5	5.0	(12:10)
07/02/15	8.6	14.3	83.0	1014.4	0.9	SE	172.0	10:10	15.7	4.1	6.0	(11:40)
08/02/15	8.1	14.3	77.5	1011.2	1.5	NW	261.8	10:20	3.8	4.5	5.8	(12:00)
09/02/15	4.2	14.4	56.4	1016.1	4.9	N	309.0	10:30	0.0	4.7	5.9	(11:40)
10/02/15	10.0	14.7	48.5	1020.8	2.4	NW	355.3	10:40	0.0	4.5	5.5	(12:20)
11/02/15	11.1	14.8	60.5	1023.2	1.4	NE	339.6	10:30	0.0	4.4	5.8	(11:40)
12/02/15	10.8	14.8	64.1	1024.0	0.4	NE	298.2	10:30	0.0	4.7	5.8	(12:40)
13/02/15	11.0	14.8	62.5	1023.8	0.5	NW	348.1	10:40	0.0	4.4	5.4	(13:20)
14/02/15	10.6	14.9	66.8	1019.4	0.7	--	332.2	10:50	0.0	4.7	5.7	(13:20)
15/02/15	10.9	14.9	78.1	1015.5	1.0	SE	132.8	10:10	3.8	4.2	5.5	(12:20)
16/02/15	11.9	14.7	82.0	1015.6	0.6	NW	87.6	10:20	6.8	4.3	5.0	(13:20)
17/02/15	13.0	14.7	63.8	1021.4	3.3	N	318.6	10:50	0.0	4.6	6.9	(11:50)
18/02/15	10.8	14.7	55.9	1029.3	3.9	NE	357.8	11:00	0.0	4.9	6.1	(12:30)
19/02/15	10.2	14.7	53.3	1031.2	1.6	NW	369.7	11:00	0.0	4.8	6.1	(12:40)
20/02/15	10.1	14.8	61.5	1026.1	0.5	SW	355.6	11:10	0.0	4.9	5.8	(11:40)
21/02/15	10.6	14.7	73.2	1013.8	1.7	SE	153.7	10:50	1.5	4.3	5.8	(11:30)
22/02/15	12.5	14.3	89.5	997.7	1.8	SE	119.7	9:50	48.7	4.4	5.5	(11:10)
23/02/15	13.1	14.4	79.1	1003.7	0.6	NW	262.5	11:00	0.0	4.6	6.0	(11:50)
24/02/15	11.5	14.5	84.2	1002.1	1.7	SE	79.2	10:30	4.3	4.6	**7.1**	**(11:40)**
25/02/15	9.6	14.4	88.8	1002.6	0.7	NE	58.2	10:30	16.7	3.7	4.7	(08:30)
26/02/15	11.4	14.5	69.9	1011.2	1.9	N	247.3	11:20	0.3	4.7	6.6	(11:50)
27/02/15	10.9	14.6	74.7	1010.4	1.7	N	131.4	11:10	1.5	4.7	5.5	(14:50)
28/02/15	11.7	14.7	73.9	1015.8	0.4	SE	342.8	11:10	0.0	5.0	6.3	(11:30)

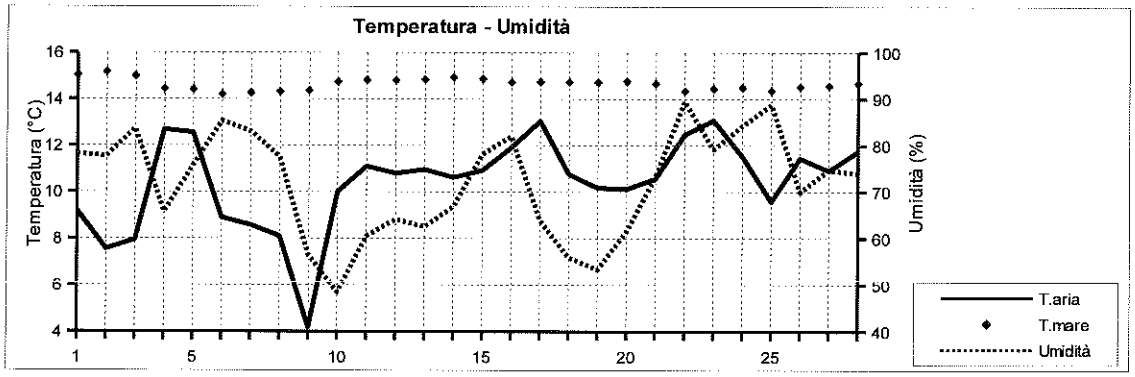

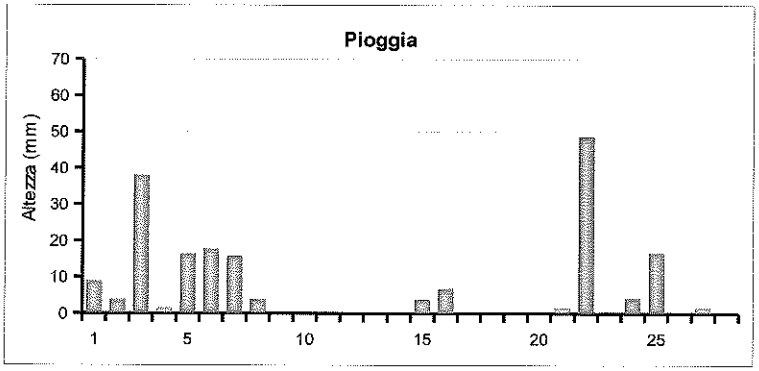

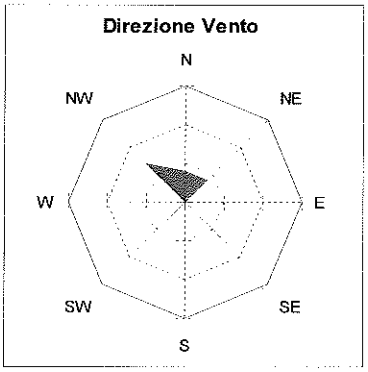

FEBBRAIO 2015

(estremi giornalieri)

Data	Temperatura (°C) min	(ore)	max	(ore)	Umidità (%) min	(ore)	max	(ore)	Pressione (hPa) min	(ore)	max	(ore)	Vento (m/s) max	(ore)	Radiazione (W/m²) max	(ore)
01/02/15	6.9	(06:20)	12.2	(12:20)	53.0	(12:50)	94.0	(00:00)	**987.8**	**(00:00)**	999.2	(00:00)	15.6	(11:10)	715.0	(12:10)
02/02/15	4.8	(08:30)	9.4	(15:40)	63.0	(03:40)	87.0	(02:20)	998.7	(00:30)	1007.5	(22:30)	9.8	(08:10)	673.0	(13:10)
03/02/15	4.8	(05:00)	12.4	(23:30)	64.0	(02:30)	95.0	(20:50)	1000.2	(23:40)	1008.4	(05:30)	16.1	(23:40)	519.0	(10:10)
04/02/15	9.7	(01:10)	14.4	(00:00)	59.0	(03:50)	80.0	(00:10)	1000.1	(00:20)	1006.7	(12:20)	**22.4**	**(00:40)**	782.0	(12:20)
05/02/15	8.1	(20:40)	15.2	(01:20)	54.0	(03:30)	91.0	(19:10)	999.3	(14:00)	1004.5	(00:00)	13.4	(06:50)	592.0	(12:30)
06/02/15	7.5	(07:20)	10.7	(13:20)	76.0	(23:50)	92.0	(08:10)	997.1	(03:40)	1011.2	(00:00)	11.2	(02:10)	751.0	(12:00)
07/02/15	6.9	(21:30)	11.2	(14:10)	68.0	(13:50)	90.0	(00:00)	1011.1	(00:10)	1017.1	(23:00)	10.7	(14:30)	752.0	(13:40)
08/02/15	5.4	(22:30)	11.3	(15:00)	53.0	(00:00)	90.0	(00:00)	1007.5	(16:20)	1016.3	(00:10)	19.2	(00:00)	823.0	(12:20)
09/02/15	**2.2**	**(13:30)**	6.2	(20:40)	45.0	(06:10)	75.0	(14:40)	1011.1	(00:00)	1019.5	(23:00)	19.2	(00:00)	700.0	(11:40)
10/02/15	5.7	(00:00)	14.9	(15:00)	39.0	(15:20)	60.0	(00:00)	1019.2	(00:10)	1023.4	(23:50)	9.4	(16:10)	594.0	(14:00)
11/02/15	8.3	(05:40)	14.4	(15:00)	50.0	(13:00)	69.0	(05:40)	1021.7	(15:40)	1024.3	(08:20)	9.8	(11:30)	591.0	(12:10)
12/02/15	6.7	(07:00)	14.0	(14:40)	49.0	(14:50)	79.0	(07:10)	1023.0	(04:40)	1025.2	(22:00)	6.7	(16:30)	**824.0**	**(13:40)**
13/02/15	9.0	(05:20)	13.6	(12:20)	47.0	(10:50)	71.0	(05:20)	1022.1	(00:00)	1025.1	(00:00)	5.4	(15:00)	650.0	(13:20)
14/02/15	7.6	(03:30)	13.6	(15:10)	50.0	(10:50)	76.0	(21:10)	1017.2	(23:30)	1022.1	(00:00)	5.4	(14:20)	647.0	(13:20)
15/02/15	9.2	(03:40)	12.6	(12:40)	70.0	(12:10)	85.0	(03:10)	1014.5	(16:00)	1017.2	(00:00)	7.6	(15:10)	617.0	(12:30)
16/02/15	10.1	(03:10)	13.9	(17:00)	72.0	(16:50)	91.0	(11:20)	1013.9	(05:40)	1018.0	(23:30)	6.3	(09:40)	206.0	(11:40)
17/02/15	10.6	(06:40)	**16.6**	**(14:10)**	47.0	(14:50)	76.0	(06:50)	1018.0	(00:00)	1026.0	(23:50)	12.1	(11:40)	751.0	(13:10)
18/02/15	7.6	(00:00)	13.8	(14:50)	41.0	(14:50)	68.0	(06:50)	1026.0	(00:00)	1032.8	(21:20)	12.1	(10:20)	629.0	(12:30)
19/02/15	6.9	(04:30)	14.4	(15:20)	**35.0**	**(15:20)**	63.0	(23:10)	1029.1	(17:30)	**1032.9**	**(00:20)**	6.7	(01:00)	635.0	(12:40)
20/02/15	6.6	(06:50)	13.5	(14:10)	48.0	(15:20)	71.0	(22:40)	1021.9	(23:40)	1029.4	(00:00)	7.2	(14:40)	636.0	(12:10)
21/02/15	9.3	(05:10)	12.9	(23:20)	64.0	(07:50)	84.0	(23:50)	1003.2	(00:00)	1021.9	(00:00)	13.0	(23:20)	446.0	(09:30)
22/02/15	10.7	(08:20)	13.6	(16:50)	82.0	(17:00)	**95.0**	**(07:40)**	995.1	(15:00)	1003.2	(00:00)	15.6	(01:30)	315.0	(11:10)
23/02/15	10.9	(06:50)	16.6	(15:00)	66.0	(15:00)	89.0	(00:00)	1000.3	(00:00)	1006.9	(23:00)	7.6	(17:50)	816.0	(11:50)
24/02/15	10.3	(19:20)	12.6	(13:50)	72.0	(22:20)	92.0	(04:00)	997.1	(22:20)	1006.8	(00:00)	9.8	(14:20)	253.0	(11:50)
25/02/15	8.0	(20:20)	10.9	(00:00)	82.0	(14:20)	93.0	(05:00)	997.1	(00:00)	1008.7	(00:00)	6.7	(06:00)	178.0	(12:00)
26/02/15	8.2	(03:20)	15.5	(14:20)	49.0	(14:20)	87.0	(03:10)	1008.7	(00:00)	1013.0	(11:00)	9.8	(17:20)	782.0	(12:10)
27/02/15	10.0	(05:50)	12.2	(12:00)	67.0	(10:20)	82.0	(15:50)	1009.0	(05:20)	1013.5	(00:00)	6.7	(01:20)	288.0	(14:00)
28/02/15	8.7	(03:30)	15.2	(15:20)	58.0	(11:50)	84.0	(23:00)	1013.3	(03:30)	1018.6	(23:40)	5.8	(15:30)	805.0	(12:20)

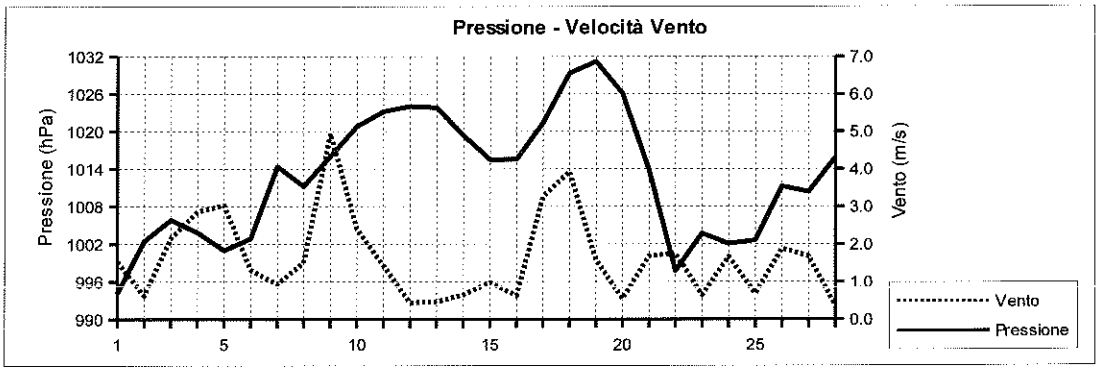

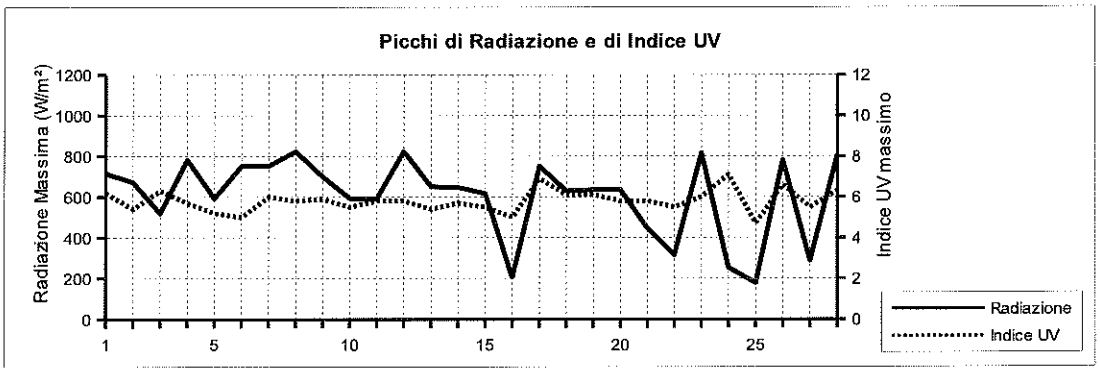

MARZO 2015

(medie giornaliere)

Data	Temperatura aria (°C)	Temperatura mare (°C)	Umidità %	Pressione hPa	Vento m/s	Vento direzione	Rad. Solare W/m²	Rad. Solare durata	Pioggia mm	Indice UV medio	Indice UV max	Indice UV (ore)
01/03/15	12.2	14.8	77.0	1020.0	0.7	SW	366.0	11:30	0.0	5.1	6.2	(11:30)
02/03/15	12.9	14.7	85.7	1020.1	1.4	S	61.9	10:30	0.8	3.5	5.5	(12:00)
03/03/15	14.4	14.7	89.8	1021.4	0.6	S	332.7	11:20	0.3	5.0	7.1	(11:20)
04/03/15	13.8	15.0	86.8	1021.1	1.1	S	299.9	10:40	13.4	5.2	7.5	(12:20)
05/03/15	10.5	15.0	80.1	1006.8	2.6	NW	190.8	11:20	6.3	5.0	6.8	(11:00)
06/03/15	9.6	14.8	54.2	1015.8	6.0	N	172.8	11:30	0.0	4.2	5.7	(13:40)
07/03/15	9.6	14.6	49.2	1021.2	5.0	N	277.4	11:30	0.0	4.8	6.5	(12:10)
08/03/15	10.6	14.4	57.3	1020.7	4.1	NE	396.5	11:50	0.0	5.1	6.5	(12:20)
09/03/15	11.7	14.5	60.2	1022.0	2.9	N	352.3	11:50	0.0	4.9	6.5	(12:20)
10/03/15	11.5	14.6	63.8	1023.0	1.2	NW	329.7	11:30	0.0	4.7	6.3	(12:10)
11/03/15	12.0	14.6	63.2	1020.6	0.3	SW	374.9	11:50	0.0	5.0	6.6	(12:00)
12/03/15	10.1	14.6	65.0	1016.8	2.8	NE	270.5	11:10	1.5	4.9	6.8	(11:30)
13/03/15	11.1	14.5	59.3	1018.0	1.8	NW	365.3	12:00	0.0	4.9	6.6	(12:00)
14/03/15	11.7	14.6	72.2	1020.9	0.5	S	409.8	12:00	0.0	5.3	6.9	(12:10)
15/03/15	11.7	14.7	72.1	1023.4	0.6	NW	87.3	12:00	1.0	4.3	5.9	(13:20)
16/03/15	13.8	14.5	70.9	1023.4	1.2	NW	79.9	11:30	0.5	4.0	5.3	(11:30)
17/03/15	13.1	14.4	82.6	1022.3	1.4	NW	113.8	11:30	1.5	4.2	5.1	(11:40)
18/03/15	14.4	14.5	69.5	1022.1	1.5	NW	387.0	12:10	0.0	5.5	7.2	(11:50)
19/03/15	14.1	14.8	76.2	1021.9	0.8	NW	403.2	12:10	0.0	5.3	7.4	(12:10)
20/03/15	13.7	14.9	46.5	1022.5	1.2	NW	407.7	12:10	0.0	5.3	7.7	(12:00)
21/03/15	12.2	14.9	47.3	1019.9	0.5	NW	354.1	12:20	0.0	5.0	7.2	(12:00)
22/03/15	12.1	14.7	73.7	1011.6	1.5	NW	72.9	12:10	5.8	3.3	5.2	(12:50)
23/03/15	14.5	14.8	69.8	1013.1	1.2	NW	431.4	12:20	0.0	5.3	7.3	(12:00)
24/03/15	15.8	15.0	67.4	1011.5	0.7	SW	348.4	12:00	0.3	5.3	7.3	(11:30)
25/03/15	15.0	14.9	81.0	1001.3	3.1	SE	124.1	11:50	3.0	3.8	7.8	(11:20)
26/03/15	17.5	14.9	67.4	1006.0	0.5	SW	375.4	12:20	0.0	5.0	7.1	(12:10)
27/03/15	15.8	14.9	76.2	1003.6	1.4	NW	323.0	12:20	0.0	4.9	6.7	(13:20)
28/03/15	15.2	14.9	50.1	1009.9	3.5	NE	459.6	12:30	0.0	5.5	7.5	(11:50)
29/03/15	14.1	15.0	50.8	1013.7	1.5	NW	489.0	12:30	0.0	5.8	8.2	(12:40)
30/03/15	14.1	15.0	82.6	1010.4	1.5	SE	208.9	12:20	0.0	4.6	7.8	(14:30)
31/03/15	15.1	15.1	85.9	1014.3	1.5	S	422.1	12:20	0.0	6.0	**8.6**	**(13:20)**

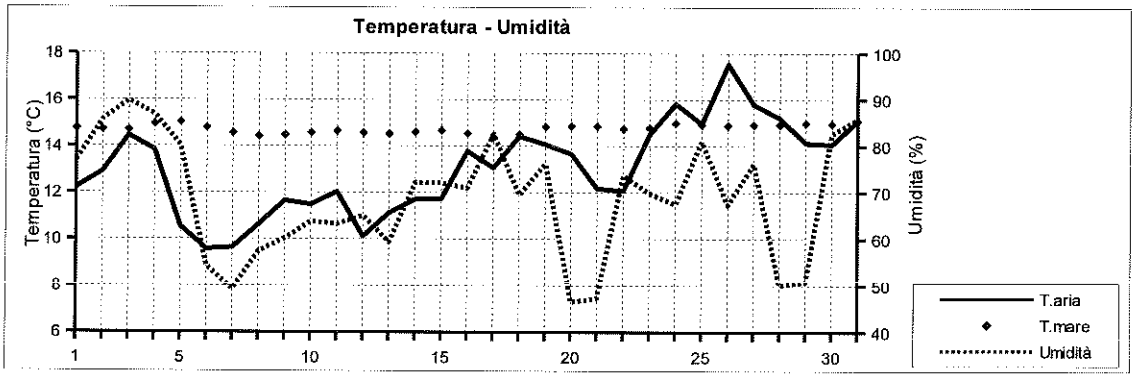

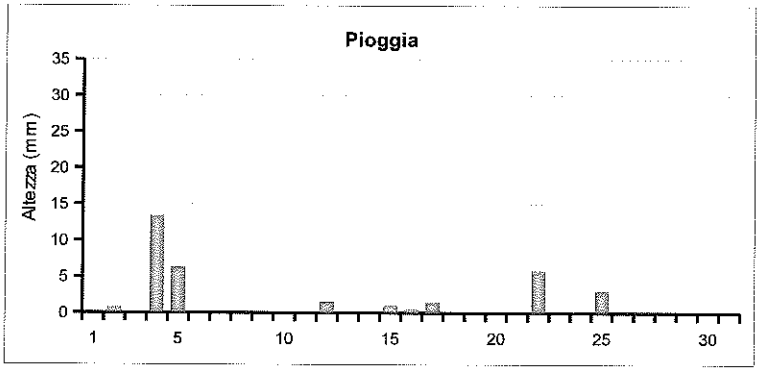

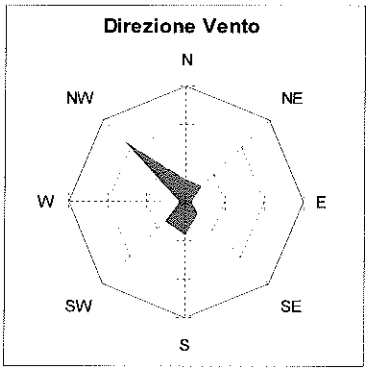

MARZO 2015

(estremi giornalieri)

Data	Temperatura (°C)				Umidità (%)				Pressione (hPa)				Vento (m/s)		Radiazione (W/m²)	
	min	(ore)	max	(ore)	min	(ore)	max	(ore)	min	(ore)	max	(ore)	max	(ore)	max	(ore)
01/03/15	9.2	(07:00)	15.3	(13:30)	53.0	(13:10)	88.0	(05:10)	1018.3	(04:40)	1022.0	(22:50)	6.7	(15:00)	840.0	(12:00)
02/03/15	11.5	(05:40)	14.1	(23:40)	76.0	(04:00)	93.0	(19:40)	1017.9	(17:50)	1022.1	(09:10)	9.4	(11:50)	283.0	(12:00)
03/03/15	12.8	(04:30)	16.9	(13:20)	79.0	(13:10)	95.0	(04:50)	1018.0	(00:30)	**1024.9**	**(22:50)**	5.8	(15:30)	810.0	(11:00)
04/03/15	12.1	(21:50)	16.1	(12:30)	73.0	(14:20)	**95.0**	**(20:30)**	1010.5	(00:00)	1024.9	(01:20)	7.2	(15:30)	902.0	(12:10)
05/03/15	**6.7**	**(23:40)**	14.2	(04:20)	58.0	(12:40)	94.0	(00:00)	1004.2	(05:10)	1010.5	(00:00)	12.1	(04:30)	838.0	(12:10)
06/03/15	6.8	(00:00)	11.4	(14:20)	41.0	(23:40)	76.0	(00:00)	1008.8	(00:00)	1021.3	(23:50)	19.2	(12:40)	656.0	(14:20)
07/03/15	8.1	(06:40)	11.3	(11:30)	39.0	(10:20)	62.0	(21:40)	1020.4	(15:20)	1022.0	(01:40)	16.5	(00:00)	963.0	(12:10)
08/03/15	8.4	(06:20)	13.6	(12:30)	47.0	(12:30)	64.0	(23:20)	1019.8	(15:10)	1021.9	(22:00)	16.5	(00:00)	719.0	(12:20)
09/03/15	8.1	(05:40)	15.9	(13:50)	47.0	(12:50)	70.0	(06:20)	1020.9	(14:10)	1023.6	(22:30)	13.4	(15:20)	751.0	(14:20)
10/03/15	8.8	(06:40)	15.1	(12:30)	47.0	(12:40)	72.0	(00:30)	1021.6	(16:00)	1024.2	(09:10)	6.3	(00:10)	835.0	(12:20)
11/03/15	8.9	(06:30)	15.5	(14:30)	46.0	(11:50)	80.0	(23:30)	1018.3	(23:30)	1022.6	(00:00)	8.0	(14:50)	831.0	(12:40)
12/03/15	6.9	(07:50)	12.4	(12:50)	45.0	(13:00)	87.0	(06:00)	1015.5	(13:30)	1018.3	(00:00)	12.1	(16:40)	933.0	(12:50)
13/03/15	7.9	(05:50)	15.1	(14:00)	43.0	(13:00)	74.0	(23:50)	1016.9	(13:50)	1019.4	(22:20)	8.9	(09:50)	758.0	(13:20)
14/03/15	8.3	(05:40)	14.9	(13:40)	63.0	(13:30)	82.0	(05:30)	1019.2	(00:20)	1023.0	(23:10)	5.8	(14:30)	821.0	(11:20)
15/03/15	9.7	(03:30)	13.5	(16:40)	65.0	(08:50)	80.0	(03:30)	1021.7	(04:00)	1024.5	(12:40)	4.9	(18:40)	399.0	(13:20)
16/03/15	11.9	(04:20)	15.6	(18:00)	64.0	(07:50)	77.0	(11:50)	1021.7	(06:10)	1024.7	(08:40)	7.6	(18:10)	230.0	(14:00)
17/03/15	11.6	(06:50)	14.9	(00:00)	68.0	(00:00)	89.0	(06:40)	1020.9	(16:30)	1023.4	(11:20)	9.8	(01:20)	237.0	(12:10)
18/03/15	11.9	(04:20)	18.9	(13:00)	46.0	(12:40)	84.0	(23:30)	1021.5	(16:40)	1022.8	(10:20)	7.6	(09:10)	819.0	(13:20)
19/03/15	11.7	(06:10)	17.7	(14:40)	51.0	(00:00)	87.0	(01:40)	1020.5	(15:10)	1023.1	(23:20)	7.2	(13:40)	895.0	(12:30)
20/03/15	11.0	(06:30)	17.1	(14:40)	**30.0**	**(12:10)**	57.0	(05:50)	1021.1	(17:10)	1023.5	(10:00)	8.0	(09:40)	788.0	(12:30)
21/03/15	9.2	(05:30)	15.1	(16:00)	32.0	(10:40)	62.0	(21:30)	1015.4	(00:00)	1022.6	(01:00)	4.9	(13:10)	858.0	(11:50)
22/03/15	10.9	(22:10)	13.6	(09:50)	56.0	(09:40)	90.0	(16:00)	1009.8	(17:40)	1015.4	(00:00)	5.4	(16:40)	513.0	(09:00)
23/03/15	10.8	(03:10)	19.1	(12:20)	55.0	(12:10)	82.0	(00:10)	1011.7	(00:10)	1014.4	(22:00)	6.7	(11:20)	**965.0**	**(13:30)**
24/03/15	11.6	(05:40)	18.7	(10:30)	56.0	(18:10)	81.0	(05:40)	1005.8	(00:00)	1014.2	(00:00)	7.2	(23:10)	731.0	(11:30)
25/03/15	13.8	(08:50)	15.7	(07:30)	70.0	(03:00)	92.0	(08:40)	**994.6**	**(07:20)**	1005.8	(00:00)	**20.6**	**(07:50)**	817.0	(11:20)
26/03/15	13.7	(05:40)	**21.5**	**(15:20)**	44.0	(15:40)	85.0	(05:40)	1004.8	(15:40)	1007.6	(10:10)	6.3	(17:40)	860.0	(12:40)
27/03/15	13.9	(05:20)	19.2	(13:20)	64.0	(13:30)	86.0	(06:30)	1001.5	(14:10)	1005.9	(00:20)	9.4	(15:00)	851.0	(11:40)
28/03/15	12.2	(00:00)	18.6	(14:20)	39.0	(12:20)	68.0	(00:00)	1005.5	(00:00)	1013.7	(22:20)	12.1	(11:30)	819.0	(11:50)
29/03/15	10.7	(07:20)	18.8	(13:20)	27.0	(13:00)	77.0	(00:00)	1012.8	(04:50)	1014.8	(11:10)	7.6	(15:40)	833.0	(13:00)
30/03/15	13.0	(05:10)	15.8	(16:30)	76.0	(00:20)	90.0	(13:50)	1006.5	(16:00)	1014.4	(01:10)	10.3	(11:40)	898.0	(14:40)
31/03/15	13.7	(05:20)	17.7	(13:30)	75.0	(11:40)	92.0	(04:00)	1012.3	(01:00)	1017.2	(11:40)	8.9	(15:40)	842.0	(11:40)

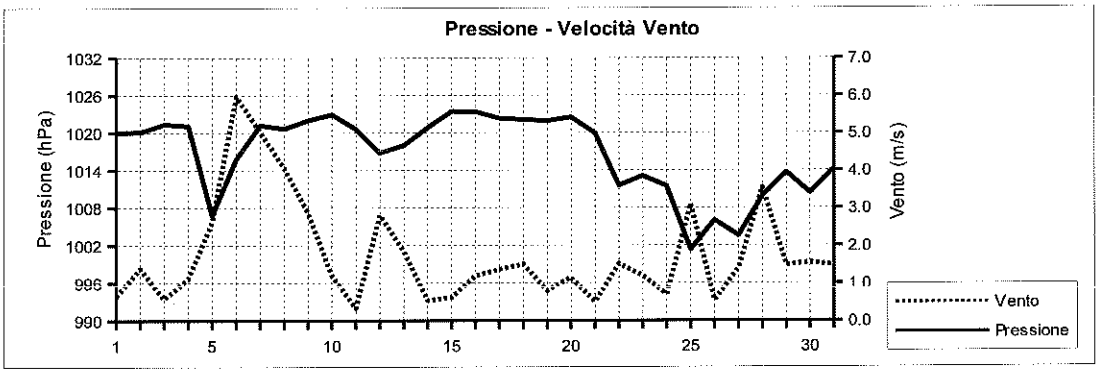

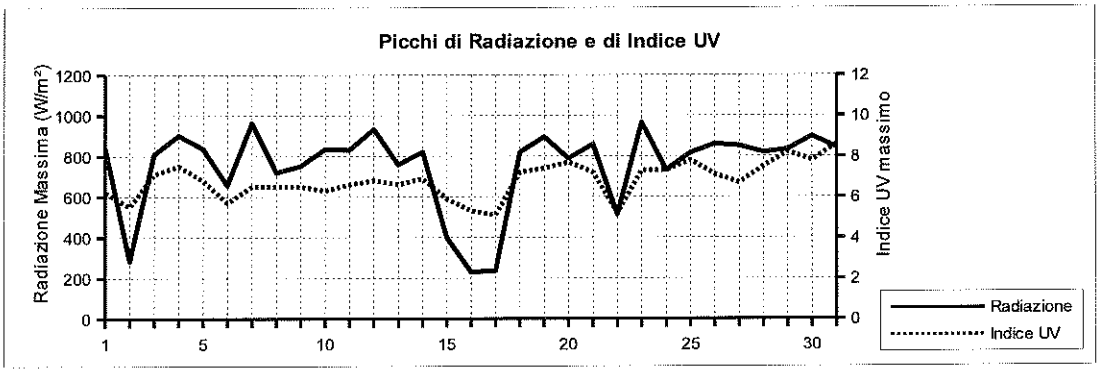

APRILE 2015

(medie giornaliere)

Data	Temperatura aria (°C)	Temperatura mare (°C)	Umidità %	Pressione hPa	Vento m/s	Vento direzione	Rad. Solare W/m²	Rad. Solare durata	Pioggia mm	Indice UV medio	Indice UV max	Indice UV (ore)
01/04/15	15.6	15.4	81.6	1012.6	1.2	S	444.2	12:50	0.0	5.6	8.9	(12:00)
02/04/15	15.0	15.3	71.9	1017.0	1.5	S	471.0	12:50	0.0	5.5	7.9	(12:50)
03/04/15	14.8	15.5	61.6	1015.8	2.0	NE	427.3	12:50	0.0	5.6	8.9	(13:20)
04/04/15	13.2	15.4	62.3	1013.0	2.1	SE	135.6	13:00	6.9	4.1	7.5	(12:30)
05/04/15	11.5	15.3	80.8	1005.3	1.4	NW	145.0	12:40	19.5	3.6	7.0	(14:00)
06/04/15	10.8	15.3	59.0	1013.2	2.2	NE	209.5	12:30	0.0	4.6	7.7	(13:10)
07/04/15	9.0	15.2	54.9	1022.7	2.3	N	297.8	13:10	0.0	4.6	7.6	(13:20)
08/04/15	11.4	15.2	47.3	1026.0	2.7	NW	388.5	13:00	0.0	4.8	7.5	(12:50)
09/04/15	13.4	15.1	53.4	1027.5	2.2	NW	362.1	13:10	0.0	5.0	8.2	(13:00)
10/04/15	13.9	15.3	63.1	1029.9	0.7	SW	493.3	13:10	0.0	5.3	7.6	(13:30)
11/04/15	13.8	15.3	72.1	1028.8	0.8	S	457.9	13:10	0.0	5.4	8.4	(13:00)
12/04/15	15.5	15.4	73.5	1028.2	0.5	SE	464.5	13:10	0.0	5.3	7.6	(12:50)
13/04/15	16.5	15.6	70.9	1027.7	0.7	SE	478.9	13:20	0.0	5.3	7.6	(13:50)
14/04/15	15.6	15.7	82.9	1026.2	1.4	S	435.6	13:10	0.0	5.5	7.9	(13:10)
15/04/15	16.3	16.0	83.9	1024.4	0.9	SE	474.7	13:10	0.0	5.8	8.2	(12:50)
16/04/15	16.1	16.3	83.3	1022.9	1.2	S	451.8	13:10	0.0	5.6	8.1	(12:50)
17/04/15	17.0	16.1	73.3	1019.1	1.6	S	387.1	13:00	0.5	5.1	8.0	(12:40)
18/04/15	16.5	16.5	84.8	1015.7	1.2	S	252.3	13:30	0.0	4.7	9.0	(13:40)
19/04/15	16.5	16.5	61.8	1015.2	2.3	N	414.9	13:20	0.0	5.2	8.6	(12:50)
20/04/15	16.3	16.8	52.9	1017.8	1.5	NW	476.9	13:40	0.0	5.3	7.8	(12:50)
21/04/15	17.7	16.6	50.9	1021.2	1.6	N	498.4	13:40	0.0	5.4	8.0	(12:40)
22/04/15	18.4	16.4	48.9	1023.4	0.9	SW	498.6	13:40	0.0	5.6	8.3	(12:40)
23/04/15	17.2	16.3	71.6	1020.7	1.1	S	433.8	13:50	0.0	5.4	8.6	(13:50)
24/04/15	17.6	16.5	68.3	1017.0	0.8	SE	351.2	13:40	0.0	5.1	8.6	(12:40)
25/04/15	18.1	16.7	77.5	1017.5	0.8	SW	435.3	13:50	0.0	5.3	8.2	(12:50)
26/04/15	17.5	16.9	82.7	1016.0	1.1	SE	412.1	13:30	0.0	5.3	8.8	(13:00)
27/04/15	16.4	16.8	83.4	1010.7	1.1	--	120.0	13:00	13.9	4.3	6.8	(13:40)
28/04/15	16.0	16.6	83.7	1007.5	2.3	SW	145.5	13:50	10.4	3.9	9.7	(12:40)
29/04/15	17.0	16.7	82.2	1016.9	1.0	S	395.2	13:50	0.0	5.4	**9.8**	**(13:30)**
30/04/15	16.4	16.8	74.8	1020.1	1.3	W	286.7	13:50	0.0	4.9	9.5	(13:10)

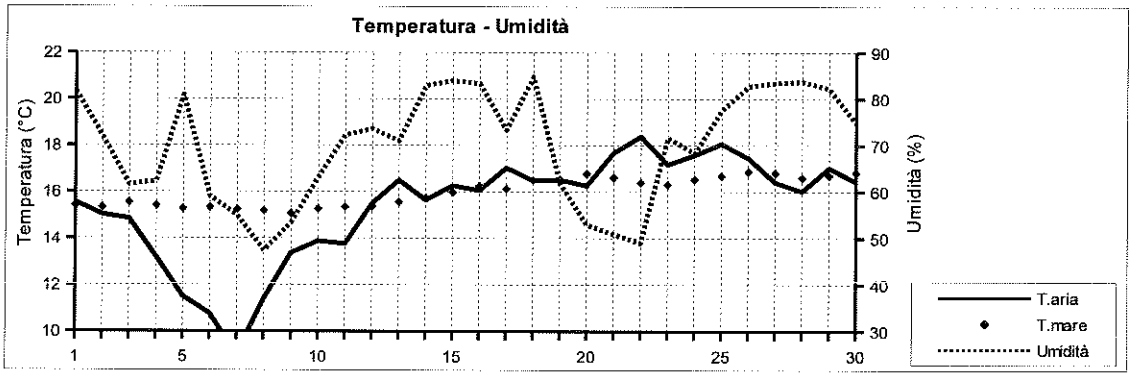

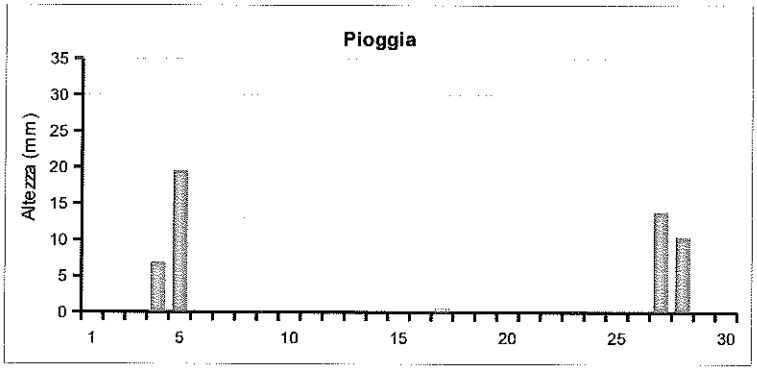

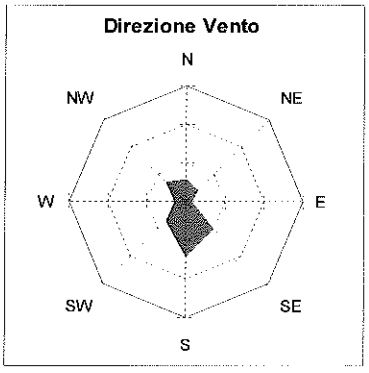

APRILE 2015

(estremi giornalieri)

Data	Temperatura (°C)				Umidità (%)				Pressione (hPa)				Vento (m/s)		Radiazione (W/m²)	
	min	(ore)	max	(ore)	min	(ore)	max	(ore)	min	(ore)	max	(ore)	max	(ore)	max	(ore)
01/04/15	13.8	(05:10)	17.6	(16:10)	70.0	(18:20)	91.0	(03:30)	1010.4	(05:10)	1015.9	(00:00)	7.2	(14:30)	1044.0	(12:10)
02/04/15	12.7	(07:20)	17.5	(10:30)	44.0	(10:30)	86.0	(01:10)	1015.8	(18:20)	1019.0	(10:40)	6.7	(13:20)	819.0	(13:10)
03/04/15	12.9	(23:50)	18.6	(12:30)	37.0	(23:00)	83.0	(00:10)	1014.1	(05:30)	1017.6	(21:40)	13.4	(15:30)	1097.0	(13:20)
04/04/15	11.9	(06:20)	14.6	(09:30)	31.0	(04:00)	91.0	(16:20)	1006.8	(00:00)	1017.5	(00:20)	13.4	(20:30)	708.0	(12:30)
05/04/15	9.8	(14:50)	14.6	(09:40)	69.0	(02:20)	91.0	(16:50)	**1003.9**	**(05:10)**	1008.0	(00:00)	**20.1**	**(01:00)**	555.0	(09:20)
06/04/15	8.9	(00:00)	14.4	(13:50)	43.0	(13:40)	75.0	(00:10)	1008.0	(00:00)	1019.8	(00:00)	11.6	(17:50)	1067.0	(14:00)
07/04/15	**6.3**	**(05:50)**	11.8	(15:10)	40.0	(12:10)	68.0	(06:40)	1019.6	(00:40)	1026.2	(23:40)	10.7	(20:40)	1085.0	(13:20)
08/04/15	8.5	(00:20)	15.0	(15:50)	34.0	(15:20)	63.0	(00:10)	1024.5	(15:40)	1027.2	(23:00)	10.7	(15:00)	1074.0	(13:20)
09/04/15	9.8	(06:40)	17.6	(16:00)	41.0	(15:10)	72.0	(23:30)	1026.4	(01:00)	1029.4	(23:00)	10.7	(12:10)	1018.0	(13:00)
10/04/15	10.1	(06:40)	17.7	(16:10)	48.0	(17:20)	72.0	(07:20)	1029.2	(16:40)	**1031.0**	**(10:50)**	7.2	(14:40)	863.0	(13:20)
11/04/15	10.3	(06:40)	16.9	(15:30)	59.0	(16:00)	82.0	(06:10)	1027.7	(16:40)	1030.0	(00:00)	7.2	(14:00)	967.0	(13:00)
12/04/15	11.7	(06:40)	21.1	(16:20)	56.0	(16:20)	87.0	(23:50)	1026.5	(16:20)	1029.4	(10:20)	4.5	(14:30)	819.0	(13:10)
13/04/15	12.3	(06:50)	22.3	(15:30)	43.0	(15:00)	89.0	(00:50)	1025.9	(16:20)	1029.0	(10:10)	5.8	(15:40)	828.0	(12:50)
14/04/15	14.4	(03:20)	17.7	(15:10)	74.0	(11:10)	90.0	(04:00)	1024.8	(17:50)	1027.3	(10:20)	6.7	(13:50)	1007.0	(11:40)
15/04/15	13.6	(06:30)	21.1	(16:30)	61.0	(16:40)	93.0	(23:40)	1022.7	(17:10)	1025.9	(11:40)	6.7	(13:40)	844.0	(13:10)
16/04/15	14.4	(01:50)	18.5	(16:20)	72.0	(12:20)	**93.0**	**(00:00)**	1021.2	(19:20)	1024.8	(10:30)	6.7	(14:50)	844.0	(13:20)
17/04/15	13.1	(07:10)	21.9	(15:20)	38.0	(15:20)	93.0	(07:10)	1015.8	(18:50)	1022.0	(05:30)	8.0	(18:30)	1083.0	(12:40)
18/04/15	15.4	(06:40)	18.7	(16:50)	72.0	(16:50)	93.0	(00:50)	1014.4	(18:30)	1017.1	(00:10)	7.2	(14:50)	1162.0	(13:50)
19/04/15	13.6	(06:40)	20.6	(15:30)	41.0	(17:00)	90.0	(04:10)	1014.2	(15:50)	1017.0	(23:50)	9.4	(09:00)	1083.0	(13:50)
20/04/15	12.6	(02:30)	20.5	(16:30)	38.0	(11:40)	83.0	(23:50)	1016.4	(18:40)	1019.4	(11:00)	6.3	(01:10)	868.0	(12:50)
21/04/15	13.6	(06:20)	22.8	(15:30)	29.0	(14:00)	85.0	(01:30)	1018.7	(00:20)	1024.0	(00:00)	10.7	(12:10)	1002.0	(13:30)
22/04/15	13.2	(06:40)	**23.6**	**(13:50)**	**27.0**	**(13:50)**	74.0	(01:10)	1022.3	(15:50)	1024.7	(09:40)	11.2	(15:20)	868.0	(12:40)
23/04/15	15.3	(06:30)	19.9	(13:30)	54.0	(13:30)	89.0	(05:50)	1018.7	(20:00)	1022.4	(00:00)	6.7	(14:40)	932.0	(13:50)
24/04/15	15.8	(06:10)	20.2	(13:40)	44.0	(09:20)	87.0	(23:30)	1015.8	(19:00)	1018.9	(00:20)	7.2	(12:50)	1146.0	(12:40)
25/04/15	14.6	(06:10)	22.3	(14:30)	61.0	(14:20)	88.0	(03:30)	1016.2	(19:00)	1018.6	(11:00)	6.7	(13:50)	853.0	(12:40)
26/04/15	15.7	(05:40)	20.0	(13:40)	69.0	(16:20)	90.0	(07:10)	1014.1	(23:40)	1018.0	(00:00)	6.3	(13:50)	963.0	(13:00)
27/04/15	14.2	(21:50)	19.7	(15:20)	60.0	(15:30)	91.0	(09:20)	1006.4	(00:00)	1014.5	(01:10)	9.8	(00:00)	490.0	(13:00)
28/04/15	14.7	(15:50)	17.8	(13:20)	74.0	(14:20)	92.0	(16:10)	1005.3	(05:10)	1012.5	(00:00)	13.4	(19:20)	1127.0	(12:30)
29/04/15	14.6	(05:50)	19.8	(17:10)	70.0	(14:40)	92.0	(06:50)	1012.5	(00:00)	1020.0	(00:00)	8.0	(00:10)	**1220.0**	**(14:00)**
30/04/15	15.2	(06:00)	18.7	(12:50)	61.0	(12:20)	86.0	(00:00)	1018.8	(05:00)	1021.2	(22:20)	9.4	(15:40)	1125.0	(11:40)

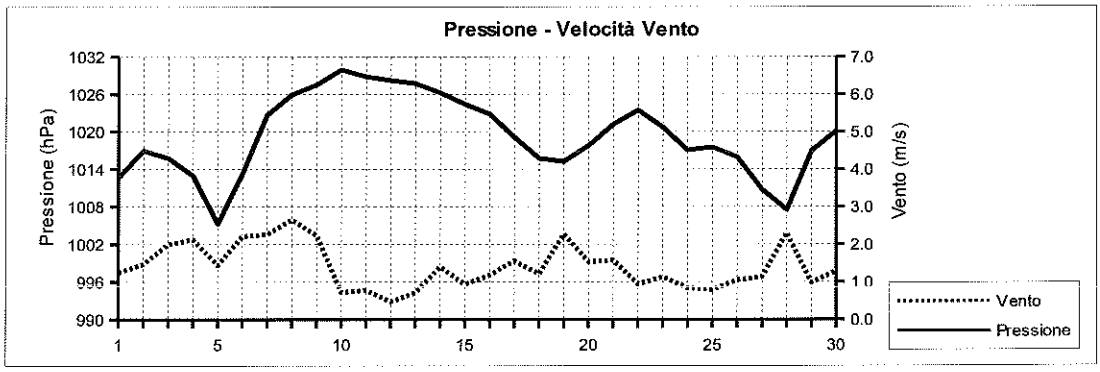

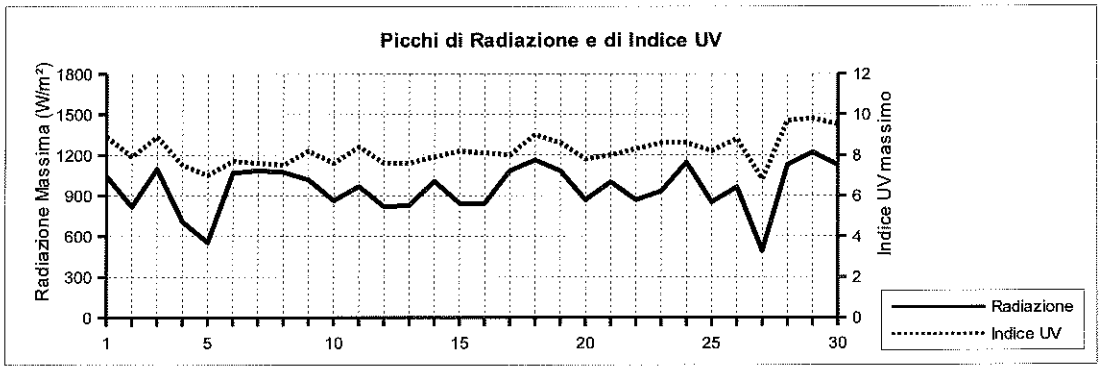

MAGGIO 2015

(medie giornaliere)

Data	Temperatura aria (°C)	Temperatura mare (°C)	Umidità %	Pressione hPa	Vento m/s	Vento direzione	Rad. Solare W/m²	Rad. Solare durata	Pioggia mm	Indice UV medio	Indice UV max	Indice UV (ore)
01/05/15	16.6	16.9	77.0	1020.1	1.2	S	504.7	13:50	0.0	6.2	9.3	(12:40)
02/05/15	17.7	18.1	76.5	1015.8	1.5	S	417.0	13:50	0.0	5.9	9.3	(12:40)
03/05/15	19.2	17.9	74.9	1016.2	0.8	S	491.7	14:00	0.0	6.2	**10.5**	**(12:40)**
04/05/15	21.1	18.0	67.6	1016.0	0.5	SE	501.8	14:10	0.0	6.2	9.7	(13:30)
05/05/15	24.7	18.0	53.4	1014.8	0.0	–	441.5	14:00	0.0	5.2	8.8	(13:10)
06/05/15	23.6	18.4	60.4	1014.3	0.8	S	443.0	14:00	0.0	5.7	9.4	(12:50)
07/05/15	21.9	18.5	72.6	1014.8	1.5	SE	470.6	14:20	0.0	5.9	9.1	(12:40)
08/05/15	20.5	18.5	80.8	1016.4	1.5	S	473.1	14:20	0.0	6.2	10.1	(13:00)
09/05/15	20.6	19.2	75.7	1015.1	1.0	S	493.3	14:00	0.0	5.6	8.6	(12:40)
10/05/15	22.5	19.7	58.0	1018.7	1.9	NE	435.2	14:20	0.0	5.2	8.5	(13:10)
11/05/15	22.8	19.0	44.5	1022.5	2.1	NW	490.0	14:30	0.0	5.8	8.9	(13:00)
12/05/15	22.1	18.2	41.1	1023.2	1.8	NE	522.2	14:30	0.0	6.0	9.4	(13:10)
13/05/15	20.4	18.4	74.8	1022.5	1.2	SE	499.2	14:20	0.0	6.0	9.6	(12:40)
14/05/15	20.2	19.2	80.6	1016.9	1.7	S	443.3	14:20	0.0	5.8	9.4	(12:40)
15/05/15	22.6	19.5	60.6	1010.2	1.7	SW	294.0	14:10	0.0	4.7	9.0	(12:30)
16/05/15	19.6	19.4	71.9	1015.0	1.4	NW	223.9	14:20	1.3	4.4	8.1	(11:50)
17/05/15	23.3	19.4	55.9	1012.5	2.8	NE	297.3	14:30	0.0	4.6	8.2	(12:30)
18/05/15	24.2	19.4	49.5	1010.8	2.0	NW	477.3	14:40	0.0	5.4	8.4	(12:40)
19/05/15	21.5	19.7	75.8	1010.6	1.2	SE	489.9	14:30	0.0	5.7	8.9	(12:40)
20/05/15	20.9	19.7	79.2	1012.8	1.1	S	353.6	14:40	0.0	5.4	9.3	(13:30)
21/05/15	18.1	19.6	73.0	1015.2	0.9	NW	128.8	14:30	1.5	3.7	6.5	(14:00)
22/05/15	16.9	19.5	61.9	1012.0	1.4	SW	420.0	14:40	4.6	4.8	8.7	(13:20)
23/05/15	16.9	19.4	75.4	1012.7	1.4	S	373.8	14:40	3.5	5.6	10.3	(12:40)
24/05/15	17.5	19.7	71.1	1013.4	0.8	NE	334.8	14:40	13.7	5.1	9.5	(13:10)
25/05/15	17.7	19.9	76.8	1014.1	0.9	S	361.7	14:50	2.0	5.0	9.5	(13:10)
26/05/15	18.6	19.9	77.6	1011.0	1.1	SE	461.0	14:40	1.0	5.5	9.1	(13:10)
27/05/15	19.0	19.7	70.8	1011.6	1.1	NW	308.5	14:40	3.3	4.9	9.3	(12:00)
28/05/15	20.4	19.6	56.2	1016.2	1.2	NW	543.3	16:20	0.0	6.1	9.2	(14:30)
29/05/15	20.2	19.4	70.6	1016.9	1.1	SE	456.3	15:10	0.0	5.6	9.3	(14:10)
30/05/15	20.8	19.5	68.8	1017.6	1.1	SE	515.5	14:50	0.0	5.8	8.8	(14:10)
31/05/15	21.3	19.8	74.9	1018.2	1.0	SE	495.9	15:00	0.0	5.5	8.5	(14:40)

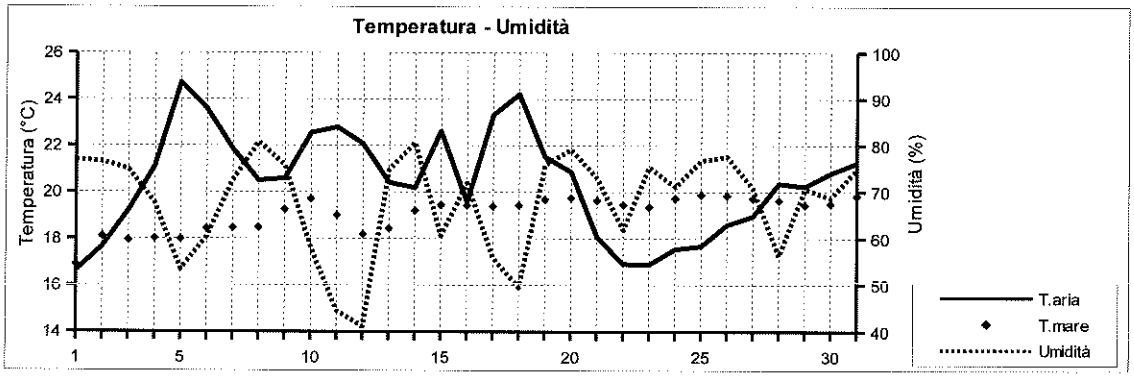

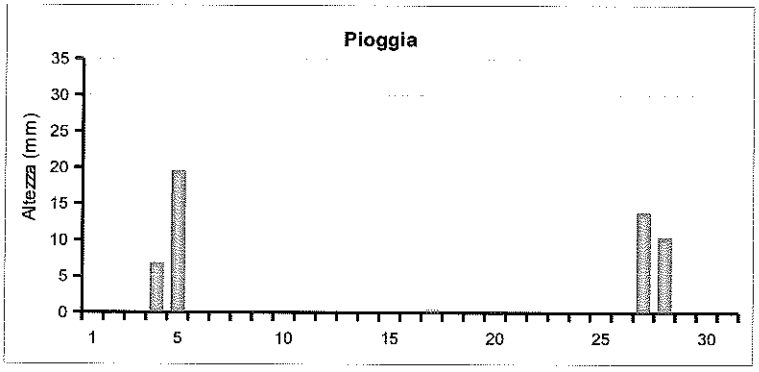

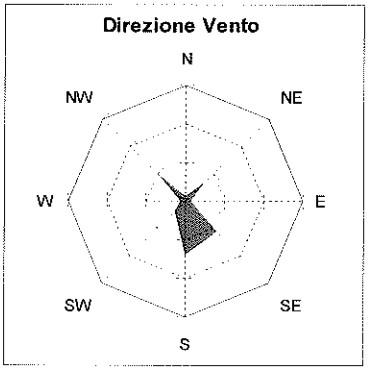

MAGGIO 2015

(estremi giornalieri)

Data	Temperatura (°C) min	(ore)	max	(ore)	Umidità (%) min	(ore)	max	(ore)	Pressione (hPa) min	(ore)	max	(ore)	Vento (m/s) max	(ore)	Radiazione (W/m²) max	(ore)
01/05/15	14.9	(06:30)	18.5	(15:20)	70.0	(12:20)	83.0	(02:10)	1017.8	(23:50)	1021.3	(08:50)	6.7	(12:20)	900.0	(11:20)
02/05/15	16.2	(02:40)	20.0	(15:40)	69.0	(08:40)	**90.0**	**(00:00)**	1014.6	(16:30)	1018.0	(00:10)	7.2	(16:20)	914.0	(13:20)
03/05/15	15.6	(06:10)	22.2	(16:40)	59.0	(17:20)	90.0	(00:00)	1015.1	(17:40)	1017.1	(10:50)	4.9	(11:30)	951.0	(13:50)
04/05/15	17.7	(04:50)	25.8	(16:20)	45.0	(14:50)	82.0	(20:00)	1014.7	(19:10)	1017.1	(00:00)	4.9	(12:00)	874.0	(13:20)
05/05/15	19.8	(05:20)	**30.9**	**(14:00)**	33.0	(13:40)	70.0	(00:10)	1013.9	(18:40)	1015.9	(00:20)	3.6	(17:10)	933.0	(13:10)
06/05/15	19.9	(06:00)	27.9	(10:30)	37.0	(09:50)	79.0	(20:00)	1012.9	(23:30)	1015.3	(07:40)	9.8	(12:10)	962.0	(12:50)
07/05/15	19.7	(00:00)	25.0	(00:30)	40.0	(00:20)	89.0	(19:20)	1013.0	(04:50)	1016.6	(22:10)	7.6	(15:10)	909.0	(13:30)
08/05/15	18.7	(06:00)	22.7	(13:40)	69.0	(16:30)	89.0	(01:00)	1014.7	(21:00)	1017.6	(11:40)	8.9	(17:40)	1000.0	(13:00)
09/05/15	17.8	(06:30)	24.7	(16:40)	58.0	(16:40)	89.0	(05:50)	1013.7	(16:20)	1016.2	(22:10)	6.3	(14:50)	919.0	(12:10)
10/05/15	18.6	(05:50)	26.5	(14:10)	37.0	(16:30)	83.0	(06:10)	1016.2	(00:00)	1022.5	(23:50)	11.2	(14:50)	1014.0	(12:40)
11/05/15	19.2	(05:20)	27.1	(15:30)	32.0	(15:40)	55.0	(03:10)	1020.7	(18:40)	1023.7	(09:20)	11.2	(19:50)	933.0	(13:00)
12/05/15	18.5	(06:00)	26.8	(15:50)	**22.0**	**(14:20)**	61.0	(22:00)	1021.8	(04:50)	**1024.3**	**(10:30)**	11.6	(09:30)	921.0	(13:20)
13/05/15	18.3	(05:10)	23.5	(14:30)	61.0	(00:00)	89.0	(21:50)	1020.7	(23:20)	1024.2	(00:10)	6.3	(11:40)	925.0	(13:00)
14/05/15	18.3	(06:20)	22.4	(14:10)	57.0	(15:20)	90.0	(00:10)	1013.0	(22:50)	1020.7	(00:00)	8.5	(16:00)	911.0	(12:40)
15/05/15	18.0	(06:30)	27.6	(11:40)	33.0	(14:10)	84.0	(21:30)	**1007.7**	**(15:20)**	1013.6	(00:30)	**12.1**	**(15:20)**	998.0	(12:30)
16/05/15	16.3	(08:10)	22.8	(16:10)	57.0	(13:00)	83.0	(04:00)	1012.4	(03:00)	1017.7	(13:20)	8.0	(03:40)	940.0	(11:50)
17/05/15	19.5	(05:00)	27.1	(13:00)	42.0	(13:10)	68.0	(05:00)	1011.2	(18:50)	1014.0	(05:50)	11.6	(12:40)	916.0	(12:30)
18/05/15	21.5	(06:50)	29.7	(13:20)	25.0	(11:50)	75.0	(23:20)	1009.4	(18:20)	1012.0	(00:00)	9.8	(00:50)	956.0	(12:00)
19/05/15	19.6	(23:50)	24.4	(13:50)	52.0	(13:20)	88.0	(20:50)	1008.7	(05:40)	1012.6	(23:30)	7.2	(15:10)	874.0	(13:20)
20/05/15	18.6	(05:30)	23.8	(11:20)	57.0	(16:00)	89.0	(01:10)	1012.1	(03:10)	1014.3	(23:00)	6.7	(15:30)	986.0	(14:30)
21/05/15	15.3	(11:10)	20.2	(02:20)	56.0	(22:20)	89.0	(00:30)	1013.6	(04:20)	1017.1	(10:50)	8.5	(06:40)	613.0	(14:00)
22/05/15	**14.2**	**(23:10)**	19.6	(10:20)	49.0	(10:00)	84.0	(23:20)	1010.9	(15:40)	1014.4	(00:00)	11.2	(17:10)	1136.0	(13:20)
23/05/15	14.6	(08:00)	20.3	(16:30)	58.0	(15:40)	89.0	(09:40)	1011.5	(04:20)	1013.9	(22:20)	7.6	(16:40)	1190.0	(12:40)
24/05/15	15.7	(18:20)	20.3	(14:10)	61.0	(11:20)	82.0	(18:10)	1012.1	(04:30)	1014.9	(22:30)	7.6	(12:30)	**1285.0**	**(14:20)**
25/05/15	15.1	(02:10)	20.6	(18:00)	65.0	(18:40)	84.0	(02:10)	1012.7	(19:20)	1015.1	(08:50)	7.6	(14:00)	1111.0	(13:10)
26/05/15	16.7	(03:20)	21.2	(12:40)	65.0	(18:20)	86.0	(21:10)	1009.5	(17:50)	1013.0	(00:00)	8.5	(14:50)	965.0	(13:50)
27/05/15	16.4	(02:10)	23.7	(12:50)	48.0	(13:00)	86.0	(00:00)	1009.3	(03:40)	1014.9	(23:50)	9.4	(14:10)	1208.0	(12:00)
28/05/15	16.8	(03:30)	24.4	(18:10)	40.0	(20:20)	67.0	(03:20)	1014.9	(00:00)	1018.0	(12:30)	7.2	(14:20)	918.0	(14:30)
29/05/15	17.3	(07:10)	24.1	(17:50)	47.0	(19:10)	83.0	(05:20)	1016.3	(02:40)	1017.7	(13:10)	7.2	(13:30)	1034.0	(16:40)
30/05/15	17.6	(07:10)	24.7	(17:30)	51.0	(21:00)	80.0	(07:10)	1016.8	(05:40)	1018.4	(23:00)	7.2	(14:40)	904.0	(14:30)
31/05/15	18.1	(06:40)	24.9	(19:50)	63.0	(10:40)	86.0	(07:10)	1017.4	(19:50)	1018.7	(23:40)	8.0	(15:30)	881.0	(14:50)

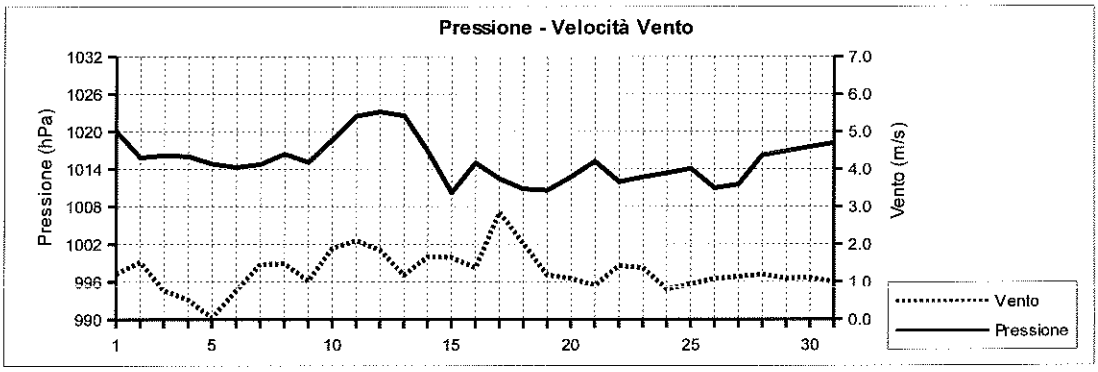

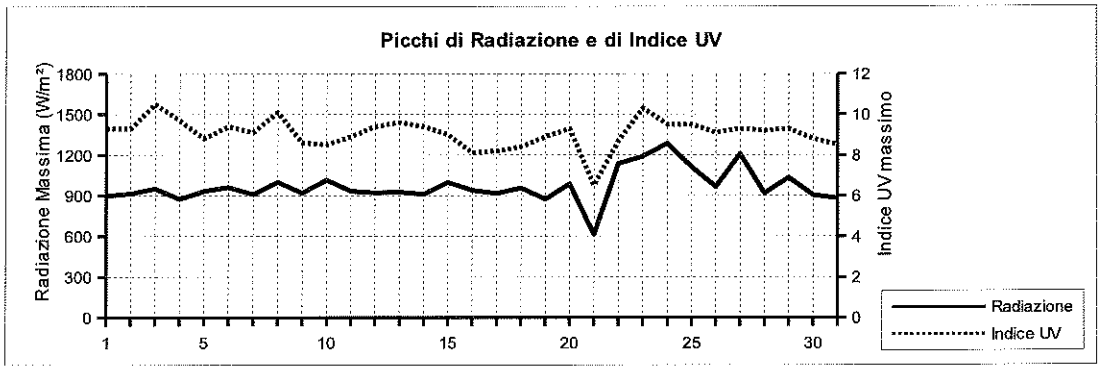

GIUGNO 2015

(medie giornaliere)

Data	Temperatura aria (°C)	Temperatura mare (°C)	Umidità %	Pressione hPa	Vento m/s	Vento direzione	Rad. Solare W/m²	Rad. Solare durata	Pioggia mm	Indice UV medio	Indice UV max	Indice UV (ore)
01/06/15	22.4	20.5	76.8	1018.2	2.0	S	461.4	14:30	0.0	5.3	8.3	(12:50)
02/06/15	24.1	20.8	69.2	1019.4	1.7	S	330.3	14:30	0.0	5.8	9.3	(13:00)
03/06/15	24.0	20.9	82.0	1020.7	1.9	S	362.6	14:40	0.0	6.1	8.1	(11:40)
04/06/15	23.8	21.7	80.9	1020.9	1.5	SE	423.6	14:50	0.0	6.2	9.0	(13:00)
05/06/15	25.3	21.9	70.1	1018.8	0.5	SE	441.7	14:50	0.0	5.2	8.4	(12:20)
06/06/15	26.5	21.9	56.4	1019.8	0.8	SW	395.1	15:00	0.0	5.4	9.3	(12:50)
07/06/15	25.1	21.7	65.9	1019.7	1.1	SW	413.6	14:10	0.0	5.8	8.8	(12:20)
08/06/15	22.7	22.5	73.5	1017.3	1.1	NE	421.1	14:50	11.9	6.1	9.2	(12:00)
09/06/15	22.0	22.8	72.8	1015.9	1.1	SE	455.4	15:00	13.5	5.8	9.3	(13:20)
10/06/15	23.9	22.4	71.6	1017.3	0.9	NW	480.0	15:00	0.0	5.8	9.0	(13:00)
11/06/15	24.9	22.4	72.2	1017.1	0.7	SE	495.0	15:10	0.0	5.6	9.1	(13:10)
12/06/15	26.0	22.6	65.4	1017.0	0.6	--	449.7	15:00	0.0	5.8	9.8	(13:00)
13/06/15	27.3	22.7	53.3	1015.3	0.5	SW	365.9	15:00	0.0	5.0	9.1	(13:20)
14/06/15	25.3	23.8	68.5	1014.3	1.3	S	437.1	15:00	0.0	5.9	9.1	(13:00)
15/06/15	24.4	24.3	72.3	1016.0	0.9	SW	361.4	14:50	0.0	5.4	**10.4**	**(13:40)**
16/06/15	24.3	23.4	70.2	1016.4	1.5	NW	446.3	15:00	0.0	5.8	9.9	(13:20)
17/06/15	22.1	22.7	71.6	1013.2	1.2	NW	363.4	15:00	25.4	5.0	9.3	(11:50)
18/06/15	22.5	22.0	53.0	1012.3	1.7	N	455.8	15:00	0.0	5.4	9.4	(13:30)
19/06/15	22.6	21.0	63.6	1011.9	1.1	SE	503.7	15:00	0.0	5.8	9.6	(12:50)
20/06/15	23.1	21.8	73.7	1011.3	1.2	SE	503.9	15:00	0.0	5.8	9.3	(12:40)
21/06/15	23.6	22.9	49.5	1014.0	1.7	NW	484.0	15:00	0.0	5.4	9.4	(13:00)
22/06/15	23.5	22.5	49.0	1017.7	1.1	SW	512.6	15:20	0.0	5.3	8.6	(12:50)
23/06/15	23.1	22.4	74.0	1015.7	1.4	SE	482.1	15:10	0.0	5.1	8.8	(12:40)
24/06/15	24.5	22.6	57.6	1015.6	1.1	SE	443.2	15:10	0.0	4.9	8.8	(12:50)
25/06/15	24.6	22.6	47.7	1018.8	1.8	N	506.8	15:10	0.0	5.3	8.9	(13:00)
26/06/15	24.9	22.6	41.4	1017.3	2.5	NW	506.5	15:10	0.0	5.2	8.7	(13:00)
27/06/15	25.0	22.2	45.5	1016.8	1.7	NW	502.5	15:10	0.0	5.3	9.0	(13:00)
28/06/15	24.2	21.5	72.1	1016.4	0.7	SE	376.8	15:10	0.0	4.4	8.1	(13:10)
29/06/15	26.4	21.6	47.0	1019.1	1.1	NW	462.3	15:10	0.0	4.7	8.1	(13:10)
30/06/15	26.7	21.7	53.7	1019.3	0.9	SW	482.4	15:10	0.0	4.9	8.1	(13:00)

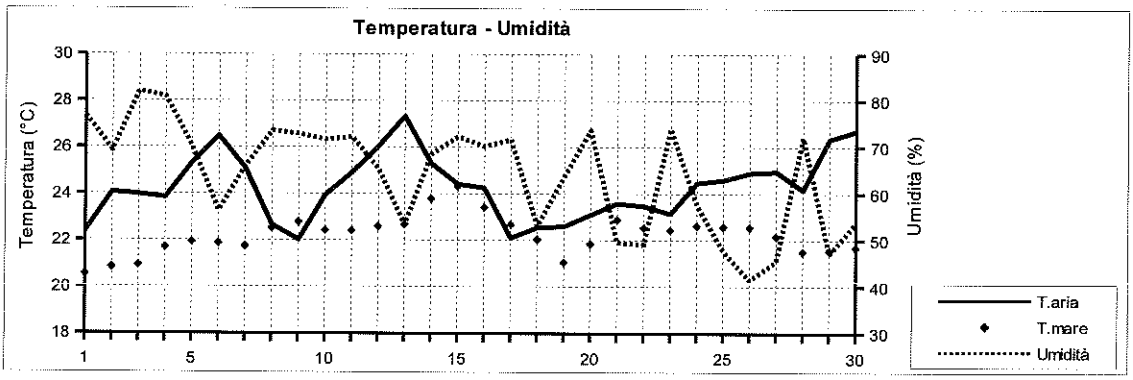

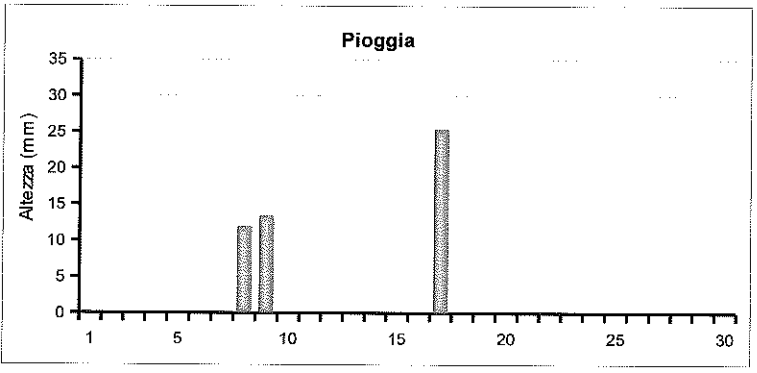

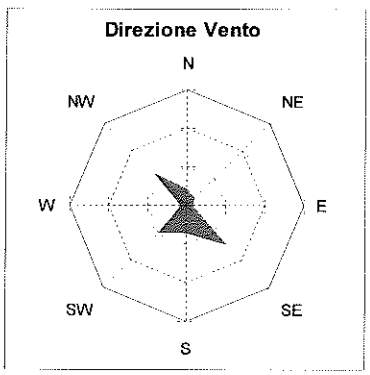

GIUGNO 2015

(estremi giornalieri)

Data	Temperatura (°C) min	(ore)	max	(ore)	Umidità (%) min	(ore)	max	(ore)	Pressione (hPa) min	(ore)	max	(ore)	Vento (m/s) max	(ore)	Radiazione (W/m²) max	(ore)
01/06/15	19.4	(05:00)	25.3	(17:10)	61.6	(08:10)	88.9	(00:00)	1017.5	(15:20)	1019.2	(22:40)	4.6	(13:10)	982.6	(13:00)
02/06/15	20.4	(04:10)	29.8	(15:20)	45.7	(14:00)	88.9	(00:00)	1018.0	(13:50)	1021.0	(21:40)	4.5	(12:20)	961.6	(11:20)
03/06/15	21.4	(04:40)	28.0	(15:30)	64.9	(15:30)	94.4	(05:30)	1019.9	(14:10)	1021.7	(07:20)	4.1	(11:30)	963.4	(11:20)
04/06/15	22.3	(04:40)	27.6	(17:00)	62.0	(17:10)	93.4	(01:10)	1019.2	(18:10)	**1022.3**	**(11:40)**	6.3	(13:10)	977.9	(11:20)
05/06/15	20.3	(06:20)	31.1	(16:00)	41.0	(11:50)	**90.0**	**(00:40)**	1017.1	(18:40)	1020.3	(00:00)	10.3	(16:20)	923.0	(13:50)
06/06/15	22.7	(01:30)	30.6	(14:10)	40.0	(13:20)	88.0	(01:00)	1018.8	(04:20)	1020.8	(22:00)	8.9	(15:10)	1071.0	(12:50)
07/06/15	22.1	(00:00)	30.2	(14:50)	44.0	(15:00)	79.0	(04:20)	1017.4	(16:20)	1020.6	(00:00)	8.5	(20:10)	1030.0	(12:20)
08/06/15	20.1	(17:50)	26.7	(14:00)	65.0	(09:00)	81.0	(05:10)	1015.4	(15:30)	1019.4	(00:00)	9.8	(17:30)	877.0	(13:20)
09/06/15	18.6	(04:50)	26.1	(16:10)	63.0	(07:50)	84.0	(17:50)	1014.7	(14:40)	1017.0	(00:00)	9.8	(17:40)	1020.0	(13:10)
10/06/15	19.8	(05:00)	28.1	(16:00)	58.0	(18:00)	84.0	(05:50)	1016.6	(16:20)	1018.1	(00:00)	7.2	(15:50)	882.0	(13:20)
11/06/15	21.3	(05:50)	29.6	(18:20)	48.0	(18:10)	86.0	(00:00)	1015.6	(18:10)	1018.1	(00:00)	6.3	(14:20)	891.0	(13:20)
12/06/15	22.3	(05:20)	29.7	(17:30)	44.0	(14:50)	87.0	(00:20)	1014.7	(20:40)	1018.8	(11:10)	6.3	(16:20)	1041.0	(11:10)
13/06/15	23.5	(05:50)	31.6	(13:00)	36.0	(11:10)	66.0	(14:20)	1012.7	(19:20)	1017.1	(09:10)	11.6	(16:10)	1009.0	(13:30)
14/06/15	23.3	(23:00)	27.3	(12:00)	53.0	(00:00)	82.0	(20:20)	1012.9	(03:40)	1015.8	(23:00)	7.6	(15:50)	882.0	(11:40)
15/06/15	22.6	(05:40)	28.0	(17:00)	46.0	(17:00)	82.0	(00:50)	1014.6	(03:00)	1017.8	(11:20)	7.2	(19:10)	998.0	(13:50)
16/06/15	21.4	(05:20)	27.8	(13:40)	53.0	(13:40)	84.0	(05:10)	1014.4	(21:40)	1017.5	(00:00)	8.9	(20:30)	930.0	(13:20)
17/06/15	**17.8**	**(10:10)**	25.2	(15:40)	52.0	(15:10)	89.0	(10:30)	1011.6	(18:00)	1015.3	(00:40)	**14.3**	**(10:10)**	1046.0	(12:00)
18/06/15	20.5	(03:40)	25.8	(17:40)	36.0	(14:00)	73.0	(00:00)	1011.3	(17:20)	1013.2	(11:00)	12.1	(11:40)	1044.0	(14:10)
19/06/15	19.6	(06:30)	25.2	(16:20)	53.0	(19:50)	79.0	(23:40)	1010.5	(18:00)	1013.0	(00:00)	7.2	(11:10)	896.0	(13:00)
20/06/15	20.8	(23:30)	25.4	(16:10)	62.0	(16:00)	81.0	(04:20)	**1009.6**	**(17:40)**	1012.5	(00:20)	7.6	(13:00)	904.0	(13:10)
21/06/15	19.9	(04:40)	27.1	(14:40)	31.0	(14:50)	74.0	(01:30)	1012.0	(00:00)	1017.0	(23:30)	8.0	(13:00)	1023.0	(13:10)
22/06/15	20.1	(05:50)	26.0	(12:10)	34.0	(11:10)	74.0	(00:00)	1016.9	(00:00)	1018.9	(12:00)	7.6	(15:30)	909.0	(13:00)
23/06/15	20.7	(05:40)	25.1	(13:30)	67.0	(14:20)	80.0	(04:10)	1014.0	(20:20)	1017.5	(00:00)	7.2	(13:50)	896.0	(13:10)
24/06/15	21.0	(05:50)	26.8	(19:50)	42.0	(10:30)	72.0	(00:00)	1014.0	(05:30)	1018.7	(23:40)	6.7	(21:10)	1042.0	(11:30)
25/06/15	20.8	(04:40)	29.1	(18:00)	36.0	(13:00)	60.0	(00:00)	1017.5	(18:20)	1019.8	(06:20)	10.3	(08:30)	905.0	(13:00)
26/06/15	21.7	(05:00)	28.7	(14:10)	**28.0**	**(14:00)**	60.0	(21:30)	1016.1	(15:50)	1018.6	(00:00)	9.8	(10:50)	928.0	(13:40)
27/06/15	21.3	(06:00)	29.6	(14:20)	31.0	(13:40)	63.0	(23:00)	1015.5	(16:00)	1018.1	(00:00)	9.4	(16:20)	900.0	(13:00)
28/06/15	21.8	(05:30)	27.7	(17:40)	57.0	(21:10)	84.0	(04:20)	1015.3	(04:10)	1018.3	(23:50)	6.3	(13:50)	**1078.0**	**(11:60)**
29/06/15	22.8	(05:20)	30.5	(13:20)	31.0	(13:20)	68.0	(00:00)	1018.1	(05:00)	1020.3	(22:10)	9.8	(17:00)	986.0	(13:50)
30/06/15	23.1	(06:20)	**31.2**	**(16:10)**	39.0	(18:00)	76.0	(22:00)	1018.1	(18:00)	1020.4	(23:40)	6.7	(15:10)	896.0	(13:20)

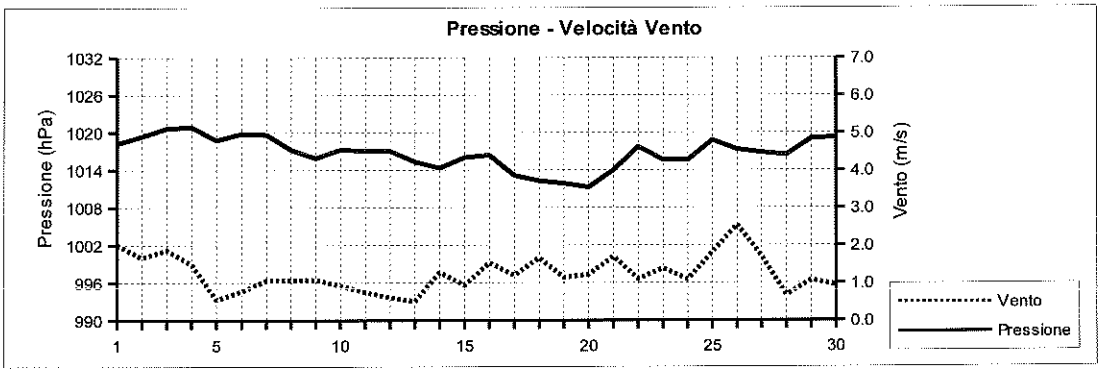

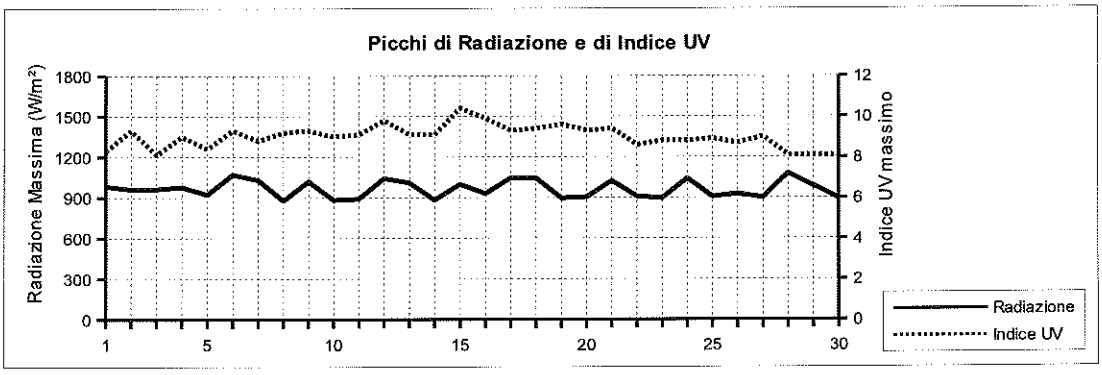

LUGLIO 2015

(medie giornaliere)

Data	Temperatura aria (°C)	Temperatura mare (°C)	Umidità %	Pressione hPa	Vento m/s	Vento direzione	Rad. Solare W/m²	Rad. Solare durata	Pioggia mm	Indice UV medio	Indice UV max	Indice UV (ore)
01/07/15	27.3	22.2	43.2	1020.2	1.1	NW	493.1	15:10	0.0	4.9	8.3	(13:00)
02/07/15	27.2	22.5	47.7	1022.1	0.9	NW	483.9	15:10	0.0	4.8	8.0	(12:30)
03/07/15	28.1	22.7	51.6	1022.8	0.6	SE	479.6	15:00	0.0	4.8	8.0	(12:50)
04/07/15	29.3	22.8	45.5	1021.3	1.0	NW	478.4	15:10	0.0	4.9	8.2	(13:10)
05/07/15	27.5	23.3	62.0	1019.6	0.8	SE	488.6	15:00	0.0	4.8	8.0	(12:40)
06/07/15	26.6	23.8	83.3	1019.2	1.0	SE	463.2	15:00	0.0	4.9	8.3	(12:40)
07/07/15	27.4	24.1	81.5	1017.1	0.6	SE	444.8	14:50	0.0	4.9	8.2	(12:40)
08/07/15	27.3	24.7	81.7	1012.9	0.8	SE	409.7	14:50	0.0	5.1	8.7	(13:00)
09/07/15	27.7	25.2	74.5	1010.5	1.0	S	461.0	15:00	0.0	4.9	8.2	(13:00)
10/07/15	29.4	25.1	53.8	1013.7	1.4	NE	387.5	15:00	0.0	4.6	8.4	(13:30)
11/07/15	28.6	25.1	53.6	1017.0	1.2	SW	461.8	15:00	0.0	5.0	8.5	(13:30)
12/07/15	27.8	25.2	72.0	1016.4	0.9	SW	470.2	14:50	0.0	5.1	8.4	(13:00)
13/07/15	27.2	25.3	76.1	1015.1	0.8	S	469.6	14:50	0.0	5.0	8.4	(13:00)
14/07/15	28.4	25.3	71.2	1015.0	0.4	S	444.3	15:10	0.0	4.8	8.3	(12:50)
15/07/15	30.0	25.7	70.6	1016.3	0.3	SE	457.1	14:50	0.0	4.7	7.9	(13:00)
16/07/15	29.7	26.2	67.3	1017.8	0.4	SE	473.0	14:50	0.0	4.9	8.5	(13:20)
17/07/15	31.4	26.2	52.8	1018.0	0.5	SW	468.8	14:50	0.0	5.0	8.4	(13:00)
18/07/15	30.9	26.4	52.9	1016.7	0.5	SW	466.5	14:50	0.0	5.1	8.4	(13:10)
19/07/15	30.0	26.5	59.6	1014.7	0.8	SE	472.3	14:50	0.0	5.3	8.8	(13:10)
20/07/15	29.2	26.4	71.2	1013.0	0.5	S	461.1	14:50	0.0	5.4	8.8	(13:00)
21/07/15	29.4	26.2	75.8	1013.8	1.3	SE	437.4	14:50	0.0	5.4	8.8	(12:30)
22/07/15	29.7	26.8	75.1	1013.1	1.4	SE	444.3	14:50	0.0	5.6	8.9	(13:10)
23/07/15	27.5	27.1	74.8	1010.9	1.9	--	426.8	13:00	20.3	6.1	8.7	(13:30)
24/07/15	27.0	26.4	65.7	1010.4	1.3	--	461.5	14:20	7.6	6.7	10.6	(13:40)
25/07/15	27.3	25.8	72.4	1011.2	1.1	SW	464.1	14:40	0.0	7.3	11.0	(13:00)
26/07/15	28.3	25.9	68.3	1012.1	1.1	SW	459.6	14:40	0.0	7.3	11.1	(13:10)
27/07/15	27.0	25.6	68.0	1011.1	1.0	SW	360.1	14:30	0.0	7.0	**12.5**	**(13:30)**
28/07/15	27.6	25.6	70.3	1010.8	1.1	SW	418.3	14:40	0.0	7.2	11.7	(13:00)
29/07/15	26.8	24.1	68.8	1011.4	1.4	SW	498.2	14:30	0.0	7.7	11.9	(12:50)
30/07/15	27.6	20.5	76.3	1011.3	1.2	S	453.7	14:30	0.0	7.1	11.1	(13:00)
31/07/15	29.5	25.5	61.0	1010.4	1.2	--	429.7	14:20	0.0	6.4	10.6	(12:20)

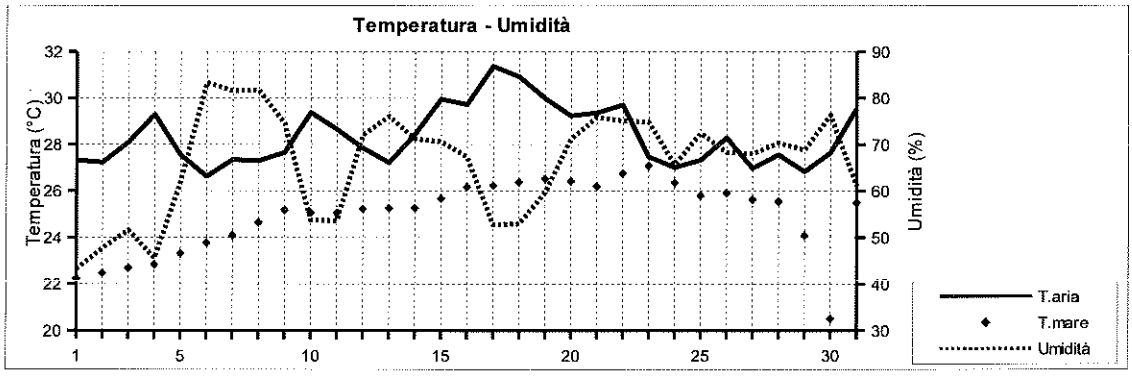

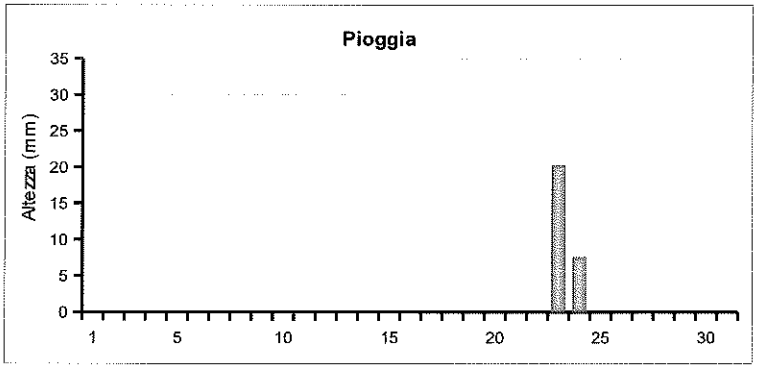

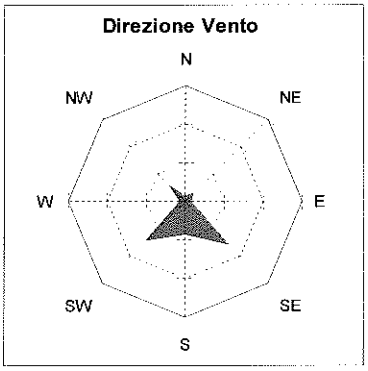

LUGLIO 2015

(estremi giornalieri)

Data	Temperatura (°C)				Umidità (%)				Pressione (hPa)				Vento (m/s)		Radiazione (W/m²)	
	min	(ore)	max	(ore)	min	(ore)	max	(ore)	min	(ore)	max	(ore)	max	(ore)	max	(ore)
01/07/15	23.6	(05:40)	30.9	(16:50)	33.0	(16:30)	65.0	(22:40)	1019.3	(16:10)	1021.8	(00:00)	8.0	(15:40)	872.0	(13:30)
02/07/15	23.9	(05:40)	30.9	(16:00)	35.0	(11:30)	83.0	(00:00)	1021.5	(03:20)	1023.6	(23:50)	7.6	(14:40)	872.0	(13:30)
03/07/15	**23.4**	**(05:30)**	32.8	(15:50)	34.0	(19:00)	84.0	(00:20)	1021.7	(15:30)	**1023.6**	**(11:10)**	6.3	(14:40)	853.0	(13:00)
04/07/15	26.7	(22:00)	32.8	(15:50)	36.0	(20:10)	69.0	(21:40)	1019.8	(18:00)	1023.5	(00:00)	8.5	(14:30)	893.0	(13:00)
05/07/15	25.2	(23:40)	31.1	(13:40)	37.0	(09:10)	92.0	(23:50)	1018.8	(16:50)	1020.3	(00:00)	6.7	(14:10)	870.0	(13:20)
06/07/15	24.3	(03:30)	30.1	(19:00)	67.0	(18:50)	**94.0**	**(03:40)**	1018.0	(18:10)	1020.1	(08:10)	7.2	(13:40)	960.0	(12:30)
07/07/15	25.0	(03:50)	30.6	(18:10)	65.0	(18:10)	93.0	(02:20)	1014.6	(20:30)	1018.6	(00:00)	6.3	(13:30)	826.0	(12:40)
08/07/15	25.3	(05:40)	29.7	(15:00)	71.0	(16:10)	92.0	(05:00)	1010.6	(20:40)	1015.1	(00:00)	7.2	(12:30)	842.0	(13:50)
09/07/15	25.5	(05:40)	30.1	(16:50)	36.0	(23:00)	90.0	(03:10)	1009.7	(04:30)	1011.9	(23:50)	6.7	(15:10)	833.0	(13:30)
10/07/15	26.4	(05:00)	33.3	(14:40)	44.0	(14:30)	70.0	(00:40)	1011.7	(01:50)	1016.8	(00:00)	8.5	(09:00)	933.0	(13:40)
11/07/15	25.5	(05:40)	31.7	(15:10)	42.0	(09:20)	71.0	(23:40)	1016.2	(18:20)	1017.9	(09:20)	6.7	(13:40)	842.0	(13:30)
12/07/15	25.7	(05:30)	31.8	(15:40)	52.0	(15:50)	84.0	(04:20)	1015.2	(18:30)	1017.2	(11:10)	7.6	(16:20)	831.0	(13:20)
13/07/15	25.3	(05:20)	29.6	(14:40)	60.0	(20:20)	86.0	(05:00)	1014.3	(18:10)	1016.2	(00:00)	7.2	(12:30)	856.0	(13:40)
14/07/15	25.1	(05:50)	31.9	(17:30)	58.0	(17:00)	82.0	(04:50)	1014.2	(04:10)	1016.1	(23:20)	5.8	(14:10)	816.0	(13:10)
15/07/15	26.6	(05:20)	34.2	(16:40)	52.0	(15:30)	86.0	(04:10)	1015.5	(17:20)	1017.4	(23:20)	6.7	(15:30)	826.0	(13:10)
16/07/15	27.6	(05:30)	32.8	(14:50)	48.0	(14:10)	85.0	(21:00)	1017.0	(04:00)	1018.7	(12:30)	6.7	(12:10)	842.0	(13:30)
17/07/15	27.0	(06:00)	36.6	(15:00)	29.0	(15:20)	78.0	(03:30)	1016.8	(18:50)	1018.8	(09:00)	7.2	(16:20)	835.0	(14:10)
18/07/15	26.9	(05:50)	**36.7**	**(16:10)**	**22.0**	**(15:30)**	74.0	(12:50)	1015.0	(18:30)	1018.1	(00:00)	5.8	(17:50)	830.0	(13:30)
19/07/15	26.6	(05:40)	35.1	(15:00)	34.0	(17:40)	81.0	(04:30)	1012.9	(19:30)	1016.1	(00:00)	7.2	(19:40)	837.0	(13:10)
20/07/15	25.8	(05:50)	32.6	(17:10)	57.0	(18:50)	83.0	(23:40)	1012.1	(18:00)	1014.0	(23:00)	7.2	(14:20)	823.0	(12:50)
21/07/15	26.6	(06:10)	33.8	(16:10)	52.0	(19:50)	85.0	(02:10)	1012.7	(17:10)	1014.6	(10:20)	11.6	(11:40)	800.0	(13:30)
22/07/15	27.3	(06:10)	32.1	(17:50)	59.0	(19:40)	83.0	(00:20)	1011.4	(16:50)	1014.4	(08:30)	8.0	(14:50)	809.0	(13:20)
23/07/15	20.3	(17:40)	31.2	(12:40)	58.0	(23:30)	90.0	(17:50)	**1008.9**	**(15:50)**	1012.7	(17:20)	**19.2**	**(17:30)**	831.0	(12:40)
24/07/15	23.6	(04:30)	30.8	(10:00)	46.0	(09:40)	79.0	(19:40)	1009.5	(17:00)	1011.0	(11:10)	8.5	(15:10)	904.0	(13:50)
25/07/15	24.3	(03:30)	30.5	(16:30)	61.0	(16:00)	80.0	(03:10)	1010.1	(01:40)	1012.4	(23:10)	7.2	(18:00)	907.0	(14:00)
26/07/15	26.2	(00:00)	31.8	(16:00)	45.0	(15:50)	81.0	(02:20)	1011.2	(18:10)	1012.8	(10:30)	8.0	(15:40)	916.0	(13:10)
27/07/15	25.2	(04:50)	29.2	(15:40)	58.0	(15:50)	79.0	(22:30)	1010.1	(19:00)	1012.3	(00:00)	7.6	(15:30)	**1041.0**	**(12:50)**
28/07/15	26.1	(04:50)	30.3	(15:20)	55.0	(19:20)	82.0	(05:00)	1010.2	(04:30)	1012.0	(22:50)	7.6	(18:20)	1009.0	(12:00)
29/07/15	25.2	(05:30)	28.7	(17:30)	62.0	(07:40)	79.0	(23:30)	1010.4	(18:20)	1012.1	(00:00)	8.0	(13:20)	928.0	(12:10)
30/07/15	25.2	(05:50)	32.0	(16:30)	52.0	(12:30)	87.0	(06:40)	1010.1	(18:10)	1012.1	(00:00)	8.5	(14:40)	854.0	(13:20)
31/07/15	26.2	(04:50)	33.9	(15:50)	32.0	(15:40)	82.0	(03:00)	1008.3	(05:00)	1011.8	(01:50)	5.8	(06:50)	947.0	(12:20)

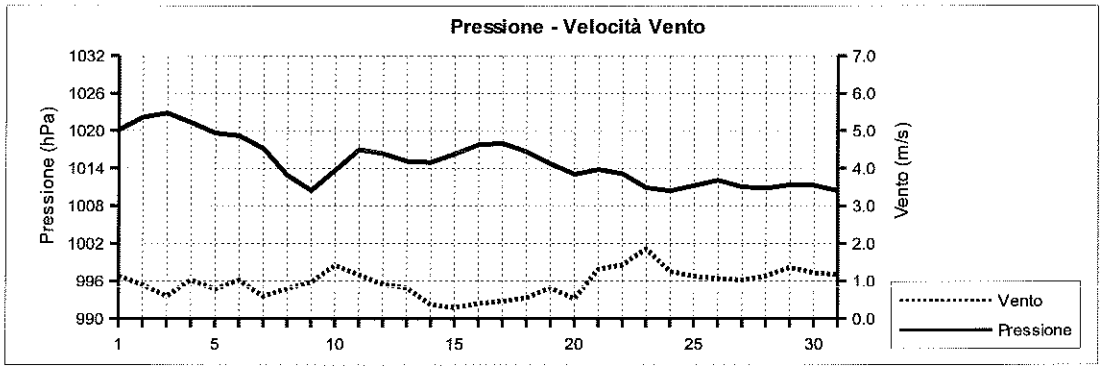

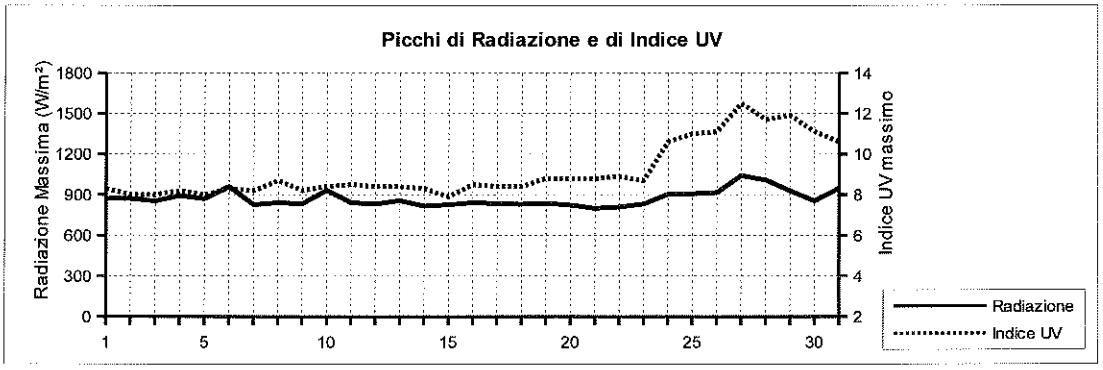

AGOSTO 2015

(medie giornaliere)

Data	Temperatura aria (°C)	Temperatura mare (°C)	Umidità %	Pressione hPa	Vento m/s	Vento direzione	Rad. Solare W/m²	Rad. Solare durata	Pioggia mm	Indice UV medio	Indice UV max	Indice UV (ore)
01/08/15	29.2	25.8	61.1	1013.4	1.3	NW	463.0	14:30	0.0	6.9	10.3	(12:50)
02/08/15	29.2	26.4	68.6	1015.2	1.0	S	430.7	14:20	0.0	6.3	10.1	(13:10)
03/08/15	29.8	26.0	66.0	1014.0	1.6	NE	465.2	14:20	0.0	6.4	10.5	(13:00)
04/08/15	29.9	25.6	56.8	1013.3	1.2	NW	472.6	14:10	0.0	6.1	9.5	(12:40)
05/08/15	30.0	26.1	65.3	1013.6	1.1	SE	462.3	14:10	0.0	5.9	9.5	(12:50)
06/08/15	31.5	26.1	50.3	1013.4	1.0	NW	457.5	14:10	0.0	5.7	9.2	(13:10)
07/08/15	31.7	25.6	48.6	1013.4	1.2	NE	391.8	14:10	0.0	5.7	8.3	(12:20)
08/08/15	30.8	25.5	54.3	1014.9	1.6	--	391.4	14:00	0.8	5.4	8.5	(13:00)
09/08/15	28.1	26.2	68.6	1015.6	1.4	--	432.8	13:50	0.0	5.7	8.6	(13:10)
10/08/15	27.0	26.1	67.0	1013.4	1.2	--	336.6	13:50	0.0	5.3	7.8	(11:30)
11/08/15	25.8	26.5	68.4	1011.8	1.9	--	353.1	13:40	2.3	6.0	10.8	(13:20)
12/08/15	28.0	26.6	61.8	1013.8	1.6	NE	246.1	14:00	0.0	5.1	10.2	(12:40)
13/08/15	30.4	26.4	49.4	1013.4	1.1	NW	454.6	13:50	0.0	5.5	8.2	(12:40)
14/08/15	28.8	26.5	71.7	1011.8	1.1	S	434.8	13:50	0.0	5.6	8.5	(13:10)
15/08/15	27.4	26.6	74.8	1010.6	1.3	S	297.1	13:50	0.5	5.2	9.8	(13:00)
16/08/15	23.7	26.6	77.4	1010.1	1.0	SW	208.3	13:30	31.2	5.1	8.5	(15:20)
17/08/15	25.0	26.3	64.4	1012.2	1.4	SW	466.2	13:50	0.0	6.4	9.9	(13:10)
18/08/15	25.5	26.2	69.2	1014.3	1.2	SW	461.1	14:00	0.0	6.1	10.1	(13:20)
19/08/15	24.7	26.4	76.7	1014.5	1.1	SE	354.7	13:50	0.8	5.6	**10.8**	**(12:40)**
20/08/15	24.9	26.6	72.0	1017.4	1.4	SW	490.5	13:50	0.0	6.4	9.6	(12:40)
21/08/15	25.4	26.5	63.6	1018.5	1.3	N	441.9	13:40	0.0	6.0	9.2	(12:10)
22/08/15	25.1	26.2	63.1	1016.7	1.4	NW	469.8	13:30	0.0	6.2	9.3	(12:30)
23/08/15	25.0	25.9	66.4	1015.6	1.2	SE	468.4	13:30	0.0	6.3	9.5	(13:10)
24/08/15	26.2	25.9	59.9	1016.0	0.9	SE	372.2	13:30	0.0	5.6	9.8	(14:00)
25/08/15	27.1	26.0	71.7	1016.8	2.0	S	430.1	13:40	0.0	6.0	9.6	(13:10)
26/08/15	26.2	26.2	65.0	1017.4	1.2	NW	468.2	13:30	0.0	6.2	9.0	(12:50)
27/08/15	27.0	26.1	65.0	1017.5	0.9	--	452.3	13:40	0.0	6.1	9.1	(13:10)
28/08/15	27.8	26.1	63.4	1019.6	1.0	NE	447.2	13:30	0.0	5.8	8.7	(13:00)
29/08/15	29.0	26.1	56.0	1020.9	1.0	NW	446.4	13:20	0.0	5.7	8.5	(12:50)
30/08/15	29.4	26.1	52.5	1020.2	1.1	SW	448.3	13:20	0.0	5.7	8.5	(12:30)
31/08/15	27.9	26.6	65.1	1017.8	0.9	SE	433.3	13:20	0.0	5.9	8.7	(12:40)

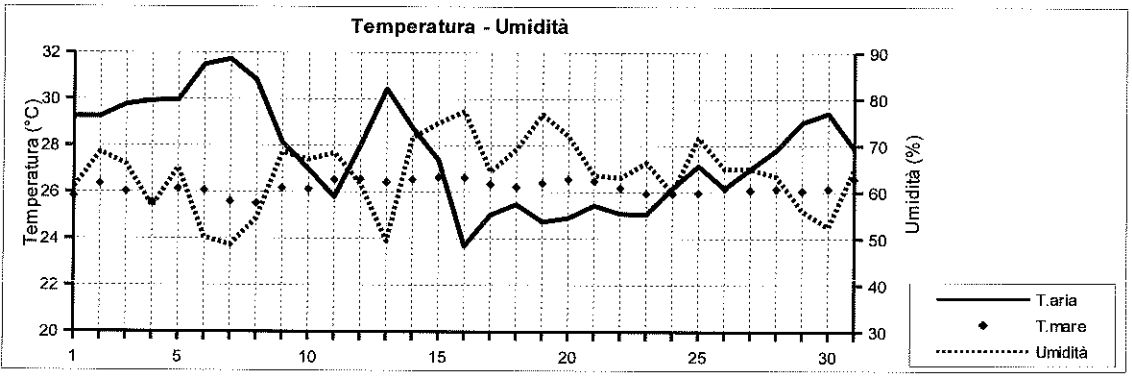

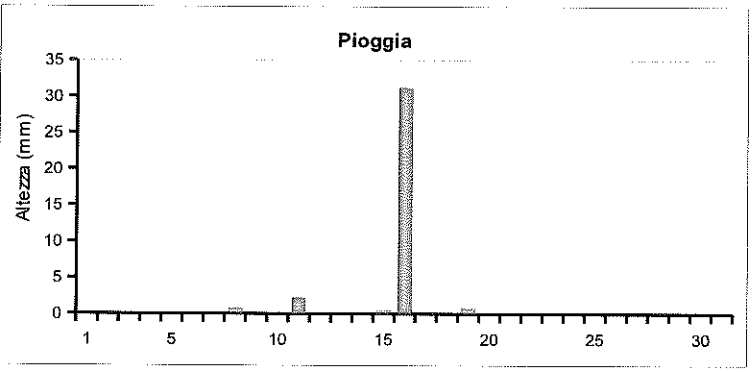

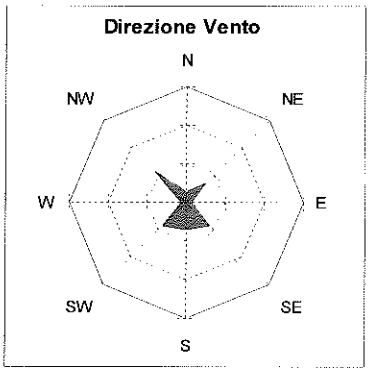

AGOSTO 2015

(estremi giornalieri)

Data	Temperatura (°C)				Umidità (%)				Pressione (hPa)				Vento (m/s)		Radiazione (W/m²)	
	min	(ore)	max	(ore)	min	(ore)	max	(ore)	min	(ore)	max	(ore)	max	(ore)	max	(ore)
01/08/15	25.7	(06:40)	32.9	(12:30)	49.0	(12:20)	76.0	(17:50)	1011.1	(04:10)	1015.6	(21:50)	8.0	(14:30)	835.0	(13:10)
02/08/15	26.6	(06:20)	32.0	(16:10)	55.0	(09:10)	82.0	(03:50)	1013.9	(19:30)	1016.5	(13:10)	8.9	(21:30)	990.0	(13:10)
03/08/15	26.2	(06:40)	33.9	(16:00)	49.0	(16:00)	87.0	(03:00)	1012.5	(16:40)	1015.1	(00:00)	9.8	(16:50)	925.0	(13:00)
04/08/15	26.3	(06:00)	33.2	(15:20)	41.0	(16:40)	73.0	(00:00)	1012.2	(17:50)	1014.2	(00:10)	7.6	(15:10)	826.0	(12:50)
05/08/15	26.7	(06:00)	33.8	(19:00)	44.0	(18:50)	79.0	(06:20)	1012.3	(17:50)	1014.5	(09:50)	6.3	(13:50)	835.0	(13:00)
06/08/15	27.4	(05:10)	35.7	(15:10)	39.0	(17:00)	66.0	(00:10)	1011.9	(18:50)	1014.5	(07:20)	7.6	(15:20)	830.0	(13:10)
07/08/15	28.1	(21:30)	36.8	(15:10)	35.0	(11:10)	73.0	(21:20)	1011.9	(15:40)	1015.1	(20:50)	8.5	(18:10)	786.0	(13:20)
08/08/15	28.1	(22:10)	**37.1**	**(15:00)**	35.0	(15:10)	74.0	(21:30)	1013.3	(16:20)	1016.3	(22:40)	**14.8**	**(15:20)**	835.0	(15:00)
09/08/15	24.3	(21:50)	31.0	(13:40)	56.0	(18:50)	80.0	(18:10)	1013.8	(16:20)	1016.6	(21:40)	14.8	(18:40)	796.0	(13:20)
10/08/15	24.4	(06:00)	30.1	(16:30)	56.0	(04:20)	76.0	(18:40)	1011.2	(18:10)	1016.0	(00:00)	8.0	(21:10)	865.0	(11:30)
11/08/15	22.7	(10:40)	28.2	(15:10)	57.0	(15:10)	83.0	(09:20)	1010.1	(04:30)	1013.4	(23:00)	10.7	(01:10)	**1136.0**	**(13:30)**
12/08/15	24.8	(00:10)	32.7	(15:20)	44.0	(16:00)	72.0	(00:00)	1012.7	(03:50)	1015.3	(00:00)	11.2	(13:40)	1121.0	(12:50)
13/08/15	25.4	(07:00)	35.5	(14:40)	**31.0**	**(13:50)**	73.0	(00:40)	1011.8	(19:20)	1015.5	(00:10)	8.0	(15:40)	798.0	(13:20)
14/08/15	26.6	(06:20)	31.5	(14:40)	60.0	(00:00)	87.0	(19:20)	1010.5	(18:30)	1012.9	(10:50)	6.7	(16:00)	777.0	(13:10)
15/08/15	25.6	(15:50)	29.8	(12:50)	52.0	(17:00)	86.0	(01:10)	1009.7	(20:10)	1011.4	(01:10)	7.2	(14:50)	962.0	(13:00)
16/08/15	**19.8**	**(08:10)**	26.5	(00:00)	64.0	(15:50)	**92.0**	**(09:20)**	**1009.0**	**(07:10)**	1011.7	(23:30)	11.2	(19:00)	925.0	(15:20)
17/08/15	22.2	(04:10)	28.2	(15:40)	48.0	(13:10)	76.0	(06:10)	1011.2	(04:20)	1013.9	(00:00)	8.5	(08:20)	895.0	(12:10)
18/08/15	22.7	(05:00)	27.5	(18:00)	63.0	(02:10)	74.0	(20:30)	1013.3	(03:30)	1015.4	(21:40)	7.6	(12:40)	1021.0	(13:20)
19/08/15	21.6	(15:10)	27.4	(12:10)	68.0	(12:20)	85.0	(15:10)	1013.7	(05:30)	1016.0	(00:00)	11.6	(14:10)	1014.0	(13:00)
20/08/15	22.3	(05:50)	27.5	(17:20)	52.0	(17:50)	85.0	(04:40)	1015.9	(04:50)	1019.0	(23:00)	6.3	(11:40)	870.0	(11:40)
21/08/15	22.7	(05:50)	28.8	(16:40)	53.0	(14:40)	74.0	(01:40)	1017.5	(17:20)	1019.3	(08:50)	7.2	(17:40)	995.0	(12:20)
22/08/15	22.2	(06:20)	28.2	(14:10)	48.0	(11:20)	71.0	(06:00)	1015.3	(18:20)	1018.6	(00:00)	6.7	(15:00)	946.0	(14:10)
23/08/15	22.3	(06:00)	27.7	(15:00)	59.0	(14:00)	72.0	(04:00)	1014.6	(06:20)	1016.3	(10:20)	7.6	(15:30)	812.0	(13:20)
24/08/15	22.4	(07:10)	29.8	(16:40)	44.0	(12:20)	78.0	(06:20)	1015.3	(05:20)	1016.8	(09:40)	4.9	(14:10)	1032.0	(14:00)
25/08/15	25.2	(23:30)	29.5	(16:00)	53.0	(00:10)	82.0	(04:00)	1015.4	(06:40)	1018.4	(23:30)	7.6	(10:00)	965.0	(11:40)
26/08/15	22.8	(06:30)	30.2	(15:10)	45.0	(15:40)	78.0	(01:20)	1016.2	(19:20)	1018.4	(00:20)	7.2	(16:00)	807.0	(12:50)
27/08/15	23.4	(06:30)	31.1	(15:50)	42.0	(15:50)	79.0	(03:40)	1016.6	(04:00)	1018.7	(23:30)	5.8	(12:50)	793.0	(13:00)
28/08/15	23.4	(05:40)	32.2	(15:10)	45.0	(10:40)	81.0	(06:00)	1018.6	(00:00)	1020.8	(22:00)	5.8	(14:30)	789.0	(13:20)
29/08/15	24.5	(05:50)	33.7	(15:50)	40.0	(17:40)	80.0	(05:40)	1019.9	(17:20)	**1021.8**	**(10:50)**	5.8	(13:20)	780.0	(12:50)
30/08/15	26.7	(03:30)	34.1	(16:10)	38.0	(16:40)	75.0	(19:40)	1018.9	(17:00)	1021.3	(09:10)	6.3	(14:30)	791.0	(13:00)
31/08/15	25.1	(06:30)	30.8	(17:00)	48.0	(09:20)	81.0	(23:20)	1016.0	(19:30)	1019.6	(00:00)	6.3	(13:00)	773.0	(13:10)

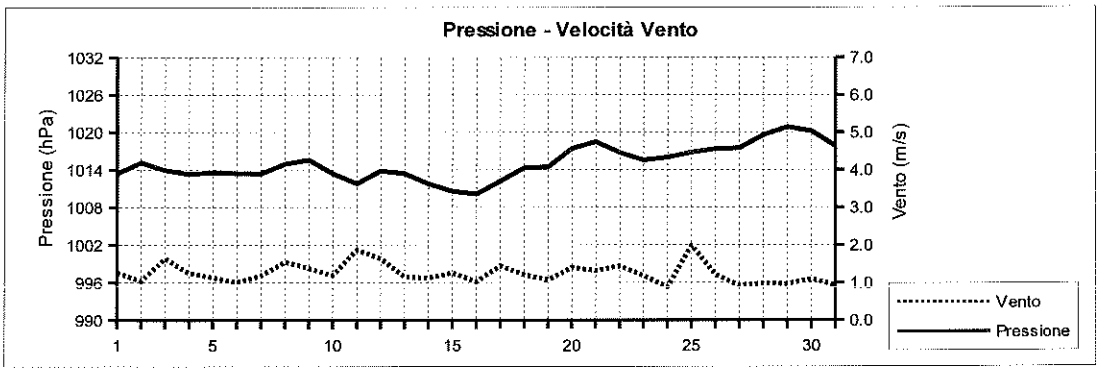

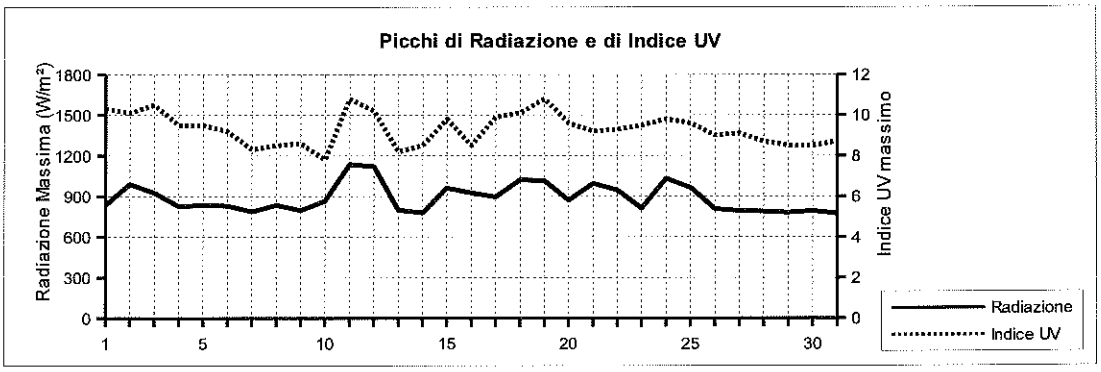

SETTEMBRE 2015

(medie giornaliere)

Data	Temperatura aria (°C)	Temperatura mare (°C)	Umidità %	Pressione hPa	Vento m/s	Vento direzione	Rad. Solare W/m²	Rad. Solare durata	Pioggia mm	Indice UV medio	Indice UV max	Indice UV (ore)
01/09/15	27.3	26.5	69.5	1014.9	1.0	SE	433.6	13:20	0.0	6.1	8.7	(12:50)
02/09/15	26.9	26.3	70.0	1014.3	1.3	S	437.3	13:00	0.0	6.3	9.1	(13:00)
03/09/15	26.5	26.4	76.5	1014.8	1.4	S	438.4	13:00	0.0	6.3	9.1	(11:20)
04/09/15	25.8	26.5	77.8	1015.3	1.3	SE	331.4	13:00	10.4	5.7	8.8	(12:50)
05/09/15	25.3	26.2	76.3	1014.1	2.3	NW	194.7	12:40	12.7	4.3	7.7	(13:50)
06/09/15	24.0	26.1	67.2	1017.5	1.0	NW	318.4	12:40	0.0	5.9	**10.0**	**(12:50)**
07/09/15	24.1	26.1	62.4	1017.2	1.3	NW	451.3	13:00	0.0	6.0	8.5	(12:40)
08/09/15	23.6	25.7	48.7	1017.0	2.3	NE	356.4	13:00	0.0	5.8	8.9	(13:40)
09/09/15	22.5	24.9	46.6	1013.1	2.5	NE	167.7	12:40	0.0	5.0	7.1	(13:30)
10/09/15	22.8	24.4	52.5	1013.2	1.5	NE	422.2	12:30	0.0	6.0	8.4	(12:40)
11/09/15	22.9	24.2	58.6	1019.5	1.5	NW	342.0	12:50	0.0	5.3	7.5	(13:20)
12/09/15	23.5	24.2	64.6	1022.3	1.0	--	431.3	12:50	0.0	5.9	8.2	(13:00)
13/09/15	24.0	24.2	60.7	1019.8	1.2	--	420.0	12:40	0.0	5.9	8.6	(12:20)
14/09/15	25.3	24.1	62.7	1016.6	1.5	SW	399.7	12:30	0.0	5.6	8.1	(12:40)
15/09/15	25.9	24.3	82.9	1015.9	2.4	S	363.3	12:40	0.0	5.3	7.9	(12:30)
16/09/15	27.6	24.6	62.6	1015.0	0.9	SW	404.9	12:20	0.0	5.3	7.8	(13:20)
17/09/15	29.4	24.8	43.7	1014.9	0.8	NW	408.6	12:30	0.0	5.5	7.8	(12:50)
18/09/15	29.0	25.1	48.7	1016.4	0.9	SW	400.5	12:30	0.0	5.4	8.0	(12:30)
19/09/15	25.9	25.3	78.7	1016.9	0.8	NW	276.7	12:30	0.0	4.8	8.0	(14:00)
20/09/15	23.4	25.5	65.8	1013.0	1.5	NW	330.0	12:20	1.0	5.2	8.3	(13:30)
21/09/15	23.7	25.4	50.2	1010.9	2.0	N	419.3	12:10	0.0	5.8	8.0	(12:50)
22/09/15	22.3	25.3	58.5	1010.7	1.6	NW	394.4	12:20	0.0	5.5	7.6	(13:00)
23/09/15	22.8	25.2	70.0	1010.4	1.8	SW	263.2	12:00	11.7	5.0	8.2	(12:40)
24/09/15	19.7	24.8	72.5	1010.3	1.4	W	309.0	12:10	15.2	5.2	8.2	(13:10)
25/09/15	19.9	24.8	72.7	1012.7	1.0	--	346.3	12:00	0.0	5.8	8.5	(12:30)
26/09/15	21.0	24.5	59.8	1014.6	2.2	NE	323.8	12:10	0.0	6.0	8.0	(13:00)
27/09/15	21.2	24.3	55.7	1017.2	2.5	NE	383.0	12:00	0.0	6.2	8.5	(12:40)
28/09/15	20.6	24.2	57.2	1019.3	2.7	NE	407.1	12:00	0.0	6.2	8.5	(12:30)
29/09/15	20.0	23.9	54.4	1020.5	2.1	NE	379.8	12:00	0.0	6.1	8.2	(13:30)
30/09/15	20.1	23.8	54.3	1020.8	1.8	NE	392.3	12:00	0.0	6.1	8.6	(12:30)

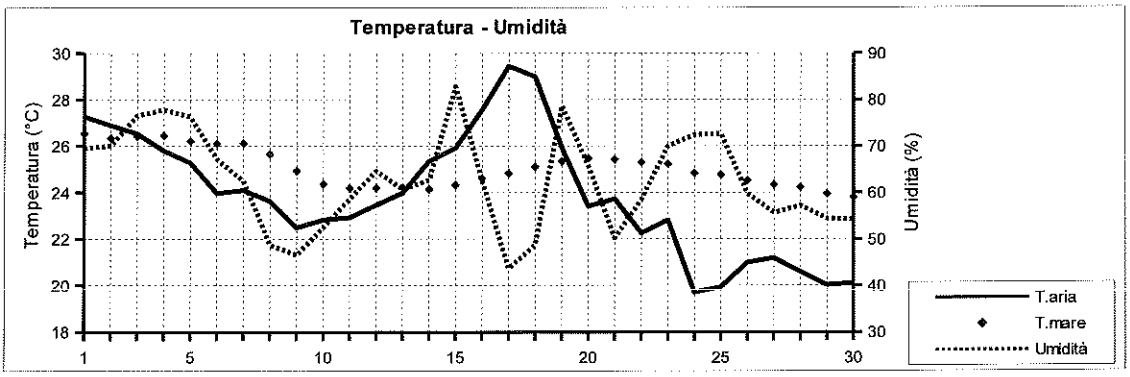

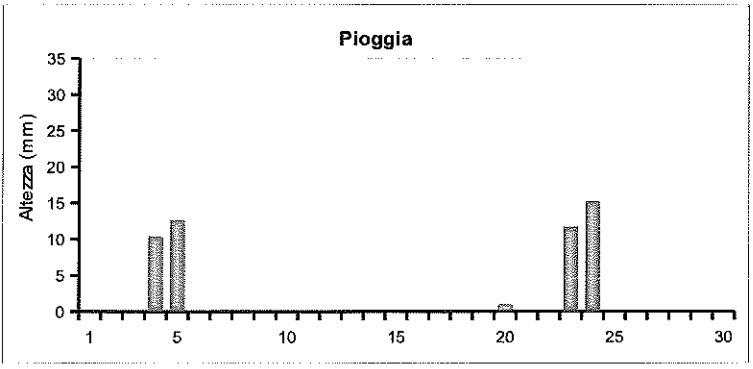

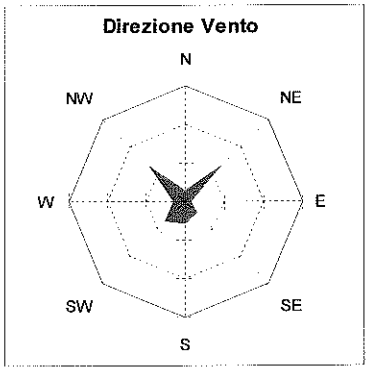

SETTEMBRE 2015

(estremi giornalieri)

Data	Temperatura (°C)				Umidità (%)				Pressione (hPa)				Vento (m/s)		Radiazione (W/m²)	
	min	(ore)	max	(ore)	min	(ore)	max	(ore)	min	(ore)	max	(ore)	max	(ore)	max	(ore)
01/09/15	24.2	(06:30)	29.8	(13:30)	55.0	(20:10)	82.0	(00:20)	1013.7	(18:50)	1016.1	(00:00)	7.2	(15:00)	770.0	(13:10)
02/09/15	24.6	(05:10)	29.9	(16:50)	41.0	(17:00)	83.0	(06:50)	1013.6	(05:20)	1015.5	(00:00)	7.2	(14:40)	756.0	(13:20)
03/09/15	24.6	(06:20)	28.4	(14:10)	65.0	(16:30)	82.0	(02:00)	1013.4	(18:00)	1015.7	(11:00)	6.7	(13:20)	765.0	(13:10)
04/09/15	22.2	(17:30)	28.9	(13:10)	70.0	(19:10)	88.0	(17:20)	1014.4	(03:50)	1017.2	(23:40)	**17.4**	**(16:50)**	773.0	(13:40)
05/09/15	22.7	(06:00)	28.7	(10:40)	59.0	(10:40)	90.0	(12:40)	1012.5	(09:00)	1016.5	(23:50)	14.3	(04:10)	912.0	(14:00)
06/09/15	22.0	(05:00)	26.4	(14:30)	61.0	(00:50)	75.0	(04:30)	1016.4	(00:00)	1018.7	(21:20)	7.2	(00:00)	**1041.0**	**(11:30)**
07/09/15	20.3	(06:30)	27.2	(15:20)	48.0	(16:40)	79.0	(05:50)	1015.7	(16:50)	1018.7	(00:50)	6.7	(22:50)	796.0	(12:50)
08/09/15	20.9	(07:00)	27.0	(14:50)	34.0	(18:10)	58.0	(02:50)	1015.7	(16:40)	1018.1	(10:00)	8.9	(11:20)	854.0	(13:40)
09/09/15	20.1	(05:50)	25.0	(14:00)	36.0	(14:10)	65.0	(23:10)	1009.8	(18:30)	1016.6	(00:40)	11.2	(21:10)	490.0	(09:30)
10/09/15	20.2	(01:10)	26.4	(17:00)	40.0	(13:00)	64.0	(00:00)	1011.0	(00:20)	1017.3	(23:50)	9.4	(00:00)	837.0	(11:10)
11/09/15	19.9	(06:10)	26.1	(15:00)	49.0	(10:50)	69.0	(00:00)	1017.1	(00:00)	1022.6	(00:00)	6.7	(15:10)	816.0	(13:20)
12/09/15	19.7	(06:50)	27.2	(15:30)	48.0	(16:00)	76.0	(23:40)	1021.2	(18:20)	**1023.5**	**(10:30)**	6.3	(14:40)	742.0	(13:00)
13/09/15	20.0	(04:50)	27.2	(14:20)	40.0	(16:50)	79.0	(02:50)	1018.3	(19:20)	1021.6	(00:00)	7.2	(15:00)	835.0	(12:20)
14/09/15	22.1	(03:20)	28.4	(15:10)	45.0	(09:00)	80.0	(18:50)	1015.1	(17:00)	1018.4	(00:00)	8.5	(16:10)	812.0	(12:00)
15/09/15	24.7	(23:50)	27.4	(14:00)	76.0	(00:00)	89.0	(06:00)	1014.8	(18:40)	1017.2	(11:20)	8.5	(12:00)	849.0	(11:40)
16/09/15	23.4	(05:10)	32.6	(14:20)	36.0	(14:20)	89.0	(01:50)	1014.5	(17:30)	1015.6	(11:10)	5.8	(14:40)	802.0	(13:40)
17/09/15	25.3	(07:40)	**34.1**	**(14:40)**	31.0	(14:30)	59.0	(01:40)	1014.3	(05:00)	1015.6	(10:40)	4.5	(13:20)	715.0	(13:00)
18/09/15	26.0	(03:50)	33.3	(15:20)	**31.0**	**(12:20)**	85.0	(20:50)	1015.2	(00:00)	1017.7	(23:40)	4.5	(12:30)	701.0	(12:50)
19/09/15	23.9	(06:00)	29.8	(16:00)	65.0	(16:10)	90.0	(06:00)	1015.3	(23:30)	1018.7	(10:40)	8.0	(10:40)	809.0	(14:00)
20/09/15	21.4	(04:50)	26.2	(13:40)	42.0	(14:30)	78.0	(01:50)	1010.6	(19:20)	1015.8	(00:20)	9.8	(01:30)	900.0	(11:50)
21/09/15	20.7	(06:00)	27.7	(14:00)	35.0	(14:20)	68.0	(06:10)	1009.2	(15:40)	1012.0	(23:10)	9.4	(14:20)	733.0	(13:00)
22/09/15	19.4	(04:30)	25.4	(13:40)	48.0	(10:30)	70.0	(23:50)	1009.6	(15:50)	1011.7	(00:00)	7.6	(14:40)	717.0	(13:00)
23/09/15	18.3	(23:40)	24.8	(12:50)	54.0	(10:00)	89.0	(00:00)	1009.2	(23:00)	1011.5	(09:40)	13.4	(23:40)	837.0	(12:30)
24/09/15	**16.8**	**(01:10)**	22.9	(16:50)	52.0	(16:20)	**92.0**	**(03:30)**	**1008.0**	**(03:50)**	1012.6	(23:30)	8.9	(17:20)	935.0	(12:40)
25/09/15	17.3	(07:30)	22.9	(16:30)	62.0	(13:20)	85.0	(07:20)	1011.4	(05:10)	1014.4	(22:50)	7.2	(16:30)	907.0	(12:00)
26/09/15	17.8	(06:40)	25.1	(15:40)	44.0	(15:00)	71.0	(06:40)	1013.5	(05:30)	1016.6	(23:50)	7.6	(11:00)	666.0	(13:20)
27/09/15	18.3	(06:00)	25.2	(14:50)	42.0	(14:20)	66.0	(03:20)	1016.1	(03:00)	1019.1	(22:20)	8.5	(16:50)	770.0	(14:30)
28/09/15	17.9	(06:50)	23.8	(14:30)	47.0	(16:30)	68.0	(07:10)	1018.5	(15:40)	1020.2	(22:20)	10.3	(19:40)	705.0	(13:10)
29/09/15	17.6	(07:10)	23.8	(15:30)	45.0	(13:30)	63.0	(07:20)	1019.4	(04:40)	1022.0	(23:10)	8.5	(09:40)	756.0	(12:20)
30/09/15	16.6	(06:50)	24.3	(14:50)	42.0	(14:30)	65.0	(07:00)	1019.6	(18:50)	1021.9	(02:20)	8.9	(10:00)	838.0	(13:10)

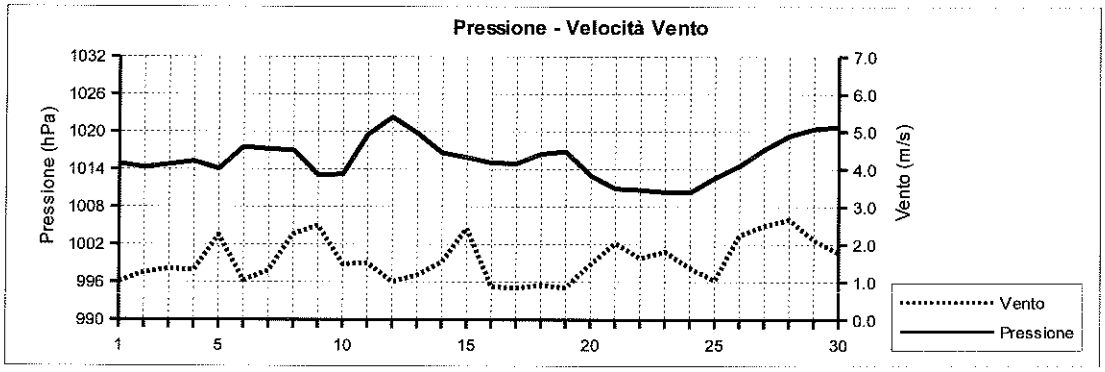

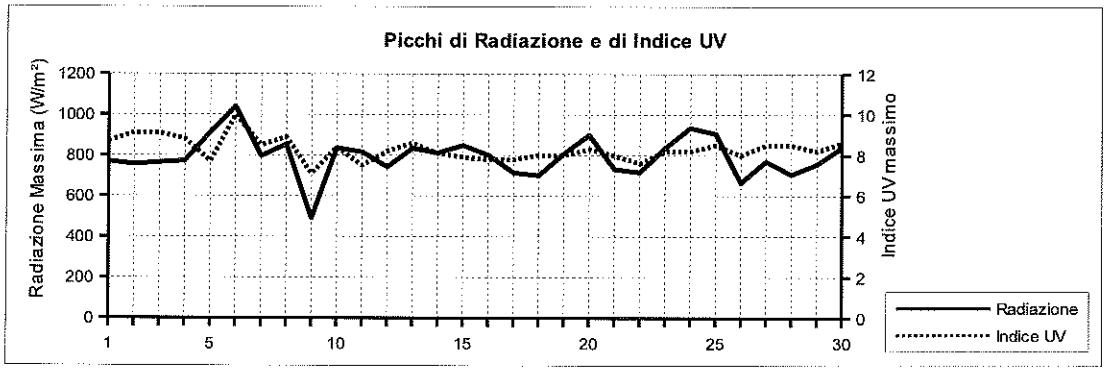

OTTOBRE 2015

(medie giornaliere)

Data	Temperatura aria (°C)	Temperatura mare (°C)	Umidità %	Pressione hPa	Vento m/s	Vento direzione	Rad. Solare W/m²	Rad. Solare durata	Pioggia mm	Indice UV medio	Indice UV max	Indice UV (ore)
01/10/15	18.7	23.6	75.2	1020.1	1.8	NW	71.6	11:00	10.1	3.6	4.8	(12:40)
02/10/15	21.2	23.4	79.8	1020.8	1.5	--	259.6	10:10	7.1	5.1	8.1	(12:50)
03/10/15	21.5	23.4	79.5	1023.1	0.8	S	402.5	11:40	0.0	6.1	8.2	(13:00)
04/10/15	20.8	23.4	78.6	1023.1	0.9	SW	321.2	11:50	0.0	5.7	7.9	(12:50)
05/10/15	21.6	23.3	84.1	1018.5	1.4	S	183.1	11:20	2.0	4.8	**8.4**	**(12:40)**
06/10/15	22.7	23.3	84.6	1013.6	1.8	S	270.9	11:10	0.0	5.6	7.6	(13:40)
07/10/15	22.3	23.4	79.6	1009.7	1.3	NW	293.9	11:40	1.0	5.0	7.3	(12:30)
08/10/15	20.7	23.3	76.3	1014.3	1.2	--	327.4	11:40	0.0	5.3	7.3	(12:50)
09/10/15	19.9	23.2	72.5	1015.4	1.3	NW	164.9	11:20	4.0	5.1	7.0	(12:30)
10/10/15	19.0	23.0	89.3	1003.2	3.3	--	44.0	10:10	32.9	3.3	4.6	(14:10)
11/10/15	18.4	22.6	86.2	1003.9	1.2	NW	188.0	11:00	6.1	4.8	7.8	(12:50)
12/10/15	18.6	22.9	77.2	1015.7	0.9	--	365.8	11:30	0.0	5.7	7.6	(12:50)
13/10/15	20.4	22.7	74.6	1016.7	1.8	S	157.2	11:10	0.0	4.9	6.8	(12:20)
14/10/15	23.0	22.3	78.3	1011.8	3.7	S	302.2	11:00	16.3	5.5	7.4	(13:10)
15/10/15	20.4	22.4	80.1	1012.4	2.2	SW	136.2	11:10	11.2	5.2	7.9	(13:40)
16/10/15	18.4	22.6	67.3	1016.9	0.9	NW	335.0	11:00	0.0	5.8	7.8	(13:30)
17/10/15	18.2	22.7	75.3	1018.8	0.8	--	328.9	11:00	0.5	5.8	7.5	(12:20)
18/10/15	19.8	22.7	66.5	1017.7	0.8	NW	195.8	11:00	0.0	5.4	7.3	(12:50)
19/10/15	21.5	22.6	78.3	1013.2	2.1	S	85.3	10:50	5.1	4.5	6.7	(13:20)
20/10/15	17.8	22.4	89.6	1012.1	2.0	NW	58.7	9:30	34.0	4.3	5.8	(13:50)
21/10/15	15.6	22.4	73.9	1010.0	3.5	N	95.6	10:10	5.6	5.1	6.3	(11:40)
22/10/15	13.8	22.3	76.1	1007.1	1.7	N	116.5	10:30	8.6	5.7	6.7	(13:10)
23/10/15	15.8	22.1	56.8	1013.8	2.1	NE	348.8	10:50	0.0	6.5	8.0	(12:20)
24/10/15	17.8	21.9	58.2	1019.6	1.1	NE	353.5	10:50	0.0	6.2	7.6	(12:40)
25/10/15	16.6	21.7	70.2	1022.6	0.4	--	259.9	10:40	0.0	5.9	7.1	(12:10)
26/10/15	16.9	21.5	77.0	1021.8	0.6	--	214.0	10:40	0.0	5.8	7.0	(11:00)
27/10/15	18.2	21.3	76.0	1020.2	0.7	NW	289.7	10:40	0.0	5.8	7.2	(11:20)
28/10/15	18.3	21.1	73.5	1018.9	0.7	--	128.6	10:50	0.0	5.1	6.7	(12:20)
29/10/15	17.5	21.1	84.4	1015.7	1.8	SW	187.7	8:50	12.4	5.2	7.0	(11:50)
30/10/15	16.4	21.0	77.3	1017.7	2.4	N	67.0	10:20	1.3	4.4	5.8	(10:40)
31/10/15	17.8	20.9	62.9	1021.7	3.3	NE	116.0	10:20	0.0	5.8	6.7	(11:20)

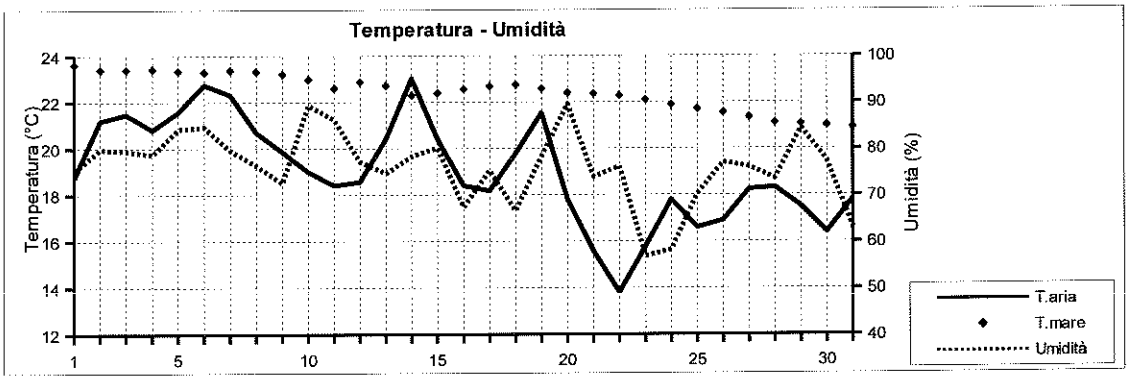

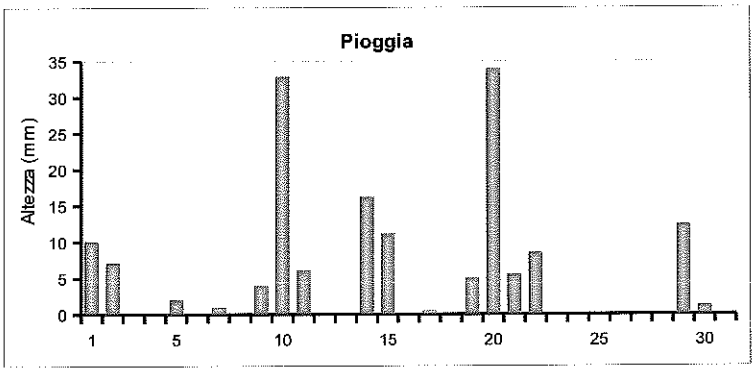

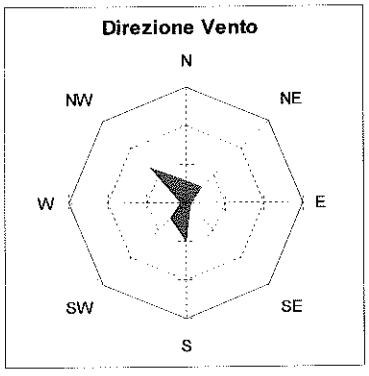

OTTOBRE 2015

(estremi giornalieri)

Data	Temperatura (°C)				Umidità (%)				Pressione (hPa)				Vento (m/s)		Radiazione (W/m²)	
	min	(ore)	max	(ore)	min	(ore)	max	(ore)	min	(ore)	max	(ore)	max	(ore)	max	(ore)
01/10/15	16.3	(08:00)	20.1	(18:40)	57.0	(01:40)	87.0	(15:10)	1018.9	(05:30)	1020.8	(22:10)	6.7	(03:40)	171.0	(10:30)
02/10/15	18.4	(09:10)	**23.9**	**(14:40)**	67.0	(12:20)	91.0	(09:30)	1019.0	(06:10)	1022.3	(23:30)	7.6	(14:10)	**905.0**	**(13:00)**
03/10/15	19.2	(07:10)	23.8	(13:30)	68.0	(12:40)	89.0	(03:50)	1022.2	(04:00)	1024.0	(10:50)	5.8	(12:40)	696.0	(13:00)
04/10/15	17.8	(05:00)	23.4	(15:10)	60.0	(14:40)	87.0	(04:50)	1021.5	(23:40)	**1024.8**	**(11:10)**	5.8	(13:10)	712.0	(12:50)
05/10/15	19.7	(07:30)	23.7	(13:20)	78.0	(12:40)	89.0	(07:50)	1015.8	(18:00)	1021.6	(00:00)	7.2	(15:00)	830.0	(13:20)
06/10/15	21.7	(05:20)	24.1	(15:00)	74.0	(15:20)	91.0	(05:00)	1011.1	(00:00)	1016.1	(00:00)	7.2	(15:20)	654.0	(13:40)
07/10/15	20.3	(00:00)	24.2	(10:40)	58.0	(17:20)	89.0	(02:20)	1008.5	(16:10)	1011.6	(23:10)	8.0	(02:30)	833.0	(12:20)
08/10/15	17.9	(04:50)	24.3	(13:30)	56.0	(16:10)	86.0	(01:20)	1011.4	(00:00)	1017.4	(23:50)	8.0	(15:20)	879.0	(13:30)
09/10/15	17.3	(22:50)	23.2	(14:00)	56.0	(14:10)	90.0	(23:00)	1011.7	(23:10)	1017.4	(00:00)	7.2	(20:00)	482.0	(12:30)
10/10/15	17.4	(01:40)	20.8	(20:20)	82.0	(14:00)	93.0	(16:30)	**997.7**	**(23:30)**	1012.2	(00:30)	**14.3**	**(20:20)**	163.0	(14:10)
11/10/15	16.3	(09:30)	20.9	(16:20)	68.0	(17:30)	95.0	(03:50)	997.8	(00:00)	1011.4	(00:00)	8.0	(13:40)	881.0	(12:50)
12/10/15	15.2	(06:30)	22.0	(17:00)	61.0	(13:10)	89.0	(06:50)	1011.4	(00:00)	1018.5	(23:50)	5.4	(15:50)	638.0	(13:00)
13/10/15	16.9	(06:50)	22.9	(00:00)	67.0	(10:40)	83.0	(01:20)	1014.6	(23:50)	1018.5	(02:10)	8.9	(20:10)	508.0	(12:20)
14/10/15	20.4	(23:40)	24.4	(11:30)	65.0	(00:40)	93.0	(23:50)	1008.5	(23:30)	1014.6	(00:00)	23.7	(23:40)	636.0	(12:20)
15/10/15	17.7	(23:40)	22.3	(01:50)	62.0	(17:20)	94.0	(00:50)	1009.1	(00:00)	1016.7	(23:40)	13.9	(00:10)	752.0	(13:40)
16/10/15	15.6	(06:40)	21.2	(13:10)	49.0	(13:00)	80.0	(06:40)	1015.5	(04:10)	1018.7	(22:30)	6.3	(13:30)	749.0	(14:50)
17/10/15	14.9	(08:30)	21.3	(15:50)	62.0	(16:00)	86.0	(08:20)	1017.4	(04:30)	1019.8	(11:20)	5.4	(14:30)	652.0	(13:10)
18/10/15	16.8	(07:40)	22.8	(14:40)	50.0	(15:30)	80.0	(01:10)	1015.6	(23:20)	1019.7	(00:00)	3.6	(22:50)	752.0	(12:50)
19/10/15	20.3	(00:00)	22.6	(13:30)	63.0	(03:00)	91.0	(19:00)	1011.1	(16:40)	1015.8	(00:10)	10.7	(12:50)	396.0	(09:30)
20/10/15	15.6	(19:40)	20.3	(00:00)	78.0	(23:20)	**95.0**	**(05:40)**	1010.5	(03:50)	1013.0	(12:10)	10.3	(06:10)	244.0	(12:50)
21/10/15	13.1	(17:40)	17.9	(11:40)	62.0	(11:50)	89.0	(17:50)	1006.6	(23:50)	1012.7	(00:00)	11.6	(22:00)	265.0	(11:40)
22/10/15	**11.9**	**(06:40)**	15.1	(17:20)	67.0	(00:00)	87.0	(03:40)	1005.8	(04:30)	1009.8	(00:00)	10.7	(00:10)	271.0	(13:10)
23/10/15	12.9	(00:30)	18.7	(14:00)	46.0	(13:50)	74.0	(01:00)	1009.8	(00:00)	1018.1	(00:00)	13.0	(16:30)	638.0	(13:10)
24/10/15	14.6	(04:10)	22.3	(16:30)	**45.0**	**(16:00)**	71.0	(23:50)	1017.9	(00:10)	1022.0	(23:00)	8.5	(09:50)	598.0	(12:40)
25/10/15	12.8	(06:20)	20.6	(12:30)	53.0	(11:50)	85.0	(22:00)	1021.7	(15:20)	1023.6	(22:00)	4.0	(13:10)	628.0	(12:50)
26/10/15	13.9	(05:50)	19.7	(10:30)	67.0	(10:10)	85.0	(03:00)	1020.0	(17:10)	1023.2	(00:00)	4.9	(07:30)	652.0	(10:20)
27/10/15	15.3	(03:40)	22.8	(12:30)	54.0	(12:20)	85.0	(03:20)	1019.5	(13:40)	1021.2	(09:10)	4.5	(13:00)	564.0	(12:00)
28/10/15	15.7	(06:20)	20.7	(15:10)	60.0	(13:00)	84.0	(00:50)	1017.4	(00:00)	1020.2	(08:10)	4.0	(18:30)	376.0	(14:50)
29/10/15	14.3	(23:50)	20.0	(05:30)	72.0	(15:40)	94.0	(07:50)	1014.2	(05:30)	1017.5	(00:10)	10.3	(05:30)	724.0	(10:50)
30/10/15	13.8	(02:30)	18.4	(18:30)	67.0	(21:00)	88.0	(11:50)	1016.2	(03:50)	1019.8	(21:50)	9.4	(20:50)	230.0	(10:40)
31/10/15	16.7	(00:00)	19.3	(12:20)	53.0	(12:30)	70.0	(05:10)	1019.3	(04:10)	1024.8	(22:40)	13.4	(16:00)	483.0	(11:30)

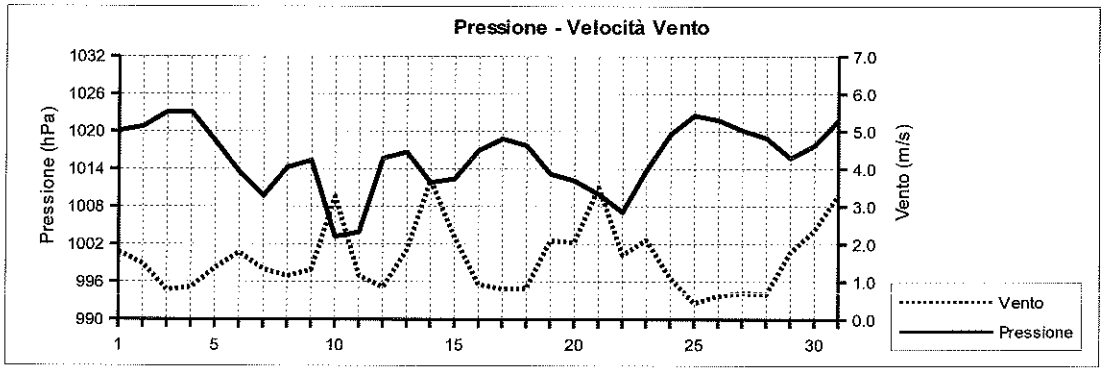

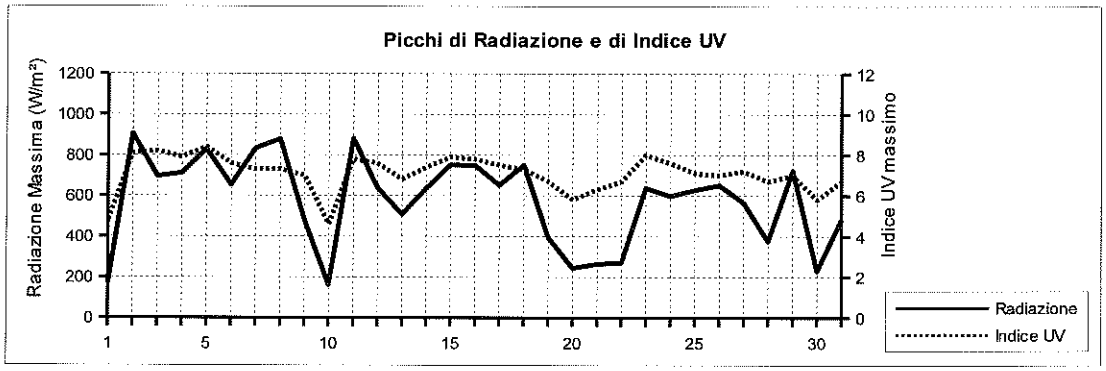

NOVEMBRE 2015

(medie giornaliere)

Data	Temperatura aria (°C)	Temperatura mare (°C)	Umidità %	Pressione hPa	Vento m/s	Vento direzione	Rad. Solare W/m²	Rad. Solare durata	Pioggia mm	Indice UV medio	Indice UV max	Indice UV (ore)
01/11/15	17.7		52.8	1025.9	2.5	NE	317.1	10:40	0.0	6.1	7.4	(11:40)
02/11/15	17.6		59.1	1028.4	2.0	NW	311.6	10:30	0.0	6.4	**8.3**	**(10:40)**
03/11/15	17.6		63.9	1028.1	1.0	NW	302.2	10:30	0.0	6.5	7.6	(11:20)
04/11/15	17.5		77.0	1023.6	0.6	N	285.3	10:30	0.0	6.4	7.5	(11:10)
05/11/15	17.9		83.7	1021.6	0.8	NW	241.2	10:20	0.0	6.2	7.0	(11:30)
06/11/15	18.2		83.3	1023.1	0.8	NW	253.3	10:30	0.0	6.2	7.0	(12:00)
07/11/15	18.8		59.0	1025.9	1.3	NW	305.1	10:20	0.0	6.5	7.5	(11:30)
08/11/15	18.4		62.5	1029.3	0.6	NE	297.0	10:20	0.0	6.5	7.6	(11:20)
09/11/15	17.5		80.9	1028.8	0.8	SE	268.4	10:10	0.0	6.3	7.3	(11:40)
10/11/15	17.5		82.1	1026.4	0.7	SW	247.3	10:30	0.0	6.4	7.3	(12:20)
11/11/15	17.2		83.2	1025.5	0.6	NW	215.3	10:00	0.0	6.0	6.7	(11:00)
12/11/15	17.0		77.7	1026.3	1.0	NW	143.9	10:00	0.0	5.9	6.6	(11:30)
13/11/15	15.9		80.8	1028.6	0.5	NW	88.8	9:50	0.0	5.9	6.6	(11:50)
14/11/15	17.3		69.8	1026.4	0.8	NW	134.0	9:30	0.0	5.8	6.7	(13:00)
15/11/15	16.1		66.8	1021.5	1.5	NW	272.5	10:00	0.0	6.4	7.2	(11:10)
16/11/15	15.8		80.4	1020.3	0.7	--	253.6	10:10	0.0	6.0	6.6	(11:10)
17/11/15	16.1		80.0	1022.3	0.7	NW	170.2	10:00	0.0	5.6	6.4	(11:10)
18/11/15	16.9		73.1	1023.3	0.8	NW	174.4	9:50	0.0	5.7	6.9	(12:00)
19/11/15	16.4		72.9	1023.8	0.8	NW	240.0	9:50	0.0	5.9	6.8	(11:20)
20/11/15	17.4		80.1	1019.2	1.3	SW	98.0	9:40	0.0	5.3	6.7	(11:20)
21/11/15	18.2		80.6	1001.0	2.8	SW	87.4	9:20	3.0	5.1	6.2	(11:20)
22/11/15	13.4		63.7	1004.4	2.1	W	160.6	9:50	3.8	4.7	7.1	(11:40)
23/11/15	11.3		80.8	1016.7	1.0	NW	61.6	9:30	12.4	4.2	6.1	(10:10)
24/11/15	12.2		82.3	1017.8	1.3	NW	102.8	9:30	1.0	4.6	5.7	(13:20)
25/11/15	12.7		70.4	1007.6	2.0	NW	219.3	9:40	1.3	6.1	6.8	(11:10)
26/11/15	9.2		83.7	996.0	2.4	N	41.0	9:10	11.6	3.7	4.8	(12:30)
27/11/15	10.7		74.6	1001.3	2.1	N	228.8	9:20	1.3	6.1	7.1	(11:10)
28/11/15	11.5		66.2	1013.3	0.6	NW	230.4	9:40	0.0	6.7	7.6	(12:40)
29/11/15	11.5		66.2	1024.1	0.7	NW	261.1	9:40	0.0	6.6	7.2	(11:30)
30/11/15	12.9		71.5	1028.8	0.7	NW	229.8	9:50	0.0	6.4	7.0	(11:20)

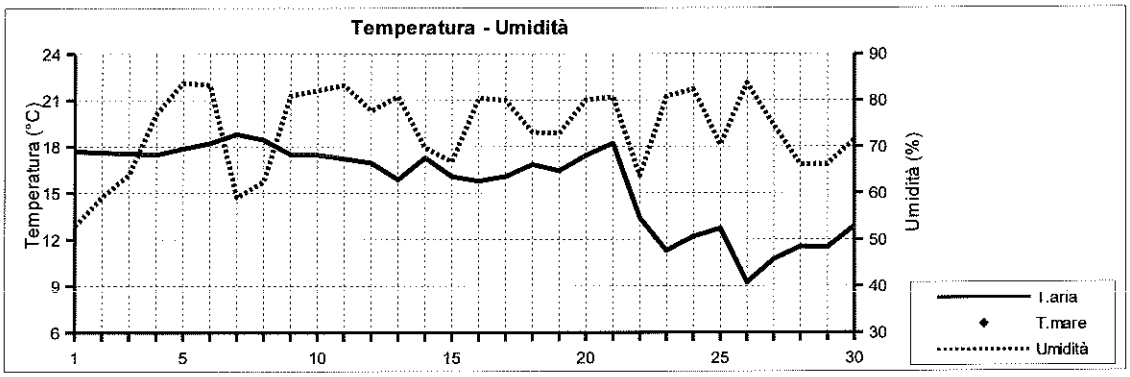

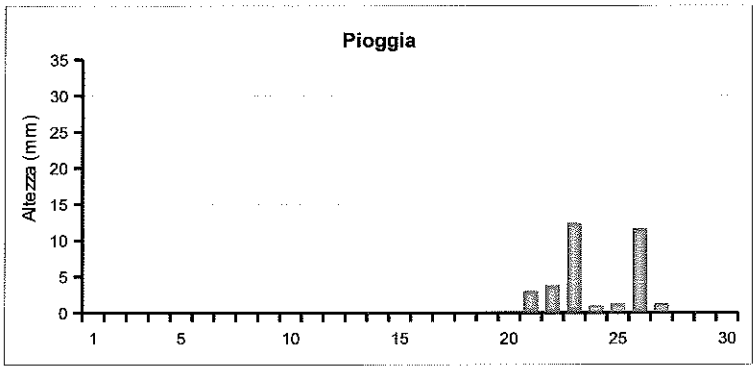

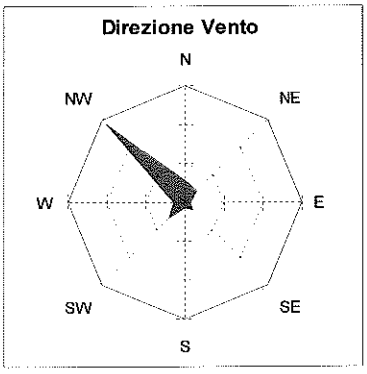

NOVEMBRE 2015

(estremi giornalieri)

Data	Temperatura (°C)				Umidità (%)				Pressione (hPa)				Vento (m/s)		Radiazione (W/m²)	
	min	(ore)	max	(ore)	min	(ore)	max	(ore)	min	(ore)	max	(ore)	max	(ore)	max	(ore)
01/11/15	15.1	(23:10)	20.8	(13:30)	41.0	(13:30)	66.0	(00:10)	1024.5	(04:20)	1027.8	(22:50)	11.2	(02:30)	554.0	(11:10)
02/11/15	14.4	(01:30)	22.2	(13:10)	48.0	(10:40)	69.0	(06:50)	1027.1	(04:40)	1029.7	(19:30)	7.2	(00:30)	531.0	(11:20)
03/11/15	14.2	(06:00)	21.9	(14:20)	50.0	(15:10)	79.0	(00:00)	1026.5	(23:40)	1029.6	(00:10)	4.5	(03:40)	510.0	(11:50)
04/11/15	14.2	(05:30)	21.3	(14:50)	63.0	(15:00)	89.0	(22:10)	1021.4	(16:20)	1026.5	(00:00)	4.5	(14:30)	487.0	(11:10)
05/11/15	15.3	(05:00)	21.3	(15:10)	73.0	(15:30)	90.0	(01:00)	1020.4	(14:30)	1022.5	(21:40)	4.5	(14:10)	547.0	(12:20)
06/11/15	14.9	(07:00)	22.0	(13:20)	68.0	(15:10)	**94.0**	**(05:30)**	1022.0	(03:50)	1024.6	(23:20)	4.0	(12:50)	497.0	(13:00)
07/11/15	14.9	(07:20)	**23.7**	**(15:10)**	**33.0**	**(15:20)**	83.0	(00:00)	1024.3	(04:10)	1028.2	(23:50)	5.8	(17:00)	519.0	(12:00)
08/11/15	14.8	(06:40)	22.6	(10:50)	43.0	(10:20)	84.0	(21:20)	1027.8	(02:40)	**1030.7**	**(10:40)**	4.0	(02:20)	584.0	(12:00)
09/11/15	14.7	(06:50)	20.6	(12:00)	70.0	(09:20)	88.0	(22:10)	1027.5	(17:20)	1030.3	(08:50)	5.8	(12:50)	499.0	(11:40)
10/11/15	15.2	(04:30)	19.7	(11:00)	68.0	(11:00)	91.0	(04:40)	1025.6	(14:10)	1027.5	(00:00)	4.5	(12:50)	563.0	(11:40)
11/11/15	14.6	(05:20)	19.8	(14:40)	75.0	(16:00)	91.0	(06:00)	1024.7	(16:10)	1026.3	(10:30)	4.0	(14:10)	520.0	(10:20)
12/11/15	14.5	(23:40)	19.1	(14:50)	69.0	(14:50)	86.0	(23:50)	1025.4	(03:20)	1027.6	(23:30)	4.5	(17:50)	338.0	(14:00)
13/11/15	13.1	(07:10)	17.8	(14:40)	70.0	(20:20)	89.0	(05:50)	1027.5	(03:00)	1030.0	(10:20)	3.6	(18:50)	171.0	(11:50)
14/11/15	15.3	(00:00)	18.8	(13:00)	61.0	(13:30)	81.0	(06:20)	1024.1	(00:00)	1028.5	(00:00)	4.5	(20:40)	330.0	(13:00)
15/11/15	13.7	(07:00)	19.8	(15:00)	52.0	(13:40)	82.0	(22:50)	1019.8	(18:00)	1024.1	(00:00)	5.8	(16:00)	515.0	(12:40)
16/11/15	13.3	(06:50)	18.4	(13:00)	70.0	(10:10)	87.0	(22:50)	1019.6	(03:50)	1021.5	(22:40)	4.0	(12:20)	573.0	(11:20)
17/11/15	14.1	(02:30)	18.6	(13:40)	67.0	(13:40)	89.0	(02:50)	1021.3	(03:30)	1023.5	(21:40)	4.5	(15:10)	475.0	(11:10)
18/11/15	15.0	(00:00)	18.9	(14:10)	63.0	(09:30)	80.0	(21:30)	1022.7	(14:40)	1024.0	(21:40)	5.4	(13:00)	**638.0**	**(12:00)**
19/11/15	13.6	(04:00)	20.2	(13:50)	56.0	(13:40)	81.0	(01:50)	1023.2	(05:00)	1024.8	(09:30)	4.0	(14:20)	527.0	(10:20)
20/11/15	15.6	(02:30)	19.1	(13:40)	73.0	(13:50)	86.0	(10:30)	1011.4	(00:00)	1023.5	(00:00)	10.3	(23:40)	501.0	(11:20)
21/11/15	15.9	(00:00)	19.6	(12:00)	59.0	(00:00)	88.0	(18:00)	**994.2**	**(17:40)**	1011.4	(00:00)	**16.5**	**(17:40)**	410.0	(10:00)
22/11/15	11.2	(08:00)	15.9	(00:00)	47.0	(05:40)	81.0	(13:30)	998.5	(00:10)	1013.5	(23:50)	15.6	(06:30)	628.0	(11:00)
23/11/15	10.5	(23:40)	12.4	(15:30)	71.0	(00:00)	90.0	(23:20)	1013.4	(00:00)	1018.7	(22:40)	8.0	(11:00)	158.0	(14:30)
24/11/15	10.4	(00:10)	14.5	(15:00)	76.0	(15:30)	91.0	(00:20)	1013.8	(23:40)	1020.1	(10:20)	8.5	(22:50)	605.0	(13:20)
25/11/15	10.8	(03:20)	15.4	(14:50)	55.0	(19:10)	86.0	(03:20)	1002.1	(00:00)	1014.0	(00:00)	8.0	(03:50)	531.0	(12:40)
26/11/15	8.1	(16:00)	11.2	(00:00)	74.0	(22:20)	92.0	(05:50)	993.8	(12:10)	1002.1	(00:00)	11.2	(05:00)	120.0	(11:40)
27/11/15	**7.8**	**(05:10)**	13.7	(13:30)	64.0	(14:00)	89.0	(05:20)	996.8	(00:20)	1008.2	(23:50)	10.3	(14:00)	587.0	(10:30)
28/11/15	9.8	(02:40)	14.5	(11:30)	53.0	(14:50)	74.0	(23:40)	1008.2	(00:00)	1019.4	(23:40)	8.9	(12:40)	605.0	(11:30)
29/11/15	8.2	(07:40)	15.4	(12:40)	43.0	(13:50)	78.0	(07:40)	1019.4	(00:00)	1027.9	(23:30)	4.0	(14:20)	462.0	(12:40)
30/11/15	9.4	(04:10)	16.6	(15:10)	54.0	(15:50)	81.0	(03:30)	1027.0	(04:00)	1030.1	(10:40)	5.4	(13:50)	571.0	(11:30)

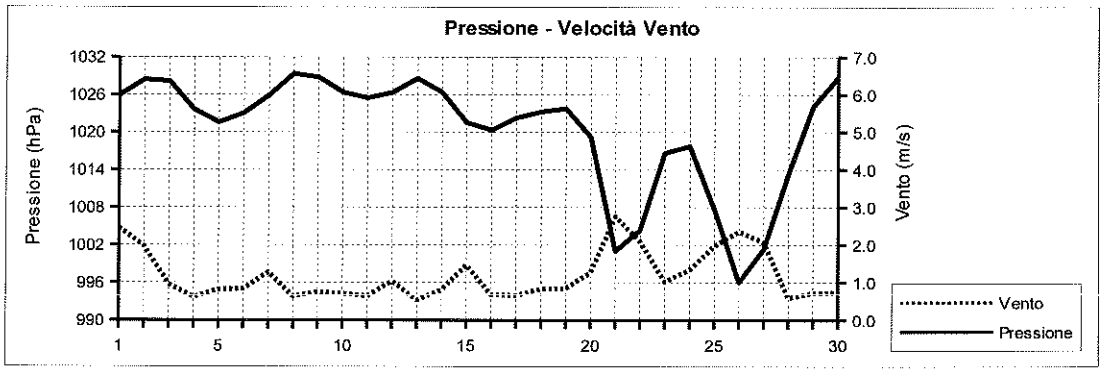

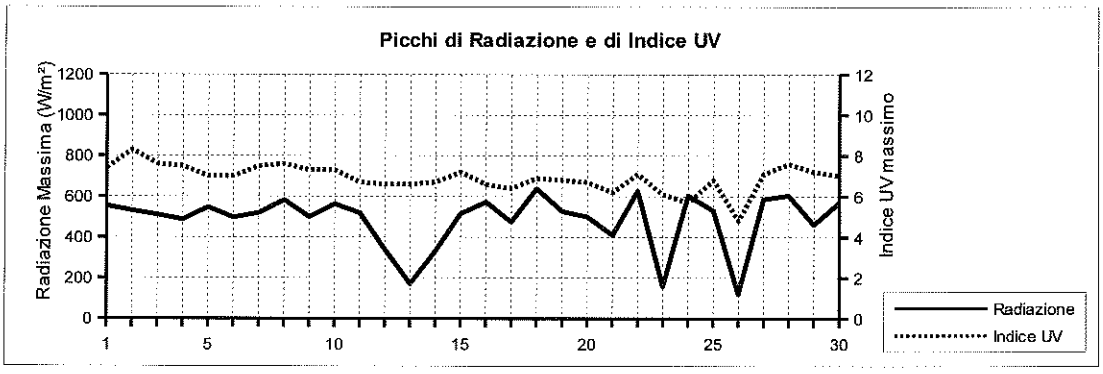

DICEMBRE 2015

(medie giornaliere)

Data	Temperatura aria (°C)	Temperatura mare (°C)	Umidità %	Pressione hPa	Vento m/s	Vento direzione	Rad. Solare W/m²	Rad. Solare durata	Pioggia mm	Indice UV medio	Indice UV max	Indice UV ora
01/12/15	15.1		78.3	1028.1	0.7	NW	120.8	9:40	0.0	5.6	6.7	(11:30)
02/12/15	14.7		78.4	1029.8	0.8	NW	238.4	9:40	0.0	6.1	6.7	(11:00)
03/12/15	14.3		77.7	1031.9	0.8	N	133.7	9:20	0.0	5.9	6.3	(11:30)
04/12/15	14.8		70.8	1034.0	0.9	NW	94.6	9:10	0.0	5.9	6.1	(11:30)
05/12/15	14.8		67.4	1035.5	0.5	N	252.1	9:20	0.0	5.7	6.3	(11:50)
06/12/15	14.2		69.0	1036.4	0.4	NE	221.1	9:20	0.0	6.0	6.6	(12:10)
07/12/15	14.3		68.2	1036.1	0.8	NW	222.4	9:40	0.0	5.7	6.5	(11:20)
08/12/15	13.6		76.2	1034.5	0.6	--	213.1	9:30	0.0	6.0	6.6	(11:20)
09/12/15	13.9		80.8	1032.0	0.7	NW	120.4	9:20	0.0	5.3	6.1	(12:50)
10/12/15	13.2		65.8	1030.7	2.3	N	216.7	9:30	0.0	6.2	7.0	(12:20)
11/12/15	12.2		65.0	1031.0	1.8	NW	236.1	9:30	0.0	6.4	6.9	(11:00)
12/12/15	11.6		72.0	1029.0	0.8	NW	229.9	9:30	0.0	6.5	6.8	(10:20)
13/12/15	12.9		73.2	1026.9	0.6	NW	142.7	9:10	0.0	5.6	6.6	(12:10)
14/12/15	11.6		75.0	1026.0	0.8	NE	208.6	9:20	0.0	5.9	6.4	(11:10)
15/12/15	11.4		68.8	1028.4	1.0	NW	223.8	9:20	0.0	5.9	6.5	(10:40)
16/12/15	12.1		64.0	1029.5	1.1	NW	216.1	9:20	0.0	5.9	6.6	(12:10)
17/12/15	12.4		62.5	1030.2	1.5	NW	228.9	9:30	0.0	6.0	6.6	(10:50)
18/12/15	11.4		70.9	1029.8	0.8	NW	216.6	9:30	0.0	5.9	6.5	(11:40)
19/12/15	12.3		77.8	1028.8	0.8	NW	157.1	9:10	0.0	5.7	6.4	(11:30)
20/12/15	13.5		70.8	1029.9	1.4	NW	221.8	9:20	0.0	5.9	6.6	(11:50)
21/12/15	13.3		72.7	1034.5	0.9	NW	218.9	9:20	0.0	5.9	**7.3**	**(11:00)**
22/12/15	12.3		78.6	1036.7	0.9	NW	208.6	9:20	0.0	5.8	6.3	(11:20)
23/12/15	12.1		79.9	1035.7	0.6	NW	185.7	9:20	0.0	5.8	6.3	(10:50)
24/12/15	12.5		83.2	1035.0	0.7	NW	178.6	9:20	0.0	5.8	6.2	(10:50)
25/12/15	12.4		78.0	1035.6	1.2	NW	167.6	9:20	0.0	5.7	6.4	(12:10)
26/12/15	12.8		71.3	1033.7	1.3	NW	191.2	9:20	0.0	5.7	6.5	(12:10)
27/12/15	12.4		72.4	1033.5	0.8	NW	227.2	9:20	0.0	5.7	6.3	(11:00)
28/12/15	12.0		76.6	1032.8	0.7	NW	211.6	9:20	0.0	5.9	6.4	(11:30)
29/12/15	12.0		80.6	1030.3	0.9	NW	169.3	9:10	0.0	5.5	6.1	(12:30)
30/12/15	11.8		68.5	1026.9	1.7	N	191.3	9:20	0.0	5.8	6.5	(11:50)
31/12/15	9.9		56.4	1027.3	1.7	N	235.3	9:20	0.0	6.5	7.1	(11:50)

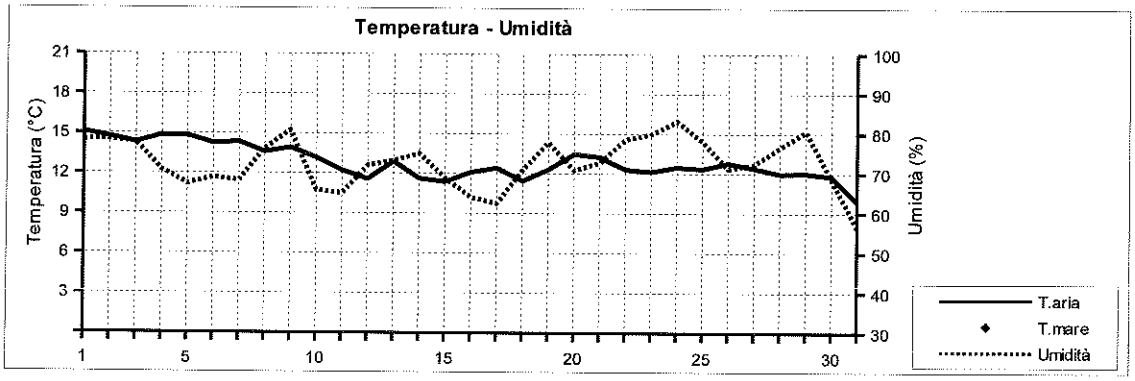

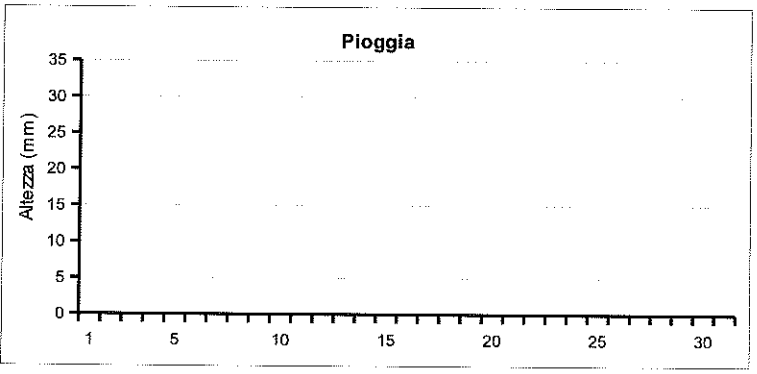

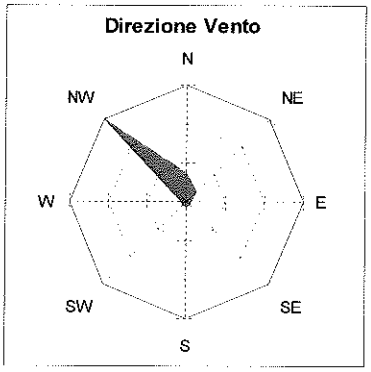

DICEMBRE 2015

(estremi giornalieri)

Data	Temperatura (°C)				Umidità (%)				Pressione (hPa)				Vento (m/s)		Radiazione (W/m²)	
	min	(ore)	max	(ore)	min	(ore)	max	(ore)	min	(ore)	max	(ore)	max	(ore)	max	(ore)
01/12/15	13.2	(01:00)	16.9	(12:20)	71.0	(11:50)	83.0	(22:40)	1027.1	(14:20)	1029.4	(00:00)	6.3	(13:50)	**599.0**	**(11:50)**
02/12/15	12.4	(05:20)	17.8	(14:20)	66.0	(11:40)	86.0	(05:30)	1028.4	(03:30)	1031.2	(22:20)	3.6	(14:50)	466.0	(11:30)
03/12/15	11.4	(03:20)	16.3	(14:30)	68.0	(13:40)	88.0	(03:30)	1030.8	(00:30)	1033.0	(23:10)	3.6	(03:20)	397.0	(10:50)
04/12/15	13.7	(07:00)	16.4	(14:00)	62.0	(13:30)	78.0	(00:00)	1032.6	(00:50)	1035.4	(10:10)	2.7	(04:10)	225.0	(12:00)
05/12/15	12.4	(06:40)	**18.5**	**(14:10)**	51.0	(13:40)	78.0	(06:40)	1034.7	(13:50)	1036.5	(22:40)	3.6	(13:00)	466.0	(12:10)
06/12/15	10.8	(08:00)	18.0	(13:40)	53.0	(12:20)	79.0	(07:20)	1035.8	(04:30)	**1037.4**	**(23:20)**	3.6	(13:30)	415.0	(12:50)
07/12/15	11.3	(06:30)	18.2	(13:10)	57.0	(13:10)	75.0	(06:30)	1035.0	(14:30)	1037.3	(00:00)	4.0	(03:30)	425.0	(12:20)
08/12/15	10.6	(06:40)	17.7	(14:20)	63.0	(12:10)	84.0	(22:00)	1033.2	(17:00)	1036.0	(10:00)	3.6	(10:30)	394.0	(12:00)
09/12/15	12.0	(07:00)	17.0	(13:50)	72.0	(14:40)	86.0	(05:20)	1030.7	(00:00)	1033.6	(00:00)	3.6	(10:50)	504.0	(12:50)
10/12/15	11.0	(23:30)	15.6	(12:30)	54.0	(14:30)	82.0	(00:10)	1029.7	(14:20)	1031.8	(10:20)	8.5	(11:50)	424.0	(11:40)
11/12/15	10.2	(02:50)	15.3	(13:40)	49.0	(12:10)	77.0	(21:10)	1029.9	(23:50)	1032.4	(10:00)	5.8	(13:00)	417.0	(11:50)
12/12/15	8.0	(04:20)	14.9	(14:30)	60.0	(14:50)	79.0	(00:00)	1028.0	(14:30)	1029.9	(00:00)	6.3	(14:50)	429.0	(13:00)
13/12/15	11.1	(00:00)	15.2	(11:40)	65.0	(15:00)	80.0	(00:30)	1025.8	(14:30)	1028.5	(00:00)	4.9	(15:10)	464.0	(12:10)
14/12/15	8.7	(08:00)	14.9	(13:20)	64.0	(11:50)	82.0	(06:10)	1025.1	(13:40)	1027.5	(23:00)	4.5	(08:10)	450.0	(13:00)
15/12/15	8.4	(05:10)	15.3	(13:50)	50.0	(14:50)	82.0	(23:30)	1027.3	(00:40)	1029.8	(22:20)	4.5	(05:50)	394.0	(12:10)
16/12/15	8.7	(04:40)	15.9	(15:20)	47.0	(13:30)	80.0	(00:00)	1028.7	(14:30)	1030.6	(23:00)	4.9	(22:30)	497.0	(12:10)
17/12/15	10.2	(04:20)	15.8	(14:40)	48.0	(13:30)	73.0	(03:10)	1029.1	(14:40)	1031.4	(09:50)	6.7	(10:50)	406.0	(11:50)
18/12/15	8.1	(07:30)	14.8	(13:50)	55.0	(12:10)	82.0	(21:30)	1029.1	(14:20)	1030.6	(09:40)	4.0	(01:20)	383.0	(12:20)
19/12/15	9.9	(03:40)	15.7	(14:00)	66.0	(14:00)	84.0	(02:40)	1027.5	(15:00)	1030.1	(09:40)	3.6	(23:40)	439.0	(11:40)
20/12/15	9.7	(03:00)	17.6	(14:00)	57.0	(13:00)	81.0	(03:00)	1028.2	(01:10)	1033.1	(23:30)	4.5	(01:10)	396.0	(12:10)
21/12/15	10.3	(07:10)	17.1	(12:10)	58.0	(11:50)	83.0	(22:20)	1032.8	(00:50)	1036.4	(23:30)	3.6	(13:30)	381.0	(11:50)
22/12/15	9.7	(05:00)	16.0	(13:20)	63.0	(15:00)	89.0	(05:10)	1036.0	(04:10)	1038.4	(10:20)	4.0	(09:00)	374.0	(11:40)
23/12/15	9.6	(06:10)	15.8	(12:30)	67.0	(11:30)	87.0	(20:40)	1034.7	(13:40)	1036.8	(10:00)	3.1	(13:20)	373.0	(12:20)
24/12/15	9.8	(07:20)	16.0	(15:20)	67.0	(15:20)	**90.0**	**(05:00)**	1033.9	(14:20)	1035.9	(09:40)	4.5	(15:50)	455.0	(12:30)
25/12/15	9.7	(07:00)	15.6	(13:20)	64.0	(13:40)	89.0	(02:20)	1034.5	(15:00)	1037.1	(09:20)	4.0	(08:40)	381.0	(12:00)
26/12/15	10.0	(07:30)	16.7	(13:10)	54.0	(12:50)	79.0	(07:40)	1032.0	(15:10)	1035.1	(00:00)	4.9	(05:20)	448.0	(12:10)
27/12/15	9.2	(06:40)	16.8	(13:00)	50.0	(12:40)	82.0	(02:10)	1032.5	(14:00)	1034.6	(10:00)	3.6	(10:50)	415.0	(12:10)
28/12/15	9.2	(06:20)	15.8	(12:50)	63.0	(10:30)	85.0	(21:00)	1031.5	(17:40)	1034.3	(09:50)	3.1	(14:20)	373.0	(12:10)
29/12/15	9.5	(07:10)	14.4	(11:20)	71.0	(12:40)	90.0	(04:30)	1029.0	(19:40)	1031.9	(00:20)	6.3	(14:10)	475.0	(12:20)
30/12/15	10.2	(06:10)	14.8	(13:20)	53.0	(14:30)	82.0	(02:50)	**1025.0**	**(14:20)**	1029.2	(00:00)	**7.2**	**(21:50)**	397.0	(11:50)
31/12/15	**7.7**	**(21:10)**	12.4	(13:30)	**44.0**	**(12:50)**	66.0	(00:10)	1026.2	(14:00)	1028.3	(19:40)	6.7	(12:00)	410.0	(12:00)

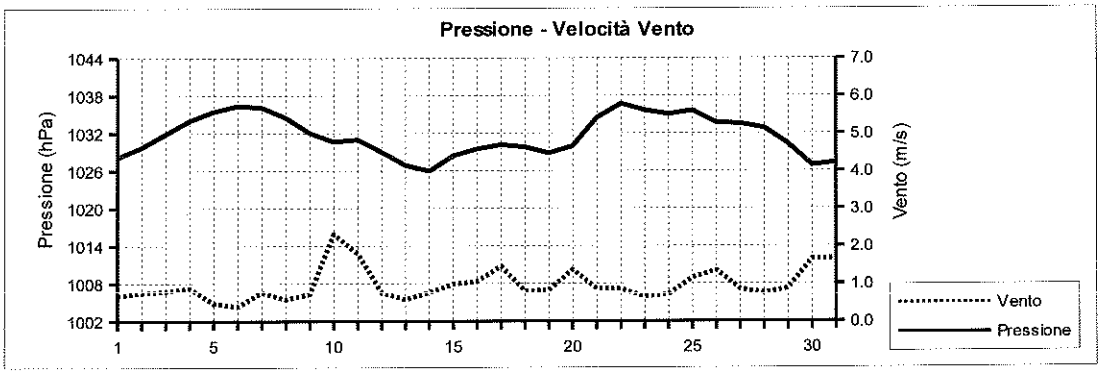

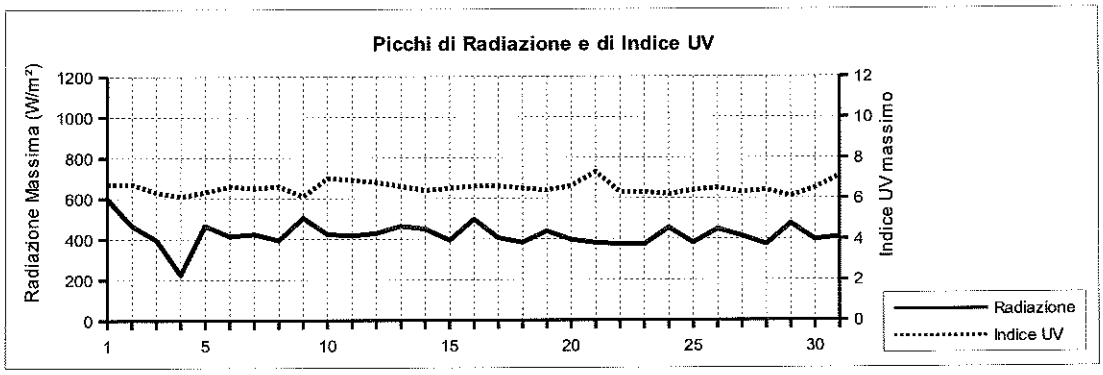

MEDIE MENSILI 2015

Mese	Temperatura aria (°C)	Temperatura mare (°C)	Umidità %	Pressione hPa	Vento m/s	Vento direzione	Radiazione Solare W/m²	Radiazione Solare Indice UV	Pioggia mm
Gennaio	10.9	15.8	73.5	1018.2	1.4	NE	160.5	2.6	177.7
Febbraio	10.4	14.6	71.9	1012.8	1.6	N	229.3	4.4	189.3
Marzo	13.0	14.7	68.8	1016.8	1.8	SW	299.6	4.9	34.3
Aprile	15.4	16.0	70.0	1019.3	1.4	SW	374.9	5.1	51.1
Maggio	20.4	19.1	68.0	1015.4	1.3	SW	424.6	5.5	30.9
Giugno	24.3	22.2	64.0	1016.8	1.2	S	444.2	5.4	50.8
Luglio	28.4	25.0	66.1	1015.0	1.0	SW	454.5	5.6	27.9
Agosto	27.7	26.2	64.0	1015.1	1.2	SW	417.7	5.9	35.5
Settembre	23.9	25.1	62.7	1015.6	1.6	SW	364.9	5.6	51.0
Ottobre	19.0	22.5	76.1	1015.8	1.6	--	215.1	5.3	157.9
Novembre	15.6	--	73.6	1020.3	1.2	N	208.1	5.9	34.3
Dicembre	12.8	--	72.6	1031.6	1.0	N	196.8	5.9	0.0
Anno	**18.5**	**20.1**	**69.3**	**1017.7**	**1.4**	**SW**	**315.8**	**5.2**	**840.7**

Mese	Temperatura (°C) min	Temperatura (°C) max	Umidità (%) min	Umidità (%) max	Pressione (hPa) min	Pressione (hPa) max	Raffiche m/s	Radiazione Massima W/m²	Radiazione Massima Indice UV
Gennaio	8.5	13.3	61.1	83.3	1015.1	1021.2	8.8	450.5	3.6
Febbraio	7.9	13.1	58.0	82.5	1009.4	1016.4	10.8	606.1	5.8
Marzo	10.5	15.9	54.0	81.0	1014.1	1019.0	9.4	751.5	6.8
Aprile	12.8	18.8	52.0	85.3	1017.2	1021.6	9.0	952.0	8.2
Maggio	17.6	24.0	50.3	82.0	1013.8	1017.1	8.2	967.1	9.1
Giugno	21.1	28.0	47.5	79.7	1015.3	1018.2	8.2	963.1	9.0
Luglio	25.4	31.9	48.1	82.2	1013.8	1016.3	7.8	872.2	9.1
Agosto	24.5	31.2	48.8	78.4	1013.8	1016.4	8.2	887.9	9.3
Settembre	21.0	27.2	48.1	76.6	1014.2	1017.3	8.5	794.6	8.3
Ottobre	16.5	21.5	62.2	86.8	1013.5	1018.3	8.7	579.4	7.1
Novembre	13.1	18.5	60.3	84.5	1017.8	1023.2	6.8	485.2	6.9
Dicembre	10.2	16.1	59.1	82.0	1030.5	1033.0	4.6	421.7	6.5
Anno	**15.7**	**21.6**	**54.1**	**82.0**	**1015.7**	**1019.8**	**8.2**	**727.6**	**7.5**

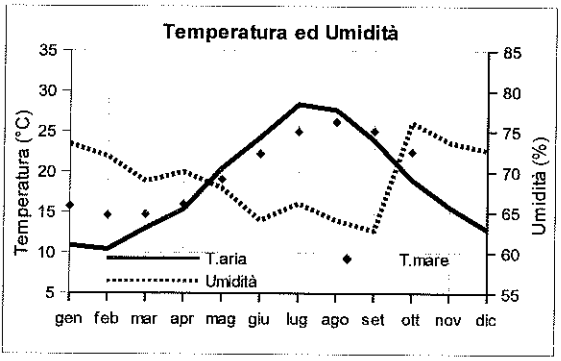

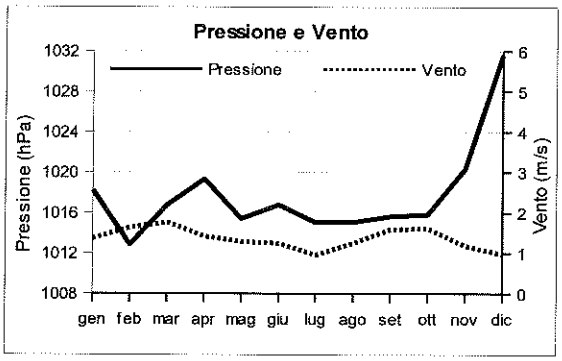

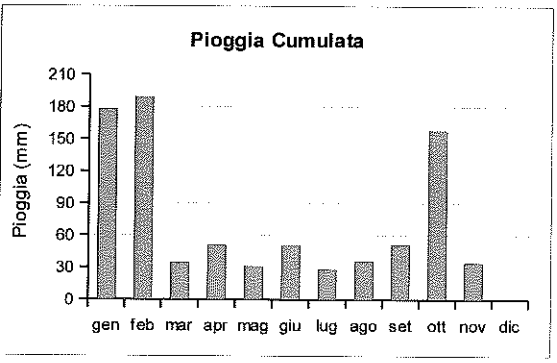

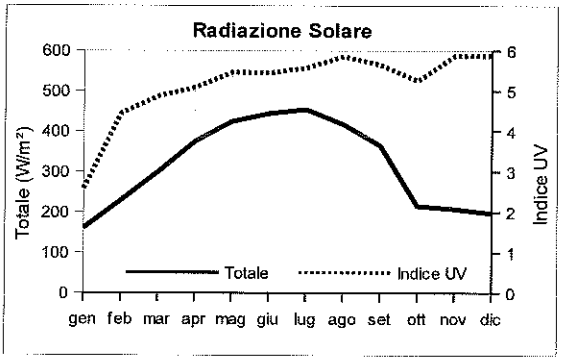

Riepilogo mensile delle precipitazioni

Mese	Pioggia Totale mm.	N. Totale giorni con pioggia	N. giorni con pioggia fino ad 1 mm	N. giorni con pioggia da 1.1 a 10 mm	N. giorni con pioggia da 10.1 a 20 mm	N. giorni con pioggia da 20.1, a 40 mm	N. giorni con pioggia da 40.1 a 60 mm	N. giorni con pioggia maggiore di 60 mm
Gennaio	177.7	15	6	2	3	4	0	0
Febbraio	189.3	16	1	9	4	1	1	0
Marzo	34.3	11	4	6	1	0	0	0
Aprile	51.1	5	1	1	3	0	0	0
Maggio	30.9	8	0	7	1	0	0	0
Giugno	50.8	3	0	0	2	1	0	0
Luglio	27.9	2	0	1	0	1	0	0
Agosto	35.5	4	2	1	0	1	0	0
Settembre	51.0	5	0	1	4	0	0	0
Ottobre	157.9	16	1	9	4	2	0	0
Novembre	34.3	7	1	4	2	0	0	0
Dicembre	0.0	0	0	0	0	0	0	0
Totali	840.7	92	16	41	24	10	1	0

Riepilogo mensile delle Tmax

Mese	N. giorni con Tmax > 10°C	N. giorni con Tmax > 20°C	N. giorni con Tmax > 30°C	N. giorni con Tmax > 35°C
Gennaio	30	0	0	0
Febbraio	26	0	0	0
Marzo	31	1	0	0
Aprile	5	10	0	0
Maggio	31	28	1	0
Giugno	30	30	6	0
Luglio	31	31	27	3
Agosto	22	22	10	1
Settembre	30	30	3	0
Ottobre	31	24	0	0
Novembre	30	10	0	0
Dicembre	31	0	0	0
Totali	328	186	47	4

Riepilogo mensile delle Tmin

Mese	N. giorni con Tmin ≤ 15°C	N. giorni con Tmin ≤ 10°C	N. giorni con Tmin ≤ 5°C	N. giorni con Tmin ≤ 0°C
Gennaio	31	26	1	0
Febbraio	28	23	3	0
Marzo	31	13	0	0
Aprile	25	5	0	0
Maggio	3	0	0	0
Giugno	0	0	0	0
Luglio	0	0	0	0
Agosto	0	0	0	0
Settembre	0	0	0	0
Ottobre	9	0	0	0
Novembre	24	5	0	0
Dicembre	31	16	0	0
Totali	182	88	4	0